ABSTRACT

Title of Dissertation: Studies in Tip Vortex Formation, Evolution and Control

Karthikeyan Duraisamy, Doctor of Philosophy, 2005

Dissertation directed by: Dr. James D. Baeder
Department of Aerospace Engineering

A high resolution computational methodology is developed for the solution of the Compressible Reynolds Averaged Navier Stokes (RANS) equations. This methodology is used to study the formation and evolution of tip vortices from fixed wings and rotary blades. The numerical error is reduced by using high order accurate schemes on appropriately refined meshes. For vortex evolution problems, the equations are solved on multiple *overset* grids that ensure adequate resolution in an efficient manner. For the RANS closure, a one equation wall-based turbulence model is used with a correction to the production term in order to account for the stabilizing effects of rotation in the core of the tip vortex.

A theoretical analysis of the accuracy of high resolution schemes on stretched meshes is performed as a precursor to the numerical simulations. The developed methodology is validated with an extensive set of experimental measurements ranging from fixed wing vortex formation studies to far-field vortex evolution on

a two bladed hovering rotor. Comparisons include surface pressure distributions, vortex trajectory and wake velocity profiles. During the course of these validations, numerical issues such as mesh spacing, order of accuracy and fidelity of the turbulence model are addressed. These findings can be used as guidelines for future simulations of the tip vortex flow field.

A detailed investigation is conducted on the generation of tip vortices from fixed wings. Streamwise vorticity is seen to originate from the cross-flow boundary layer on the wing tip. The separation and subsequent roll-up of this boundary layer forms the trailing vortex system. The initial development of the vortex structure is observed to be sensitive to tip shape, airfoil section and Reynolds number.

While experimental comparison of the computed vortex structure beyond a few chord lengths downstream of the trailing edge is lacking in the literature, for a single bladed hovering rotor, good validations of the vortex velocity profiles are achieved upto a distance of 50 chord lengths of evolution behind the trailing edge. For the two bladed rotor case, the tip vortex could be tracked upto 4 revolutions with minimal diffusion. The accuracy of the computed blade pressures and vortex trajectories confirm that the inflow distribution and blade-vortex interaction are represented correctly.

Finally, utilizing a surface boundary condition to represent a spanwise jet, the effect of tip blowing on the vortex structure is investigated. The interaction of the jet with the cross-flow boundary layer is shown to reduce the vortex strength with a marginal loss in performance.

Overall, this level of consistent performance has not been demonstrated previously over such a wide range of test cases. The accuracy achieved in the

validation studies establishes the viability of the methodology as a reliable tool that can be used to predict the performance of lift generating devices and to better understand the underlying flow physics.

Studies in Tip Vortex Formation, Evolution and Control

by

Karthikeyan Duraisamy

Dissertation submitted to the Faculty of the Graduate School of the
University of Maryland, College Park in partial fulfillment
of the requirements for the degree of
Doctor of Philosophy
2005

Advisory Committee:

Dr. James D. Baeder, Chairman/Advisor
Dr. Jewel B. Barlow,
Dr. Inderjit Chopra,
Dr. John G. Leishman,
Dr. Charles D. Levermore, Dean's Representative

ACKNOWLEDGEMENTS

No words can measure up to the sense of gratitude that I have towards my advisor Dr. James D. Baeder for making this work possible. At the expense of modesty, I would have to admit that this thesis represents just a small portion of my research exploits at the University of Maryland. Dr. Baeder, with his unique style of advising kept me focused enough to finish this work, while stimulating me to work on many other topics, in addition to letting me pursue my own research interests. The fact that we shared the same wavelength on so many problems helped in a big way. I consider myself incredibly lucky to have had him as my advisor. I would like to thank the members of my doctoral committee for their comments and suggestions that helped improve the quality of work.

I have the greatest sense of appreciation to my buddies at work for making the past four and a half years so enjoyable. In addition, Jaina and Vinit helped me so much in my research that I feel deeply indebted. The intensity with which the Aero team competed in intramural soccer will be an indelible memory that I will always cherish.

I had the oppurtunity to make so many wonderful friends outside of work that made my stint at College Park fun. It really felt like home. In particular, I'd have to thank Beer for putting up with my eccentricities and sharing my apartment for the better part of 3 years.

Needless to say, my family has always been there for support. It is they, that instilled in me the spirit of *joie de vivre* and showed me that learning is fun and encouraged me to be always curious.

TABLE OF CONTENTS

LIST OF TABLES

LIST OF FIGURES

NOMENCLATURE

Re	Reynolds Number
c	Chord
M_∞	Free-stream Mach number
U_∞	Free-stream velocity
M_{tip}	Tip mach number of the rotor blade
U_{tip}	Tip speed of the rotor blade
Ω	Angular velocity of blade rotation
α	Angle of attack
AR	Aspect ratio of wing/blade
R	Spanwise distance from axis of rotation to blade tip
θ_o	Collective pitch of blade
C_L	Lift coefficient
C_D	Drag coefficient
C_T	Thrust coefficient
FM	Figure of Merit
r_c	Core radius of vortex
x, y, z	Cartesian coordinates
u, v, w	Velocity components in the Cartesian directions
v_r, v_θ, v_x	Vortex velocity components in the radial, tangential and axial directions
r	Radial distance
ψ	Azimuthal angle ($\psi = 0$) at the trailing edge of wing tip
ρ	Density
ρ_∞	Ambient Density

ν	Kinematic viscosity
ν_t	Turbulent eddy viscosity
$\bar{\nu}$	Working variable in Spalart Allmaras turbulence model
τ_w	Wall shear stress
y^+	Wall normal distance in wall units
p	Pressure
p_∞	Ambient Pressure
C_p	$= \frac{p-p_\infty}{\frac{1}{2}\rho_\infty U_\infty^2}$ Pressure coefficient
e	Total Energy
Γ	$= 2\pi r v_\theta$ Local circulation strength of the vortex
Γ_o	Far-field circulation strength of the vortex
$\prime$	Denotes Fluctuating quantity
$< . >$	Denotes Reynolds averaging
Re_v	$= \frac{\Gamma_o}{\nu}$ Vortex Reynolds number
k	Wave number in Fourier expansion
k^*	Modified wave number in Fourier expansion
$\lvert\omega\rvert$	Magnitude of vorticity vector
$\lvert D\rvert$	Magnitude of Strain-rate tensor
C_μ	Mass blowing coefficient
U_{jet}	Jet blowing velocity

Chapter 1

Introduction

Tip vortices are formed whenever a finite lifting body such as an airplane wing or a helicopter blade moves relative to a fluid. Lift is generated primarily as the result of a difference in pressure between the upper and lower surfaces. This inequality drives the flow from the lower surface (high pressure) to sweep over to the upper surface (low pressure). Figure 1.1 shows the flow streamlines near the tip region of a simple fixed wing. Fluid particles from the lower surface of the wing are seen to be accelerated over the wing-tip. These particles cannot move indefinitely in the spanwise direction along the upper surface because of the gradual equalization of the pressure and the presence of free-stream flow, and are hence swept downstream of the wing in a swirling fashion. The resulting concentrated rotational flow structure is called the tip-vortex. The vortex continues to evolve downstream of the trailing edge, entraining vorticity from the wing boundary layer. The tip vortex and the wing boundary layer together constitute the so-called *trailed wake system*.

Within a few chord-lengths downstream of the trailing edge, the circulation strength of the tip vortex approximately equals that of the wing. Accordingly,

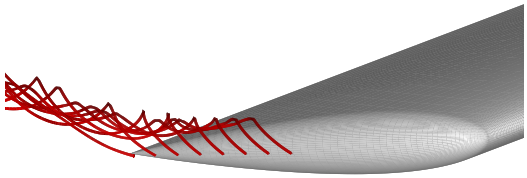

Figure 1.1: Fixed wing: Streamtraces near tip region

since airplane wings and helicopter blades are required to generate large lift (and are hence associated with large circulation strengths), practical tip vortices are found to be very strong. The swirl velocities in a tip vortex are of the same order of magnitude as the free-stream velocity (or blade-tip speed in a helicopter). For instance, a tower fly-by test conducted by Page et al. [1] revealed that the peak swirl velocity in the wake of a Boeing 757 airplane reached $100m/s$. In addition to the high strength, tip vortices are also known to be very persistent [2].

The formation and evolution of the trailed wake is highly dependent on the loading conditions on the lifting surface. In turn, the velocities induced by the wake significantly affect the loading. In the case of helicopter blades, the trailed wake from the preceding blades is known to considerably affect the structural characteristics and response [3]. Hence, there is a huge incentive to study tip vortices and trailed wakes in general.

1.1 Technological relevance

Tip vortices are found in a multitude of physical applications that include lift-generating surfaces. Typical examples include marine propellers, turbomachinery blades etc. The scope of this thesis is, however, restricted to airplane and helicopter wakes and the following paragraphs briefly describe the relevance of tip vortices and their study for these vehicles.

1.1.1 Airplane wakes

The presence of the strong tip vortex near the wing surface causes a significant downwash, reducing the effective angle of attack. This results in an *induced drag* on the wing. For a typical transport aircraft, induced drag contributes to around 35% of the total drag [4]. Further, the high energy contained in the tip vortices ultimately comes from the engine power. In typical airplane wakes, tip vortices primarily decay as a result of sinusoidal instabilities[1]that are mutually excited by the pair of counter-rotating vortices from either wings. However, it takes hundreds of span lengths for these instabilities to take effect [2] and as a result, the tip vortices remain sufficiently strong for an undesirable amount of time. This proves to be a severe hazard to other aircraft as can be seen from Fig. 1.2. The strong tip vortices can induce severe rolling moments or even cause structural damages to following aircraft. The Federal Aviation Administration (FAA) recommends a separation distance of at least 5 miles between airplanes [2]. This can restrict the capacity of airports and air-traffic in general.

[1]This is termed the Crow instability and was initially suggested by S.C. Crow [5].

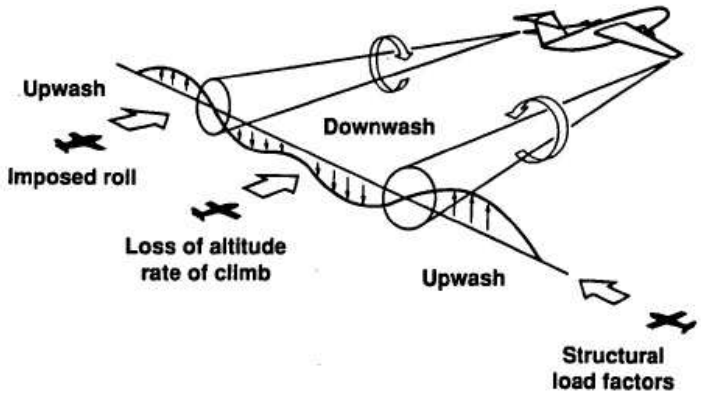

Figure 1.2: Schematic of the hazard created by airplane wakes. [6]

.

1.1.2 Helicopter wake system

Unlike an airplane wing, helicopter blades constantly operate in the wake trailed from the preceding blades and itself. The interaction of the wake with the blade (this phenomena is commonly known as Blade Vortex Interaction or BVI [7]) has profound effects on the aerodynamics and structural dynamics of the rotor system. The situation is exacerbated by the fact that these interactions can occur before the vortex has undergone any significant decay. The velocities induced by the unsteady wake results in impulsive changes in the flow encountered by the rotor blades, and can cause high noise and vibration levels. Fig. 1.3 shows a schematic of the wake generated by a typical helicopter in low speed forward flight. The shaded circles represent interactions of the blade with the tip vortices. Fig. 1.4 shows a schematic of direct interaction of the wake with the rotor blades in different flight conditions.

In flight conditions like hover, climb/descent and low-speed forward flight,

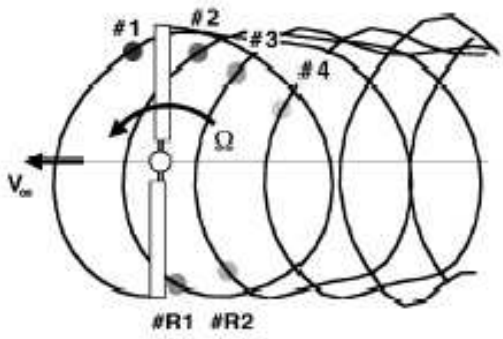

Figure 1.3: Schematic of Blade Vortex Interaction (BVI) in low-speed forward flight. [7]

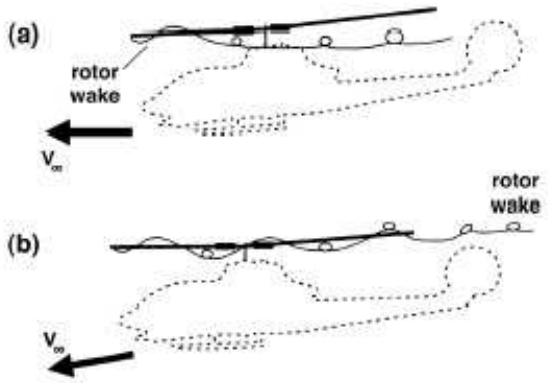

Figure 1.4: Schematic of blade-wake Interaction in (a) low-speed level flight and (b) descending flight. [7]

multiple turns of the wake remain under the rotor at all times and the resulting induced inflow has a significant effect on the performance. In addition to the effects on the main rotor, the trailed wake can interact with the fuselage, tail rotor etc. The complexity engendered by the returning wake makes the design prediction of helicopter performance very difficult.

The above discussions highlight the importance and need to understand the physics of airplane and helicopter wakes. Also, in both cases, it is apparent that reducing the strength of tip vortices without a significant loss of performance can prove to be very beneficial. Although the study of tip vortex flow-fields has been an extremely active area of research over the past century in the form of analytical, experimental and computational studies, comprehensive understanding of the intricate details of vortex formation and evolution is more qualitative than quantitative. The broad objective of this thesis is to develop a high fidelity numerical methodology that can help in understanding the process of vortex formation, roll-up and evolution. This is supplemented with theoretical studies and further numerical simulation of vortex control strategies.

1.2 Background

While studying tip vortices, it is important to make the distinction between the physics in the near-field and the far-field:

The near-field is generally considered to be the region near to and including the blade, where the vortex originally forms and rolls up, entraining the turbulent boundary layer shed from the surface.

The far-field can be considered to be the region where the vortex is fully

rolled up and is fairly independent of initial conditions [8].

However, the demarcation between the above-mentioned regions is subjective and ultimately depends on the type of problem being analyzed.

1.2.1 Physical Understanding

The physics of the flow is extremely complex in the near-field region since the process is largely turbulent (under flight conditions, the chord based Reynolds numbers for typical airplanes and helicopters can be expected to be in the range of $10^6 - 10^7$ [3]), highly three dimensional and involves high flow gradient regions involving multiple flow separations [9]. As mentioned earlier, the pressure difference accelerates the flow from the lower surface around the wing tip. This, combined with the free-stream flow, results in the formation of the tip vortex as shown in fig. 1.1. But this is an inviscid description and masks the actual near-field physics. In practice, the viscous nature of the flow introduces additional effects as shown in fig. 1.5. The cross-flow streamlines (fig. 1.5a) show transport of fluid particles from the lower surface to the upper surface. As seen from fig. 1.5b, the associated boundary layer tends to separate once the pressure gradient weakens on the top surface. In addition, a weaker secondary vortex of opposite sense (to the tip vortex) is formed. These phenomena have also been observed, for instance, in the experiments of Chow et al. [9]. These structures continue to evolve on the upper surface of the wing and are ultimately convected downstream of the trailing edge. As observed by Devenport et al. [10], the primary and secondary vortices orbit around each other and ultimately merge into one coherent vortex. Part of the wake shed by the wing is also entrained into the tip vortex. The formation and structure of the wake system is very sensitive to

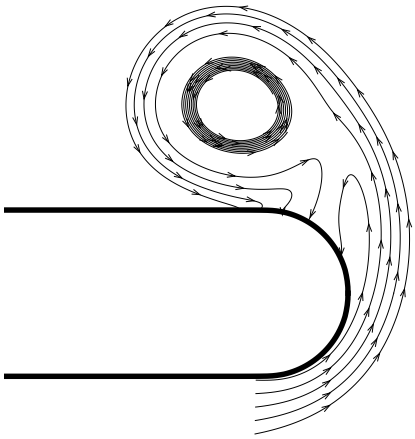

(a) Cross-flow Streamlines

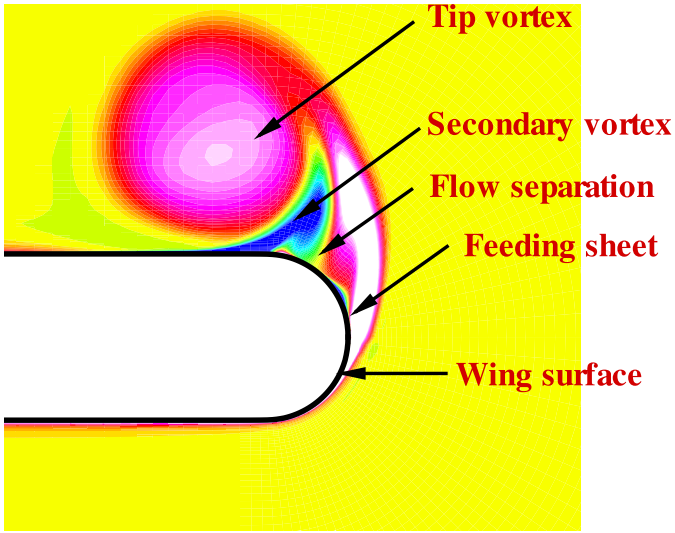

(b) Streamwise Vorticity

Figure 1.5: Vortex formation along spanwise section of a simple fixed wing

loading conditions, surface geometry etc.

In the far-field, the vortex is fully rolled-up and is found to be largely axisymmetric [10]-[13]. Many studies on wing tip vortices [9, 10] have reported largely reduced turbulence levels in the vortical core even in the near-field. This has been attributed to the near-solid body rotation that exists in the inner core. Analytical studies, based on linear stability theory of isolated vortices ([14] and references therein), have also supported this argument by showing the damping of imposed small disturbances in the core. The decay rate is primarily governed by the axial and tangential velocities that exist in the vortical core [15, 16] and in cases with small axial velocities (in relation to the tangential velocities), the major diffusion mechanism seems to be laminar rather than turbulent.

In the case of rotary wing tip vortices, different turns of the wake interact with each other [3] and could possibly merge together, a process that could change the turbulence structure drastically [17]. The magnitude of noise and vibration on a helicopter rotor is very sensitive to the core structure of the vortex and also to the distance and attitude of different turns of the wake with respect to the blades [7]. Under some flight conditions, the core of the returning tip vortex could be so close to the blade that it can mutually exchange vorticity with the blade boundary layer.

1.2.2 Numerical simulations - Levels of Analysis

As mentioned in the preceding paragraphs, the physics involved in wake formation and evolution is complicated and hence any attempts to numerically simulate the process can be expected to be arduous. Any fluid dynamic modeling of the problem has to involve the compressible Navier-Stokes equations

[18] or some approximation of the same. Usually, the cost of the computation decreases with increasing levels of approximation.

Turbulent flows are known to exhibit a wide range of length and time scales. The largest length scales can be expected to be of the order of some characteristic length of the surface, and the smallest length scales (η) are known to be the Kolmogorov scales [19]. The ratio of these scales is known to be given by the relation $\frac{L}{\eta} \approx Re^{\frac{3}{4}}$. Hence it becomes obvious that for large Reynolds numbers, the disparity of these length scales is tremendous. Turbulence theory is based on the fact that most of the energy resides in the largest scales and this energy is *cascaded* down to the smallest scales and eventually dissipated [19]. Hence, computations have to account for the whole range of scales. The cost of computing the surface pressures and wake roll-up for a simple fixed wing of aspect ratio 10 using different approximations is shown in table 1.1 - the procedure is shown in Appendix A.

Direct Numerical Simulations (DNS):

In DNS, all the scales of the flow are attempted to be resolved and there are no further modeling assumptions. Since the possible range of scales is very large, DNS is impractical in the foreseeable future even for moderate Reynolds numbers. A review of DNS applications can be found in [20].

Large Eddy Simulations (LES):

The idea of LES arises from the fact that the small scales mainly serve to drain energy from the larger scales and their effect could be modeled. The initial work in LES centered around the pioneering paper of Smagorinsky [22], in which he argued that only the large scales are affected by geometry and flow conditions and the smaller scales are more universal in nature and can hence be modeled.

Method	Modeled Turbulent scales	Resolution Requirements			
		Surf pts	Wake pts	Time steps	Tot. Ops.
DNS	No modeling	10^{16}	10^{17}	10^{8}	10^{25}
LES	Sub-grid	10^{12}	10^{9}	10^{8}	10^{20}
LES with Wall-layer model	All Near-wall, Sub-grid	10^{10}	10^{9}	10^{7}	10^{17}
RANS	All	10^{7}	10^{7}	10^{4}	10^{11}
Euler Equations	-	10^{7}	10^{7}	10^{3}	10^{10}
Inv. Vortex Method[2]	-	10^{2}	10^{2}	10^{3}	10^{5}

Table 1.1: Different levels of modeling and approximate cost of computation for a simple fixed wing at $Re \approx 5 \times 10^6$, $AR = 10$.

The *larger* eddies are resolved without modeling. Hence, the original Navier Stokes equations are *spatially filtered*, thus separating the resolved components from the modeled ones.

LES has been successfully applied to a variety of wall-bounded flows at moderate Reynolds numbers [23] and to wake flows at high Reynolds numbers. However, it has been well established [24] that LES becomes prohibitively expensive when applied to wall-bounded flows at large Reynolds numbers, because of the presence of small, but dynamically important eddies that exist near the wall. In addition to a fine discretization in the direction normal to the wall, resolution of these eddies requires fine discretizations in other spatial directions also. As seen from table 1.1, LES gives considerable savings (compared to DNS) in the wake, but not in the near-wall regions. Spalart [25] claims that an accurate LES over

[2]Involves O(N log N) computations per time-step

a simple fixed wing at flight Reynolds numbers will not possible in the next 40 years.

LES with wall-layer models:

In order to circumvent the near-wall resolution requirements in LES, hybrid methods that use Reynolds-averaged[3]treatment of the near wall region have been developed. Reference [24] presents an excellent review of such methods. In this case, all scales in the inner-layer of the near-wall boundary layer are modeled (typically using Reynolds averaged models) and coupled to an off-wall LES computation, where the larger eddies are still computed exactly. This reduces near-wall resolution requirements in directions other than the wall-normal. The savings in grid requirements are seen in table 1.1. Some issues still exist in coupling the two regions, particularly in specifying proper interface conditions [24]. Though encouraging results have been achieved on simple configurations, there do not seem to be extensive tests on wall-layer models in complex configurations.

Reynolds Averaged Navier-Stokes (RANS) Equations:

In this approach, the flow quantities are divided into a mean part and fluctuating part. The resulting equations are time or ensemble averaged, resulting in a set of equations for the mean flow that also involves the averaged turbulent quantities. These equations are presented in Chapter 3. The averaging is performed over all the turbulent scales and this results in a tremendous saving in grid requirements (as seen in table 1.1 for instance), but at the expense of more modeling requirements. The inherent deficiency of the RANS models is the fact that some of the turbulent scales (especially the large ones) depend specifically on the geometry and hence cannot be universally modeled (unlike the smaller

[3]Description of Reynolds averaging follows

more isotropic scales that are modeled in LES). Research in RANS models have been the focus of much attention in the past four decades and computations have been performed over simple and complex configurations over a wide range of Reynolds numbers. Typically, with a good knowledge of the flow-field under question along with empirical inputs to turbulence models, good validations have been obtained even for complex configurations.

Euler Equations:

The Euler equations represent the inviscid limit of the Navier-Stokes equations. In typical fixed-wing and helicopter applications, the Reynolds number is high enough that much of the flow-field can be treated in an inviscid fashion and the Euler equations can prove to provide good insight. The scope of these equations is nonetheless limited because they cannot account for near-wall effects (especially when the flow is separated), drag prediction and diffusion effects on the tip vortex. However, accurate solution of these equations can be considered to be a necessity since the same algorithms are usually used to discretize the inviscid terms in the Navier-Stokes equations [26].

Vortex and Potential-based methods:

The first studies on tip vortices were based on a vortex-filament description of lifting surfaces based on Prandtl's lifting line and lifting surface theories [27]. These *vortex based* methods are insightful, relatively inexpensive and are still very widely used in predicting lift distributions [6, 28] and even vortex roll-up [6, 29, 30]. These methods have proved to be extremely useful in rotor-wake modeling, especially in predicting vortex core positions [31], but rely heavily on empirical input. For instance, the free wake model of Bhagwat[32] assumes a vortex filament representation of the wake and hence relies on empiricism for

the vortex release locations, initial vortex strengths, core structure, viscous and turbulent diffusion.

1.2.3 Issues in Numerical simulation

In this work, numerical solution of the RANS equations will be used to study tip vortex flow fields. Over the past 20 years, there has been much research in numerical techniques for the solution of RANS equations and these methods have been applied to fixed and rotary wing tip vortex simulations [26, 33–35]. However, the fidelity and accuracy of the various methodologies have not been found to meet the industry requirements because of a variety of factors:

Numerical errors:

Even if one assumes that the governing equations exactly model the physical phenomena, numerical solution is bound to generate errors. In the case of time dependent partial differential equations like the Euler and Navier-Stokes equations, discretization errors can be viewed[4]as arising from *numerical dispersion* and *numerical dissipation* [36]. Numerical dispersion causes waves of different wave-lengths to propagate at different speeds and can result in spurious oscillations in high-gradient regions and shocks. Numerical dissipation acts as an artifical diffusion mechanism and is the primary factor that causes inaccuracy in most tip vortex calculations. Unlike non-linear features like shocks, tip vortices have no re-steepening mechanisms and hence artificial decay of the vortex will result in an irrecoverable loss of information. Typically, the use of high order accurate schemes is essential to reduce numerical errors in tip vortex simulations [38].

[4]In a linear sense

Grid requirements:

The afore-mentioned numerical errors can be reduced by using High order accurate numerical schemes in conjunction with adequate mesh resolution. In RANS-based tip vortex simulations, two different types of grid spacings are required:

In the near wall region, the normal distance between a point on the surface and the first off-surface point should be roughly one *wall-unit*[5]and the stretching in the normal direction should be small. This is required in order to accurately represent the wall shear stress in the laminar sub-layer and the buffer layers [39]. For a wing at a chord based $Re \approx 5 \times 10^6$, a wall unit would correspond to a physical spacing of $\approx 5 \times 10^{-6}c$. In addition, the spacing in the non-normal direction is also required to be orders of magnitude larger.

In the wake region, a fine mesh spacing is required to resolve the tip vortex. Based on inviscid computations on an isolated tip vortex, it is estimated that [38] at least 15 points are required across the vortical core. In addition, studies [38, 40] have also hinted at the importance of maintaining reasonable cell aspect ratios.

In practical computations, a compromise has to be achieved between maintaining the required resolution, while keeping the overall computational cost manageable.

RANS closure: The averaging of the Navier Stokes equations introduces the need for *turbulence models*. The most popularly used closure models are the linear eddy viscosity models like $k - \epsilon$ [41], Spalart-Allmaras [42] etc. In this approach, the Reynolds stress is related to the mean strain rates assuming

[5]one wall unit is defined as $\frac{\nu}{\sqrt{\frac{\tau_w}{\rho}}}$.

isotropy. Though simple, this has turned out to be the only feasible solution to turbulence modeling for complex flows and configurations.

One of the deficiencies of linear eddy viscosity closures is that these models cannot implicitly account for effects like streamline curvature and solid body rotation, which are known to be significant in tip vortex flows. On the other hand, more complex RANS closures like the so-called Second Moment Closure (SMC) [43] models can naturally account for these effects since Reynolds stresses are inherently related to flow gradients. Even though the SMC models appear to be physically appealing and have been shown to successfully model representative problems [44], consistent superiority of these models has not been established for complex problems [45]. In addition, practical implementation of these models is known to be difficult because of their inherent complexity and lack of numerical robustness [46].

As a result, there have been recent efforts addressing this deficiency of linear eddy viscosity models in that simple variants have been proposed to *sensitize* these models to streamline curvature [45–47]. In the present work, incorporation of such changes is seen to be critical to successful numerical predictions.

1.3 Motivation and Objective

The RANS equations currently represent the highest level of fluid-dynamic approximation that can be utilized in the numerical simulation of flow at Reynolds numbers relevant to flight applications. With the development of computational power over the past two decades, these simulations have been applied in the solution of complex flow-fields at high Reynolds numbers. In the case of tip

vortex simulations however, a multitude of issues serve as serious hindrances, and as a result, a successful prediction methodology has proved to be elusive to researchers.

As a case in point, the review of work conducted at United Technologies Corporation by Egolf et al. [40] is considered: Figure 1.6 shows the results of a simulation of the tip vortex trailed from a small scale wing at a Reynolds number of 140000 and an angle of attack of 5^o using 2×10^6 grid points with a Baldwin-Lomax turbulence model. It is evident that even with spatially high order accurate schemes, there is a significant underprediction of the swirl velocity and an overprediction of the radius of the vortical core. An important point to note is that these comparisons have been made very near to the trailing edge (less than 3 chord lengths). In a practical case, the wake structure has to be computed for much longer. For instance, to capture even one revolution of the rotor wake in a typical helicopter rotor, more than 60 chord lengths[6]of vortex evolution is required.

As explained in the preceding section, the issues involved in tip vortex simulations can broadly be classified under discretization effects and RANS closure effects. There has been considerable volume of work regarding the use of high order accurate schemes on fine meshes (for instance, [38, 40, 48] etc.) in an attempt to reduce discretization errors. Since the major source of error is the numerical diffusion resulting from the discretization of the inviscid terms, these studies have concentrated either on idealized isolated vortex problems or assuming inviscid conditions. In addition, none of the afore-mentioned studies addressed the issue of vortex formation. In cases where the RANS equations are used, the

[6]Typical helicopter have blade aspect ratios ≈ 10.

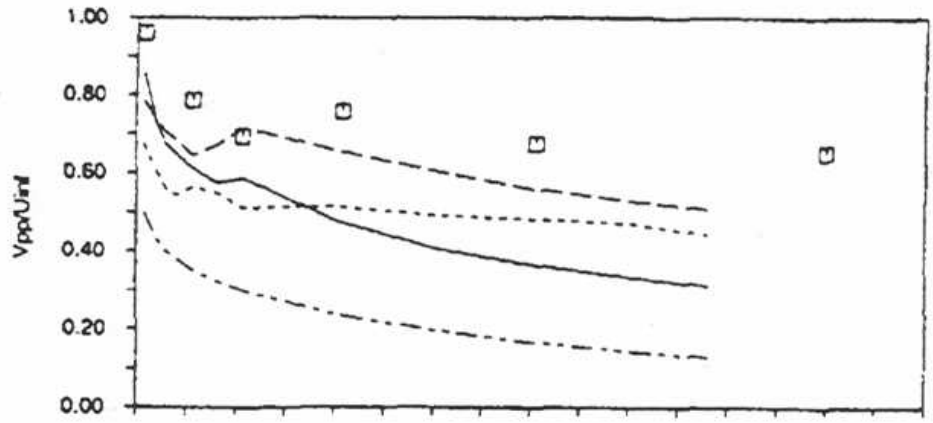

(a) Peak to peak cross flow velocity

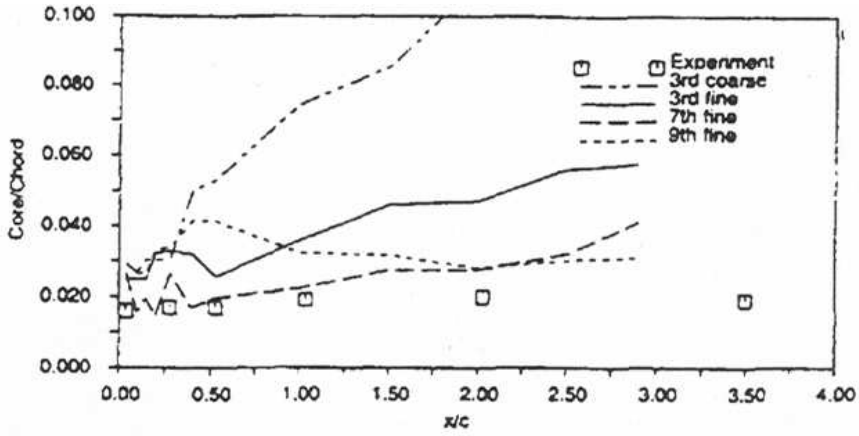

(b) Vortex core radius

Figure 1.6: Tip vortex from fixed wing at $Re = 1.5 \times 10^6$ and $\alpha = 5^o$. X axis represents streamwise distance from trailing edge.

study seems to be restricted to the very near field and experimental validations beyond a few chord lengths aft of the trailing edge are not presented. Particularly, in the case of rotary blades, comparisons of tip vortex structure with experimental measurements beyond 3 chord lengths do not seem to have been published. Most practical rotor calculations [35, 49, 51] use mesh spacings that are so coarse that accurate resolution of tip vortices becomes an unrealistic goal. Only a few studies [47, 52, 53] have questioned the capabilities of the baseline turbulence model to reasonably predict diffusion of the vortical core.

In summary, while both numerical and RANS modeling issues have been addressed in specific and in most cases, idealized situations, a comprehensive study of their effects on vortex formation *and* evolution in a practical problem is found to be lacking. In addition, comparisons of the computed tip vortex structure with experimental data is found to be particularly scarce in the literature. For rotary blades, this is compounded by the fact that reliable experimental measurements in the far-wake are difficult to come by.

The primary motivation for this thesis originates from the above-mentioned situation. In this work:

• High order accurate methods are used with enhanced grid resolution and applied to practical tip vortex problems in a RANS framework.

• With the aid of numerical validations with a wide range of experimental data sets encompassing fixed and rotary wing vortex formation and evolution, the fidelity of the numerical methodology and possible deficiencies of the RANS closure model are explored.

• Once a measure of confidence has been established, the methodology is used to understand the physics of vortex formation and evolution in detail.

• Using the baseline validations as reference points, the effect of changes in geometry and loading conditions are evaluated.

• These baseline configurations are also used as a test-bed to examine different strategies aimed at modifying the structure and reducing the strength of tip vortices.

• The attempt at physical understanding is supplemented with analytical and linear stability studies of isolated tip vortices in the far-field.

1.4 Previous Work

The primary focus of this thesis is to develop a RANS-based methodology to computationally simulate tip vortex flow fields. The broader objective is to further the understanding of the basic flow physics for existing fixed and rotary wing configurations and to evaluate various strategies of flow control. In accordance with this overall objective, a brief review of the various methods and aspects of tip vortex studies that are relevant to the current work is presented in the following paragraphs.

1.4.1 Analytical Studies

Theoretical analyses of tip vortices essentially invoke a host of assumptions and approximations to the Navier-Stokes equations such that simplified solutions can be studied. Most existing analyses use the assumption of axisymmetric flow [55]-[60]. While this assumption is valid in the far-field (invariably confirmed by experiments [10]-[13]), it is clearly not valid in the near-field because of the presence of the boundary layer shed from the surface [9].

Assuming laminar flow, Batchelor [56] derived an axisymmetric similarity solution for a steady incompressible isolated vortex and showed that, to leading order, the tangential velocity distribution is the same as that for a Lamb-Oseen vortex [62]. Further, assuming that axial gradients are much smaller than radial gradients, he showed that inviscid flow tends to accelerate the axial flow while viscous effects tend to decelerate the flow. Thus, one can expect an axial velocity excess (in relation to the free-stream) for inviscid flow and an axial velocity deficit when viscous effects are dominant. Moore and Saffman [8] extended the above analysis to the near-field by using the *light loading* (or small axial velocity perturbation) approximation. They were able to relate the vortex structure of a rectangular wing to the Reynolds number and angle of attack.

Hoffman and Joubert [55] used an isotropic eddy viscosity assumption to represent the turbulence field and used dimensional reasoning to show the logarithmic radial variation of circulation near the edge of the vortical core. Iversen [57] used the mixing length analogy of Prandtl and derived a similarity solution using empirical inputs and predicted the structure of a turbulent vortex as a function of the Vortex Reynolds number $\frac{\Gamma_o}{\nu}$. Phillips [58] studied the turbulent roll-up of a vortex sheet and was able to make detailed predictions of the structure of the tangential velocity and Reynolds stress profiles. In addition, he predicts two modes of decay of the peak tangential velocity with time depending on the relative size of the vortical core to that of the wing span.

Cotel [59] used Bradshaw's analogy [63] between streamline curvature and stratification to explain the possible re-laminarization in the vortex core. Ramasamy and Leishman [60] extended Iverson's similarity solution to account for the relaminarization and were able to correlate the tangential velocity profiles

with experiments.

1.4.2 Experimental Studies

Experimental work on tip vortices from fixed and rotary wings have mainly concentrated on mean flow measurements in the far-field. However, these measurements are complicated by the the phenomenon of apparently random *meandering* [10, 11, 79, 81, 82] of the vortical core. Meandering (or Wandering) has been attributed to a variety of reasons including free-stream turbulence [74], intermittency [75], amplification of vortex instabilities [76], perturbation due to the rolling up shear layer [77] etc. As a result of wandering, any time-averaged Eulerian point measurement becomes a weighted average in both space and time [79] and hence the measured data has to be *corrected* [10, 81]. Use of uncorrected data gives an apparent "smeared-out" version of the actual flow-field and may contribute to large errors. Empirical wandering correction models have been suggested in [10, 81, 82]. Most experimental measurements prior to the 1990s do not account for the effect of wandering and should be interpreted with caution. While the far-field vortex studies are affected by meandering, near-field studies are complicated by the fact that the flow gradients and turbulence intensities are large. In the following paragraphs, a few experiments that are relevant to the present study will be briefly surveyed:

Fixed wing studies: Singh et al. [76] used hot wire measurements to study the structure of a vortex trailed from a square-tipped rectangular wing. An initial axial velocity excess was observed and it quickly decelerated into a deficit within a downstream distance of 5 chord lengths. Measurements up to a maximum downstream distance of 85 chord lengths showed a decay of the peak

swirl velocity and turbulence levels at a rate proportional to approximately $t^{-\frac{1}{2}}$. Bandyophadhyay et al. [75] found that the Rossby number (ratio of axial velocity excess or deficit to the peak tangential velocity) was the controlling parameter for the turbulence structure in the vortex core. They found evidence of high intermittency in the vortical core and a low Rossby number was found to promote relaminarization.

Green and Acosta [79] measured the *instantaneous* flowfield around a low Reynolds number rounded tip rectangular wing. A low frequency instability was noticed in the axial and tangential velocity fields, with the axial field showing much larger amplitude fluctuations (25% of the free-stream velocity). Davenport et al. [10] made an extensive set of hot-wire measurements on a NACA 0012 wing. The vortex wandering was found to increase linearly with distance from the trailing edge. The raw measurements, when corrected for wandering suggested a core structure that was predominantly laminar. They attributed the measured high Reynolds stress levels in the core to wandering effects. Very little decay of mean quantities was observed within a downstream distance of 5-30 chord lengths.

Chow et al. [9] performed a comprehensive study of the near-field of a low aspect ratio NACA 0012 wing at a Reynolds number of 4.6×10^6 and an angle of attack of 10^o. Extensive measurements were made on the mean flow velocities, static pressure and turbulent quantities upto a distance of 0.68 chord lengths behind the trailing edge. As a result of the high Reynolds number, a very large axial velocity excess $0.77U_\infty$ was measured near the wing trailing edge. A rapid decay of the turbulent quantities was observed with downstream distance.

Rotating blade studies: Measurement in the near-field of a rotating blade

flow-field is further complicated by the blade motion and hence, most of the existing data sets do not present detailed information very close to the blade surface.

Tangler et al. [109] conducted a comprehensive study of the effects of tip shape, airfoil section, tip Mach number and collective pitch on the tip vortex structure of a hovering rotor. For the range of collective pitch that was tested, the swirl velocity was found to be of the order of $20\% - 50\%$ of the tip speed. Caradonna and Tung [83] performed hot wire velocity measurements in the wake of a two bladed hovering rotor. The measured peak swirl velocities were found to reach a maximum of 40% of the tip speed and the initial vortex core radius was found to be around 4% of the blade chord. In addition, pressure measurements were made on the blade surface.

Martin and Leishman [11] measured the swirl and axial velocities in the vortex system trailed from an isolated blade in hover. The measured data in select planes over one rotor revolution was corrected for wandering. The peak swirl velocity was found to decay at a rate that was much slower than that for the measured axial velocity deficit. The effects of blade tip shape modification were also evaluated. Ramasamy and Leishman [60], MacAlister [13] measured velocity profiles for an isolated rotor in hover. They were able to show that the swirl velocity and circulation profiles are approximately self-similar.

1.4.3 Numerical Computations

Numerical simulation of flow over fixed and rotary wings has been an extremely active area of research over the past 20 years. Most of this research has, however, concentrated on on-surface load distributions. In rotary wings, most compre-

Authors	Type	Equation	Max. downstream loc.
Mansour [33]	Fixed wing	RANS	On-blade
Srinivasan et al. [89]	Fixed wing	RANS	On-blade
Dacles-Mariani et al. [47]	Fixed wing	RANS	0.678 c
Lockard et al. [90]	Fixed wing	Euler	5 c
Spall [91]	Fixed wing	Euler	10 c
Egolf et al. [40]	Fixed wing	RANS	4 c
Russell et al. [94]	Hovering rotor	RANS	3 c
Tang [96]	Hovering rotor	Euler	30 c[7]

Table 1.2: Summary of previous work on numerical comparison of vortex profiles with experiments

hensive analyses use a prescribed/Lagrangian wake model to simulate the tip vortex induced inflow [84]. More recently, overset meshes [49–51, 85] have been used to "capture" the wake instead of modeling the same. Even though these calculations showed reasonable comparison of integrated coefficients (and sometimes surface pressures) with experimental/flight test data, only the "overall" effects of the wake were captured as a result of excessive numerical dissipation. Thus, the internal structure of the tip vortex is not addressed. While there have been many attempts in explicitly addressing grid requirements and numerical dissipation ([38, 48, 52, 86–88]), the following survey (though not all encompassing) concentrates only on those computational works that present validations of tip vortex structure with experiments. Table 1.2 presents a summary of the following review.

[7]Only peak swirl velocity compared with experiments

Fixed wing computations: Mansour [33] used the RANS equations to study the transonic flow-field of a swept wing. The vortex roll-up in the tip region was resolved and the contribution of the boundary layer circulation to the tip vortex circulation was confirmed. However, the grid resolution and numerical accuracy was insufficient to achieve good comparison with experiments. Srinivasan et al. [89] performed a RANS study of the effects of wing planform and tip shape on vortex roll-up using the ARC3D code with a Baldwin-Lomax turbulence model. When compared with experiments, the qualitative features showed good agreement, but surface pressures near the wing tip showed poor comparison.

Dacles-Mariani et al. [47] validated the experiments of Chow et al. [9] using a RANS formulation with the Baldwin-Barth turbulence model. They studied the effects of numerical schemes, grid requirements and turbulence model modifications in resolving the vortex formation and rollup. They were able to demonstrate that using 15 points per vortex core diameter, fifth order spatial accuracy for inviscid terms and a modification of the turbulence model, the mean flow characteristics could be reasonably captured. They however concluded that the use of isotropic turbulence closure could be deficient in accurately representing the turbulence field.

Lockard and Morris [90] solved the inviscid Euler equations using a fourth order central differencing scheme to validate the measurements of Devenport et al. [10]. Even with the use of a 2 million grid point mesh, the vortex was found to diffuse rapidly. The core-size was found to grow to more than 2 times the experimental value within a few chord-lengths of evolution. The disagreement was attributed to numerical dissipation and also to the inviscid approximation.

Spall [91] conducted an inviscid simulation of the afore-mentioned test case of Devenport et al. using a second order accurate scheme with highly refined meshes in the tip vortex region. The peak swirl velocity was over-predicted and the core-radius was smaller compared to the experiments. The numerical diffusion was found to be small in that the peak swirl velocity diminished by 15% over a distance of 10 chord lengths.

Egolf et al. [40] present a review of research at the Universal Technologies Research Center (UTRC) on tip vortex simulation. A comprehensive study was made on the numerical diffusion in terms of mesh spacing, mesh alignment and order of accuracy. For an idealized vortex problem, it is shown that numerical diffusion can be negligible using a ninth order accurate scheme with approximately 12 points in the vortical core. In addition, the mesh points had to be aligned with the vortex axis. However, practical tip vortex simulations using the RANS equations were found to be very dissipative, probably because of the ill-effects of the Baldwin-Lomax turbulence model. (fig. 1.6).

Rotary blade computations: Compared to fixed wing calculations, it is very difficult to come across numerical validation of tip vortex structure with experiments for rotating blades. A significant contributor to this fact is the scarcity of accurate and reliable experimental measurements. A few of these works [26, 50, 92] compare the trajectory of the vortex core, such as the radial contraction and downward convection with experiments. Actual comparisons of the details of the vortex structure are very rare. Russell et al. [93, 94] have performed RANS simulations using the Baldwin-Lomax turbulence model to validate the experimental hover measurements of MacAlister et al. [97]. Computed vortex velocity profiles are compared with measurements at distances of 0.5 and

3 chord lengths behind the trailing edge. The axial velocity excess is overpredicted and the swirl velocity is underpredicted. The computed core radius is seen to be larger by 60% compared to the measurement at the 3 chord length downstream location. Usta [34] used upto eighth order accurate symmetric TVD schemes [95] (for inviscid terms) with the Spalart-Allmaras turbulence model to simulate the Caradonna and Tung [83] 2 bladed hovering rotor. Though high order schemes performed better than the low order schemes in predicting blade surface pressures, numerical diffusion was found to reduce the vortex strength significantly. Tang [96] used a high order accurate Euler solver with adaptive mesh refinement and compared the evolution of the peak swirl velocity with wake-age for the isolated hovering rotor test case of Martin and Leishman [11]. The use of high order accuracy and mesh adaption was seen to reduce numerical dissipation. No details of the vortex velocity profile were compared with experiments.

1.4.4 Tip Vortex Control

The maximum swirl velocity associated with a trailing vortex usually scales as $v_{\theta,max} \approx \frac{\Gamma_o}{2\pi r_c}$, where Γ_o is the circulation or strength of the vortex and r_c is the core radius (usually defined as the radius at which v_θ is a maximum). The primary objective in trailing vortex control is the reduction of $v_{\theta,max}$ since it directly contributes to increased wake hazard. One can achieve this by:

Increasing the diffusion - Increased turbulent activity in the core can cause a higher core growth rate and hence, lower swirl velocity. However, turbulent diffusion does not diminish the circulation.

Decreasing the circulation - By having cross diffusion and cancellation with a counter-rotating vortex, the circulation strength of a given vortex can be diminished.

Inducing instabilities - It is known that tip vortex flows are unstable to small perturbations because of the presence of an axial velocity deficit. If these instabilities can be excited, the coherence of the vortex can be reduced. Over the past three decades, a large number of vortex alleviation concepts have been investigated through experiments, numerics and theoretical analyses. A few of these concepts will be outlined in the following paragraphs.

The earliest attempts used splines, wing-tip mounted propellers or spoilers to inject large amounts of turbulence into the vortex core [98, 99]. The idea was to diffuse the vortex by making the core turbulent and also to make it more susceptible to instabilities, eventually causing a breakdown of the core. In its simplest form, the swirl velocity induced by an isolated straight line vortex (of circulation strength Γ_o) is given by, $v_\theta = \frac{\Gamma_o}{2\pi r}[1 - exp\frac{-r^2}{4t(\nu+\epsilon)}]$, where ν is the laminar viscosity and ϵ is the turbulent eddy viscosity. Then, $r_c \approx 2.241\sqrt{(\nu+\epsilon)t}$. The main focus was thus, to increase the turbulence intensity. These devices proved to be effective in reducing the swirl velocities several chord lengths downstream of the wing, but the net decay far away was not greatly influenced. Further, some of these devices caused significant drag penalties.

Rossow [100] proposed a method which modifies the spanwise lift distribution in such a way that the trailed wake system is dispersed in a non-hazardous manner. The ideal spanwise loading should be such that the trailed vortex sheet does not roll up into concentrated vortical structures, and is instead dispersed as a single unit. Using the Betz rollup theory, he showed that a saw-tooth shaped

lift distribution theoretically gives a vortex sheet that translates downwards as a single unit. In a $40 \times 80ft$ wind tunnel test, this loading was obtained by using a set of 7 flaps (on each wing), the deflections of which control the spanwise lift distribution. For moderate angles of attack, a highly mitigated tip vortex was observed. An extensive set of flight tests were conducted on a Boeing 747 (using the in-board and out-board flaps) and the resulting tip vortex strengths were determined using the loads and rolling moments encountered by a Lear Jet flying behind the 747. With proper flap deflections, the tests indeed showed that more diffuse tip-vortices were formed. It was concluded however, that the airplane performance and efficiency were adversely affected because of the requirement of the flap deflections.

Quackenbush et al. [101] proposed the use of active surfaces to create periodic control vortices which promote the de-intensification of the primary vortex wake systems of submarines. Termed *vortex leveraging*, they show by means of computations that the control vortices interact with the primary tip vortices causing mutual instabilities between the two tip vortices. Eventually the trailed vortex system is weakened. Liu et al. [102] have done some preliminary studies of using spoilers and upper surface blowing as a means of reducing the tip vortex strength of a hovering rotor. Other methods include using wing fins, spanwise blowing [103] and sub-wings [104]. A more complete survey of these techniques can be found in Rossow [100] and references therein.

Ortega [105] presents a novel idea in trailing vortex mitigation: Using a towing tank, a study was performed on the trailed vortex system of a wing shaped as shown in fig. 1.7. The triangular shaped flap region creates a vortex that counter-rotates with the tip-vortex and the subsequent interaction drastically

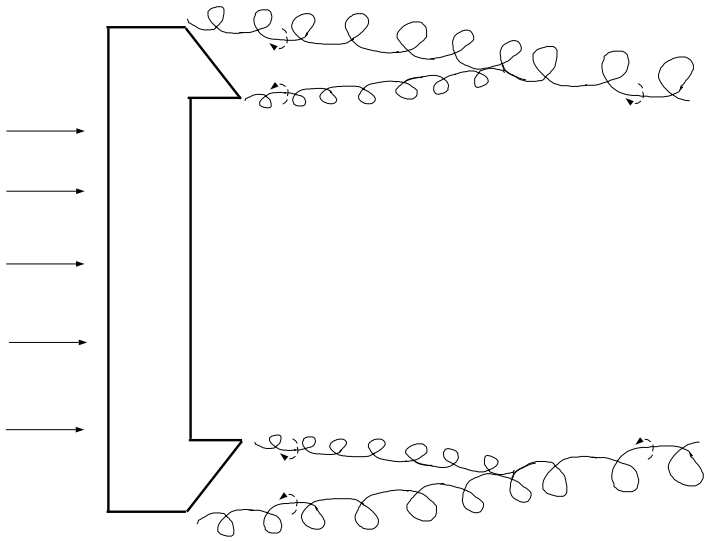

Figure 1.7: Wing with triangular flaps [105] - Flap vortices counter-rotate with Tip vortices and ultimately weaken them

reduces the intensity of the tip-vortex. As discussed in his work, though this is a very promising concept, the creation of the strong counter-rotating vortex results in a higher induced downwash and structural problems could result from the outboard loading and weight. Orlandi et al. [106], based on direct numerical simulations, suggest that perturbing trailing vortices by temperature variations can initiate some instabilities that can destroy the coherence and strength of a pair of counter-rotating trailing vortices.

Many studies in helicopter tip vortex control have concentrated on the modification of the tip shape ([107]-[109]) in such a way that the loading would result in a more diffuse trailed vortex system. Fluidic control opportunities were explored by Gowanlock et al. [110], in which discrete jets were introduced at the tip of a single blade in hover. Experimental results show a reduction in swirl velocity and reduced coherence of the tip-vortex. More recently, the effect of spanwise blowing at the tip was investigated experimentally by Han et al. [111]

for a single hovering blade. In their test, air was bled at the leading edge and injected at the tip through a set of 4 circular orifices. Their conception was that this would inject turbulent structures directly into the core of the tip vortex and thus diffuse it. They were able to demonstrate a 50% reduction in swirl velocity within a wake age of 90^o. Data on the effect on lift and drag coefficients are not currently available. Liu et al. [102] performed some preliminary numerical studies of using upper surface blowing. Their scheme was to disrupt the spanwise bound circulation and thus, reduce the tip vortex strength.

Other methods that are specific to helicopter BVI control like Higher Harmonic Control (HHC) [112] and Individual Blade Control (IBC) [113] essentially use control inputs that are tuned at particular frequencies and are phased such that the level of noise and vibration is reduced. Though these concepts were relatively successful experimentally, implementation on a helicopter would be difficult given the complexity and sometimes, the size of the control system.

1.5 Scope and organization of the thesis

The review of the literature highlights the difficulties in achieving a detailed understanding of vortex formation and evolution. In particular, it becomes evident that past computational efforts in tip vortex simulations have been found to be very lacking in terms of accurate validation of the numerical results with experiments. The overall objective of this work is to develop a high fidelity RANS based computational methodology that can be used as a reliable tool to help understand the process of tip vortex formation and evolution. In principle, this methodology can also be used as a tool to evaluate control effects and

configuration changes that can enhance the performance of lifting surfaces in general.

In Chapter 2, a study is performed on the theoretical aspects of axisymmetric vortices in the far-field. The objective of the study is to better understand the characteristics of realistic tip vortices in terms of their persistence and control.

In Chapter 3, the formulation of the RANS-based computational methodology is presented. Various issues that pertain to the present simulations are discussed.

Chapter 4 presents the simulation of the formation and roll-up of a tip vortex generated by a fixed wing in a wind tunnel. With the aid of validation with experimental data, issues such as grid requirements, solver accuracy and turbulence model modifications are addressed. The effect of airfoil thickness and tip shape on vortex rollup is also studied. Next, simulations of the evolution of a fixed wing tip vortex in the extended near-field are performed.

Chapter 5 is devoted to the computational study of the flow-field of lifting rotors in hover. Detailed comparisons with experimental data are presented for the case of single and two bladed rotors. In addition, the effect of the loading distribution on tip vortex formation and evolution are studied in detail.

In Chapter 6, the methodology is used to simulate the effects of flow control in the form of blowing at the wing tip. Results are evaluated on fixed wings and helicopter rotors.

The final chapter summarizes the main observations on the various aspects of the methodology and simulations. Recommendations are suggested for future work.

Chapter 2

Theoretical Studies on Tip Vortices

The main objective of this thesis is to develop an accurate methodology to compute tip vortex flows using the RANS equations. In this chapter, certain aspects of tip vortices that are of a more theoretical nature are addressed. A brief review of literature on the vortex structure in the far-field is followed by an examination of the relationship between the swirl and axial velocities. Finally, a linear analysis is performed on the stability of realistic tip vortex velocity profiles. The objective of this study is to better understand the role of axial velocity and the mechanisms of persistence and destabilization of tip vortices.

2.1 Tip vortex structure in the far-field

Many experimental studies [10]-[13] on fixed and rotary wings have shown that the tip vortex structure is largely axisymmetric within a few chord lengths downstream of the trailing edge. From these studies it is also evident that vorticity is concentrated in an extremely small radius and the swirl (v_θ in fig. 2.1) and axial velocities (v_x) are much larger than the radial velocity (v_r).

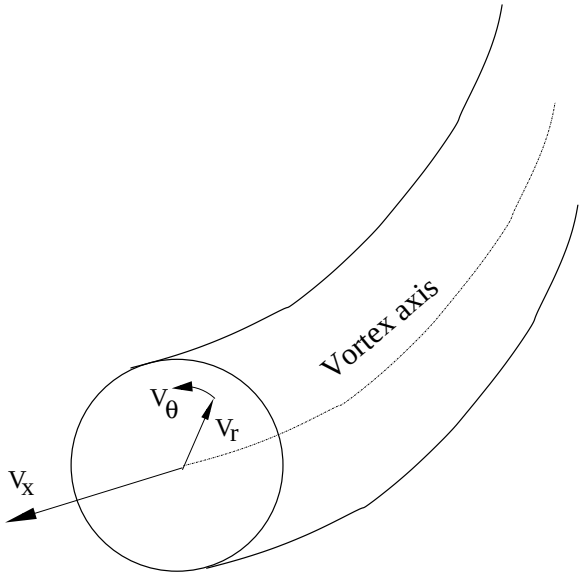

Figure 2.1: Schematic showing a tip vortex in the far-field and its velocity components.

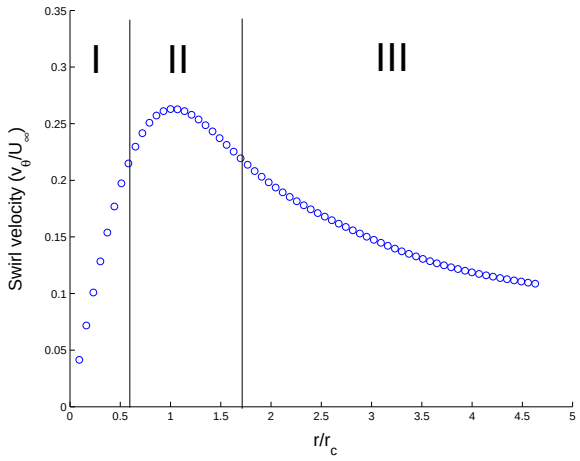

Figure 2.2: Typical measured axisymmetric swirl velocity distribution [10] 10 chords downstream of a fixed wing. Schematic of regions that define the vortex structure is also shown.

2.1.1 Swirl velocity

Using the light-loading assumption (which states that the deviation of axial velocity from the free-stream value is negligible), axisymmetry and incompressibility (along with density $\rho = 1$), the Reynolds-averaged tangential momentum equation [18] becomes

$$\frac{1}{2\pi}\frac{\partial \Gamma}{\partial t} = \frac{\nu}{2\pi r}\frac{\partial}{\partial r}\left[r^3 \frac{\partial}{\partial r}\left(\frac{\Gamma}{r^2}\right)\right] - \frac{1}{r}\frac{\partial}{\partial r}(r^2 < v_r' v_\theta' >) \tag{2.1}$$

where, $\Gamma = 2\pi r v_\theta$ is the local circulation and $< v_r' v_\theta' >$ is the Reynolds *stress*. Based on different modeling assumptions for the Reynolds stress, a variety of solutions to eqn. 2.1 have been attempted in the literature (for instance, [55, 57, 58, 60, 61]). Phillips [58], in particular, has rigorously analyzed the above equation and with the aid of some dimensional reasoning, divides the vortex structure into three regions:

(I) The innermost part, in which viscous effects must be present to bring the tangential velocity to zero at r=0. In addition, near r=0, to leading order, the rotation is close to solid body and the Reynolds stress goes to zero like r^2. In this region, the stabilizing effects of flow-rotation are believed to promote relaminarization.

(II) An intermediate region, located near the point of maximum swirl velocity, which acts like a buffer region between the nearly potential outside flow and the solid body rotation in the interior. In this highly strained turbulent region, Hoffman and Joubert's logarithmic law [55] for circulation is found to apply.

(III) The outer region, in which the flow is turbulent, but the swirl velocity decays as $1/r$ (akin to a potential vortex) and the Reynolds stress goes to zero as $1/r^2$.

Successful vortex models are seen to account atleast qualitatively for these effects. For instance, Ramasamy and Leishman [60] use a mixing length model for the Reynolds stress terms with an *intermittency function* to reduce the eddy viscosity in region I and portions of region II. Along with a set of 3 empirical constants to model the Reynolds stress, their similarity solution to eqn. 2.1 was found to match a wide range of experimental measurements.

A typical measured swirl velocity distribution (from [10]) is shown in fig. 2.2.

2.1.2 Axial velocity

The dynamic necessity of axial velocity was first established by Batchelor [56]. He derived a simplified expression by treating the inviscid axisymmetric equations, accounting for the viscous terms using a "head loss" ΔH. Assuming small axial gradients (compared to radial gradients), axisymmetric flow and small radial velocity (compared to axial and swirl velocities), the equations[1]governing incompressible flow can be written in the form:

$$\begin{aligned} \frac{\partial p}{\partial r} &= \rho\frac{v_\theta^2}{r} \quad and \\ \frac{p}{\rho} + \frac{1}{2}(v_x^2 + v_\theta^2) + \Delta H &= \frac{p_\infty}{\rho} + \frac{1}{2}U_\infty^2 \end{aligned}$$

Assuming an isolated vortex, the axial velocity is then given by [56]:

$$v_x^2(r) = U_\infty^2 + \int_r^\infty \frac{\Gamma}{2\pi^2 r^2}\frac{\partial \Gamma}{\partial r}dr - 2\Delta H$$

If one assumes a monotone non-decreasing circulation (which is indeed the case in tip vortex flows), one should expect an axial velocity *excess* (relative to free-

[1]Radial and Axial momentum equations respectively.

stream) for inviscid flow ($\Delta H = 0$) because the integrand is guaranteed to be positive at all radial positions.

The driving mechanism for the development of axial velocity is thus the low pressure that exists in the core. This low pressure is a consequence of the centrifugal forces due to the swirling flow - in order to maintain the total pressure constant, the axial velocity has to be in excess of the free-stream.

For viscous flows, the presence of the loss of head competes with the inviscid acceleration mechanism. In the case of large Reynolds numbers and high angles of attack, the inviscid mechanism wins out and an axial velocity excess has been reported in some near-field experiments. For instance, Chow et al. [9] used $Re = 4.6 \times 10^6$ and $\alpha = 10^o$ and found a peak axial velocity of $1.77U_\infty$. Under moderate angles of attack and low Reynolds numbers, the viscous losses are usually high enough and the majority of experiments have reported axial velocity deficits. Heyes et al. [146] found an axial velocity of $0.86U_\infty$ for a wing at $Re = 2.2 \times 10^5$ and $\alpha = 10^o$.

This behavior is quantified by the observation of Spalart [2], in which he rationalizes that the presence of a deficit or excess is dependent on the "circulation parameter" $\Gamma_o/(U_\infty b)$, where Γ_o is the far-field circulation strength of the vortex and b is the semi-span. A larger value of the parameter resulted in an excess. For the afore-mentioned Chow case, the value of this parameter is found to be ≈ 0.2 and for the Heyes case, ≈ 0.1. Anderson et al. [114] present a wide range of test cases for which this parameter has been evaluated and experimental axial velocity measurements are reported.

Axial velocity profiles are seen to be curve-fit by Gaussian distributions [3]. A typical measured axisymmetric axial velocity profile is shown in fig. 2.3. In

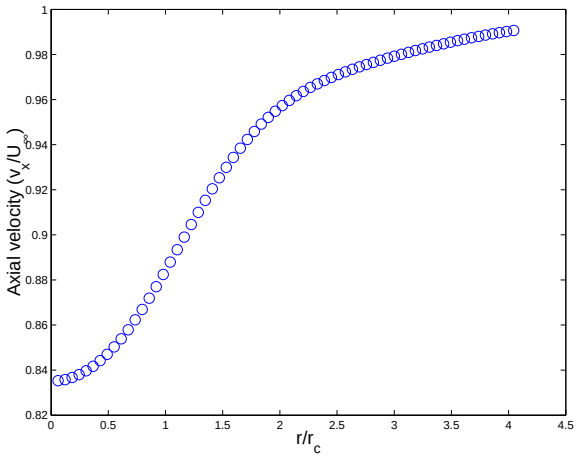

Figure 2.3: Typical measured axisymmetric axial velocity distribution [10] 10 chords downstream of a fixed wing.

this case, an axial velocity deficit is evident in the vortical core.

Unlike the swirl velocity, which, as discussed in the previous chapter, is a hazard to other aircraft and is responsible for noise and vibration in helicopters, the effects of axial velocity are subtle. Though the axial velocity defect/excess is usually smaller in comparison to swirl velocity its presence dictates to a large extent, the *stability* and *decay* of the swirl velocity. In addition, axial flow is even known to play a significant role in vortex breakdown [115].

2.2 Mechanisms of decay of tip vortices

Knowledge of the decrease of the peak swirl velocity and the increase in the core-radius of the tip vortex is crucial in determining the potential hazard caused by it. Of the variety of mechanisms that contribute to the decay of tip vortices, laminar and turbulent diffusion seem to have been addressed extensively in literature, the latter in an empirical manner. Laminar (or molecular) diffusion is given by

Lamb's solution [62] to eqn. 2.1 (without the turbulent terms): In this case, the rate of growth of the core-radius is given by:

$$r_c(t) = \sqrt{r_o^2 + 4\alpha\nu t}, \tag{2.2}$$

where $\alpha = 1.25643$ is the Lamb's constant and r_o is the core-radius at time $t = 0$. Correspondingly, the swirl velocity is given by:

$$v_\theta = \frac{\Gamma_o}{2\pi r_c}\left[\frac{1 - e^{-\alpha\bar{r}^2}}{\bar{r}}\right] \tag{2.3}$$

where, $\bar{r} = r/r_c$. Squire [64] modified the laminar core-growth model by introducing a constant eddy viscosity, thus altering the core-radius growth to

$$r_c(t) = \sqrt{r_o^2 + 4\alpha(1+\delta)\nu t}, \tag{2.4}$$

where, $\delta \geq 0$ is a parameter used to represent the turbulence. As discussed by Ramasamy and Leishman [60], the core-growth predicted by a variety of vortex models can be represented in the above framework. Experimentally measured core-radius evolution is generally found to be fit well by using an appropriate δ in eqn. 2.4. Note that in the above expressions, substituting $x = U_\infty t$ would convert the temporal problem to a steady spatial one.

However, any vortex model based on eqn. 2.1 has a fundamental deficiency as pointed out by Uberoi [66]. The effect of axial velocity has been ignored in this equation[2]. Uberoi integrated the steady incompressible axisymmetric RANS equations and obtained an expression for the flux of axial momentum, which is given by:

$$U_\infty \frac{d}{dx}\left[\int_o^\infty \Gamma r dr\right] = \frac{d}{dx}\left[(v_x - U_\infty)(\Gamma - \Gamma_o) r dr\right] - 2\nu\Gamma_o, \tag{2.5}$$

[2]This is invariably done because it is otherwise difficult to obtain a similarity solution to eqn. 2.1.

The term on the left hand side of this equation represents the rate of change of the angular momentum flux. The first term on the right hand side represents the convection of angular momentum (in the radial and axial directions). The second term on the right hand side represents the diffusion of angular momentum. Using experimental data, Uberoi showed that the convection term was more than an order of magnitude larger than the viscous term even in the far-field. He rightly points out that such *convection effects could be mistaken for turbulent diffusion when axial velocity is neglected.* Hence, when simple one-dimensional vortex models are formulated to describe experimentally observed core growth and associated phenomena, the effect of neglect of axial velocity could result in spurious Reynolds number dependence.

2.3 The Axial momentum flux

In the previous section, Uberoi's expression for the decay of tangential momentum was presented. In this section, an equivalent expression for the axial momentum flux will be derived. The objective is to deduce a relationship between the axial momentum and swirl velocities, so that a clear understanding of their decay mechanisms can be obtained. The only assumptions that will be made are that of incompressible axisymmetric flow. In addition, similar to Uberoi, the assumption that the Reynolds stress $< v_r' v_\theta' > \rightarrow 0$ atleast as fast as $1/r^2 \rightarrow 0$ as $r \rightarrow \infty$. Such a behavior is predicted by Philips as mentioned in the previous section.

Assume that the axial velocity can be represented by $v_x = U_\infty + u_x$, with $v_x(x, z)$ being the axial velocity excess or deficit. Integrating the axial momen-

tum equation and using the continuity and radial momentum equations, the following expression was derived:[3]

$$\frac{d}{dx}\left[\int_o^\infty (u_x(U_\infty + u_x) + < v_x' >^2) r dr\right] = \frac{d}{dx}\left[\int_o^\infty (\frac{< v_r' >^2 + < v_\theta' >^2 + v_\theta^2}{2}) r dr\right] \tag{2.6}$$

This equation relates the rate of change of mean momentum and fluctuating kinetic energy in the axial direction to the energy in the other directions. Integrating this equation in the axial direction between two stations, say x_1 and x_2,

$$\left[\int_o^\infty (u_x(U_\infty + u_x) + < v_x' >^2) r dr\right]_{x_1}^{x_2} = \left[\int_o^\infty (\frac{< v_r' >^2 + < v_\theta' >^2 + v_\theta^2}{2}) r dr\right]_{x_1}^{x_2} \tag{2.7}$$

More insight is obtained by considering the laminar part (only the mean flow quantities) of the equation: Then, the *change in the axial momentum flux is equal to the change in the swirling kinetic energy. Hence, the decay of the axial flux is intimately related to the decay of the swirling flow.*

Saffman [65] derived an equivalent expression for laminar flow using the light loading assumption ($v_x/U_\infty << 1$) and his following quote is applicable in this general case also: "The axial flux decays under the action of viscosity and can be interpreted physically as the transfer of induced drag from the kinetic energy of the transverse motion to the axial momentum deficit." This discussion further establishes the need and significance of understanding the axial velocity structure of the tip vortex.

[3] A similar expression for laminar flow was derived in [67]. This derivation follows the same steps, but includes the turbulent quantities.

2.4 Linear stability analysis of axisymmetric vortices

To perform a linear stability study, the continuity and momentum equations are linearized about a mean axisymmetric flow (U, V, W) in the radial, tangential and axial directions. Therefore,

$$v_r(r) = U(r) + u, \quad v_\theta = V(r) + v, \quad v_x = W(r) + w, \tag{2.8}$$

Note that this corresponds to parallel flow and this assumption is justified only if the changes in the axial direction are much smaller than that in the radial direction. Even though the basic flow is axisymmetric and parallel, the imposed disturbances (u, v, w, p) are not restricted to be and are given by [68]:

$$\{u, v, w, p\} = \{iF(r), G(r), H(r), P(r)\}e^{i(\alpha x + m\theta - \omega t)} \tag{2.9}$$

where, α is the axial wavenumber, m is the azimuthal wave number and ω is the growth rate of the disturbance. Substituting this into the NS equations defines an eigenvalue problem for the growth rate. If the imaginary part of ω (represented by ω_i) is positive, the particular flow configuration is temporally unstable, otherwise it is stable.

The full equations and the boundary conditions can be found in Appendix B. In the following discussion, the vortex Reynolds number $Re_v = \frac{\Gamma_o}{\nu}$ is used for non-dimensionalization instead of the usual chord based Reynolds number definition.

2.4.1 Summary of Previous work

The above eigenvalue problem has been solved by several researchers ([68, 70, 72]) for the Batchelor's q-vortex (which has a Lamb-Oseen swirl velocity profile and a Gaussian axial velocity distribution), defined by $U(r) = 0, V(r) = q(1 - e^{-r^2})/r, W(r) = e^{-r^2}$. In this case, the swirl ratio q relates the magnitude of the swirl velocity to the axial velocity excess or deficit. It is easy to see that the ratio of the peak swirl velocity to the axial velocity difference is $0.639q$. Note that the swirl velocity profile of the q-vortex is the same as Lamb's vortex. The following have been previously observed (and summarized from the aforementioned references):

1. For the case with no axial velocity, the vortex is found to be stable for all Reynolds numbers. This can also be inferred from Rayleigh's centrifugal stability condition [71] which states that parallel swirling flows with monotone increasing circulation are stable.

2. The introduction of axial velocity (excess/deficit) is found to be a de-stabilizing influence. However, for a given Reynolds number, such instabilities are seen to be damped out and the vortex is stable if the amount of swirl is significant enough ($q > q_{critical}$). For instance, at a Reynolds number $Re_v = 10000$, all disturbances were seen to be damped if $q > 3.235$. For inviscid flow, $q_{critical} \approx 1.5$.

3. The most critical modes are found to be the ones corresponding to the azimuthal wave number $m = -1$. These modes consistently present the largest unstable band of Reynolds numbers and in addition, are the only modes that are unstable for the Gaussian jet or wake (q=0).

4. The addition of viscosity was seen to de-stabilize some modes which were

otherwise found to be stable in the inviscid regime.

5. Though the addition of swirl is found to be stabilizing for large q, addition of incremental swirl to an otherwise non-rotating jet/wake was seen to initially amplify the instabilities. These instabilities reach a peak value at a particular q and are then seen to be damped as q approaches $q_{critical}$.

2.4.2 Current Investigations

The previous investigations were focused on the q-vortex, which is a solution of the laminar axisymmetric equations. Though it is representative of the overall features of tip vortices, the velocity profiles do not match well with experimental measurements beyond the core-region. In this work, swirl velocity profiles that match well with measurements will be analyzed for linear stability. The objective of this study is to ascertain whether changes in the velocity profile outside the core significantly affect the stability properties. In addition, the effect of the radial gradient of axial velocity will be analyzed. All the computations will be focused on the most critical mode $m = -1$.

The swirl velocity profile used in this study was chosen to be the function $V(r/r_c) = qr/r_c M(n; 1; r/r_c)$, where M is the confluent Hypergeometric function [73]. This function was chosen because it is a similarity solution to a laminar axisymmetric vortex given by Kirde (the expression can be found in Chapter 13 of [65]) and the free-parameter $0 \leq n \leq 1$ was seen to give profiles that match measured profiles as seen from fig. 2.4. It is evident that in the core-region, the velocity profiles are not much different from each other, and even the Lamb-Oseen profile (same as the $n = 1$ Kirde profile to plotting accuracy) matches well with experiments. Outside the core-region, the measured profile shows a much

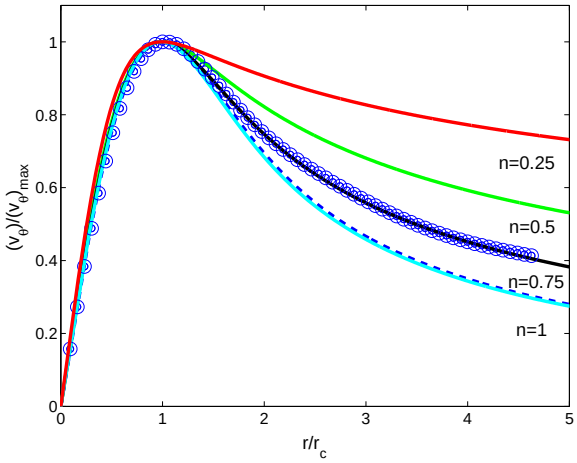

Figure 2.4: Hypergeometric velocity profile for different values of the parameter n. The open symbols correspond to a measured velocity profile, previously shown in fig. 2.2

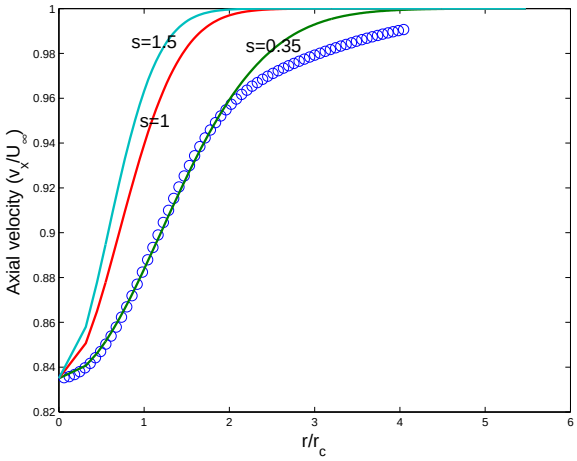

Figure 2.5: Gaussian velocity profile for different values of the parameter s. The open symbols correspond to a measured velocity profile, previously shown in fig. 2.3

smaller radial gradient compared to the Lamb-Oseen profile. It is seen that for this case, $n = 0.75$ matches the measurements well. When this velocity profile is compared to that of a q-vortex, it is ensured that both profiles have the same peak swirl velocities at the core-radius $r/r_c = 1$.

For this study, the Gaussian axial velocity profile $W(r/r_c) = exp[-s(r/r_c)^2]$ is used. The free parameter $s > 0$ is adjusted to set the steepness of the velocity profile as shown in fig. 2.5.

Sensitivity to changes in swirl velocity profile

In this section, fixing the axial velocity profile at $s = 1$, stability analysis will be performed on different swirl velocity profiles. These velocity profiles are significantly different from each other only in the potential flow region as was observed in fig. 2.2.

Figure 2.6 shows the topography of the instabilities for the q-vortex at $Re_v = 10^5$. Iso-levels of the maximum amplification rate (imaginary part of ω) are shown as a function of the axial wavenumber α and swirl ratio q. As mentioned in the previous section, a slight instability exists for the case with no swirl (q=0). When a small level of swirl is added ($q < 0.4$), the instabilities seem to be amplified, the maximum amplification being attained at $q \approx 0.5$. Larger values of the swirl ($q > 0.5$) act as a stabilizing mechanism and the growth rate of instabilities is seen to be reduced. For very large values of the swirl, the instabilities can be expected to be damped as discussed in [72]. It has to be mentioned that in practical cases, for instance, the experiments of Chow et al. [9], Heyes et al., $q > 2$, and hence addition of swirl can be assumed to be a stabilizing influence.

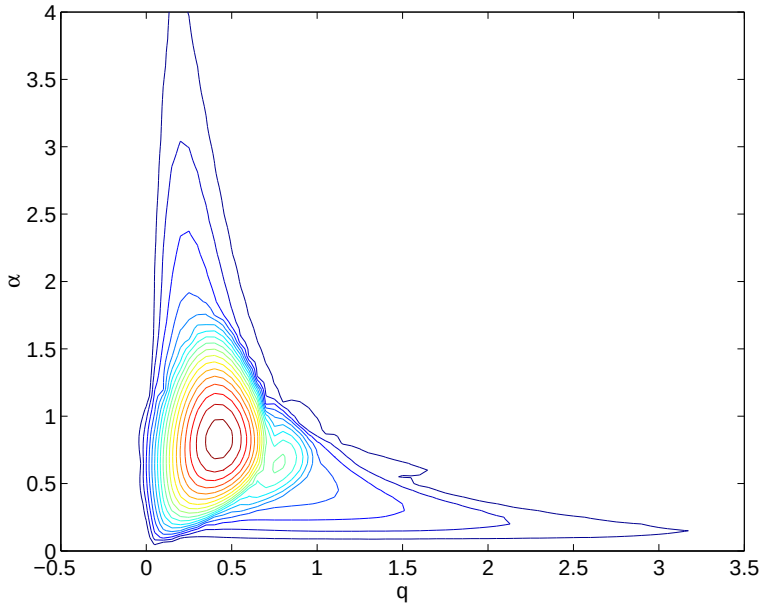

Figure 2.6: Contours of constant amplification rate ω_i of the most unstable mode for the q-vortex (Gaussian axial velocity with $s = 1$) at $Re_v = 10^5$. Outermost contour is 0.025, contour spacing=0.0125

Figure 2.7 condenses the results of fig. 2.6 into a 2D plane for ease of comparison with other cases. It is evident from figs. 2.7-2.9 that the effect of the change in velocity profile outside the core region proves to be a minor influence on the stability properties. This behavior was found to be consistent over a range of Reynolds number evaluations also.

Sensitivity to changes in axial velocity profile

To evaluate the sensitivity to changes in the axial velocity profile, the swirl velocity profile was held constant to Kirde's profile with $n = 0.75$ and the free parameter s in the Gaussian axial velocity profile was varied. As seen from figs. 2.9 and 2.10, the radial gradient of the axial velocity profile has a significant

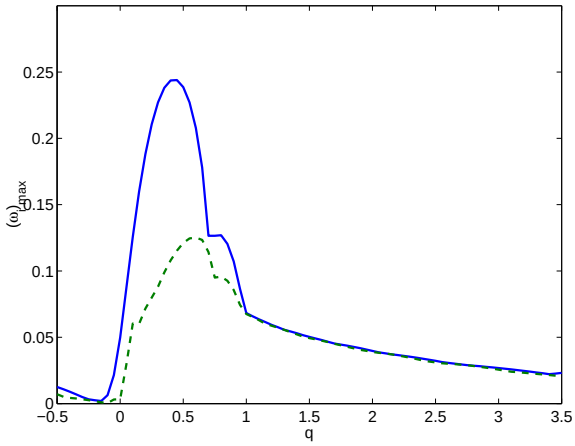

Figure 2.7: ω_i of the two most unstable modes for the q-vortex (Gaussian axial velocity with $s = 1$) at $Re_v = 10^5$

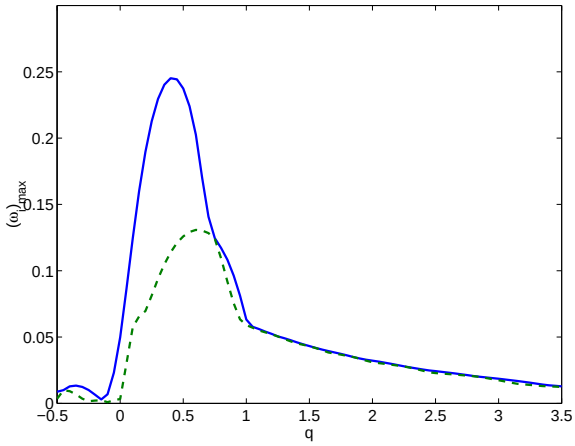

Figure 2.8: ω_i of the two most unstable modes for the Kirde profile with $n = 0.50$ (Gaussian axial velocity with $s = 1$) at $Re_v = 10^5$

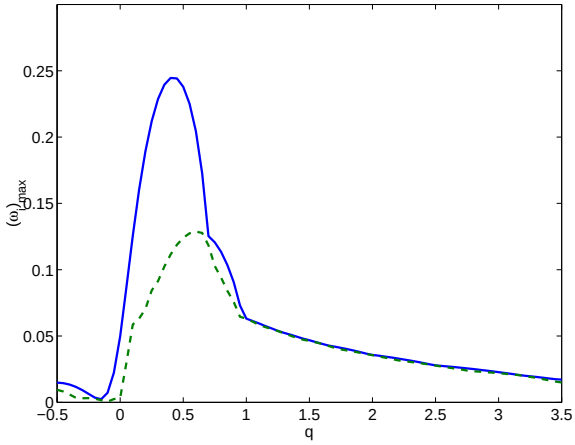

Figure 2.9: ω_i of the two most unstable modes for the Kirde profile with $n = 0.75$ (Gaussian axial velocity with $s = 1$) at $Re_v = 10^5$

effect on the stability properties. The growth rate of the instabilities ω_i is seen to increase when the axial velocity profile is steeper (larger s) inside the core.

Implications for persistence and control of trailing vortices

A few chord lengths downstream of the trailing edge, the swirl velocity in a realistic tip vortex can be expected to be larger than the axial velocity deficit/excess [9–11, 146]. The swirl ratio is thus large and hence, the rotational effects act to stabilize the flow. Figure 2.11 shows the structure of the most unstable mode for a particular combination of parameters at a moderate swirl ratio $q = 2$. For this case, the amplification rate $\omega_i = 0.01082824$. Termed "centre modes" [72], these modes are seen to be concentrated within a narrow radius inside the core. This behavior was noticed for all the velocity profiles at moderate and large swirl ratios. At larger Reynolds numbers, the modes were seen to be concentrated within a much smaller radius. *This, to an extent explains the dependence of the stability properties on the velocity profiles in the core region.*

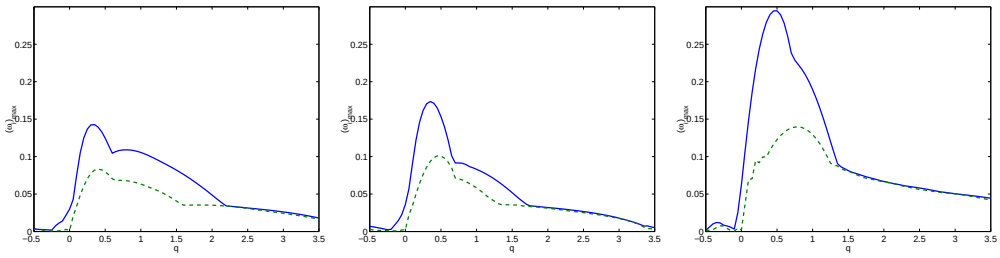

(a) s=0.35 (b) s=0.5 (c) s=1.5

Figure 2.10: ω_i of the two most unstable modes for the Kirde profile with $n = 0.75$. Gaussian axial velocity with different s at $Re_v = 10^5$

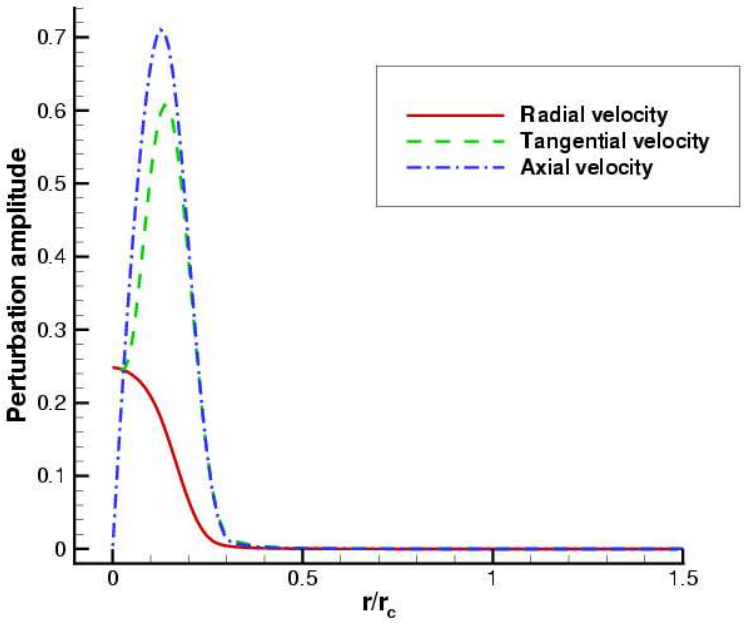

Figure 2.11: Amplitude of the perturbation eigenfunctions for the Kirde profile with $n = 0.75$ and Gaussian axial velocity with $s = 1$. $Re_v = 10^5, q = 2.0, \alpha = 0.25, m = -1$

Based on Direct Numerical Simulations (at small Reynolds numbers), Jacquin and Pantano [14] advocate the presence of a *dispersion buffer*, a region that exists in the external part of the core when the swirl ratios are significant ($q > 1$). According to their findings, perturbations that originate in the internal part of the core (such as the afore-mentioned centre-modes) are transformed into non-amplified propagating waves when they reach the dispersion buffer. These instability waves are thus diffused and virtually *no angular momentum is exchanged with the flow that exists outside outside the core.* This appears to be a key mechanism[4]behind the persistence of the strength of trailing vortices during the evolution. For low swirl ratios ($q < 1$), the dispersion buffer was seen to vanish and the vortex was observed to decay at a rapid rate.

Hence, based on these discussions, *a good strategy for vortex control could involve reducing the swirl ratio* or in other words, increasing the axial velocity deficit (or excess) in relation to the swirl velocity. As will be seen in Chapter 6 (using RANS simulations), this is possible.

2.5 Summary

In this chapter, certain theoretical aspects involving the evolution of tip vortices in the far-field were addressed. In particular, the role of axial velocity on the

[4]In addition, Cotel et al. [59], and Ramasamy et al. [60], based on an idealized experiment and an analysis of measured data, surmise that the effect of flow rotation is to induce an apparent "stratification radius" that usually exists within the core. Below this radius, even the smallest turbulent eddies from the *exterior* flow do not possess enough energy to engulf the interior of the vortical core. Thus, molecular diffusion is the only transport mechanism in the vortical core.

evolution and stability of tip vortices was examined. For an axisymmetric vortex, the axial momentum flux is seen to be intimately related to the kinetic energy of the transverse motion. Further, a linear stability analysis established the destabilizing effects of axial velocity (or in contrary, the stabilizing effects of the swirl velocity).

Chapter 3

Computational Methodology

In this work, the numerical solution of the Reynolds Averaged Navier-Stokes equations are used to study the tip vortex flow-field around wings and helicopter blades.

3.1 The RANS Equations

The 3 dimensional unsteady compressible RANS equations along with the Boussinesq assumption for isotropic eddy viscosity (a more detailed discussion can be found in sec. 3.7) are given by:

$$\frac{\partial \mathbf{Q}}{\partial t} + \frac{\partial \mathbf{F_i}}{\partial x} + \frac{\partial \mathbf{G_i}}{\partial y} + \frac{\partial \mathbf{H_i}}{\partial z} = \frac{\partial \mathbf{F_v}}{\partial x} + \frac{\partial \mathbf{G_v}}{\partial y} + \frac{\partial \mathbf{H_v}}{\partial z} + \mathbf{S}, \tag{3.1}$$

where $\mathbf{Q}$ is the vector of conserved variables, $\mathbf{F_i}, \mathbf{G_i}, \mathbf{H_i}$ are vectors representing the *inviscid* fluxes, $\mathbf{F_v}, \mathbf{G_v}, \mathbf{H_v}$ are vectors that represent the *viscous* fluxes, and $\mathbf{S}$ represents the vector that accounts for body forces if they are present. The

vector of conserved variables[1]is given by:

$$\mathbf{Q} = \left\{ \begin{array}{c} \rho \\ \rho u \\ \rho v \\ \rho w \\ e \end{array} \right\} \tag{3.2}$$

where, ρ is the density, (u, v, w) are the components of the velocity in the Cartesian directions and e is the total energy per unit volume, that can be written in terms of the velocities and pressure p as:

$$e = \frac{p}{\gamma - 1} + \frac{1}{2}\rho(u^2 + v^2 + w^2) \tag{3.3}$$

The flux vectors are given by:

$$\mathbf{F_i} = \left\{ \begin{array}{c} \rho u \\ \rho u^2 + p \\ \rho uv \\ \rho uw \\ u(e + p) \end{array} \right\} \tag{3.4}$$

$$\mathbf{G_i} = \left\{ \begin{array}{c} \rho v \\ \rho vu \\ \rho v^2 + p \\ \rho vw \\ v(e + p) \end{array} \right\} \tag{3.5}$$

[1]These quantities are Reynolds averaged [19].

$$\mathbf{H_i} = \begin{Bmatrix} \rho w \\ \rho w u \\ \rho w v \\ \rho w^2 + p \\ w(e+p) \end{Bmatrix} \tag{3.6}$$

$$\mathbf{F_v} = \begin{Bmatrix} 0 \\ \tau_{xx} \\ \tau_{yx} \\ \tau_{zx} \\ u\tau_{xx} + v\tau_{xy} + w\tau_{xz} - k\frac{\partial T}{\partial x} \end{Bmatrix} \tag{3.7}$$

$$\mathbf{G_v} = \begin{Bmatrix} 0 \\ \tau_{xy} \\ \tau_{yy} \\ \tau_{zy} \\ u\tau_{yx} + v\tau_{yy} + w\tau_{yz} - k\frac{\partial T}{\partial y} \end{Bmatrix} \tag{3.8}$$

$$\mathbf{H_v} = \begin{Bmatrix} 0 \\ \tau_{xz} \\ \tau_{yz} \\ \tau_{zz} \\ u\tau_{zx} + v\tau_{zy} + w\tau_{zz} - k\frac{\partial T}{\partial z} \end{Bmatrix} \tag{3.9}$$

With the assumption of isotropic eddy viscosity (refer sec 2.7), and Stokes' hypothesis [18], the mean and Reynolds stresses can be combined and represented by:

$$\tau_{ij} = 2(\mu + \mu_t)\left[\left(\frac{\partial u_i}{\partial x_j} + \frac{\partial u_j}{\partial x_i}\right) - \frac{1}{3}\frac{\partial u_k}{\partial x_k}\delta_{ij}\right] \tag{3.10}$$

with μ and μ_t represent the molecular and *turbulent eddy* viscosities. For the energy equation, T is the temperature and k is the coefficient of thermal conductivity and is related to the viscosity using the Prandtl number Pr and a turbulent Prandtl number Pr_t as:

$$k = \frac{\mu C_p}{Pr} + \frac{\mu_t C_p}{Pr_t} \tag{3.11}$$

For all the computations, $Pr = 0.72$ and $Pr_t = 0.9$ are assumed. The equations are finally closed by using the Sutherland's law [18] to represent the variation of molecular viscosity with temperature and the equation of state for a perfect gas $p = \rho RT$.

For all the simulations in this dissertation, no body forces are assumed. The source term vector $\mathbf{S}$ will be utilized when the equations are solved in the rotating frame for the hovering rotor problem (sec. 3.6).

In the numerical solution involving non-Cartesian geometries, grid clustering will be required along certain non-Cartesian directions, whereas, very coarse spacings will suffice along other orthogonal directions. In such cases, casting the equations in the *natural* coordinate system of the flow will prove to be convenient. Hence, the equations have to be transformed from the 'physical space' of the mesh points (x,y,z) to a 'computational space' $(\xi(x,y,z), \eta(x,y,z), \zeta(x,y,z))$. In general, this transformation would involve time if moving grids are used. In this thesis however, computations are restricted to fixed wings and rotary blades in hover and the geometry is assumed to be rigid, thus the time-dependence of the transformation drops out. The transformed equations in conservation form are given by:

$$\frac{\partial \hat{\mathbf{Q}}}{\partial t} + \frac{\partial \hat{\mathbf{F}}}{\partial \xi} + \frac{\partial \hat{\mathbf{G}}}{\partial \eta} + \frac{\partial \hat{\mathbf{H}}}{\partial \zeta} = \hat{\mathbf{S}} \tag{3.12}$$

where,

$$\hat{\mathbf{Q}} = \frac{1}{J}\mathbf{Q} \tag{3.13}$$

$$\hat{\mathbf{F}} = \frac{1}{J}\left[\xi_x(\mathbf{F_i} - \mathbf{F_v}) + \xi_y(\mathbf{G_i} - \mathbf{G_v}) + \xi_z(\mathbf{H_i} - \mathbf{H_v})\right] \tag{3.14}$$

$$\hat{\mathbf{G}} = \frac{1}{J}\left[\eta_x(\mathbf{F_i} - \mathbf{F_v}) + \eta_y(\mathbf{G_i} - \mathbf{G_v}) + \eta_z(\mathbf{H_i} - \mathbf{H_v})\right] \tag{3.15}$$

$$\hat{\mathbf{H}} = \frac{1}{J}\left[\zeta_x(\mathbf{F_i} - \mathbf{F_v}) + \zeta_y(\mathbf{G_i} - \mathbf{G_v}) + \zeta_z(\mathbf{H_i} - \mathbf{H_v})\right] \tag{3.16}$$

$$\hat{\mathbf{S}} = \frac{1}{J}\hat{\mathbf{S}} \tag{3.17}$$

with J being the Jacobian of the coordinate transformation.

3.2 Numerical solution

For all the numerical simulations, the Transonic Unsteady Rotor Navier-Stokes (TURNS) [26] flow solver was used as a reference code. This code has been extensively used over the past 15 years to study a variety of fixed wing [89] and rotary blade [26, 84, 92] problems. In this work, several modifications and additions were made to the structure and capabilities of the baseline TURNS solver and the new solver is called *Over*-TURNS[2]. The methodology of the baseline TURNS solver will be briefly explained in the following sub-section and the enhancements in *Over*-TURNS will be detailed afterward.

3.2.1 Baseline TURNS flow solver

The baseline TURNS code solves the compressible RANS equations on 2 or 3 dimensional single block structured grids. A finite volume methodology [116] is generally employed in the flow solver. In this framework, the governing equations

[2]Overset TURNS

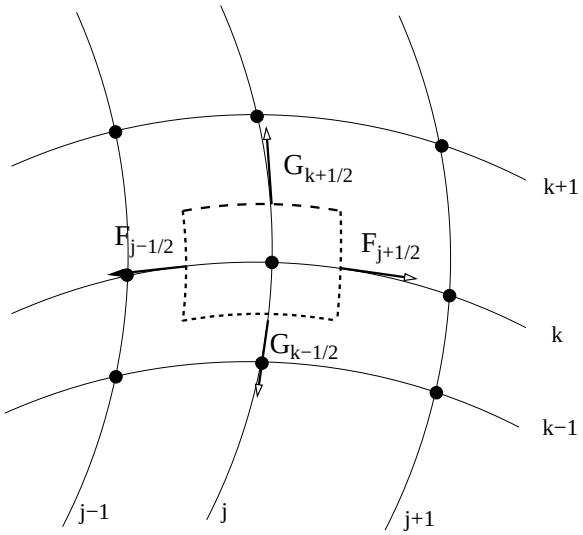

Figure 3.1: Schematic showing computational cell

are integrated over each computational cell. The resulting integral form of the equations are globally conservative. Whenever strong gradients and particularly, discontinuities are present in the flow the conservative integral form is preferred because such features can be mathematically defined in the differential form [117].

After integration in each computational cell, the governing equations 3.1 are given by:

$$\frac{\partial \bar{\mathbf{Q}}}{\partial t} = -\frac{\partial}{\partial x}\left[(\bar{\mathbf{F}}_\mathbf{i} - \bar{\mathbf{F}}_\mathbf{v})V\right] - \frac{\partial}{\partial y}\left[(\bar{\mathbf{G}}_\mathbf{i} - \bar{\mathbf{G}}_\mathbf{v})V\right] - \frac{\partial}{\partial z}\left[(\bar{\mathbf{H}}_\mathbf{i} - \bar{\mathbf{H}}_\mathbf{v})V\right] + \bar{\mathbf{S}}V, \tag{3.18}$$

where, the over-bar denotes the integral average of the quantity in the cell and V is the volume of the cell. Assuming $\mathbf{A}^\xi \Delta\eta\Delta\zeta$, $\mathbf{A}^\eta \Delta\xi\Delta\zeta$ and $\mathbf{A}^\zeta \Delta\xi\Delta\eta$ to be the area vectors in the coordinate directions at the cell interfaces, the equation

can be written in the form of 3.12, but with

$$\hat{\mathbf{Q}} = \bar{\mathbf{Q}}V \tag{3.19}$$

$$\hat{\mathbf{F}} = [\mathbf{F_i} - \mathbf{F_v}, \mathbf{G_i} - \mathbf{G_v}, \mathbf{H_i} - \mathbf{H_v}] .\mathbf{A}^{\xi} \tag{3.20}$$

$$\hat{\mathbf{G}} = [\mathbf{F_i} - \mathbf{F_v}, \mathbf{G_i} - \mathbf{G_v}, \mathbf{H_i} - \mathbf{H_v}] .\mathbf{A}^{\eta} \tag{3.21}$$

$$\hat{\mathbf{H}} = [\mathbf{F_i} - \mathbf{F_v}, \mathbf{G_i} - \mathbf{G_v}, \mathbf{H_i} - \mathbf{H_v}] .\mathbf{A}^{\zeta} \tag{3.22}$$

$$\hat{\mathbf{S}} = \bar{\mathbf{S}}V \tag{3.23}$$

The semi-discrete conservative approximation can be written as:

$$\frac{d\hat{\mathbf{Q}}}{dt} = -\frac{\hat{\mathbf{F}}_{j+\frac{1}{2}}(t) - \hat{\mathbf{F}}_{j-\frac{1}{2}}(t)}{\Delta\xi} - \frac{\hat{\mathbf{G}}_{k+\frac{1}{2}}(t) - \hat{\mathbf{G}}_{k-\frac{1}{2}}(t)}{\Delta\eta} - \frac{\hat{\mathbf{H}}_{l+\frac{1}{2}}(t) - \hat{\mathbf{H}}_{l-\frac{1}{2}}(t)}{\Delta\zeta} + \hat{\mathbf{S}}(t) \tag{3.24}$$

where, (j, k, l) are the indices corresponding to the (ξ, η, ζ) directions in the transformed coordinate system and $(j \pm \frac{1}{2}, k \pm \frac{1}{2}, l \pm \frac{1}{2})$ define the cell-interfaces of the control volumes as shown in fig. 3.1 (2D cell shown for simplicity). Note that eqn. 3.24 is space-time decoupled space-discrete version of eqn. 3.18 and can be solved as a set of ordinary differential equations in time. The spatial discretization (consisting of the inviscid and viscous fluxes) therefore, reduces to evaluating the interfacial fluxes $\hat{\mathbf{F}}_{j+\frac{1}{2}}, \hat{\mathbf{G}}_{k+\frac{1}{2}}, \hat{\mathbf{H}}_{l+\frac{1}{2}}$ for every *cell* (j, k, l) in the domain. It has to be mentioned that the above scheme is not truly multidimensional. Truly multidimensional schemes (for instance, the ADER approach of Toro et. al. [118]) would involve mixed spatial flux derivatives rather than the simple differencing mentioned above, but their application has thus far been restricted to model problems.

The inviscid part of the interfacial flux is computed using upwind schemes [119]. Upwind schemes have the advantage that the wave propagation property of the inviscid equations is accounted for (albeit approximately) in the flux cal-

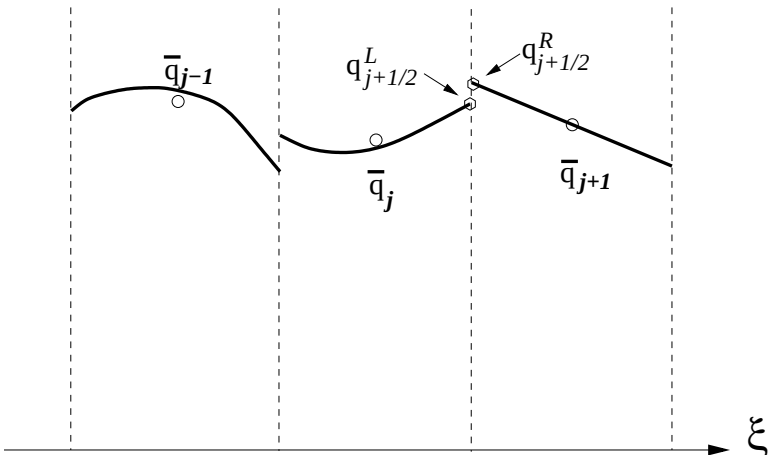

Figure 3.2: Schematic of one dimensional piecewise reconstruction (thick lines).

culation. To evaluate the interfacial fluxes, the Monotone Upstream-Centered Scheme for Conservation Laws (MUSCL) [119] approach is used. This procedure involves two steps: First, the solution (which is available as cell averages) is *reconstructed* in each cell, thus defining values on either side of the cell interface as shown in fig. 3.2. The 'left' value $\mathbf{q}^L$ represents the interface value from the cell 'j' and the 'right' value $\mathbf{q}^R$ represents the interface value from cell 'j-1'. In general, the reconstruction can be defined to any order of accuracy. The baseline TURNS code uses the third order accurate Koren's reconstruction [120]. The vectors $\mathbf{q^L}$ and $\mathbf{q^R}$ are composed of the so-called *primitive* variables. For example, $\mathbf{q^L}$ is given by:

$$\mathbf{q}^L = \left\{ \begin{array}{c} \rho \\ u \\ v \\ w \\ p \end{array} \right\} \tag{3.25}$$

Then, treating the left and right states as defining a local Riemann-problem

[117], the interfacial flux is obtained using any flux splitting scheme. The baseline TURNS code uses the Roe flux difference splitting [121] in which, the interfacial flux is given by:

$$\mathbf{F}(\mathbf{q}^L, \mathbf{q}^R) = \frac{F(\mathbf{q}^L) + F(\mathbf{q}^R)}{2} - |\hat{A}(\mathbf{q}^L, \mathbf{q}^R)|\frac{\mathbf{q}^R - \mathbf{q}^L}{2} \tag{3.26}$$

For the viscous fluxes, only the *Thin Layer* terms are considered. In this approach, derivatives that have a strong dependence on the surface normal direction are retained and all other terms are neglected. The remaining derivatives are computed using second order differencing. The algebraic turbulence model of Baldwin and Lomax [122] is used to represent the turbulent eddy viscosity.

The time integration of eqn. 3.24 is performed using either the first order implicit Euler method [123] or the second order implicit Backwards Difference method [123]. Since these are implicit methods, the Lower-Upper Symmetric Gauss Siedel (LUSGS) [124] scheme is used for inversion. The LUSGS inversion is used along with Newton sub-iterations [125] in order to remove factorization errors and to recover time accuracy.

The area vectors and cell volumes, or equivalently, the spatial metrics and the jacobians are computed using the finite volume formulation developed by Vinokur et. al. [116]. The following sections detail the modifications and enhancements made to the baseline TURNS code.

3.3 Inviscid differencing

As mentioned in the previous chapter, numerical diffusion is the primary factor that causes large inaccuracies in tip vortex calculations. Numerical error arises in the discretization of both the inviscid and viscous fluxes in eqn. 3.24, but the

errors due to the inviscid discretization can be expected to be more significant for applications considered in this dissertation because the Reynolds numbers are very high ($O(10^6)$). Hence the inviscid contribution to the total flux can be expected to be orders of magnitude larger than the viscous contribution.

In this work, a high order MUSCL [119] inviscid differencing is implemented. The spatial accuracy of MUSCL-type schemes is completely determined by the accuracy of representation of the interface values. This becomes very convenient in the finite volume framework because the interfacial fluxes naturally occur in the semi-discrete form (eqn. 3.24). In order to find the interfacial fluxes, the flow variables are *piecewise reconstructed* in each cell along coordinate lines in each of the 3 transformed directions. A schematic of the piecewise reconstruction in the ξ direction is shown in fig. 3.2. The cell averaged values (represented by an over-bar) are used to locally reconstruct the solution and thus, identify the interfacial values. For higher (than second) order accurate schemes, the cell center values are not the same as the cell-averaged values and this fact has to be taken into consideration. Also, in regions of large gradients, simple high order reconstructions may yield oscillatory solutions because of a manifestation of the the Gibbs phenomenon [126]. To avoid this, high order slope-limited [120] and Weighted Essentially Non-oscillatory (WENO) [127] are used. The different inviscid differencing schemes used in this dissertation are outlined in the following:

3.3.1 Third order differencing using Koren's limiter

In this scheme, Koren's differentiable limiter [120] is used to *limit* the high order reconstruction, so that the resulting scheme is third order accurate in smooth

regions and is progressively lower order accurate (down to first order at a solution discontinuity) in high gradient regions. Given cell averaged values $\{\bar{q}_{i+1}, \bar{q}_i, \bar{q}_{i-1}\}$, the cell reconstruction is such that the interface value $q^L_{i+1/2}$ is given by[3]:

$$q^L_{i+\frac{1}{2}} = \bar{q}_i + \phi_i \left[\frac{1}{3}(\bar{q}_{i+1} - \bar{q}_i) + \frac{1}{6}(\bar{q}_i - \bar{q}_{i-1})\right] \tag{3.27}$$

where, ϕ is a differentiable limiter which is defined by:

$$\phi_i = \frac{3\Delta\bar{q}_i\nabla\bar{q}_i + \epsilon}{2(\Delta\bar{q}_i - \nabla\bar{q}_i)^2 + 3\Delta\bar{q}_i\nabla\bar{q}_i + \epsilon} \tag{3.28}$$

where, ϵ is a small number used to prevent division by zero and Δ and ∇ are forward and backward difference operators defined by $\Delta\bar{q}_i = (\bar{q}_{i+1} - \bar{q}_i)$ and $\nabla\bar{q}_i = (\bar{q}_i - \bar{q}_{i-1})$.

3.3.2 High order WENO schemes

The slope-limiter approach in the afore-mentioned third order scheme causes the reconstruction to drop to low order accuracy in high gradient regions. WENO schemes, on the other hand, use a convex combination of stencils such that a high order of accuracy is achieved in all flow regions. The convex combination is chosen such that in high gradient regions, the smoothest stencil is assigned the maximum weight, resulting in a $(k+1)^{th}$ order accurate reconstruction for a $(2k+1)$ point stencil. In a smooth region, $(2k+1)^{th}$ order accuracy is approached. The interface values are given by:

$$q^L_{i+\frac{1}{2}} = \sum_{r=0}^{k} w_r v^L_r \tag{3.29}$$

[3] $q^R_{i-\frac{1}{2}} = \bar{q}_i - \phi_i \left[\frac{1}{3}(\bar{q}_{i+1} - \bar{q}_i) + \frac{1}{6}(\bar{q}_i - \bar{q}_{i-1})\right]$

where, w_r are the weights and v_r^L are the interpolations from the various stencils. Further,

$$w_r = \frac{\alpha_r}{\sum_{s=0}^{k} \alpha_s}, \quad with \tag{3.30}$$

$$\alpha_r = \frac{d_r}{(\beta_r + \epsilon)^2} \tag{3.31}$$

where, d_r are optimal weight coefficients, β_r are smoothness indicators and $\epsilon = 10^{-6}$. Hence, a $(2k+1)$ point scheme can be obtained by suitably defining v_r^L, d_r and β_r.

3 point WENO scheme

$$\begin{aligned}
v_0^L &= \frac{1}{2}\bar{q}_i + \frac{3}{2}\bar{q}_{i+1} \\
v_1^L &= \frac{-1}{2}\bar{q}_{i-1} + \frac{3}{2}\bar{q}_i \\
d_0 &= \frac{2}{3}, d_1 = \frac{1}{3} \\
\beta_0 &= (\bar{q}_{i+1} - \bar{q}_i)^2 \\
\beta_1 &= (\bar{q}_i - \bar{q}_{i-1})^2
\end{aligned}$$

5 point WENO scheme

$$\begin{aligned}
v_0^L &= \frac{1}{3}\bar{q}_i + \frac{5}{6}\bar{q}_{i+1} - \frac{1}{6}\bar{q}_{i+2} \\
v_1^L &= \frac{-1}{6}\bar{q}_{i-1} + \frac{5}{6}\bar{q}_i - \frac{1}{3}\bar{q}_{i+1} \\
v_2^L &= \frac{1}{3}\bar{q}_{i-2} + \frac{-7}{6}\bar{q}_{i-1} - \frac{11}{6}\bar{q}_i \\
d_0 &= \frac{3}{10}, d_1 = \frac{3}{5}, d_2 = \frac{1}{10} \\
\beta_0 &= \frac{13}{12}(\bar{q}_i - 2\bar{q}_{i+1} + \bar{q}_{i+2})^2 - \frac{1}{4}(3\bar{q}_i - 4\bar{q}_{i+1} + \bar{q}_{i+2})^2 \\
\beta_1 &= \frac{13}{12}(\bar{q}_{i-1} - 2\bar{q}_i + \bar{q}_{i+1})^2 - \frac{1}{4}(\bar{q}_{i-1} + \bar{q}_{i+1})^2 \\
\beta_2 &= \frac{13}{12}(\bar{q}_{i-2} - 2\bar{q}_{i-1} + \bar{q}_i)^2 - \frac{1}{4}(\bar{q}_{i-2} - 4\bar{q}_{i-1} + 3\bar{q}_{i+2})^2
\end{aligned}$$

7 point WENO scheme

$$
\begin{aligned}
v_0^L &= \frac{3}{12}\bar{q}_i + \frac{13}{12}\bar{q}_{i+1} - \frac{5}{12}\bar{q}_{i+2} + \frac{1}{12}\bar{q}_{i+3} \\
v_1^L &= \frac{-1}{12}\bar{q}_{i-1} + \frac{7}{12}\bar{q}_i + \frac{7}{12}\bar{q}_{i+1} - \frac{1}{12}\bar{q}_{i+2} \\
v_2^L &= \frac{1}{12}\bar{q}_{i-2} + \frac{-5}{12}\bar{q}_{i-1} + \frac{13}{12}\bar{q}_i + \frac{3}{12}\bar{q}_{i+1} \\
v_3^L &= \frac{-3}{12}\bar{q}_{i-1} + \frac{13}{12}\bar{q}_{i-2} - \frac{23}{12}\bar{q}_{i-3} + \frac{25}{12}\bar{q}_{i-4} \\
d_0 &= \frac{4}{35}, d_1 = \frac{18}{35}, d_2 = \frac{12}{35}, d_3 = \frac{1}{35} \\
\beta_0 &= \bar{q}_i(2107\bar{q}_i - 9402\bar{q}_{i+1} + 7042\bar{q}_{i+2} - 1854\bar{q}_{i+3}) \\
&+ \bar{q}_{i+1}(11003\bar{q}_{i+1} - 17246\bar{q}_{i+2} + 4642\bar{q}_{i+3}) + \bar{q}_{i+2}(7043\bar{q}_{i+2} - 3882\bar{q}_{i+3}) + 547\bar{q}_{i+3}^2 \\
\beta_1 &= \bar{q}_{i-1}(547\bar{q}_{i-1} - 2522\bar{q}_i + 1922\bar{q}_{i+1} - 494\bar{q}_{i+2}) \\
&+ \bar{q}_i(3443\bar{q}_i - 5966\bar{q}_{i+1} + 1602\bar{q}_{i+2}) + \bar{q}_{i+1}(2843\bar{q}_{i+1} - 1642\bar{q}_{i+2}) + 267\bar{q}_{i+2}^2 \\
\beta_2 &= \bar{q}_{i-2}(267\bar{q}_{i-2} - 1642\bar{q}_{i-1} + 1602\bar{q}_i - 494\bar{q}_{i+1}) \\
&+ \bar{q}_{i-1}(2843\bar{q}_{i-1} - 5966\bar{q}_i + 1922\bar{q}_{i+1}) + \bar{q}_i(3443\bar{q}_i - 2522\bar{q}_{i+1}) + 547\bar{q}_{i+1}^2 \\
\beta_3 &= \bar{q}_{i-3}(547\bar{q}_{i-3} - 3882\bar{q}_{i-2} + 4642\bar{q}_{i-1} - 1854\bar{q}_i) \\
&+ \bar{q}_{i-3}(7043\bar{q}_{i-2} - 17246\bar{q}_{i-1} + 7042\bar{q}_i) + \bar{q}_{i-1}(11003\bar{q}_{i-1} - 9402\bar{q}_i) + 2107\bar{q}_i^2
\end{aligned}
$$

3.3.3 Theoretical analysis of accuracy of high order upwind schemes

The above mentioned schemes are non-linear because the coefficients in the numerical scheme depend on the local solution. As a result of the non-linearity, theoretical evaluation of the performance of these schemes is not possible unless simplifications are made. In the case of smooth solutions (for instance, in the core of the tip vortex), the above mentioned schemes can be expected to oper-

ate near their optimal limits. In such a case, a linear analysis can be justified since the coefficients reduce to constants. Under optimal conditions the Koren's limiter $\phi = 1$ and for the WENO schemes, $w_r = d_r$ and the resulting schemes would be the same as the linear high order upwind schemes. Fourier analysis [126] would then be a very useful technique to evaluate the accuracy.

In this method, the numerical discretization of the derivatives of the harmonic function e^{ikx} is analyzed. The exact first derivative of this function is ike^{ikx}, whereas the discretized scheme would yield an expression that can be cast in the form ik^*e^{ikx}. The quantity k^*, termed the *modified* wave-number can then be used as a measure of the accuracy of the scheme with regard to the dispersive and dissipation errors. For a uniform grid, given a numerical scheme $\left(\frac{du}{dx}\right)_j \approx \frac{1}{\Delta x}\sum_{s=-m}^{n} a_s u_{j+s}$, the modified wavenumber is easily seen to be $k^*\Delta x = -i\sum_{s=-m}^{n} a_s e^{iks\Delta x}$. Fig. 3.3 shows the dispersion characteristics of the various schemes. The high order schemes exhibit much better spectral resolution characteristics.

A more quantitative picture can be obtained by comparing the attainable error ($\%Error = \frac{abs(real(k^*\Delta x) - k\Delta x)}{k\Delta x} \times 100$) using a given number of points per wavelength as seen from fig. 3.4. The ninth order (optimal) WENO scheme is seen to give an error of $< 0.01\%$ using approximately 8 points per wavelength. Fig. 3.5 and 3.6 show the dissipation errors involved with upwind schemes. Pure central differencing on uniform meshes assures zero Fourier-analytic dissipation errors, but it is well known that these schemes are unstable when applied to hyperbolic problems unless a certain amount of artificial dissipation is added [37].

The above analysis is routine and pertains to the performance of the linear

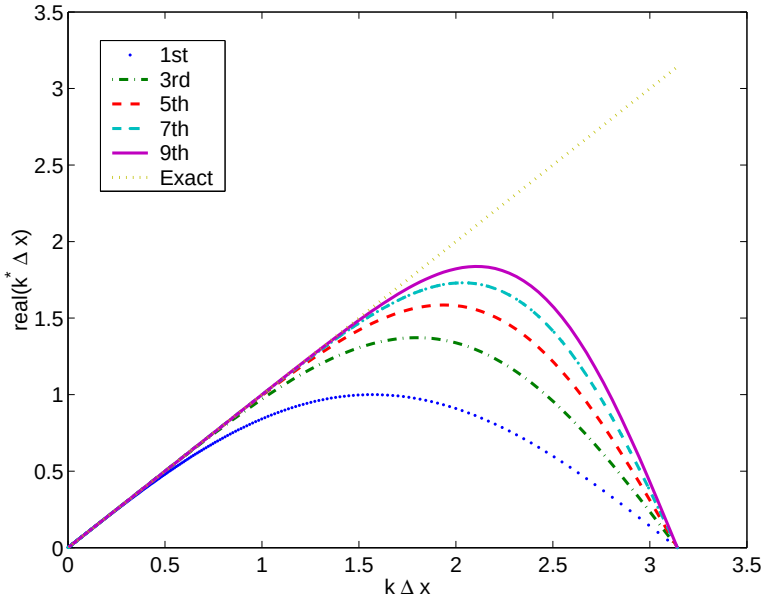

Figure 3.3: Dispersion relation for different linear upwind schemes

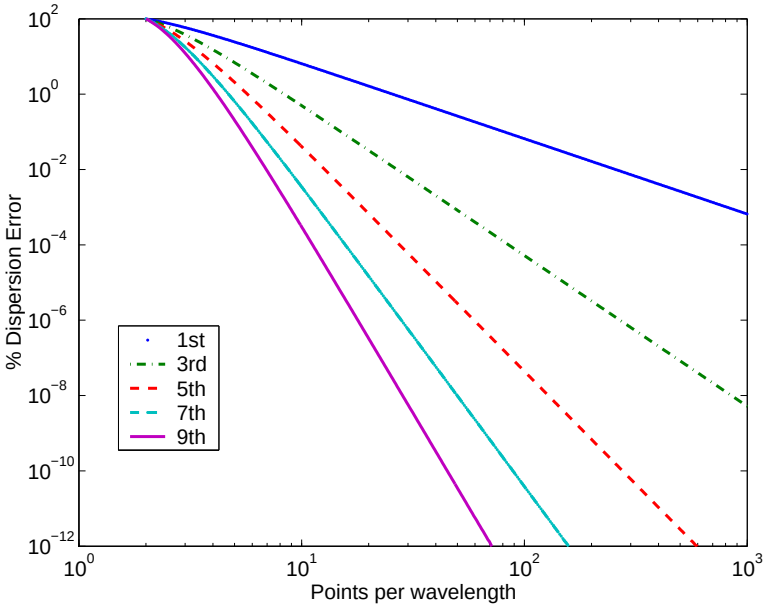

Figure 3.4: % Error in Dispersion relation. Points per wave-length $= \frac{2\pi}{k\Delta x}$.

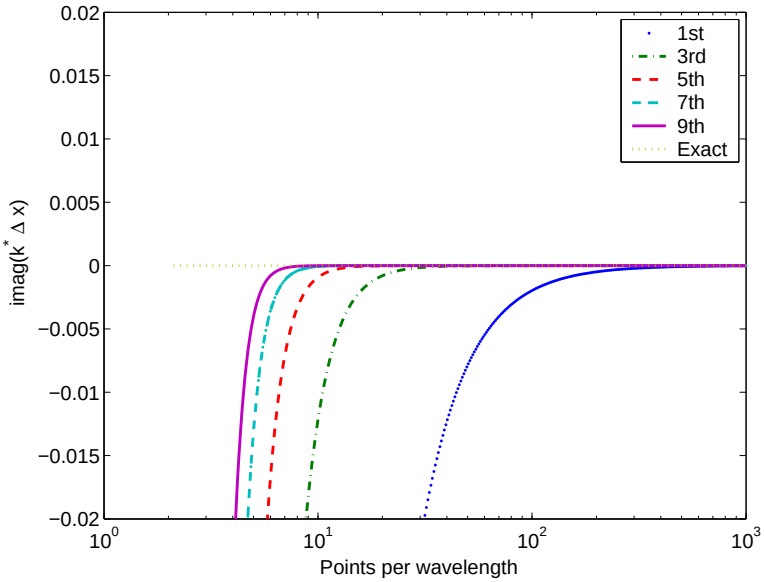

Figure 3.5: Diffusion error for different linear upwind schemes.

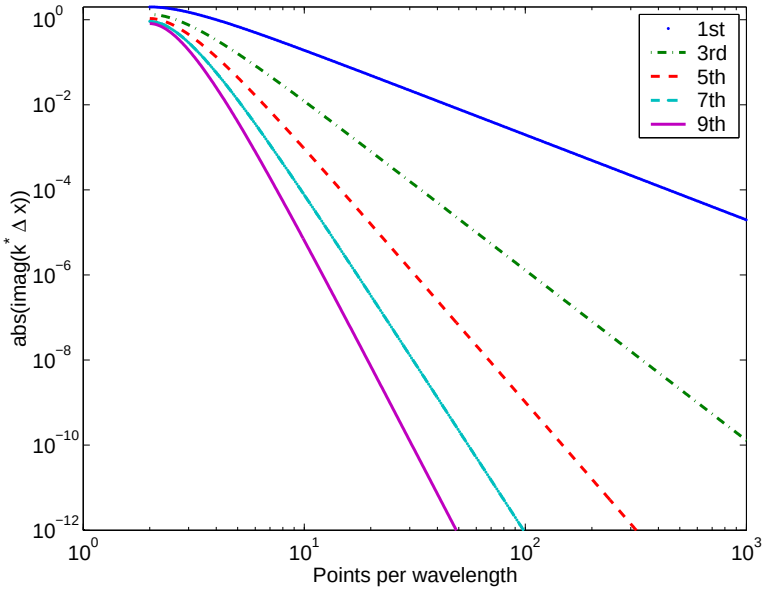

Figure 3.6: Diffusion error for different linear upwind schemes.

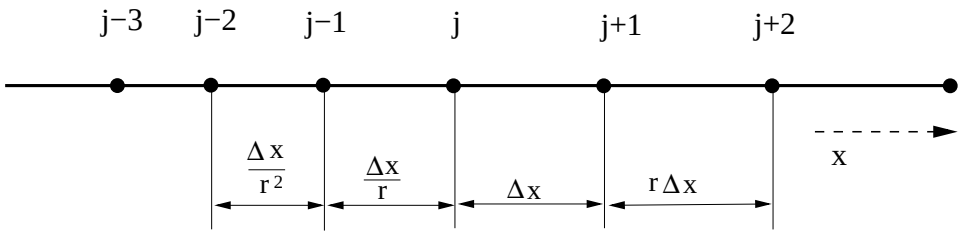

Figure 3.7: Schematic of geometrically stretched mesh with stretching ratio r.

schemes on uniform meshes. However, in practice, it will not be feasible to maintain constant spacing in all mesh regions. For instance, the ratio of the mesh spacing at the free-stream boundary to that at the wall can easily reach $O(10^6)$. Hence it is crucial to evaluate the schemes on stretched meshes. The above analysis is extended to geometrically stretched meshes with stretching ratio r as shown in fig. 3.7. A similar (in scope), but global analysis of L^2 norm of error on non-uniform grids (with an assumption of total number of grid points and analytic mapping functions) can be found in [129]. The advantage of using geometrically stretched meshes is that the analysis can be made completely local.

Consider a discretization in the transformed space ξ:

$$\left(\frac{du}{dx}\right)_j = \frac{d\xi}{dx}\frac{du}{d\xi} \tag{3.32}$$

$$= \frac{u_\xi}{x_\xi} \tag{3.33}$$

$$= \frac{\sum_{s=-m}^{n} a_s u_{j+s}}{\sum_{s=-p}^{q} b_s x_{j+s}} \tag{3.34}$$

Now, assuming $u = e^{ikx}$,

$$\left(\frac{du}{dx}\right)_j = \frac{\sum_{s=-m}^{n} a_s e^{ik(x_{j+s})}}{\sum_{s=-p}^{q} b_s x_{j+s}} \tag{3.35}$$

$$ik^* e^{ikx_j} = e^{ikx_j}\frac{\sum_{s=-m}^{n} a_s e^{ik(x_{j+s}-x_j)}}{\sum_{s=-p}^{q} b_s x_{j+s}} \tag{3.36}$$

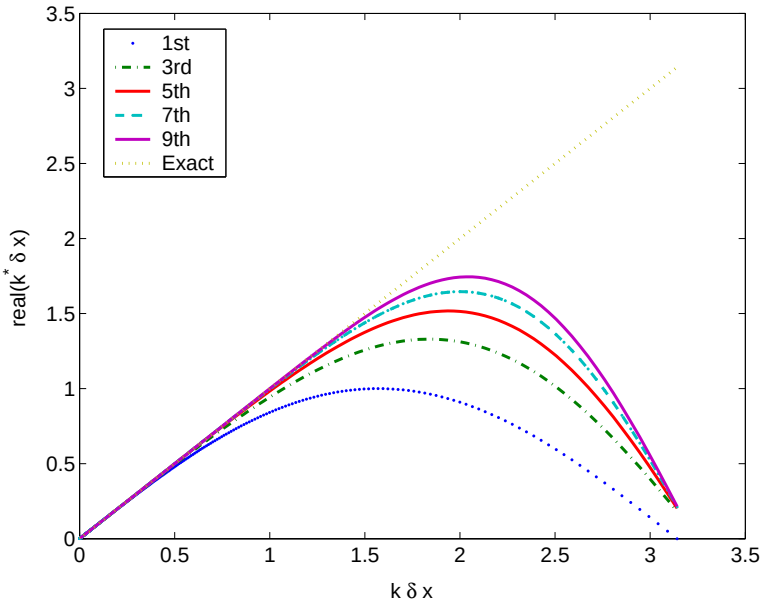

Figure 3.8: Dispersion relation with a mesh stretching ratio $r = 1.1$

Let $\delta x = x_\xi$ be the local cell length. For instance, the cell length can be computed using the same stencil as was used to determine u_ξ. The modified wave number is given by:

$$k^* \delta x = -i \delta x \left[\sum_{s=-m}^{n} a_s e^{ik(x_{j+s} - x_j)} \right] \tag{3.37}$$

$$= -i \sum_{s=-m}^{n} a_s e^{ik\delta x \frac{x_{j+s} - x_j}{\delta x}} \tag{3.38}$$

Unless mentioned otherwise, δx is calculated using the same stencil as u_ξ - i.e.,

$$x_\xi = \delta x = \sum_{s=-m}^{n} a_s (x_{j+s} - x_j) \tag{3.39}$$

The spatial difference terms are computed by:

$$\frac{x_{j+s} - x_{j+s-1}}{\delta x} = \frac{r^{s-1} \Delta x}{\delta x} \tag{3.40}$$

As seen from figs. 3.8 and 3.9, the accuracy is adversely affected when mesh stretching is introduced. A significant fact to be noted is that the formal accuracy

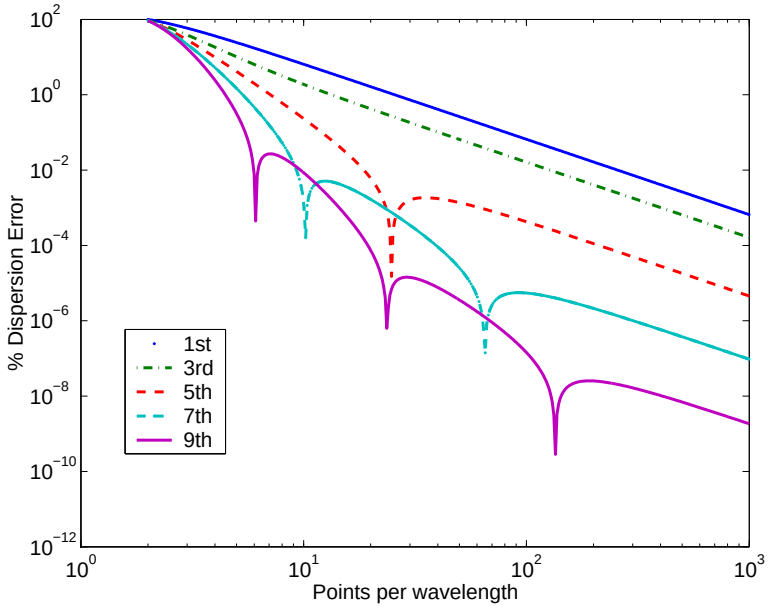

Figure 3.9: % Error in Dispersion relation with a mesh stretching ratio $r = 1.1$

(as $\Delta x \rightarrow 0$), for all the schemes on stretched meshes is just first order as evidenced by the slopes in fig. 3.9. However, in practical cases, one would expect to have an $O(10)$ points per wave length and it is evidenced that the higher order schemes are more accurate (than the first order scheme) in this region. Figs. 3.10 and 3.11 show the degradation in accuracy of the fifth order scheme with stretching in the *forward* ($r > 1$) and *backward* ($r < 1$) directions. Though the global trends are similar, backward stretching of the grid seems to be more detrimental, especially in the vicinity of the $O(10)$ points per wave length region. It has to be mentioned that in solving say, the NS equations, both stretching and contraction have to be considered since the stencils used to compute values to the left and right of the cell interface (q_L and q_R in eqn. 3.26) are usually mirror images of each other.

Figure 3.12 shows the performance of the fifth order upwind scheme when

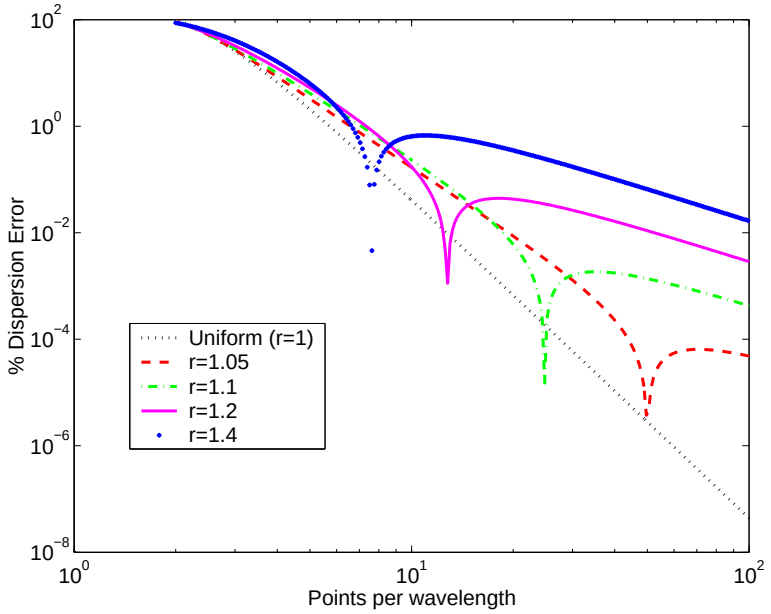

Figure 3.10: % Error in Dispersion relation for 5^{th} order upwind scheme with forward stretching

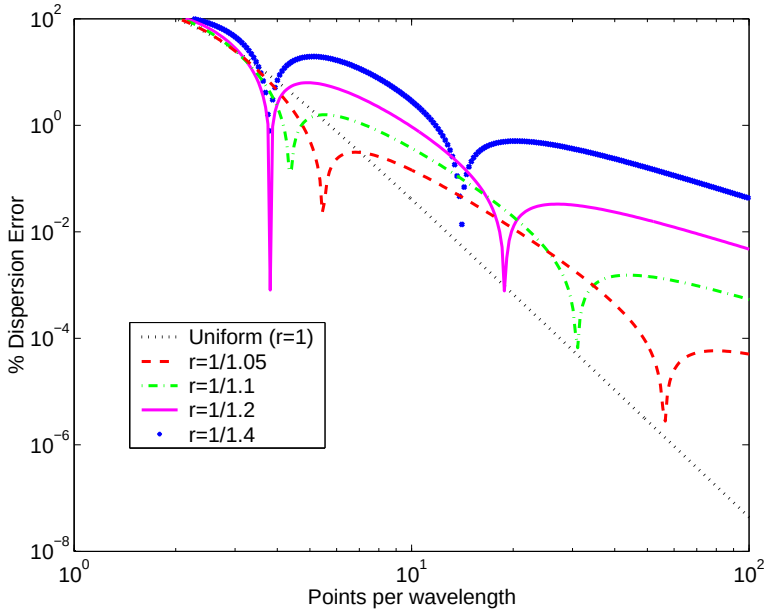

Figure 3.11: % Error in Dispersion relation for 5^{th} order upwind scheme with backward stretching

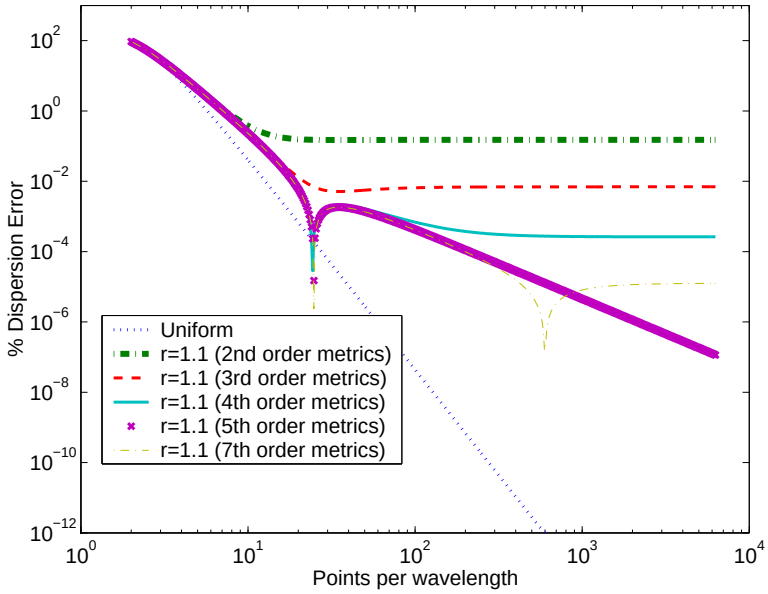

Figure 3.12: % Error in Dispersion relation for 5^{th} order upwind scheme with different metric calculations

different methods are used to determine the metrics x_ξ. It is seen that if different stencils are used to discretize u_ξ and x_ξ, then the overall accuracy is formally zeroth order and the error saturates regardless of the number of points used. Even the use of a x_ξ stencil that is wider than the u_ξ stencil is ultimately inconsistent and formally zeroth order. This also suggests that there is no benefit in defining x_ξ more accurately than u_ξ. It was also observed (not shown here) that even the use of analytically exact x_ξ will not be advantageous and the resulting scheme would still be formally zeroth order accurate. However, the use of metric terms higher than third order is seen to improve the accuracy in the practically feasible range ($< 10^2$ points per wavelength).

As seen from the comparison between figs. 3.5 and 3.13, the numerical dissipation error is aggravated on non-uniform grids. The high order schemes even exhibit slight theoretical instability (imaginary part of $k\delta x > 0$) for large stretch-

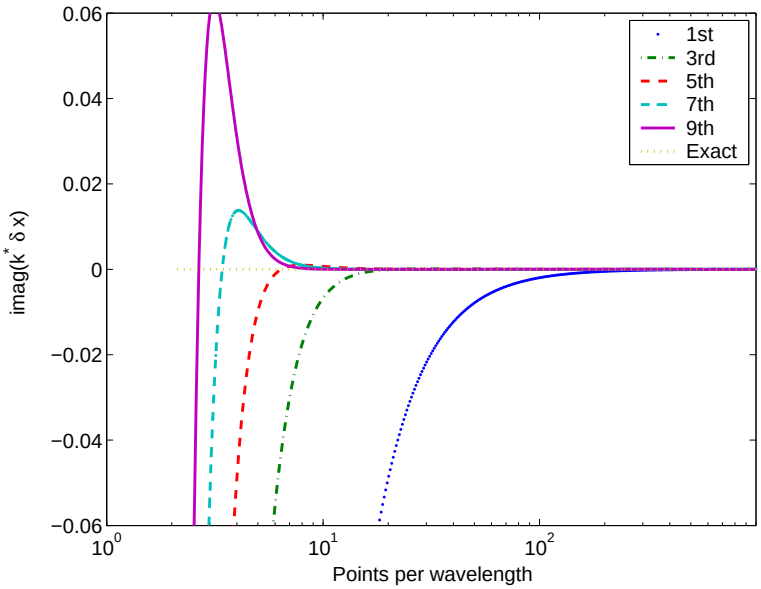

Figure 3.13: Diffusion error for different linear upwind upwind schemes for a stretching ratio $r = 1.1$

ing ratios. Hence, even *upwind schemes do not guarantee enough damping on stretched meshes*. Figure 3.14 confirms the formal first order accuracy of the diffusion error.

Sometimes, central difference schemes are preferred over upwind schemes since the symmetry of the stencil assures zero dissipation in a Fourier analysis. It is easy to see that this property does not hold if non-uniform meshes are used. Further, an empirical amount of artificial dissipation is required to stabilize central difference schemes.

As evidenced especially from fig. 3.11, numerical accuracy is severely degraded for large stretching ratios, and hence the mesh spacings in this thesis have been carefully monitored in the regions of interest. In the wall region, the stretching is kept to $r < 1.1$ and in the tip vortex roll-up region, a constant mesh spacing $r \approx 1$ is striven for at least in the cross-stream plane.

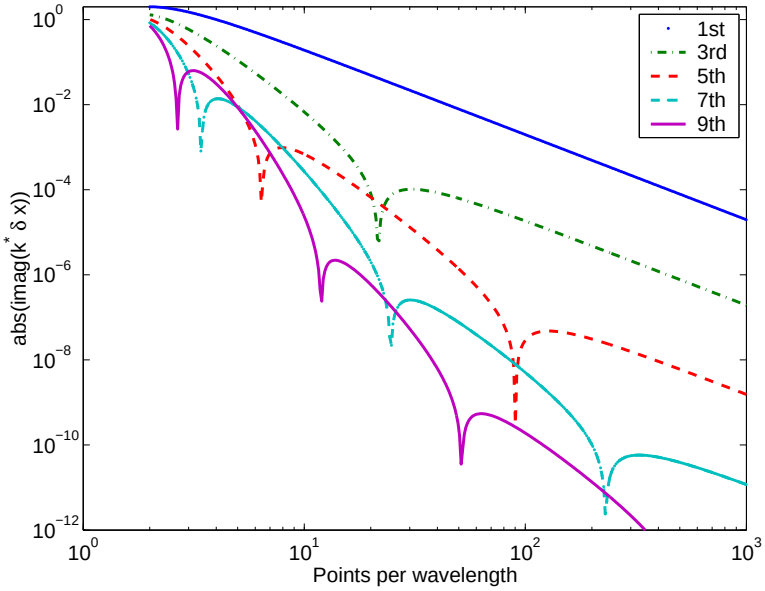

Figure 3.14: Diffusion error for different linear upwind upwind schemes for a stretching ratio $r = 1.1$

3.3.4 Performance of high order upwind schemes

In this section, the performance of upwind schemes will be evaluated based on numerical solution of vortex convection. The model problem involves isentropic convection of a two dimensional vortex in a uniform inviscid flow-field [128]. The initial conditions are set up such that:

- The spatial entropy gradient is zero,
- They correspond to an exact solution to the 2D Euler equations,

The exact solution to the above problem would then be a pure advection of the vortex at the free-stream velocity without any decay. Hence, the effects of numerical diffusion and dispersion can be evaluated.

The two dimensional Euler equations are a subset of equation 3.1 and are

given by:

$$\frac{\partial \mathbf{U}}{\partial t} + \frac{\partial \mathbf{F}}{\partial x} + \frac{\partial \mathbf{G}}{\partial x} = 0$$

where,

$$\mathbf{U} = \left\{ \begin{array}{c} \rho \\ \rho u \\ \rho v \\ e \end{array} \right\}, \quad \mathbf{F} = \left\{ \begin{array}{c} \rho u \\ p + \rho u^2 \\ \rho uv \\ (e+p)u \end{array} \right\}, \quad \mathbf{G} = \left\{ \begin{array}{c} \rho v \\ \rho uv \\ p + \rho v^2 \\ (e+p)v \end{array} \right\},$$

with $e = p/(\gamma - 1) + \rho(u^2 + v^2)/2$.

For all the cases, a grid with ($0 <= x <= 10, -5 <= y <= 5$) is used. Periodic conditions are assumed on all four grid boundaries. This is done in order to remove any effects of boundary inaccuracies and also to keep the domain small. As mentioned earlier, perturbations are added to the free-stream such that there is no entropy gradient in the flow-field.

Free-stream conditions are ($\rho = 1, u = 0.5, v = 0, p = 1/\gamma$). The perturbations are given by:

$$(\delta u, \delta v) = \frac{\beta}{2\pi} e^{\frac{1-r^2}{2}} (-(y - y_o), (x - x_o)) \tag{3.41}$$

$$\rho = \left[1 - \frac{(\gamma - 1)\beta^2}{8\gamma\pi} e^{1-r^2} \right]^{\frac{1}{\gamma - 1}} \tag{3.42}$$

$$p = \frac{\rho^\gamma}{\gamma} \tag{3.43}$$

where, $\beta = 5$ is the vortex strength and r is the distance from the vortex origin (5,0). The domain and initial pressure contours are shown in fig. 3.15. The vertical component of velocity and the pressure along the $y = 5$ line is shown in fig. 3.16. Primitive variable (eqn. 3.25) based spatial reconstruction is applied. An explicit third order Runge-Kutta scheme [130] is used for time advancement.

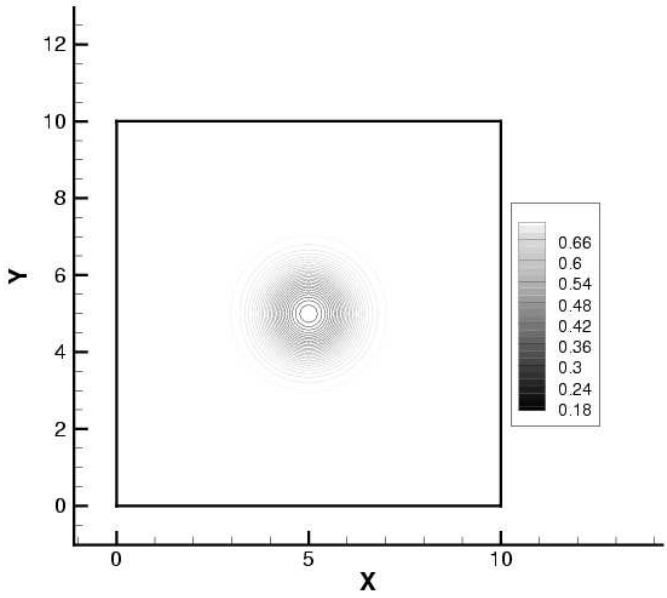

Figure 3.15: Computational domain and initial pressure contours for isentropic vortex convection

The objective of this exercise is to study the spatial discretization properties and hence the time-steps are chosen such that the error due to time integration is negligible. The CFL numbers in the x and y directions are respectively given by: $\nu_x = \frac{\Delta t}{\Delta x} max(|u| + a)$ and $\nu_y = \frac{\Delta t}{\Delta y} max(|v| + a)$.

Initial tests were performed on a uniformly spaced 41×41 mesh. The mesh spacing is thus 0.25 units, corresponding to 8 points per core diameter. A non-dimensional time-step $\Delta t = 0.05$ was used, which resulted in $\nu_x = 0.4$ and $\nu_y = 0.3$. A further reduction in time-step did not affect the solution, thus ensuring time-step independence. Figure 3.17 shows the evolution of the peak-to-peak velocity $(v_{max} - v_{min})$ computed using the various schemes. The third order schemes are found to be extremely dissipative while the seventh and ninth

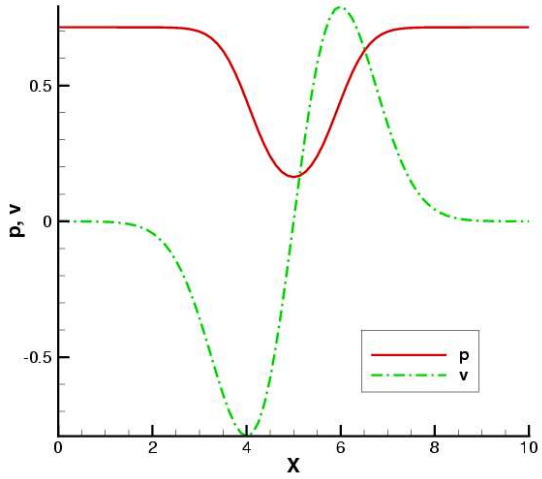

Figure 3.16: Initial conditions along the $y = 5$ line

order schemes are seen to perform well even for such a coarse discretization. The dissipative nature of the fifth order WENO scheme, in relation to the unlimited fifth order upwind scheme suggests that the smoothness indicators β_r in eqn. 3.32 do not perform well. Figure 3.18 compares the vertical velocity during different stages of evolution with the exact solution for the fifth order WENO scheme. A gradual decay is evident. Figure 3.19 shows the low extent of numerical diffusion for the seventh order WENO scheme. The % error in the computed pressure at the centre of the vortex is shown in fig. 3.20. The higher order schemes are able to compute the pressure to much less than 1% accuracy.

On the use of a uniformly spaced 81×81 mesh (16 points per core diameter), the fifth order WENO scheme performs much better as seen in fig. 3.21. For these computations, a non-dimensional time step $\Delta t = 0.025$ was used. The vortex is convected with negligible numerical diffusion. The corresponding error in the computed pressure in the vortex center is found to be 2% after convecting

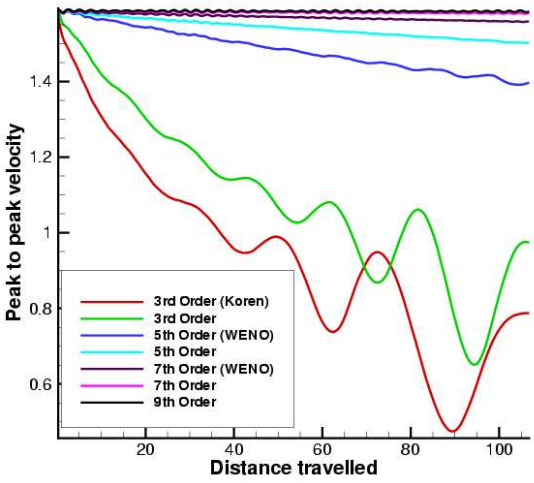

Figure 3.17: Evolution of peak-to-peak velocity as a function of traversed core-radii for 41×41 uniformly spaced mesh.

400 core-radii. The seventh and ninth order schemes show errors $< 0.1\%$ after 400 core-radii of travel (fig. 3.22). The use of a uniformly spaced 61×61 mesh (12 points per core diameter) is also seen (fig. 3.23) to yield solutions within plotting accuracy.

From the above calculations, it appears that ≈ 10 points per core diameter are probably required to accurately reconstruct and resolve a tip vortex-like flow field using high order schemes. On the other hand, the third order scheme is found to be extremely lacking when used with such coarse discretizations. The above findings have been used as guidelines for the actual 3D tip vortex simulations.

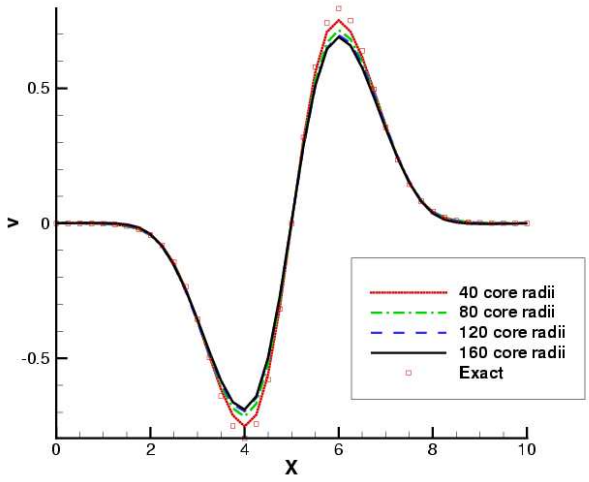

Figure 3.18: Vertical velocity profile along the $y = 5$ line using the fifth order WENO scheme on the 41×41 uniformly spaced mesh.

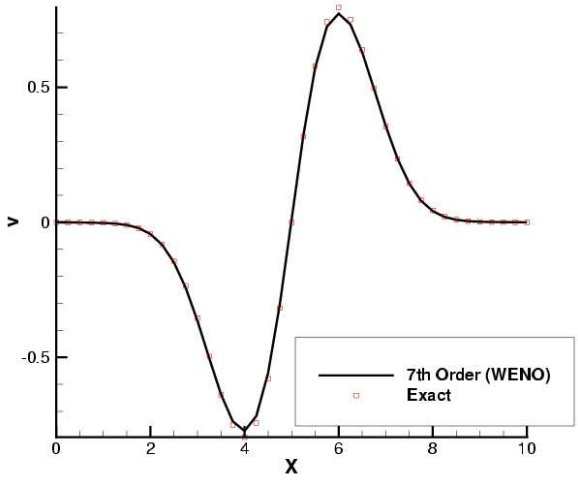

Figure 3.19: Vertical velocity profile along the $y = 5$ line using the Seventh order WENO scheme on the 41×41 mesh after 160 core radii of travel

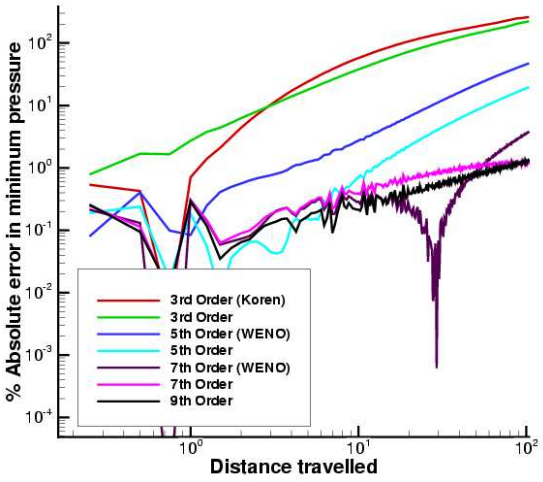

Figure 3.20: % error in computed pressure at the core center for the 41×41 uniformly spaced mesh.

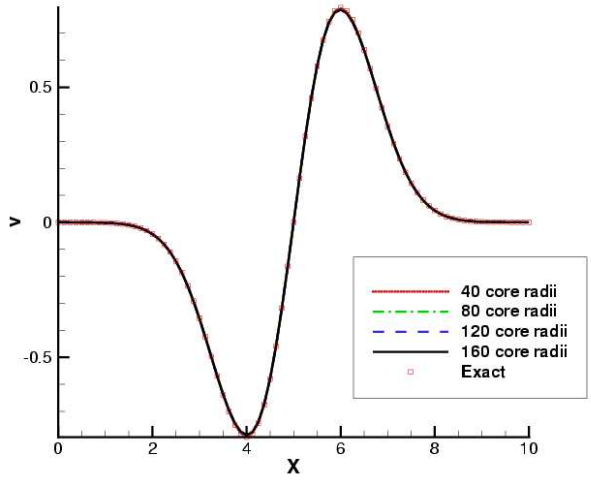

Figure 3.21: Vertical velocity profile along the $y = 5$ line using the fifth order WENO scheme on the 81×81 uniformly spaced mesh.

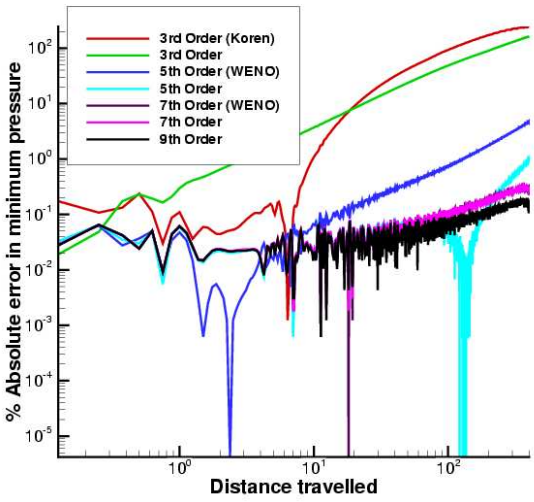

Figure 3.22: % error in computed pressure at the core center for the 81×81 uniformly spaced mesh.

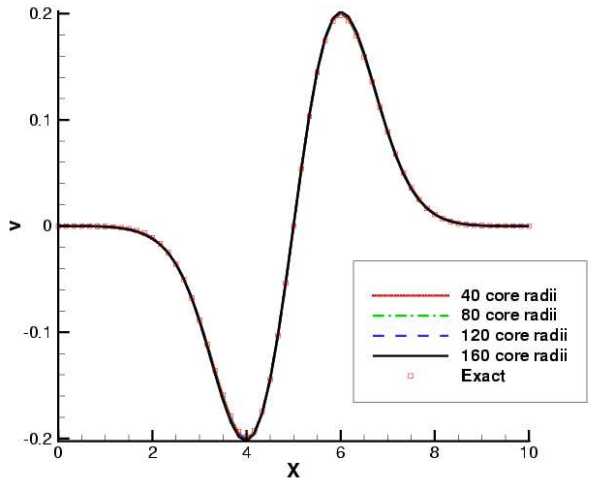

Figure 3.23: Vertical velocity profile along the $y = 5$ line using the fifth order WENO scheme on the 61×61 uniformly spaced mesh.

3.4 Viscous terms

In the baseline TURNS code, the Thin-layer approximation is used while discretizing the viscous terms (eqns. 3.7-3.9). In this approximation, only the terms that have a very strong dependence on the derivative in the wall-normal direction are considered. The basis for this argument is the fact that for attached flows, the boundary layer is very thin and the streamwise and spanwise gradients are much smaller than the wall-normal gradients. This approximation is valid in the near-wall region for high Reynolds number attached flows. Further, the grid lines have to be orthogonal to each other. However, for tip vortex flows,

a) In the near-wall region, the flow is not attached: Secondary and tertiary flow separation can be expected near the tip region,

b) In the tip vortex roll-up region, strong gradients exist in all three directions.

Under these conditions, the Thin-layer assumption fails and one has to consider the full viscous terms. A complete listing of the viscous terms after coordinate transformation can be found in [131]. Numerical discretization of these terms involves expressions of the form:

$$\frac{\partial}{\partial \xi}\left(\alpha \frac{\partial \beta}{\partial \eta}\right) \tag{3.44}$$

These terms are computed using second order accurate central differencing. For instance, the above expression would be discretized as:

$$\frac{1}{\Delta \xi}\left(\left[\alpha_{j+\frac{1}{2}} \frac{\beta_{k+1}-\beta_k}{\Delta \eta}\right]-\left[\alpha_{j-\frac{1}{2}} \frac{\beta_k-\beta_{k-1}}{\Delta \eta}\right]\right) \tag{3.45}$$

where,

$$\alpha_{j\pm\frac{1}{2}} = \frac{\alpha_j + \alpha_{j\pm 1}}{2} \tag{3.46}$$

3.4.1 Analysis of accuracy

In this section, akin to inviscid differencing on stretched meshes, an analysis of viscous differencing on stretched meshes will be presented. Consider a discretization of the second derivative in the transformed space ξ:

$$\left(\frac{d^2u}{dx^2}\right)_j = \left[\xi_x\left(\xi_x u_\xi\right)_\xi\right]_j \tag{3.47}$$

$$= \left[\frac{1}{x_\xi}\left(\frac{u_\xi}{x_\xi}\right)_\xi\right]_j \tag{3.48}$$

$$= \frac{1}{(x_\xi)_j}\sum_{s=-n}^{n-1} a_s \left(\frac{u_\xi}{x_\xi}\right)_{j+\frac{1}{2}+s} \tag{3.49}$$

$$= \frac{1}{(x_\xi)_j}\sum_{s=-n}^{n-1} a_s \left(\frac{\sum_{t=-n}^{n-1} a_t u_{j+1+s+t}}{\sum_{t=-n}^{n-1} a_t x_{j+1+s+t}}\right) \tag{3.50}$$

For instance, a second order accurate[4]scheme is given by $\{a_{-1}, a_0\} = \{1, -1\}$. A fourth order scheme results when $\{a_{-2}, a_{-1}, a_0, a_1\} = \{\frac{1}{24}, \frac{-27}{24}, \frac{27}{24}, \frac{-1}{24}\}$.

Now, assuming $u = e^{ikx}$,

$$-(k^*)^2 e^{ikx_j} = \frac{e^{ikx_j}}{(x_\xi)_j}\sum_{s=-n}^{n-1} a_s \left(\frac{\sum_{t=-n}^{n-1} a_t e^{ik(x_{j+1+s+t}-x_j)}}{\sum_{t=-n}^{n-1} a_t x_{j+1+s+t}}\right) \tag{3.51}$$

Let $\delta x = x_\xi$ be the local cell length as in the inviscid differencing (sec 2.3.3). Then the modified wave number is given by:

$$k^* = \left[-\frac{1}{\delta x}\sum_{s=-n}^{n-1} a_s \left(\frac{\sum_{t=-n}^{n-1} a_t e^{ik(x_{j+1+s+t}-x_j)}}{\sum_{t=-n}^{n-1} a_t x_{j+1+s+t}}\right)\right]^{\frac{1}{2}} \tag{3.52}$$

Therefore,

$$k^*\delta x = \left[-\sum_{s=-n}^{n-1} a_s \left(\frac{\sum_{t=-n}^{n-1} a_t e^{ik\delta x\frac{(x_{j+1+s+t}-x_j)}{\delta x}}}{\sum_{t=-n}^{n-1} a_t \frac{x_{j+1+s+t}}{\delta x}}\right)\right]^{\frac{1}{2}} \tag{3.53}$$

[4]Second order accuracy is achieved on a uniform mesh.

Notice that the same discretization stencil and coefficients have been used to difference u_ξ and x_ξ. This is not necessary.

Figure 3.24 and 3.25 show the error in the real part of the modified wave number, which corresponds to the *diffusion* error. It is evident that the inaccuracies of using a stretched mesh are not as prominent for the second order scheme. A Taylor series expansion reveals the leading error terms for the second order scheme to be: to be:

$$\frac{\Delta x}{3}\frac{d^3u}{dx^3}\left[\frac{r-1}{r}\right] + \frac{(\Delta x)^2}{12}\frac{d^4u}{dx^4}\left[\frac{r^3+1}{r^3+r^2}\right] \tag{3.54}$$

and accordingly the dispersion (third order derivative) and diffusion (fourth order derivative) terms are scaled by the respective coefficients. These coefficients are shown in fig. 3.26 and are seen to be smooth and well-behaved near $r = 1$. The fourth order scheme is more accurate in the feasible discretization range (< 100 points per wavelength).

The dispersion error is shown in fig. 3.27 for a stretching ratio $r = 1.2$.

3.5 Calculation of spatial metrics

As seen from the analysis of the inviscid and viscous discretizations, accurate calculation of the spatial metric terms is critical to achieve overall high order accuracy on non-uniform meshes. In the present work, a finite volume formulation is used and hence the metric and jacobian terms will be replaced by areas and volumes. Given a structured distribution of mesh points in three dimensional space, high order accurate schemes are used to determine the edges of the cell volume. Figure 3.28 shows a schematic of a 2D volume (for simplicity of presentation). The filled circles represent the original grid point distribution and the

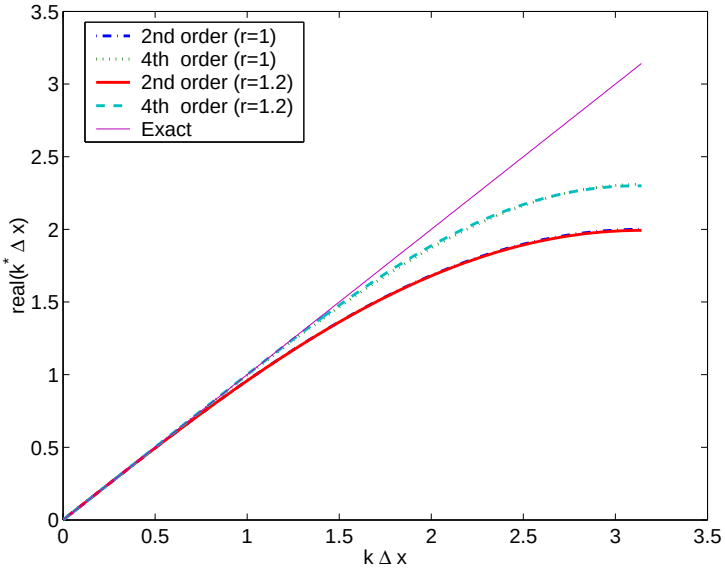

Figure 3.24: Diffusion properties of central difference schemes for discretization of second derivative.

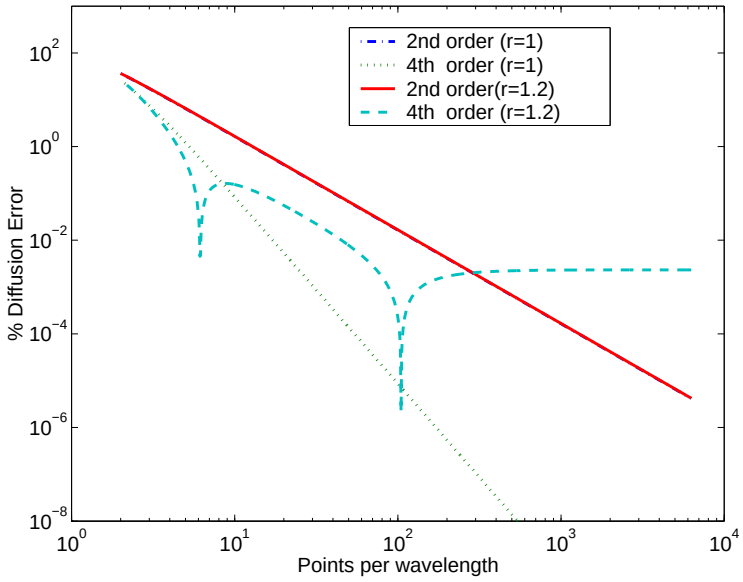

Figure 3.25: % Diffusion Error for central difference schemes.

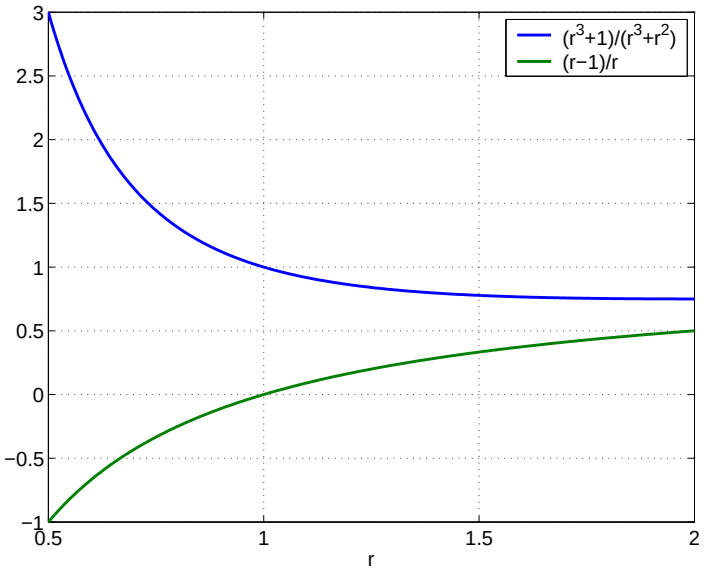

Figure 3.26: Coefficients of the leading error terms for second order differencing.

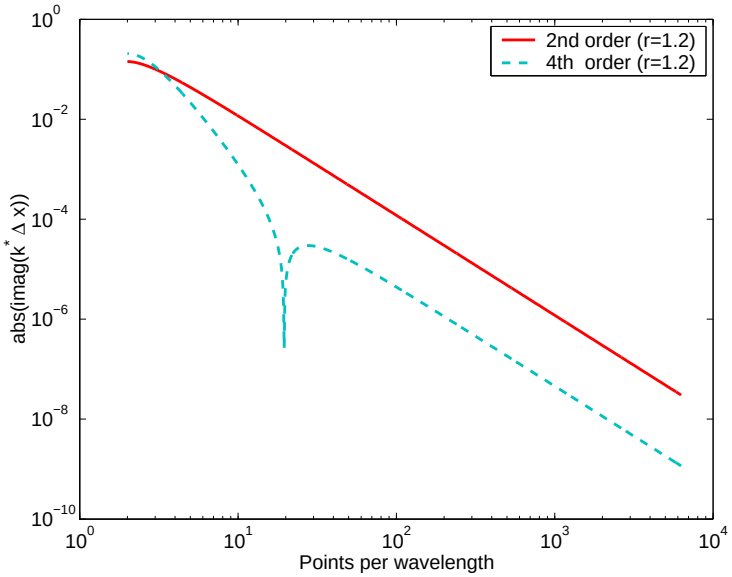

Figure 3.27: Dispersion Error for central difference schemes.

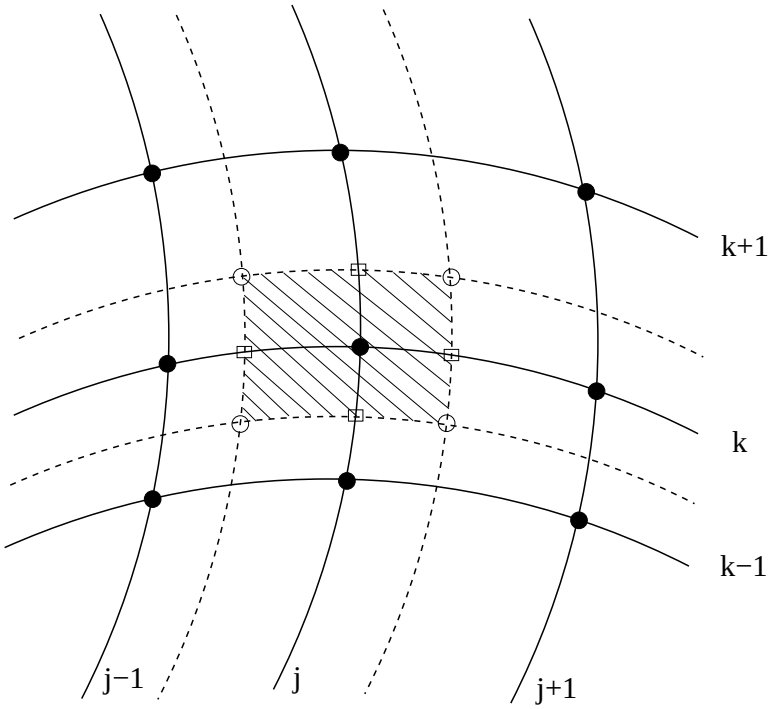

Figure 3.28: Schematic of 2D mesh point distribution and control point definition.

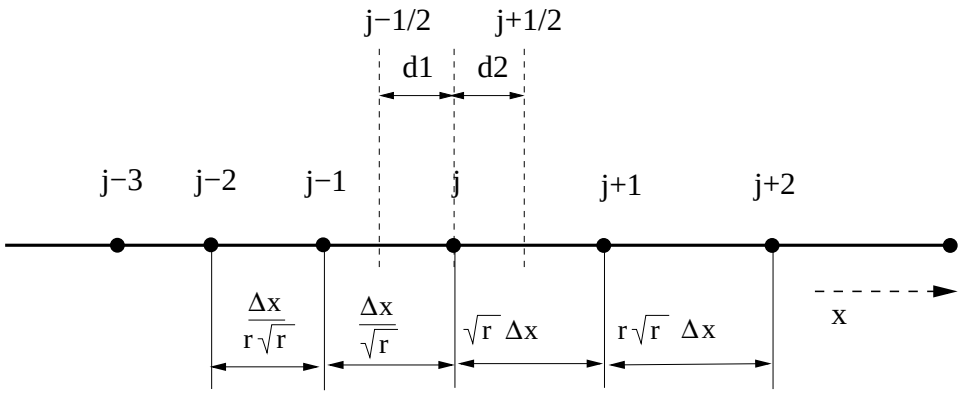

Figure 3.29: Non-uniform mesh and exact δx.

empty circles and squares represent the boundaries of the control volume. The cell area (shaded) is computed as a sum of the four quadrilaterals defined by the mesh and control points. In the three dimensional case, the corresponding eight hexahedra are used to compute the volume. The fluxes $\hat{\mathbf{F}}_{j\pm\frac{1}{2}}$ and $\hat{\mathbf{G}}_{j\pm\frac{1}{2}}$ are evaluated at the points represented by empty squares.

In a finite volume sense, accurate metric calculation boils down to using high order accurate numerical schemes to identify the location of the control points. The accuracy properties of such schemes will now be demonstrated for a case shown in fig. 3.29. For this case, the exact location of the edges of the control volume boundaries are shown and the corresponding cell length is given by

$$x_{j+\frac{1}{2}} - x_{j-\frac{1}{2}} = \delta x = d1 + d2 = \frac{\Delta x}{1+\sqrt{r}} + \frac{\sqrt{r}\Delta x}{1+\sqrt{r}} = \Delta x \qquad (3.55)$$

Without any loss of generality, $\Delta x = 1$ will be assumed. Second, fourth and sixth order schemes can be easily derived using Taylor series expansions.

In certain portions of a mesh, for instance, near the leading and trailing edges of a body conforming blade mesh, the mesh spacings could rapidly change and the associated slopes could be discontinuous. Using high order schemes to

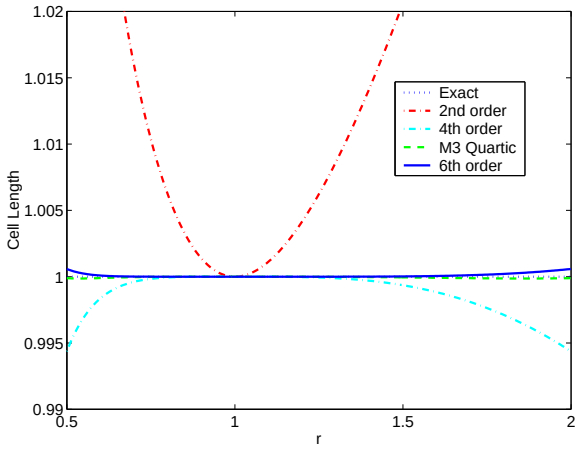

Figure 3.30: Accuracy of different numerical schemes to compute *half* points.

identify the interfaces could then become inaccurate (akin to the oscillations produced near solution discontinuities in uniform meshes). Hence, the slope-limited quartic scheme of Huynh [132] has been used.

Figures 3.30 and 3.31 compare the above-mentioned numerical schemes in identifying the *half* points $x_{j\pm\frac{1}{2}}$. It is seen that the second order scheme is extremely inaccurate and can hence introduce large inaccuracies in the overall solution as well. The Quartic and sixth order methods yield an error $< 0.01\%$ for moderately stretched meshes. For all the computations in this work, the Quartic scheme is used to evaluate the half point locations. The slope limiter is turned off in all the meshes except for the blade mesh.

3.6 Rotating reference frame

For computation of unsteady flows involving moving bodies, the governing equations are usually solved in the inertial frame of reference. This requires computation of the metric terms and connectivity information of the overset grids (if

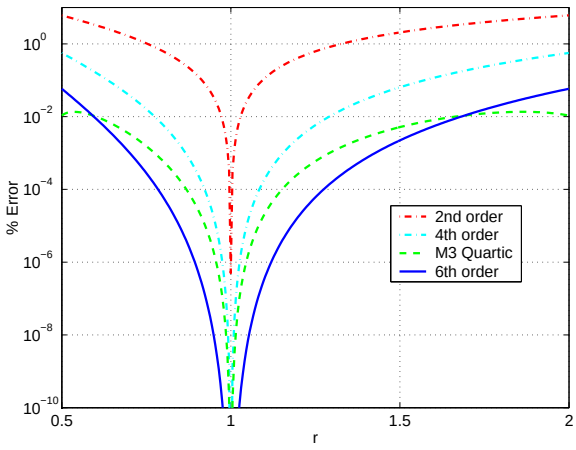

Figure 3.31: % Error in computing cell lengths using different numerical schemes.

any) at every time-step. This additional cost can be avoided for hovering rotors if the equations are solved in the rotating reference frame [26]. To account for the non-inertial reference frame, the fluxes in equation 3.1 become:

$$\mathbf{F_i} = \begin{Bmatrix} \rho(u-u_g) \\ \rho u(u-u_g)+p \\ \rho u(v-v_g) \\ \rho u(w-w_g) \\ (u-u_g)(e+p) \end{Bmatrix} \tag{3.56}$$

$$\mathbf{G_i} = \begin{Bmatrix} \rho(v-v_g) \\ \rho v(u-u_g) \\ \rho v(v-v_g)+p \\ \rho v(w-w_g) \\ (v-v_g)(e+p) \end{Bmatrix} \tag{3.57}$$

$$\mathbf{H_i} = \left\{ \begin{array}{c} \rho(w - w_g) \\ \rho w(u - u_g) \\ \rho w(v - v_g) \\ \rho w(w - w_g) + p \\ (w - w_g)(e + p) \end{array} \right\} \tag{3.58}$$

where, $\mathbf{U} = \{u, v, w\}$ is the vector of physical velocities (in the inertial frame), and $\mathbf{U}_g = \{u_g, v_g, w_g\} = \mathbf{\Omega} \times \mathbf{r}$ is the rotational velocity vector. $\mathbf{\Omega}$ is the angular velocity vector and $\mathbf{r}$ is the relative position vector from the axis of rotation. In addition, the relative acceleration terms have to be included as a source term vector $\mathbf{S}$ in eqn. 3.1:

$$\mathbf{S} = \left\{ \begin{array}{c} 0 \\ -\rho\mathbf{\Omega} \times \mathbf{U} \\ 0 \end{array} \right\} \tag{3.59}$$

3.7 Turbulence modeling

The Reynolds Averaged Navier-Stokes (RANS) equations can be derived from the Navier-Stokes (NS) equations by decomposing the flow quantities into a mean component and a *Reynolds averaged* component [18]. The motivation behind this averaging is two-fold:

• Usually, in engineering and physical processes, one is interested in the mean (or phase averaged) quantities,

• In the numerical solution, it is not required to resolve all the turbulent scales and hence the problem becomes tractable.

However, the averaging introduces new terms that have to be modeled rather than resolved. For instance, the averaged (incompressible) momentum equations

become:

$$\rho\left[\frac{\partial u_i}{\partial t}+u_j\frac{\partial u_i}{\partial x_j}\right]=-\frac{\partial p}{\partial x_i}+\frac{\partial}{\partial x_j}\left[\tau_{ij}-\rho<u_i'u_j'>\right] \tag{3.60}$$

where $'$ denotes fluctuating quantities and $<.>$ represents Reynolds averaging. The turbulence modeling problem is to close the above equation by approximating the so-called Reynolds stress term $\rho<u_i'u_j'>$. There has been extensive research over the past 4 decades on turbulence modeling, but there does not seem to be one superior model that consistently gives good predictions for different flow configurations [39]. In their most general form, turbulence models can be represented in the form [43], [46]

$$<u_i'u_j'>=a\frac{2}{3}\delta_{ij}k-pS_{ij}-q(S_{ik}W_{kj}-W_{ik}S_{kj})-r(S_{ij}^2-\frac{1}{3}|S|^2\delta_{ij}) \tag{3.61}$$

where, a is a constant, and p, q, and r are functions of mean flow quantities, $S_{ij}=\frac{1}{2}(\partial_j u_i+\partial_i u_j)$ is the mean rate-of-strain tensor and $W_{ij}=\frac{1}{2}(\partial_j u_i-\partial_i u_j)+\epsilon_{jik}\Omega_k$ is the vorticity tensor (including the angular velocity of frame rotation Ω).

The most tractable and frequently used models for complex flows invoke the linear eddy viscosity hypothesis, in which, only the first order terms are retained (q=0, r=0). In this case, the function p is determined either algebraically (such as in Baldwin-Lomax models [122]), or using one equation (e.g. Spalart-Allmaras [42], Baldwin-Barth [133]) or two equation (e.g. $k-\epsilon$, $k-\omega$ [41]) partial differential equation (PDE) based models. The advantage of these models is that these are simple, relatively inexpensive and most importantly, numerically stable. However, since the higher order terms in eqn. 3.61 are dropped, these models cannot inherently model effects like streamline curvature, flow rotation etc[5][44]. The more complicated Second Moment Closure (SMC) models retain

[4]All the un-primed quantities are averages.

the functions q and r, and are hence physically more appealing in modeling problems that involve the afore-mentioned effects along with anisotropic mechanisms. Although the SMC models have been shown to be superior in some specific situations [44, 134], they do not show sustained improvement over the linear eddy viscosity models. In addition, the complexity of these models and associated computational stiffness has limited the range of application.

The baseline TURNS code uses the algebraic Baldwin-Lomax [122] turbulence model. This model relates the turbulent viscosity to the instantaneous flow-field and is thus quasi-steady. The applicability of this model, is however restricted to steady and attached flows (as seen, for instance in [135]). Of the unsteady PDE based models, the one-equation Spalart-Allmaras (SA) turbulence model was chosen for implementation in this thesis. Though relatively recent, this model has gained enormous popularity in the Aerospace flow problems as it was developed with such applications in mind. Further, a strong emphasis was applied on its numerical implementation and behavior during the development process. This turbulence model has been validated for a variety of applications involving adverse pressure gradients and flow separation [39, 42, 136].

3.7.1 Spalart Allmaras (SA) turbulence model

In the SA model, the Reynolds stresses are related to the mean strain by the isotropic relation, $< u_i' u_j' >= -2\nu_t S_{ij}$, where ν_t is the turbulent eddy viscosity, which is obtained by solving a PDE for a related variable $\bar{\nu}$. Note that, in relation to eqn. 3.61, $a = q = r = 0$.

[5]Since the neglected terms represent exact production terms due to mean flow gradients and system rotation.

The equation for the working variable $\bar{\nu}$ in a fully turbulent flow[6]is given by:

$$\frac{\partial \bar{\nu}}{\partial t} + \mathbf{V}.(\nabla \bar{\nu}) = \frac{1}{\sigma}\left[\nabla.\left((\bar{\nu}+\nu)\nabla\bar{\nu}\right) + c_{b2}(\nabla\bar{\nu})^2\right] + c_{b1}\bar{S}\bar{\nu} - c_{w1}f_w\left[\frac{\bar{\nu}}{d}\right]^2 \quad (3.62)$$

The eddy viscosity ν_t is related to $\bar{\nu}$ by the relation,

$$\nu_t = \bar{\nu} f_{v1}, \quad (3.63)$$

where f_{v1} is a function of $\bar{\nu}$ and the molecular viscosity ν and is defined as:

$$f_{v1} = \frac{\chi^3}{\chi^3 + c_{v1}^3} \quad (3.64)$$

with $\chi = \frac{\bar{\nu}}{\nu}$ and $c_{v1} = 7.1$. The function f_{v1} is essentially an empirical damping function (equivalent to the well-known Van-Driest damping [18]) that attenuates the eddy viscosity in the viscous sub-layer. In other words, $\bar{\nu} \approx \nu_t$ everywhere, except in the sub-layer, where an attempt is made at ensuring a linear profile with the correct log-law intercept.

The left hand side of the equation 3.62 accounts for the convection of the working variable at the mean flow velocity $\mathbf{V}$. The first term on the right hand side represents the diffusion, followed by the production and destruction terms. In the production term,

$$\bar{S} = S + \frac{\bar{\nu}}{\kappa^2 d^2} f_{v2} \quad with \quad (3.65)$$

$$S = |\omega| = \nabla \times \mathbf{V} \quad (3.66)$$

$$f_{v2} = 1 - \frac{\chi}{1 + \chi f_{v1}} \quad (3.67)$$

In the destruction term,

$$f_w = g\left[\frac{1 + c_{w3}^6}{g^6 + c_{w3}^6}\right]^{\frac{1}{6}} \quad (3.68)$$

[6]In the original model, transition is accounted for by specifying the trip line. In this dissertation, all computations assume fully turbulent flow.

$$g = r + c_{w2}(r^6 - r) \tag{3.69}$$

$$r = min(\frac{\bar{\nu}}{\bar{S}\kappa^2 d^2}, 10.0) \tag{3.70}$$

where, d is the distance to the nearest wall. The various constants in the turbulence model are:

$$\sigma = \frac{2}{3} \tag{3.71}$$

$$c_{b1} = 0.1355 \tag{3.72}$$

$$c_{b2} = 0.622 \tag{3.73}$$

$$c_{w1} = \frac{c_{b1}}{\kappa^2} + \frac{1 + c_{b2}}{\sigma} \tag{3.74}$$

$$c_{w2} = 0.3 \tag{3.75}$$

$$c_{w3} = 2.0 \tag{3.76}$$

$$\kappa = 0.41 \tag{3.77}$$

$$\tag{3.78}$$

3.7.2 Initial and Boundary Conditions

Unless specified by the experiment, the initial and free-stream values of the $\bar{\nu}$ is set to the $\bar{\nu} = 0.1\nu$ as suggested in [42]. At the far-field boundaries, a characteristic treatment is used, i.e., depending on the direction of the local velocity vector, $\bar{\nu}$ is either extrapolated from the interior or set to the free-stream value. At a solid surface, $\bar{\nu} = 0$ is set, thus satisfying the Reynolds-stress boundary condition. Across wake cuts, a high order averaging similar to eqn. 3.93 is used.

3.7.3 Numerical solution

The turbulence model equations are solved in an uncoupled manner with the NS equations. In this approach, the NS equations are advanced incrementally in time, with the eddy viscosity held fixed within each time-step. Correspondingly, after every time-step of the NS solver, the mean flow-field variables are held fixed and the turbulence field is advanced one-time step. This makes the implementation of the turbulence model easier than the coupled approach. The implicit second order backward difference scheme is used with Newton sub-iterations for time integration.

3.7.4 Spatial discretization

The convection terms are discretized using a second order upwind scheme. For instance,

$$U_i \left(\frac{\partial \bar{\nu}}{\partial \xi} \right)_i = \frac{(U_i + |U_i|)}{2} \frac{[1.5\bar{\nu}_i - 0.5\bar{\nu}_{i-1}]}{\Delta\xi} + \frac{(U_i - |U_i|)}{2} \frac{[1.5\bar{\nu}_{i+1} - 0.5\bar{\nu}_i]}{\Delta\xi} \quad (3.79)$$

The diffusion terms are cast in a modified form (equation 26 in [42]) and discretized using second order central differences.

3.7.5 Implicit inversion

The semidiscrete form of eqn. 3.62 in transformed coordinates can be represented as:

$$\frac{d\bar{\nu}}{dt} = R \quad (3.80)$$

where, R represents the convection, diffusion and source terms. A linearized Euler implicit scheme would then yield the update at time $n+1$,

$$[I + \Delta t\delta_\xi A^n + \Delta t\delta_\eta B^n + \Delta t\delta_\zeta C^n + \Delta t S^n]\Delta\bar{\nu}^n = \Delta t R^n \quad (3.81)$$

$$\bar{\nu}^{n+1} = \bar{\nu}^n + \Delta\bar{\nu}^n \quad (3.82)$$

where, $\Delta\bar{\nu}^n = \bar{\nu}^{n+1} - \bar{\nu}^n$, S is the source jacobian and A, B, C are the jacobians of the combined inviscid and viscous *fluxes* in the ξ, η, ζ directions respectively. δ is the associated upwind difference.

An Alternating Direction Implicit (ADI) factorization would yield a system given by:

$$[I + \Delta t\delta_\xi A^n]\,[I + \Delta t\delta_\eta B^n + \Delta t S^n]\,[I + \Delta t\delta_\zeta C^n]\,\Delta\bar{\nu}^n = \Delta t R^n \quad (3.83)$$

Even though ADI factorization reduces the $N^3 \times N^3$ system to a $3(N \times N)$ system, convergence was seen to be very slow and the allowable time-step size was found to be very restrictive. The factorization error is seen to be $O(\Delta t)^2$ and this has a detrimental influence on the convergence characteristics. Hence, a different factorization called the Diagonally Dominant ADI (DDADI) [137] was implemented. In this case, the diagonal terms in the factored forms are made more dominant by adding the diagonal contributions in all the directions. In each direction, the difference of the jacobians are decomposed into diagonal and off-diagonal parts. For instance, $\delta_\xi A^n = L^d_\xi + L^o_\xi$. Then, defining an operator

$$D = I + \Delta t(L^d_\xi + L^d_\eta + L^d_\zeta + S^n) \quad (3.84)$$

the DDADI factored form is given by,

$$\left[D + \Delta t L^o_\zeta\right] D^{-1} \left[D + \Delta t L^o_\eta\right] D^{-1} \left[D + \Delta t L^o_\xi\right] \Delta\bar{\nu}^n = \Delta t R^n \quad (3.85)$$

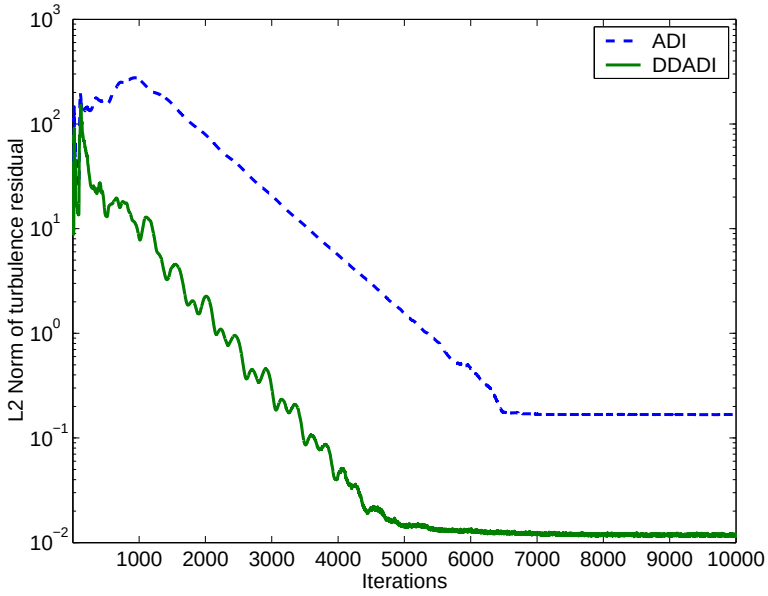

Figure 3.32: Convergence of the turbulence variable $\bar{\nu}$ using different Factorization schemes.

The factorization error in this case is $O(\Delta t)$ [137] and hence improved convergence rates can be expected. In addition, the allowable time step sizes were found to be much higher than the ADI for both steady and unsteady flows. Figure 3.32 shows the convergence of the working variable $\bar{\nu}$ for an Onera M6 [138] wing grid of size $269 \times 35 \times 67$. A Local time-stepping with $\Delta t = 1.0$ (non-dimensionalized by mean chord and free-stream speed of sound) is used for both computations. The flow conditions correspond to $\alpha = 4.08^o$, $M_\infty = 0.8359$ and $Re = 18.3 \times 10^6$. The DDADI method is clearly seen to reduce the computation cost and converges to a slightly lower residual error. The computational cost can be further reduced using grid sequencing, but the objective here is just to compare the two factorization schemes.

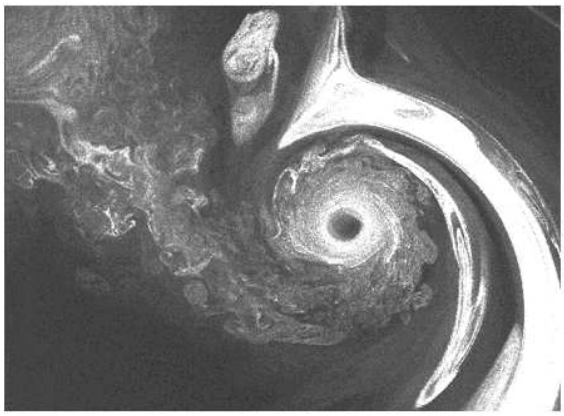

Figure 3.33: Flow visualization by experiment [139]. Wake of a single bladed hovering rotor at $\psi = 140^o$

3.7.6 Rotational correction

Many experimental studies on fixed wing tip vortices [9, 10] have reported largely reduced turbulence levels in the vortical core even in the near-field. This has been attributed to the near-solid body rotation that exists in the inner core. Analytical studies, based on linear stability theory of isolated vortices ([14] and other references therein), have also supported this argument by showing the damping of imposed small disturbances in the core.

Vizualization in a hovering rotor flow-field also hints at low turbulence levels in the core of the tip vortices. One such approach [139] utilizes the dynamic movement of *seed particles* that are introduced into the rotor flowfield. Figure 3.33 shows relatively smooth circular bands of seed near the core region, which can be attributed to reduced levels of turbulent mixing.

While using turbulence models, in order to accurately represent the physics, one has to ensure that the model does indeed replicate this behavior. Standard one-equation turbulence models like the Spalart-Allmaras and Baldwin-Barth

[133] model the production term based on the magnitude of the strain-rate tensor or on the magnitude of the vorticity vector. This is empirical and is known to perform well for wall bounded flows. However, the core region of the tip vortex is highly vortical and axisymmetrically strained, but as mentioned earlier suppresses turbulence. This issue was also addressed in [47]. The S-A model uses a production term, which in the wake region, reduces to:

$$P = c_{b1} S \nu_t, \tag{3.86}$$

Computations were performed with $S = |\omega|$ and $S = |\omega| + 2min(0, |D| - |\omega|)$, where $|\omega|$ and $|D|$ are the magnitudes of the vorticity and strain tensors respectively. The former was suggested in the original paper [42] and the latter version was used in [47], and attempts to suppress the turbulent production in regions (like tip vortices) where the vorticity is much larger than the strain-rate. The modification appears to be passive in thin shear layers. Figure 3.34 shows the extremely large turbulence levels predicted in the vortical core by the vorticity-based S-A model for the single bladed hovering rotor test case of Martin et al. [11]. Figure 3.35 reveals a much reduced core turbulence level. It is also evident from the figures that the predicted turbulence level in the wake region is similar for both models.

3.8 Overset mesh capability

In order to represent complex geometries and flow features, a single structured mesh will not be sufficient enough. In such cases, either of the following common approaches are used:

- Unstructured meshes.

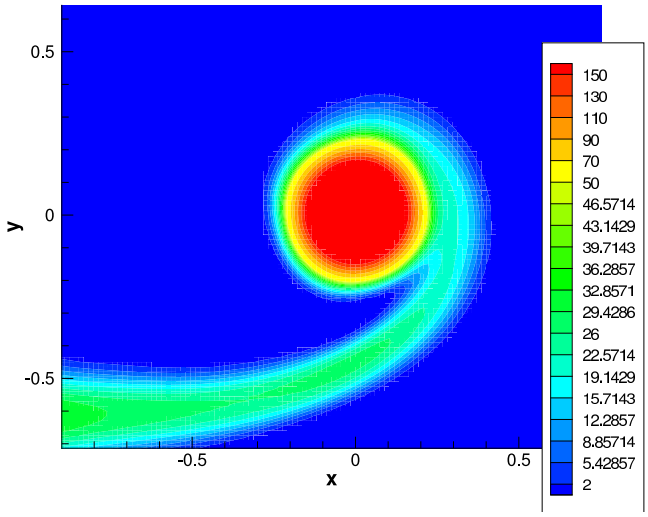

Figure 3.34: Turbulent eddy viscosity (normalized by laminar viscosity) predicted by the S-A model with production based on vorticity ($\psi = 90^o$)

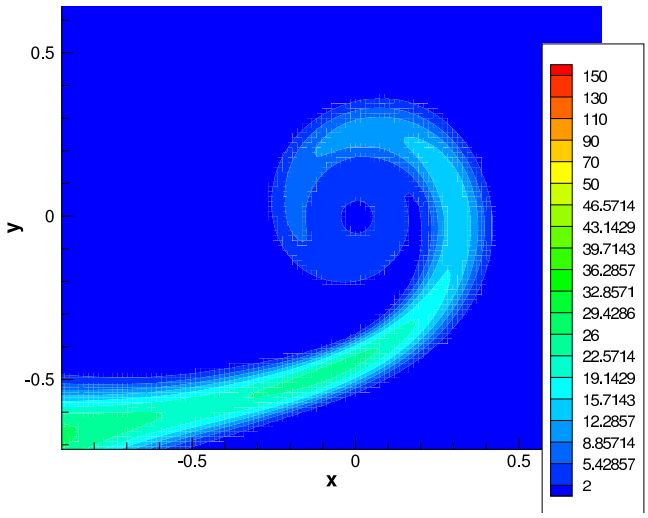

Figure 3.35: Turbulent eddy viscosity (normalized by laminar viscosity) predicted by the S-A model with production based on strain and vorticity ($\psi = 90^o$)

- Multiblock structured meshes.
- Overlapping *chimera* structured meshes.

Unstructured meshes are generally considered to be easily adaptable to complex configurations, but they require more memory and are less efficient compared to structured meshes (for a given configuration). In addition, it is more difficult to design efficient high order algorithms in an unstructured mesh framework. Overset structured grids have the advantage in that different grids can be generated independent of each other and can be placed in the region of interest *without any distortion*. Unlike block structured grids, the grid interfaces need not be matched and this greatly simplifies the grid generation process. Such a flexibility is invaluable in problems like rotorcraft applications, in which surfaces could be in relative motion to each other. The penalty to pay however, is the additional work is required in identifying points of overlap between meshes and interpolation of the solution in this overlap region. Additionally, there is a possibility of a loss of the conservation property of the numerical scheme. However, these errors can be minimized by proper selection of mesh structure and placement.

A sample application is shown in fig. 3.36. An overset grid is used to accurately resolve the downstream evolution of the tip vortex. In order to reduce numerical diffusion errors, very fine smoothly spaced cells are required and this is easily achieved as shown.

Once the overlapping meshes are generated, the chimera methodology involves four distinct steps namely,

- Hole cutting,
- Identification of hole fringe points,

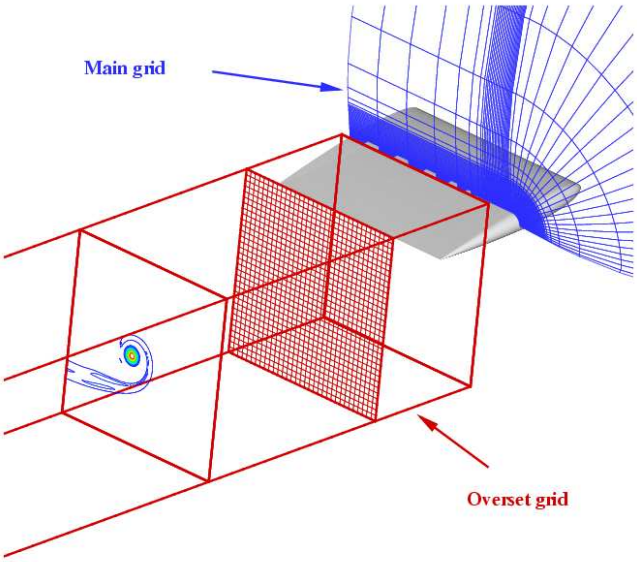

Figure 3.36: Sample application of overset grid to resolve the evolving tip vortex from a fixed wing.

- Identification of chimera and overlap fringe points,
- Finding donor cells and interpolation factors.

For all the above steps, the procedure of searching and finding the cell inside which a given point lies, is crucial. This "stencil walking" procedure is explained in [141]. For purposes of description, a simple geometry as shown in fig. 3.37 will be used. The inner circular mesh will be termed the *overset* mesh and the outer mesh is called the *background* mesh.

3.8.1 Hole cutting

Hole cutting is required when portions of a grid overlap with a solid body region of other grids. Hole-cut portions of a grid are *blanked out* and the flow equations are not solved at these points. Fig. 3.37 shows the hole points of the background grid in the vicinity of the solid surface. Hole cutting has been an active area of

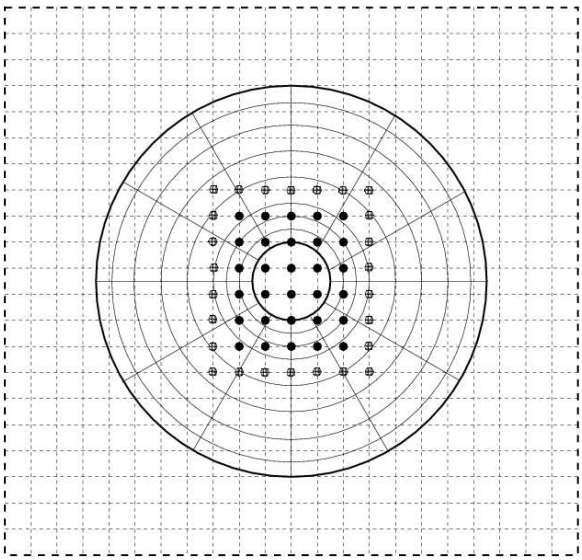

Figure 3.37: Schematic of hole cutting. Solid circles: Hole points (blanked). Patterned circles: Hole fringe points (interpolated for).

research over the past decade and many algorithms [142, 143] have been devised.

In this work, for fixed wing cases, hole cutting is not required since overset meshes are used only to resolve the tip vortex. For rotor problems, the blade mesh is itself overset in a background mesh and hence the background mesh needs to be hole cut. Instead of using a generalized method, the simplified geometry of the background mesh is utilized. The background mesh consists of identical planes that are rotated in the azimuthal direction. A sample plane is shown in fig. 3.38. The blanked out hole points in the background grid are evident. (A spanwise plane of the overset blade grid is also shown). Knowing the approximate dimensions of the solid body, a rectangle enclosing the solid body is defined in each azimuthal plane of the background grid. All the points inside this rectangle are checked as to whether they lie inside the overset grid. The points that do not are labeled as hole points. Using the neighbor information,

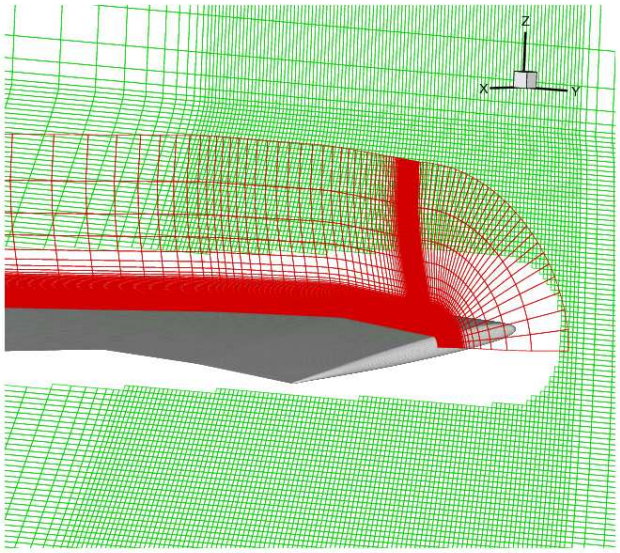

Figure 3.38: Sample application of hole cutting in a hovering rotor simulation.

this hole region is extended at least one layer outwards.

3.8.2 Identifying *hole fringe* points

Once the hole points are identified, the hole fringe points have to be determined. These points receive information from the overset grid and have to necessarily isolate the hole points from the rest of the grid. The number of fringe layers depends on the stencil of the spatial scheme. For instance, if a fifth order upwind scheme is used, at least three hole fringe layers are necessary. Fig. 3.37 shows one layer of hole fringe points.

3.8.3 Identifying chimera and *overlap fringe* points

Chimera points are defined as those boundary points on the overset mesh that require information from the background mesh. These are usually explicitly specified by the user. Overlap fringe points are those points that transfer infor-

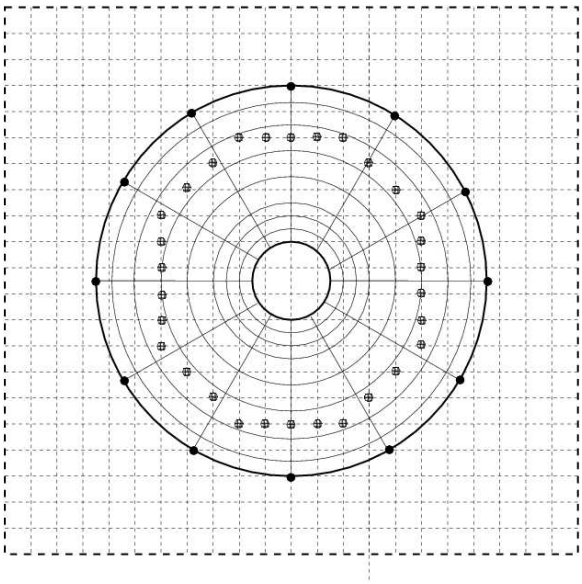

Figure 3.39: Schematic of chimera boundary points (solid circles) on the overset grid and fringe points (patterned circles) on the background grid.

mation back to the background mesh. These points, therefore lie close to the chimera boundary points. Fig. 3.39 shows the chimera and overlap fringe points. Figure 3.40 shows a schematic of identifying the fringe points. Once the chimera points are known, a set of the so-called tracer points are identified by moving n fringe layers *inside* the overset mesh. These points are finally discarded and are just meant to act as reference points. Now, the fringe points are identified as the primary nodes of the cell in the background grid inside which the tracer points lie. Usually, $n > 2$ is utilized.

3.8.4 Finding donor cells and interpolation factors

At the chimera, hole fringe and overlap fringe points, information is interpolated from the *donor cell* of the other grid. The donor cell is found using the previously mentioned "stencil walking" procedure. Once the donor cell is identified, the

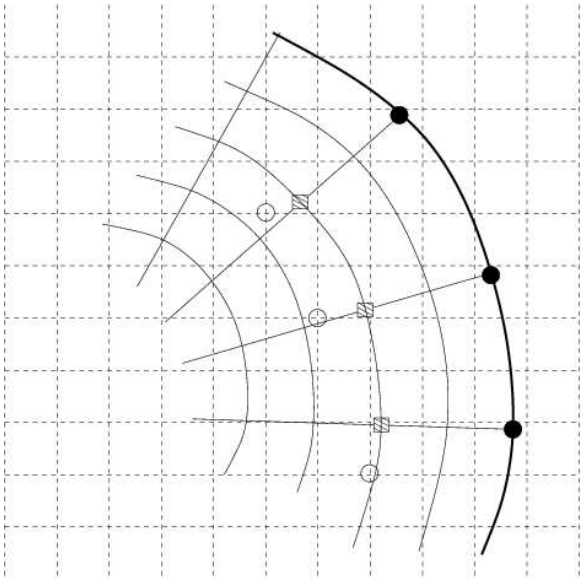

Figure 3.40: Procedure for identifying overlap fringe points (open circles). Chimera points (filled circles) and tracer points (patterned squares) are also shown.

interpolation factors in the three coordinate directions are found using tri-linear mapping.

It has to be mentioned that the use of chimera meshes makes it difficult to rigorously ensure the conservation property. However, the resulting errors can be minimized by making sure discontinuous features like shocks and shear layers do not cross the overlap boundaries. Another important factor that dictates the accuracy of chimera-based methods is the relative cell sizes of different grids in the overlap region.

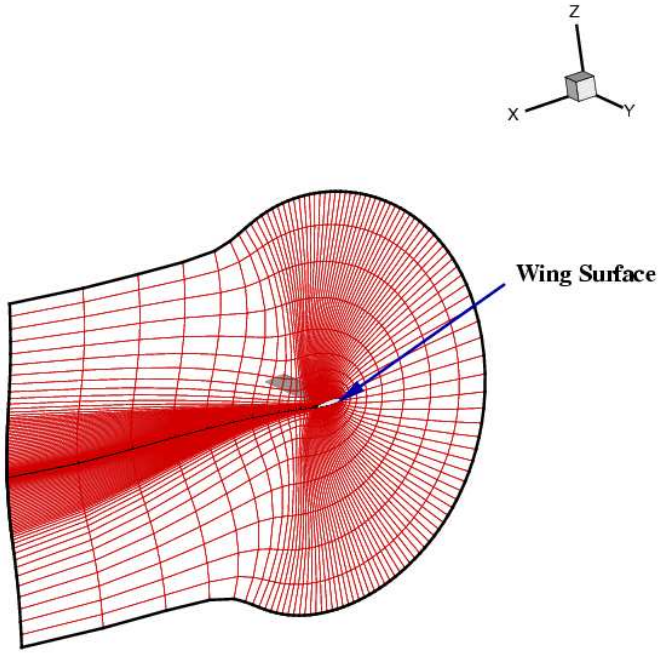

Figure 3.41: Spanwise 2-D section of a sample wing

3.9 Grid generation

In order to accurately represent the wing surface geometry, body conforming curvilinear grids are required. In this study, 2D meshes are generated at each spanwise section of the wing or blade and are stacked in the spanwise direction. As mentioned in sec. 2.3.3, the stretching ratios are carefully monitored. A representative section for a fixed wing is shown in fig. 3.41. A C-mesh topology is used for each section since it is well suited to smoothly cluster grid points near the trailing edge and in the wake. In addition, to resolve the tip vortex formation and rollup, the required clustering can be naturally achieved as shown in fig. 3.42. Near the tip region, the spanwise sections are rotated and collapsed, thus defining a C-O topology.

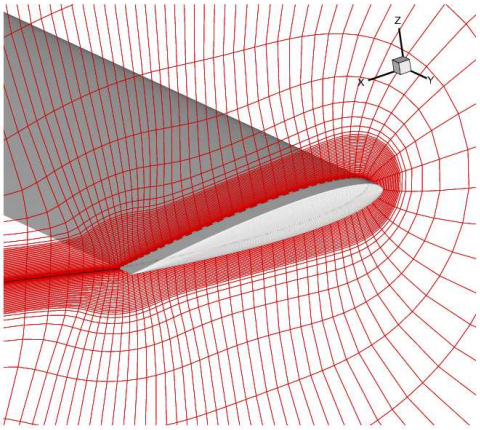

Figure 3.42: Sample clustering of grid points to resolve vortex roll-up.

3.9.1 2D mesh generation

The 2D meshes are generated using the hyperbolic grid generation code written by Tim Barth at NASA Ames Research Center. A few modifications were made to this code in order to obtain smooth grids with the required clustering. Given the surface definition in the η direction, this code "marches" in the η direction to generate grid points as shown in fig. 3.43. The governing equation for the unknowns $\mathbf{r} = (x, y)^T$ at any given instant η is given by

$$\begin{pmatrix} x_\eta^o & y_\eta^o \\ y_\eta^o & -x_\eta^o \end{pmatrix} \begin{pmatrix} x \\ y \end{pmatrix}_\xi + \begin{pmatrix} x_\xi^o & y_\xi^o \\ -y_\xi^o & x_\xi^o \end{pmatrix} \begin{pmatrix} x \\ y \end{pmatrix}_\eta = \begin{pmatrix} 0 \\ \Delta S + \Delta S^o \end{pmatrix} \tag{3.87}$$

where, the super-script o denotes quantities known at an earlier instant η_o. ΔS^o is the known local cell area at the earlier instant and ΔS is the user-specified cell area. The above equation can be represented as

$$\mathbf{r}_\eta = \mathbf{q}(\eta, \eta^o, \xi, \xi^o) \tag{3.88}$$

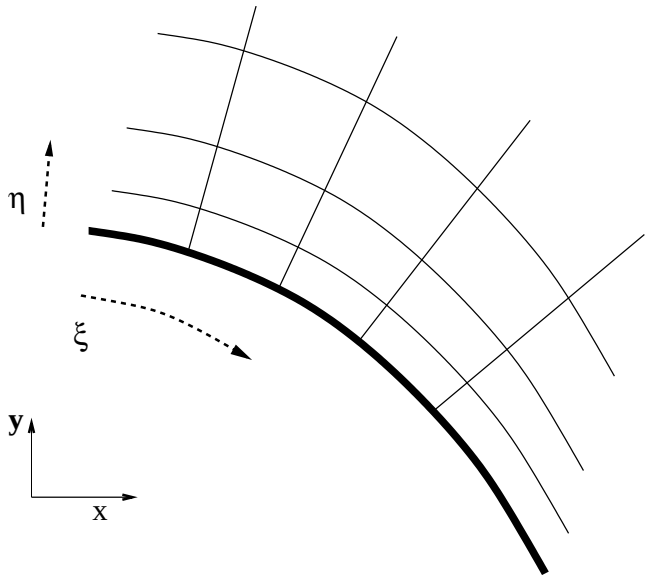

Figure 3.43: Schematic of body surface (thick line) and marching direction η.

Since explicit schemes will introduce restrictions on the step size, implicit time-marching is used. The implicit scheme[7]at an "instant" $(.)^1$ is given by:

$$\mathbf{r}^1 = \mathbf{r}^o + \alpha\mathbf{q}(\eta^1, \xi^1) + (1-\alpha)\mathbf{q}(\eta^o, \xi^o) \tag{3.89}$$

The parameter $\alpha \geq 0$ controls the level of implicitness of the scheme, with $\alpha = 0$ corresponding to a fully explicit scheme and $\alpha = 1$ corresponding to the Euler implicit scheme.

Hyperbolic grid generation schemes can be expected to perform poorly near convex surfaces since the characteristic lines tend to cross-over. This situation, for instance, arises when the wake cut is required to be aligned with the predicted tip vortex trajectory as seen from fig. 3.44. A possible way of circumventing this as suggested by the original author of the code is to take a weighted combination of the local cell area along with that of a reference polar grid to specify ΔS. This

[7]In practice, extra dissipation terms are added.

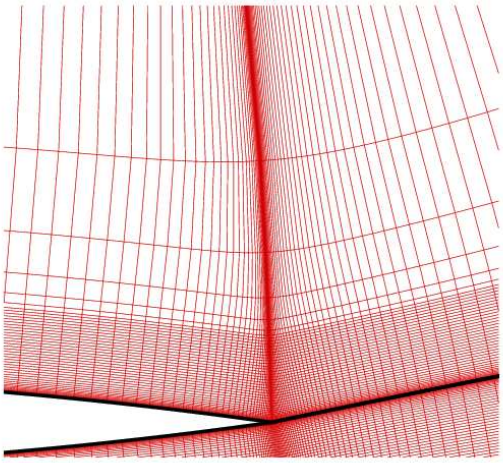

Figure 3.44: Grid-lines collapsing as a result of surface convexity.

can be represented as

$$\Delta S_{j,k} = \left[(1-\nu) + \nu \frac{(\Delta S_{j,k})_{airfoil}}{(\Delta S_{j,k})_{circle}}\right] (\Delta S_{j,k})_{circle}, \tag{3.90}$$

ν being a smooth function with $\nu \approx 1$ for small k and $\nu \approx 0$ for large k. However, it is very difficult to choose a general weighting function and this usually results in a cross-over of grid-lines as shown in fig. 3.45. The approach followed in this dissertation is to use an exponential weighting function ν along with increased numerical dissipation. The numerical dissipation is increased by smoothly varying α in eqn. 3.89 from $\alpha = 1$ to a large value, say $\alpha = 4$ with marching distance from the wall. A value of $\alpha > 1$ *over-damps* the numerical scheme causing the grid spacing to spread out as shown in fig. 3.46. A penalty to be paid is an expected loss of orthogonality of the grid lines, but it is found to be negligible in practice.

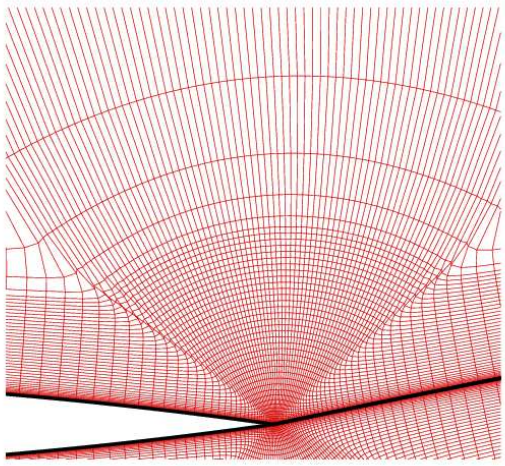

Figure 3.45: Grid-lines crossing over as a result of specified areas weighted with polar reference grid

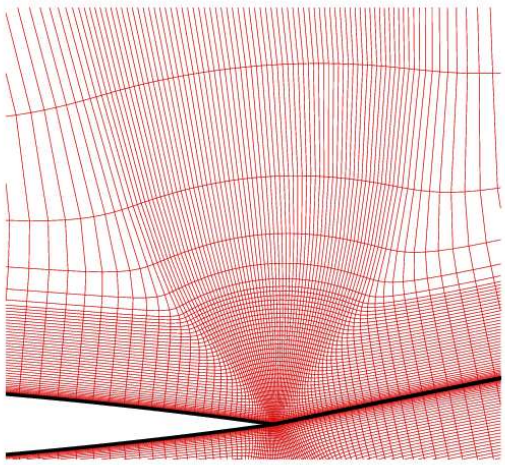

Figure 3.46: Addition of implicit dissipation and weighting resulting in a smoother grid.

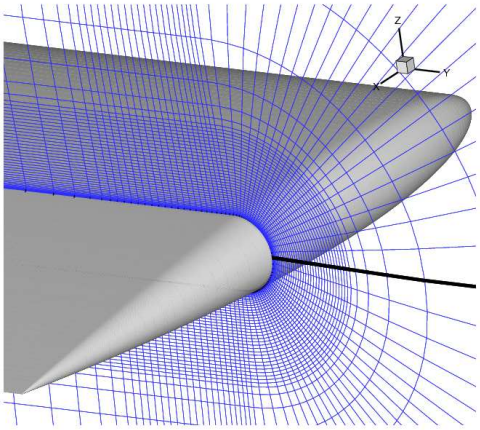

Figure 3.47: C-O mesh for a round tip configuration

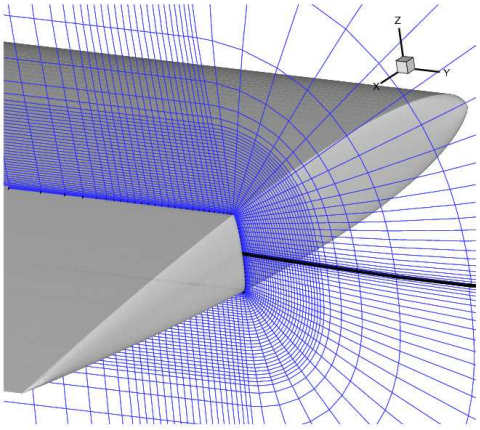

Figure 3.48: C-O mesh for a square tip configuration

3.9.2 3D meshes

In order to represent the tip shape accurately, the spanwise-stacked 2 dimensional meshes are rotated around the tip and collapsed at the mean camber-lines. Figs. 3.47 and 3.48 show chord-wise grid planes near the tip region for representative round and square-tip shapes. Grid points are clustered in the spanwise and normal directions in order to accurately resolve the tip vortex.

In order to obtain accurate results from the flow solver and to take advantage of the mesh structure, the grid points have to be *clustered* in regions of interest

and grid-lines have to be at least approximately *aligned* with the flow features. In the case of the fixed wing, the tip vortex can be approximately expected to follow the free-stream direction and hence the C-mesh wake cut is aligned as seen from fig. 3.42. For rotary blades in hover, the flow-field is essentially cylindrical and hence the streamwise planes are rotated in the azimuthal direction as explained in chapter 4.

3.9.3 Overset meshes

In order to better resolve the evolution of the tip vortex in the wake region, overset and background meshes are used. The structure and placement of these meshes will be introduced for specific cases in Chapters 4 and 5.

3.10 Boundary Conditions

3.10.1 Wall boundary condition

At the solid wall, the density (ρ) is extrapolated from the interior of the domain. For viscous calculations, the no-slip condition requires that the velocity at the wall equal the grid velocity. For inviscid flows, the contravariant velocity components (U, V, W) are extrapolated to the surface. Then, to satisfy the no-penetration condition, the contravariant component of velocity in the wall-normal direction (η) is set such that the physical velocity ($\mathbf{Q}$) equals the grid velocity. The pressure (p) is then obtained from the normal momentum equation, which is given by:

$$p_\xi(\nabla\xi.\nabla\zeta) + p_\eta(\nabla\eta.\nabla\zeta) + p_\zeta(\nabla\zeta.\nabla\zeta) = -\partial_\tau(\rho\mathbf{Q}_{jet}.\bigtriangledown_\zeta) - \rho U(\nabla\zeta.\frac{\partial\mathbf{Q}}{\partial\xi})$$

$$-\rho V(\nabla\zeta.\frac{\partial\mathbf{Q}}{\partial\eta}) - \rho W(\nabla\zeta.\frac{\partial\mathbf{Q}}{\partial\zeta}) \tag{3.91}$$

where, $\mathbf{Q}_{jet}$ is the Cartesian vector of the surface blowing velocity (if present).

3.10.2 Far-field boundary conditions

Ideally, the far-field boundaries should be placed far enough such that the prevailing conditions are very close to free-stream. This allows for the use of simple linearized boundary conditions in order to ensure that no spurious wave reflections occur at the boundary. For fixed wing computations, the boundaries are placed at approximately 20-30 chord lengths away from the airfoil surface. To determine the boundary conditions, characteristic-based Riemann invariants [37] are used. In this approach, based on the direction of the velocity vector and the sonic velocity, the corresponding Riemann invariants are extrapolated either from the interior or from the free-stream.

For a hovering rotor, the wake vortices stay under the blade at all times and the resulting induced velocities can be expected to be significant at distances of a few rotor radii. For computational efficiency, the far-field boundaries are held to less than two rotor radii away from the blade surface. In this case, the linearized characteristic free-stream boundary condition cannot be used since the flow velocities are large. For instance, simple momentum theory [3] states that the asymptotic downwash velocity from a hovering rotor is approximately $\sqrt{2C_T}$ times the tip speed. In this work, the *point-sink* boundary condition approach

of Srinivasan et. al. [26] is used. The details of this boundary condition is explained in sec. 5.1.2.

3.10.3 Inboard wing / blade boundary conditions

For fixed wing calculations, unless mentioned, symmetry conditions are applied at the root. In this method, *ghost* cells are created outboard of the symmetry plane. In these cells, the flow variables are set such that there is no flux crossing the symmetry plane. Assuming that the plane of symmetry is perpendicular to the y-direction, the values in the ghost cell (represented by a subscript "g") are given by:

$$\rho_g = \rho_2 \quad u_g = u_2 \ , \ v_g = -v_2 \ , \ w_g = w_2 \ , \ p_g = p_2 \tag{3.92}$$

where the subscript "2" denotes the cell to the "right" of the symmetry plane.

For hovering rotor calculations, the flow variables are simply extrapolated from the interior of the domain using an appropriate high order method.

3.10.4 Vortex outflow boundary conditions

In this work, fine smoothly spaced meshes are used to accurately resolve tip vortices. These meshes are approximately aligned with the axis of the tip vortex and are *overset* in a coarser *background* mesh. Figure 5.3 shows a typical vortex mesh for a hovering rotor. The boundary planes of the vortex mesh receive information (via interpolation) from the background mesh. It is observed from calculations that the vortex is highly dissipated in the background mesh and hence interpolating the solution on to the final plane of the vortex mesh can be expected to result in an inaccurate solution. To avoid this, two types of *vortex*

outflow boundary conditions were attempted.

a) Characteristic vortex outflow: In this case, Riemann invariants were used to determine the flow variables at the boundary of the overset grid. Since the flow is subsonic and uni-directional, information pertaining to one characteristic variable needs to be obtained from *outside* the vortex mesh. This information is provided from the solution interpolated from the background mesh. This approach is found to work better than interpolating entirely from the background mesh.

b) Simple extrapolation: In this approach, a high order scheme is used to extrapolate the solution from the interior of the mesh on to the boundary plane. This approach is simple and is found to perform as well as the characteristic outflow method and is applied to all the computations that involve vortex meshes in this dissertation.

3.10.5 Wake cut boundary condition

For all the wing and blade grids, a C-O topology is used. In this topology, grid surfaces collapse on to each other in the wake-cut region (fig. 3.42) and in the tip region (fig. 3.47). Along these surfaces, explicit fourth order averaging is used. The formula is given by:

$$q_{j,bc} = \frac{1}{6}(-q_{j-2} + 4q_{j-1} + 4q_{j+1} - q_{j+2}) \tag{3.93}$$

3.11 Convergence Acceleration

Convergence acceleration is required in order to efficiently solve the governing equations. This is especially important in achieving rapid convergence to steady

state. After spatial discretization, assuming the right hand side of eqn. 3.24 is represented by $\mathbf{R}(\mathbf{Q})$, the resulting implicit Euler scheme can be represented by:

$$\left[\mathbf{I} - \Delta t \left(\frac{\partial \mathbf{R}}{\partial \mathbf{Q}}\right)^n\right] \Delta \mathbf{Q}^n = \Delta t \mathbf{R}(\mathbf{Q}^n) \tag{3.94}$$

This system of equations is iterated to steady state using an LUSGS [124] algorithm to solve the resulting linear system at every time-step. Convergence is said to have been achieved if a suitable norm of the residual vector $\Delta \mathbf{Q}^n$ reaches a required level.

The spatial errors are composed of a wide variety of frequencies, ranging from the order of the smallest mesh size to the order of the largest grid dimension. Usually, the low frequency errors are damped at a much smaller rate than the higher frequency errors and this proves to be very detrimental to convergence. Most iterative methods (like Gauss-Siedel etc.) are usually efficient only in reducing the high frequency errors. The problem is exacerbated by the fact that the NS equations become inherently stiff at lower Mach numbers. In order to address this problem, a variety of convergence acceleration devices have been designed over the past few decades. In particular, [140] presents a comprehensive review of of multigrid methods, the concepts of which have been utilized.

In this work, simple grid sequencing is used in order to obtain better convergence properties. In this method, starting from a very coarse grid, the flow equations are solved on successively finer grids. The coarse grids are obtained by removing every other point in each direction, thus resulting in one eighth of the grid points of a higher level in three dimensions. The objective is to progressively remove the low frequency[8]errors.

[8]The fine grid low frequency errors appear as higher frequencies on the coarse grids and can hence be more effectively damped.

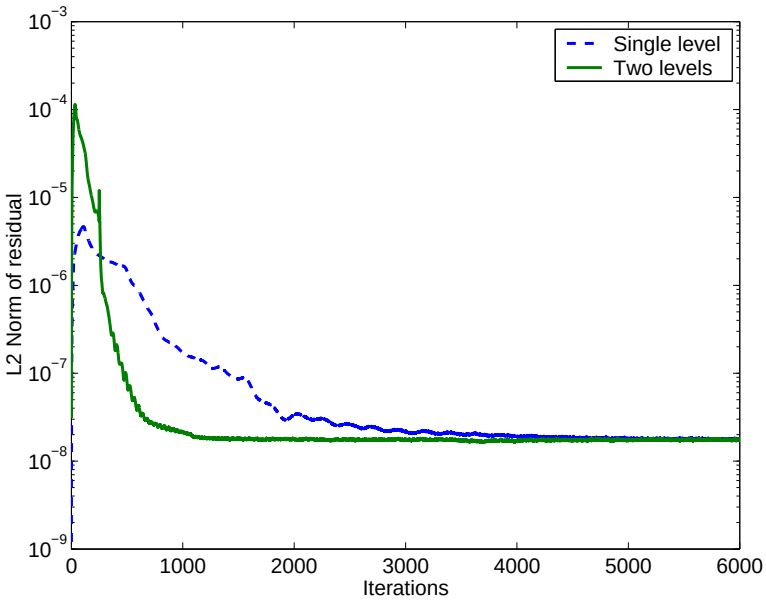

Figure 3.49: Convergence to steady state using single grid level and two grid levels.

Usually, the flow-field is initialized everywhere with free-stream conditions and this gives rise to large initial transients that propagate to all parts of the flowfield and also reflect at the boundaries. Starting on the coarsest grid can then be extremely advantageous since these transients only need to be computed on a fewer number of grid points and are ultimately damped faster.

A sample convergence history for the Onera M6 wing grid of size $269 \times 35 \times 67$ is shown in fig. 3.49. A Local time-stepping with $\Delta t = 1.0$ is used for both computations. The flow conditions correspond to $\alpha = 4.08^o$, $M_\infty = 0.8359$ and $Re = 18.3 \times 10^6$. For the grid sequenced case, 250 iterations are performed on the coarse grid and the rest on the finer grid. A drastic improvement in the rate of convergence is observed. Fig. 3.50 shows the evolution of the lift coefficient. As a consequence of using the coarse grid, the initial development of the transient is much faster: the peak lift coefficient is attained in 90 iterations compared to 200

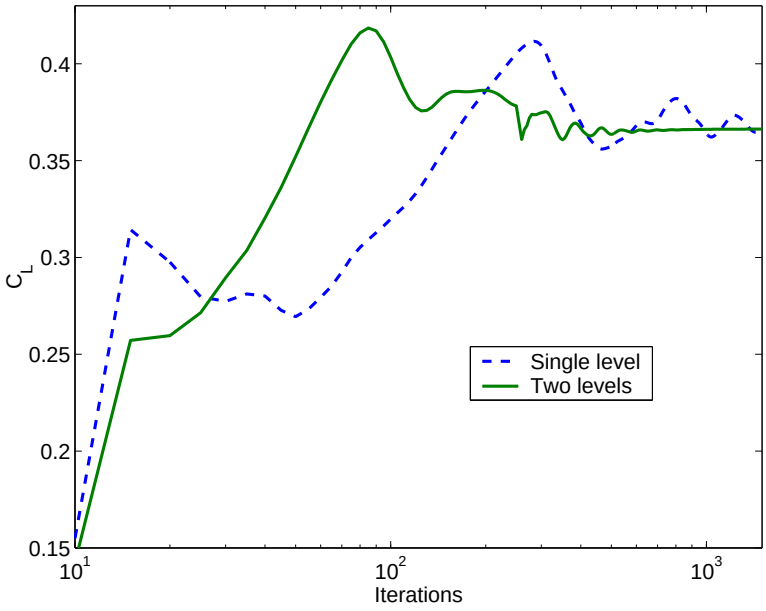

Figure 3.50: Lift convergence history for Onera-M6 wing case.

iterations on the fine grid. Subsequently, by the time the solution is transfered to the finer grid, much of the transient energy seems to have been damped out, thus improving the overall convergence. For comparison purposes, the same time-step has been used for both cases - in practice, the coarse grid allows for much larger time-steps since the problem is less stiff.

The afore-mentioned grid sequencing corresponds to a uni-directional multi-grid approach. In more complex cases, (for instance, hovering rotor computations), a full cycle was used as schematized in fig. 3.51. This is required since the high frequency errors can only be resolved on the finer grids and the coarser mesh might not be able to sense the effect of these modes. To transfer information from the coarse grid to a point on the fine grid, simple averaging of 8 neighboring points was used.

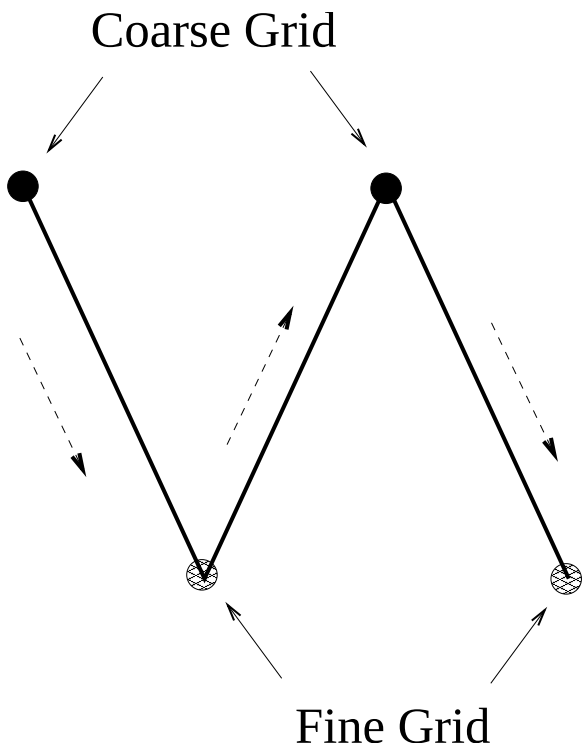

Figure 3.51: Schematic of grid sequencing cycle.

3.12 Summary

In this chapter, the computational methodology for the solution of the RANS equations was presented. The improvements to an existing solver in terms of high order accuracy, turbulence modeling, convergence acceleration and overset capability were detailed. In order to better resolve the flow features, appropriately refined structured grids are used in an overset framework.

Chapter 4

Computation of Vortex Formation and Evolution from a Fixed Wing

In this chapter, extensive validation studies will be conducted on the vortex formation in the very near field of a fixed wing. The primary objective of this study is to determine the numerical resolution and to evaluate the fidelity of the turbulence model. Once the requirements in mesh spacing and order of numerical accuracy are determined, these will be used as guidelines for further simulations in this thesis. In addition to the these validation studies, the physics of vortex formation will be studied in detail and the effect of various flow and geometry conditions will be evaluated. Finally, results will be presented on the evolution of the tip vortex in the extended near-field of a fixed wing.

4.1 Vortex formation: Validation with experiment

4.1.1 Details of experiment

The experimental test case corresponds to a rounded tip wing in a $32 \times 48in.$ wind tunnel section as shown in fig. 4.1. The relevant test conditions are shown in table 4.1. The experiments were conducted by Chow et al. [9] at NASA Ames research center. It is thus a very low aspect ratio wing with the wind tunnel walls close to the surface. However, the Reynolds number is large and as will be shown later, the effects of the low aspect ratio and the proximity of the wind tunnel walls are minimal with regard to the details of the vortex formation.

This test case was chosen because of the availability of a comprehensive set of measurements in the wake region and on the wing surface. Static pressure, mean velocity and Reynolds stress data are available at select axial planes, starting at a distance of x/c=0.591 ahead of the trailing edge to x/c=0.678 from the trailing edge. Surface pressure measurements are available from a total of 444 pressure taps located in 12 chordwise rows. The flow is tripped at the leading edge so that a fully turbulent assumption is valid.

4.1.2 Grid and boundary conditions

The baseline grid for this test case was provided by Zilliac [145]. This grid consists of $115 \times 189 \times 115$ in the streamwise, spanwise and normal directions respectively, filling the test section volume exactly. The grid distribution was smoothed and refined for use in this work. A sample axial grid plane near the

Airfoil	NACA 0012
Chord length (c)	1.22 m
Aspect Ratio	0.69
Mach Number	0.15
Chord Reynolds Number	4.6×10^6
Angle of attack	10^o

Table 4.1: Test conditions

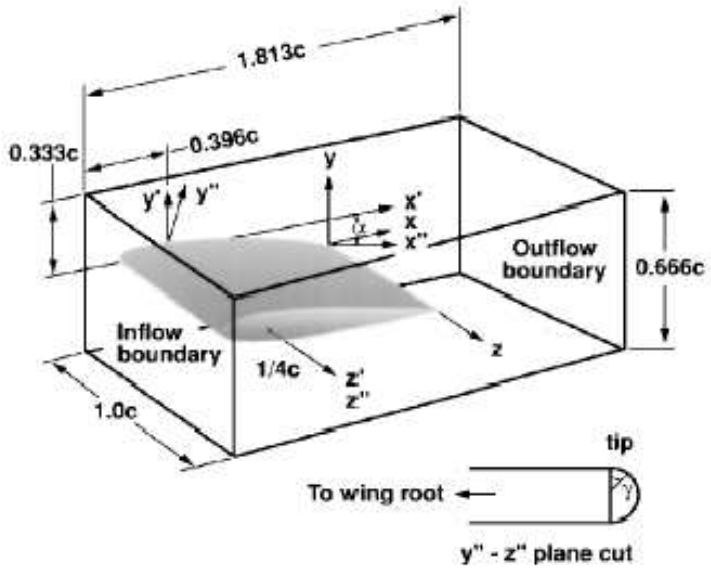

Figure 4.1: Experimental test section dimensions [9]

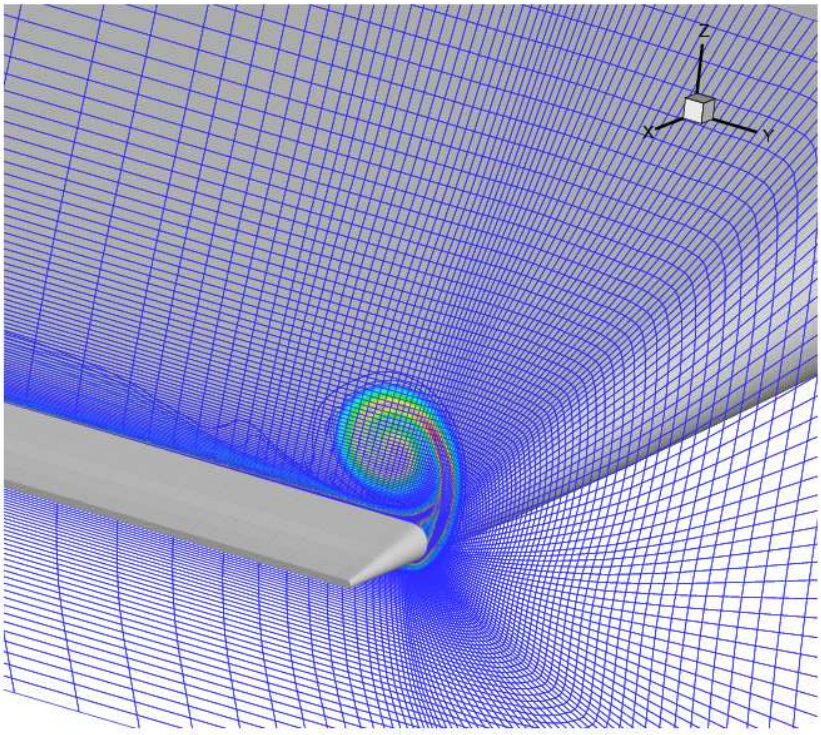

Figure 4.2: Axial plane of a sample grid

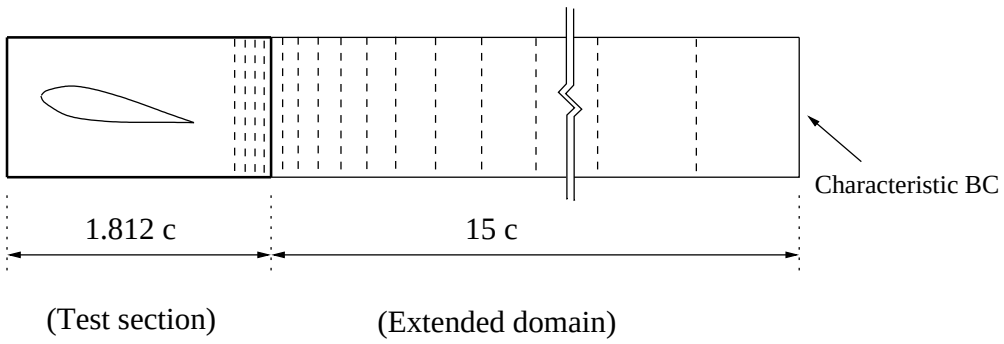

Figure 4.3: Schematic of domain extension for application of outflow BC. Dotted lines show (approximate) location of axial planes.

wing trailing edge (along with contours of computed streamwise vorticity) is shown in fig. 4.2. A spacing of $5 \times 10^{-6}c$ is used in the wall normal direction.

The inflow boundary is treated using characteristic Riemann conditions as explained in sec. 3.10.2. The airfoil surface and wind tunnel walls are treated as viscous walls. The treatment of the outflow boundary is however, more complicated because of the presence of the tip vortex. Since the outflow plane is very close to the wing trailing edge, a simple characteristic boundary condition cannot be used since it will generate spurious reflections as a result of the strong tip vortex crossing the outflow boundary. Unlike acoustic waves, vorticity waves are typically very strong and hence designing a non-reflective boundary condition is not straight forward. As an alternate method, simple extrapolation was attempted, but it was found that spurious reflections were generated and the velocities at the inflow plane were typically higher than freestream.

A more successful strategy involved using large stretching ratios downstream of the test section outflow plane and applying the characteristic boundary conditions at a *virtual* freestream plane. A schematic is shown in fig. 4.3. The coarse mesh spacing artifically diffuses the vortex and a virtual *buffer zone* is created. It was found that an extension of the domain by 15 chordlengths (using 30 extra planes) was sufficient and the velocity vectors in the inflow plane were within 1% of the freestream. For all the computations presented in this study, an extension of 15 chords is used.

4.1.3 Numerical Comparison

In order to explore and evaluate the effect of numerical and turbulence model errors, various test runs were made. Before the results from all the test runs are

presented, the "highest fidelity" numerical result will be compared in detail with experiments. This calculation is performed on the $148 \times 189 \times 115$ grid using the seventh order WENO scheme for inviscid discretization with the rotational correction added to the turbulence model. Subsequently, the other test runs will be compared. For all the results presented, *the origin of the coordinate system is assumed to be at the trailing edge of the wing at the root section.*

Figures 4.4-4.8 compare the contours of the computed swirl velocity $\sqrt{v^2 + w^2}$ along axial planes with experiments. In order to ensure a one-to-one comparison, the computed solution is interpolated on to the experimental data locations before the contours are plotted. At the farthest upstream location (fig. 4.4), there is no evidence of the tip vortex and very low levels of crossflow velocity are observed. Further downstream (fig. 4.5), the magnitude of swirl is large enough that the tip vortex is observed in its initial form. The computed swirl velocity is slightly diffused compared to the measurements. Figures 4.6-4.8 show the evolution of the swirl velocity beyond the trailing edge of the wing. Qualitatively and quantitatively, the computed results are similar to that of the experiments. Fig. 4.9 shows the vertical velocity (w) along a horizontal (spanwise) line passing through the center of the vortical core. Again, the computed velocity profiles match well with experiments, except at the $x/c = -0.296$ station, where the sharp negative peak is not captured (similar to fig. 4.5).

Fig. 4.10 shows the evolution of the peak magnitudes of the axial velocity u, vertical velocity w, total velocity $\sqrt{u^2 + v^2 + w^2}$, swirl velocity and minimum static pressure with downstream distance. There is a slight underprediction of the axial and total velocities and an overprediction of the swirl velocity. However, the computed static pressure at the vortex center (fig. 4.10c) shows an error upto

27% when compared to experiments. A similar level of disagreement has been reported in [47]. A representative profile is shown in fig. 4.11.

Fig. 4.12 shows the pressure distribution on the wing surface. At an inboard section (y/c=0.5) the pressure distribution closely resembles that of a 2 dimensional airfoil. Very close to the tip, a second suction peak appears near the trailing edge, which is a consequence of the tip vortex rolling up on the wing surface. Traversing along the tip surface, (refer fig. 4.1 for definition of γ), the suction peak near the leading edge is seen to reduce and the pressure at the top and bottom surfaces gradually equalize. The agreement of the computed results with the experiment is a direct consequence of correctly capturing the strength of the evolving tip vortex.

The contours of the Reynolds shear stress $< v'w' >$ are compared with experimental measurements in fog. 4.13. It becomes evident that although the peak levels of the computed Reynolds stress compare well with experiments, there appears to be an overall *phase shift*. This phase shift can be explained by examining the strain rates $\frac{\partial v}{\partial z} + \frac{\partial w}{\partial y}$ in fig. 4.14. The computed strain-rate aligns itself with the computed Reynolds stress, which is a consequence of the isotropic eddy viscosity approximation. However, the experimental strain rate (calculated by smoothing the measured velocity and differentiating) does not align itself with the Reynolds stress, indicating anisotropic effects as explained in [9].

4.1.4 Validation studies

Grid convergence

To evaluate grid convergence, the computations were performed on 3 different grids. The results thus far were generated using the finest grid ($148 \times 189 \times 115$),

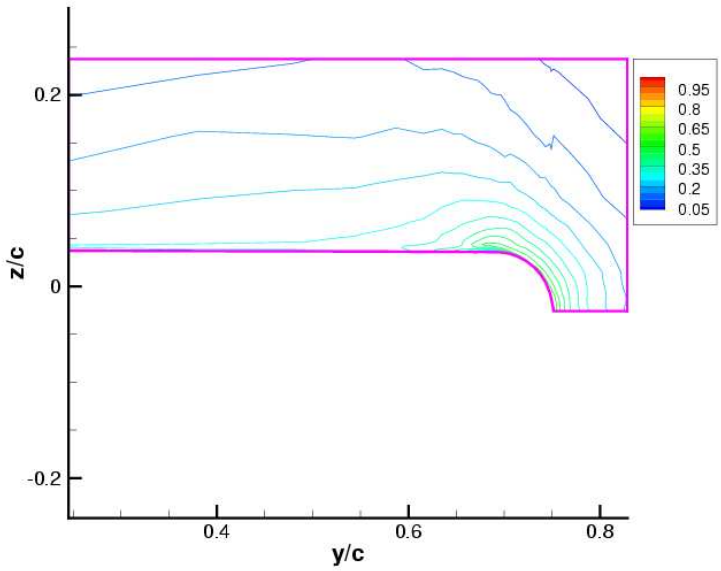

(a) Experiment

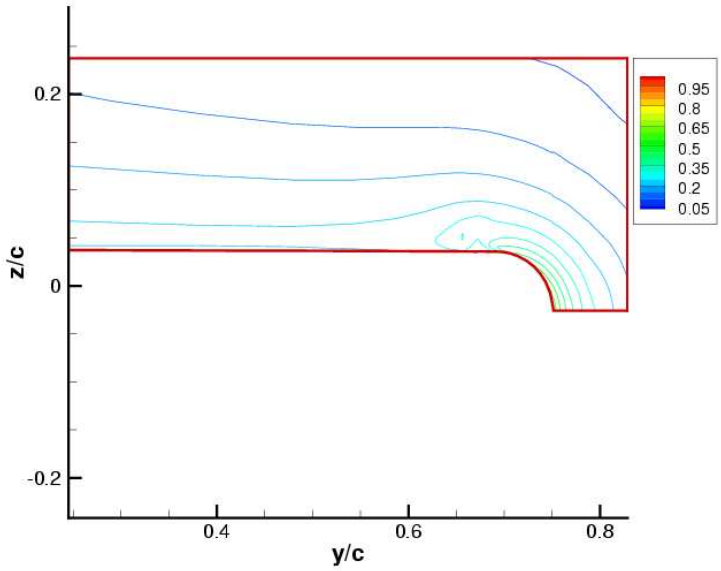

(b) Computation

Figure 4.4: Crossflow velocity magnitude (normalized by free-stream velocity) at $x/c = -0.591$

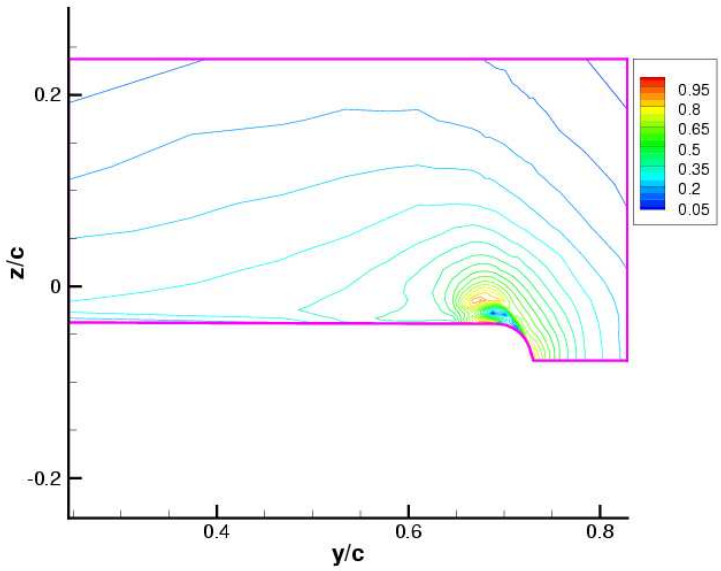

(a) Experiment

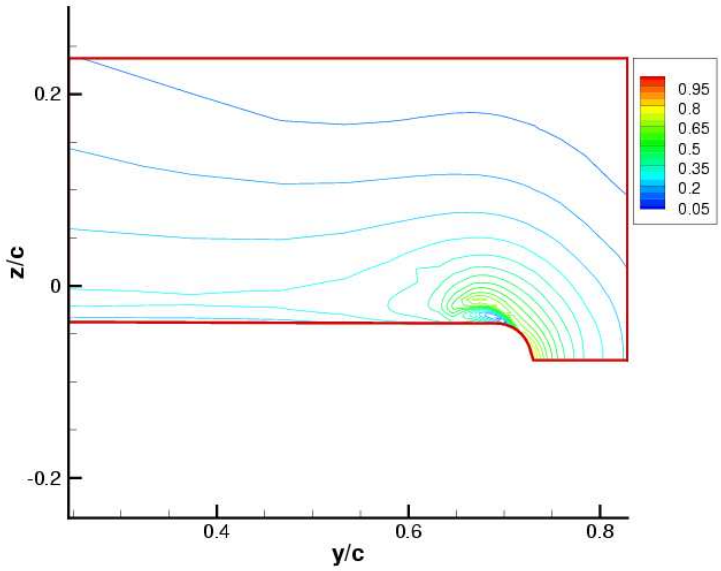

(b) Computation

Figure 4.5: Crossflow velocity magnitude at $x/c = -0.296$

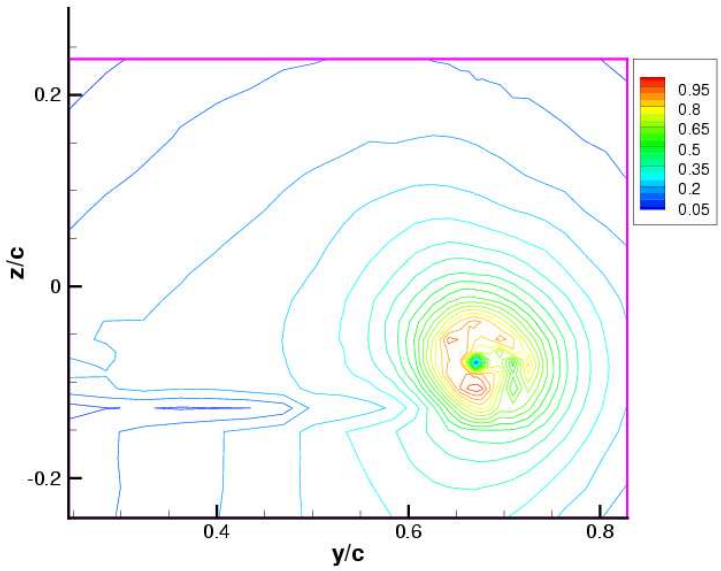

(a) Experiment

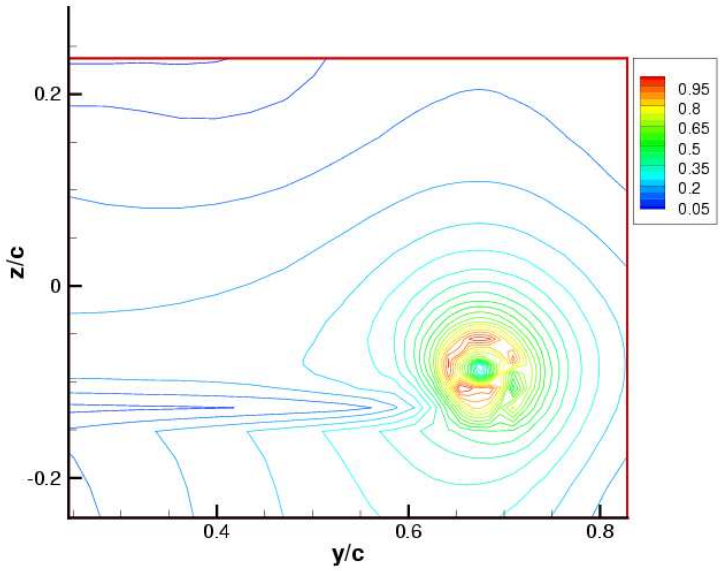

(b) Computation

Figure 4.6: Crossflow velocity magnitude at $x/c = 0.005$

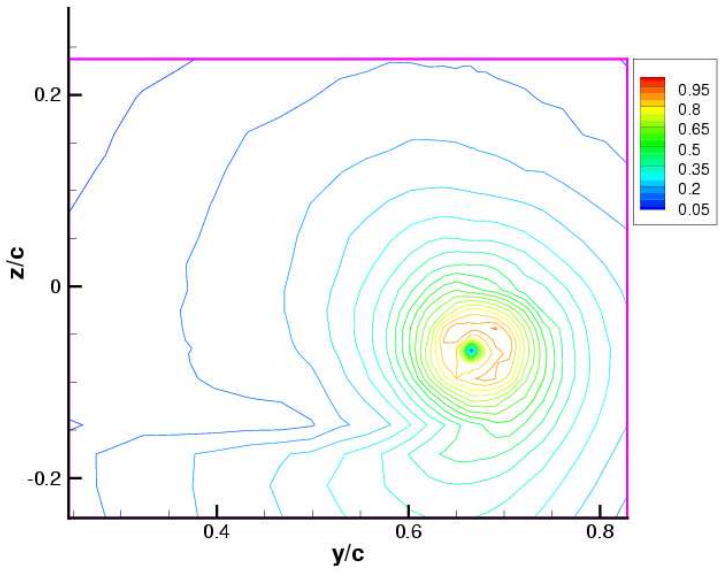

(a) Experiment

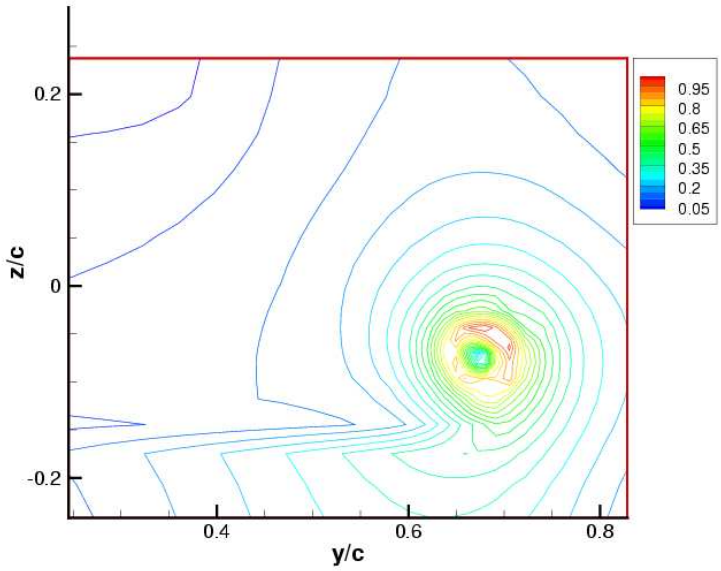

(b) Computation

Figure 4.7: Crossflow velocity magnitude at $x/c = 0.246$

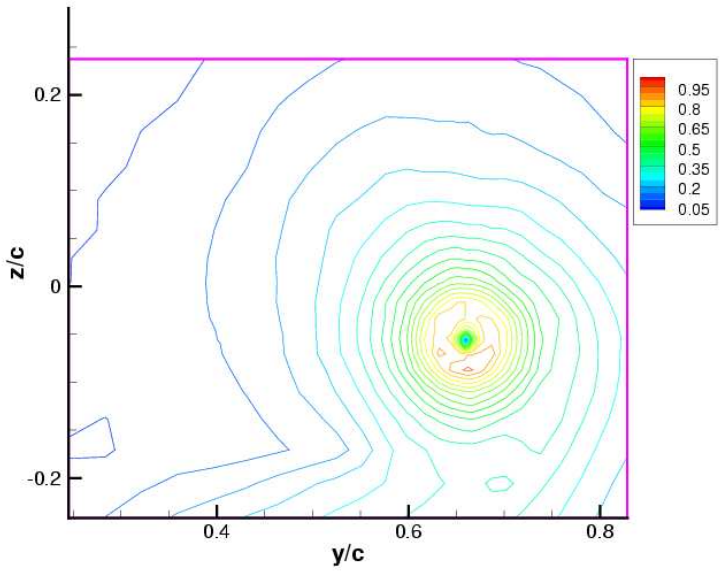

(a) Experiment

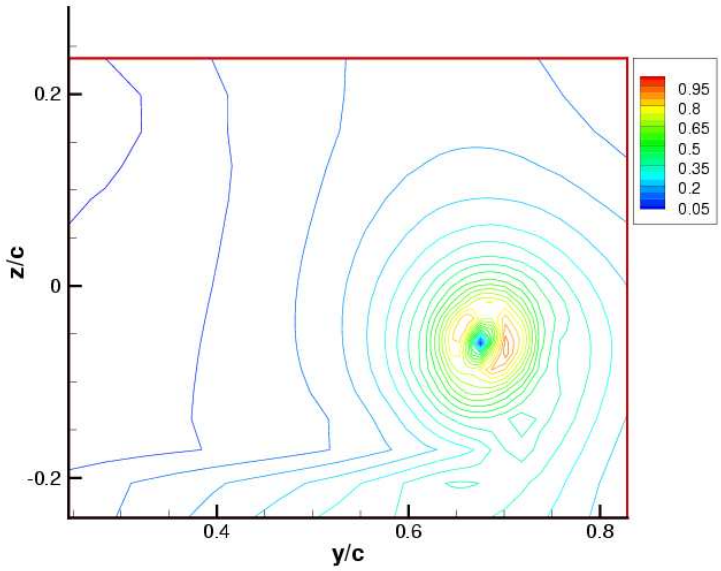

(b) Computation

Figure 4.8: Crossflow velocity magnitude at $x/c = 0.678$

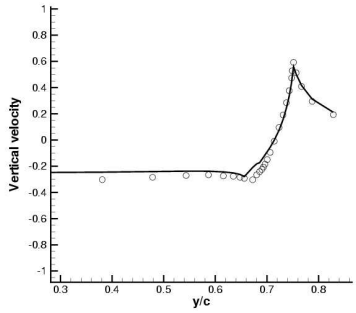

(a) x/c=-0.591

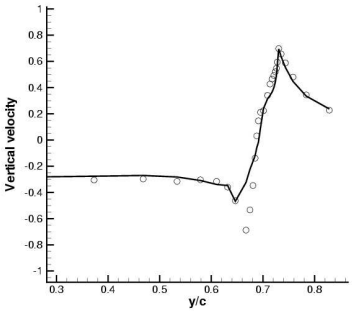

(b) x/c=-0.296

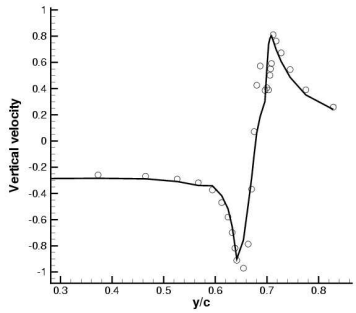

(c) x/c=-0.114

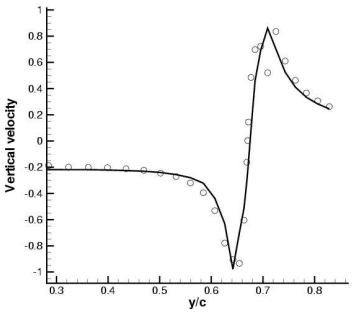

(d) x/c=-0.005

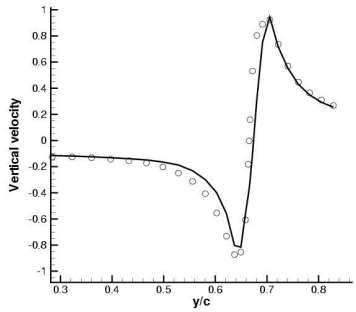

(e) x/c=0.246

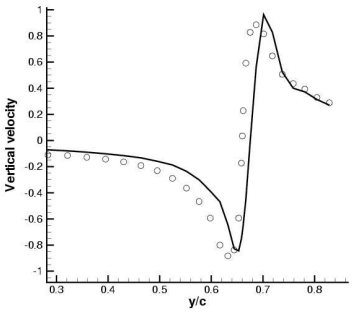

(f) x/c=0.678

Figure 4.9: Vertical velocity (w/U_∞) along a horizontal cut through vortex core

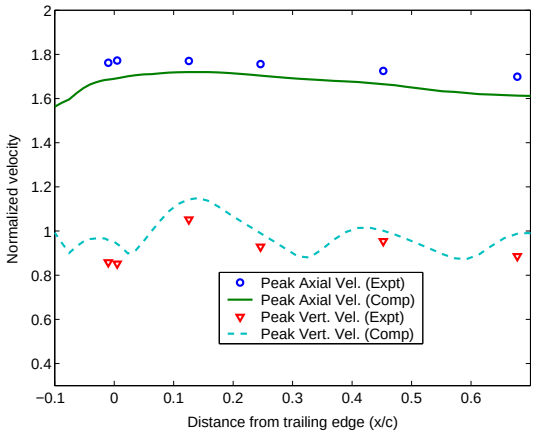

(a) Vertical and axial velocities

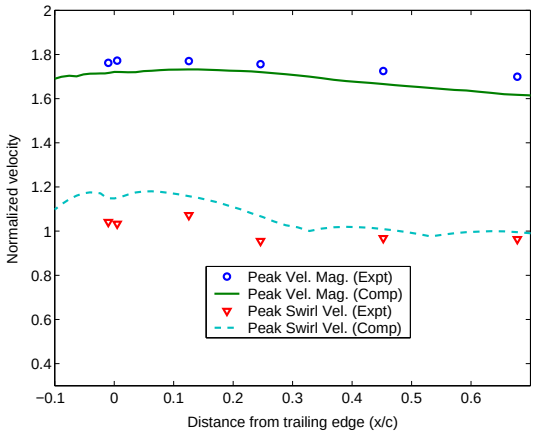

(b) Swirl and total velocities

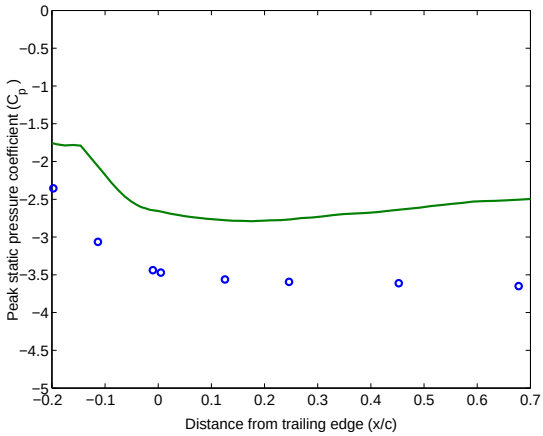

(c) Static pressure at vortex center

Figure 4.10: Evolution characteristics of the tip vortex

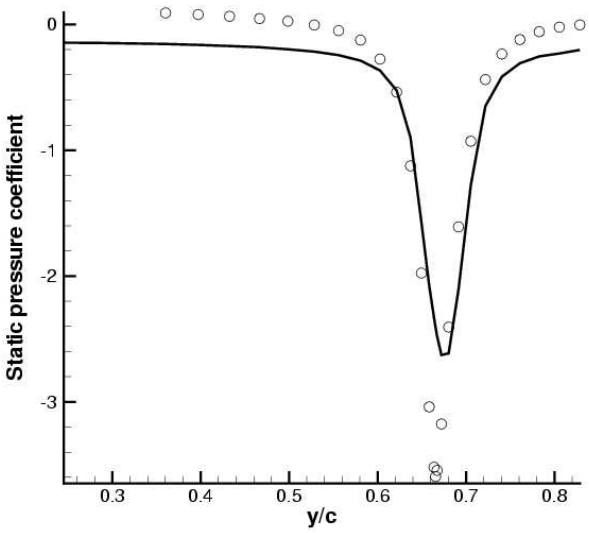

Figure 4.11: Static pressure coefficient along a line passing through the vortex center at a station $x/c = 0.462$ from trailing edge

termed Grid 3. Two coarser levels of grids were used:

- Grid 1, using every other point of Grid 3 in the cross-stream direction (factor of 4 reduction in grid points),

- Grid 2, the points of which were interpolated for from Grid 3, such that for every 3 points along a cross-stream grid line in Grid 3, two points were extracted. Given a grid-line of Grid 3, quartic interpolation was used to parameterize the line and extract the required points. Thus, this grid results in a $1.5.5 = 2.25$ factor reduction in grid points as compared to Grid 3.

As seen from fig. 4.15, the solution on the intermediate (Grid 2) and fine grid (Grid 3) are relatively close to each other compared to the more erroneous coarse grid (Grid 1) solution, implying grid convergence. Further, the surface pressure distributions were no different (to plotting accuracy) for Grid 2 and

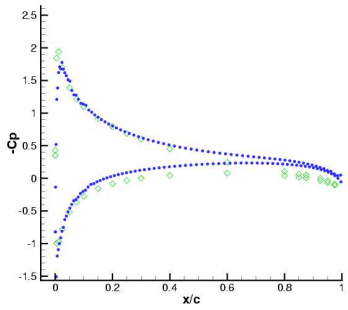

(a) y/c=0.500

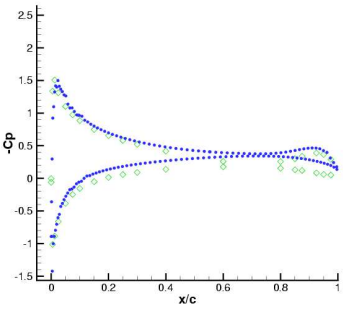

(b) y/c=0.625

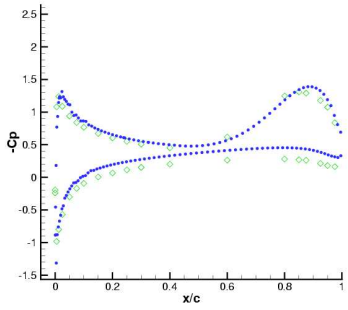

(c) y/c=0.667

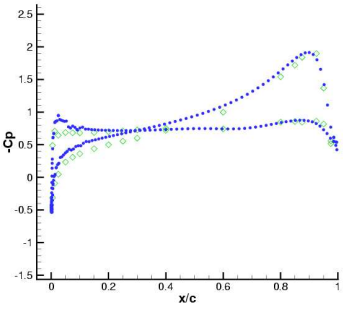

(d) $\gamma = 45^o$

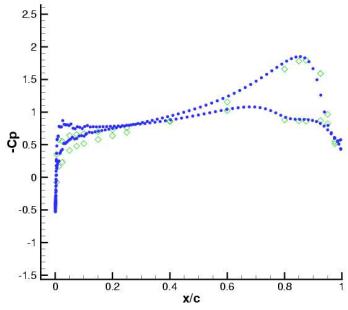

(e) $\gamma = 67.5^o$

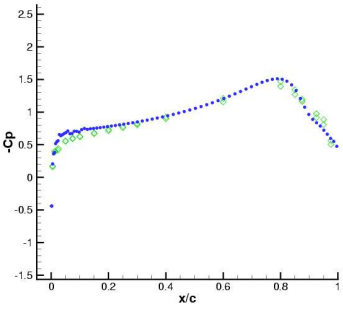

(f) $\gamma = 90^o$

Figure 4.12: Pressure distribution on wing surface. Circles: Experiment, Lines: Computation

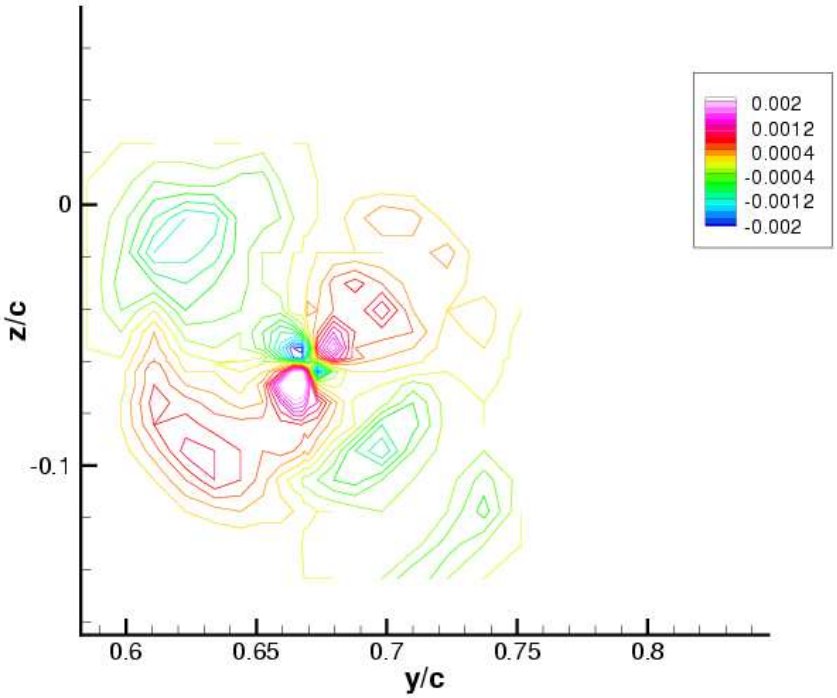

(a) Experiment

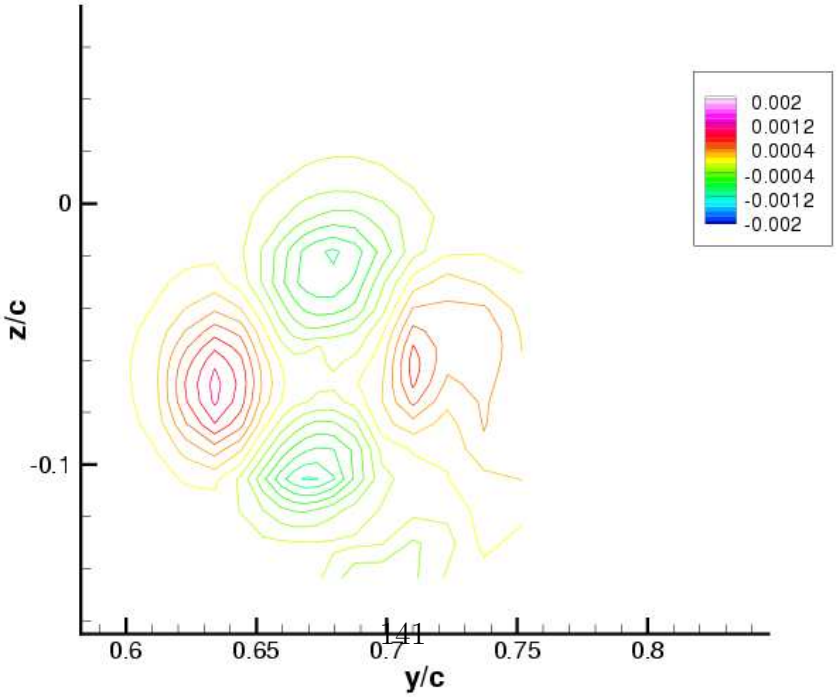

(b) Computation

Figure 4.13: Contours of primary Reynolds stress $< v'w' >$ at $x/c = 0.462$ from

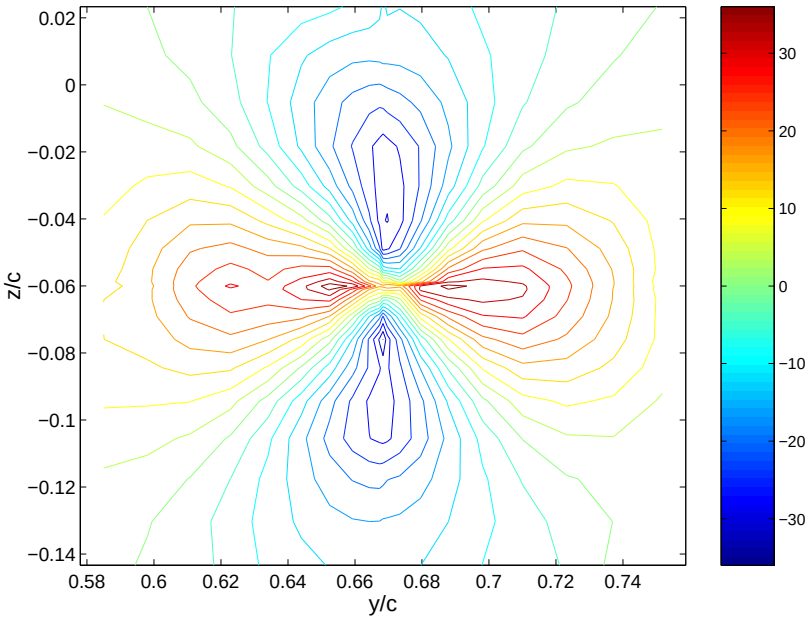

(a) Experiment

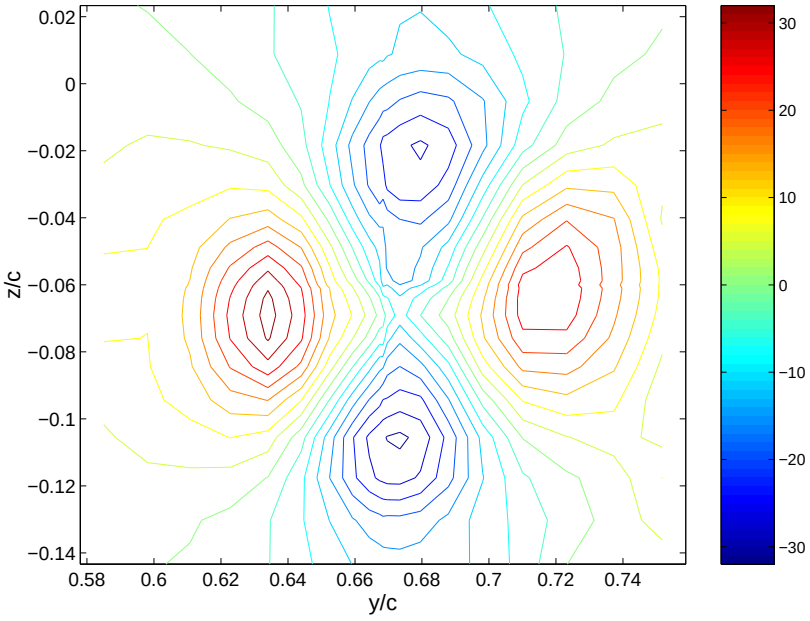

(b) Computation

Figure 4.14: Contours of strain-rate $\frac{\partial v}{\partial z} + \frac{\partial w}{\partial y}$ at $x/c = 0.462$ from trailing edge

Grid 3.

Effect of inviscid discretization

Fig. 4.16 compares the effect of high order inviscid discretization on the vortex evolution. As expected, the seventh order WENO discretization results in the least numerical diffusion error. However, the computed surface pressure distribution showed minimal variation between the different schemes.

4.1.5 Turbulence model effects

As mentioned in sec. 3.7.6, the production term in the original Spalart-Allmaras model is based solely on vorticity and this can be extremely unphysical in tip vortex flows where the solid body rotation is known to suppress turbulence. Hence, the rotational correction needs to be added to the production term. Fig. 4.17 compares the vortex evolution with and without the rotational correction. It is immediately evident that even for such short spatial lengths, the vortex significantly diffuses due to the excessive eddy viscosity predictions. Fig. 4.18 confirms this argument. The Reynolds stress contours are plotted with the same levels as in fig. 4.13. The peak values of Reynolds stress were found to be more than 10 times that of the experimentally determined values.

4.2 Physics of Vortex Formation

As seen in figs. 4.4-4.8, even though significant levels of cross-flow is present in axial planes before the quarter chord point, the evolving tip vortex is initially evident only further downstream. As seen in fig. 4.19, a very thin attached

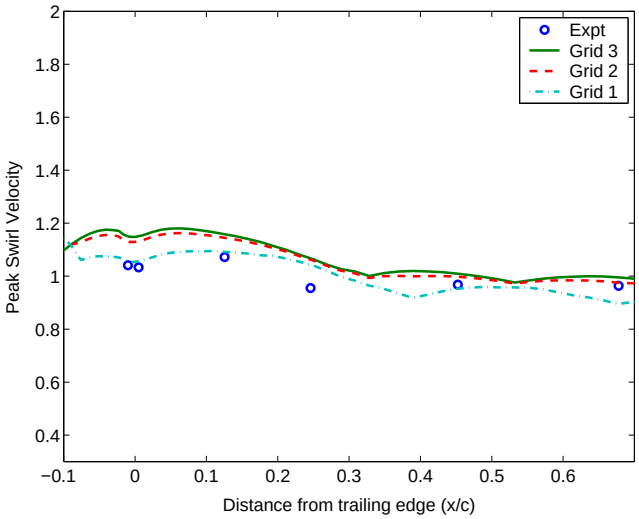

(a) Peak swirl velocity

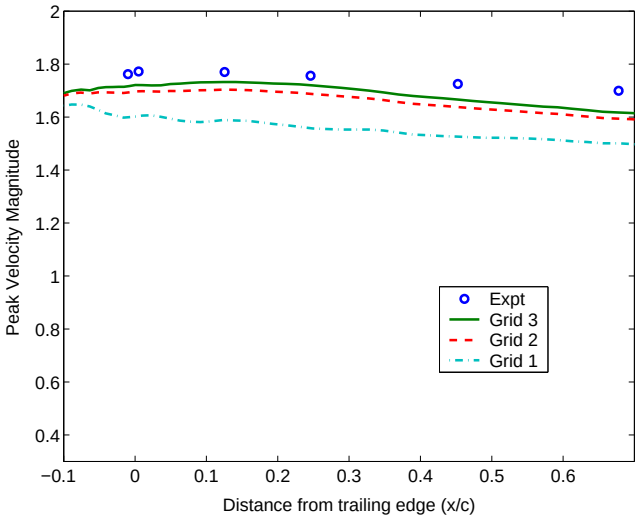

(b) Peak total velocity magnitude

Figure 4.15: Grid convergence study: Seventh order WENO for all grids.

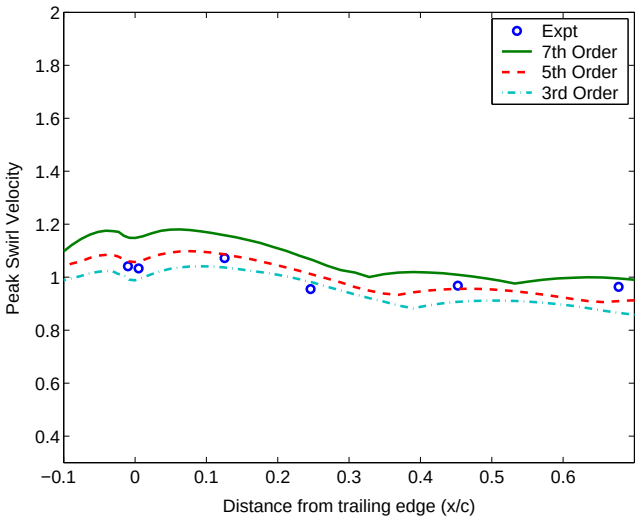

(a) Peak swirl velocity

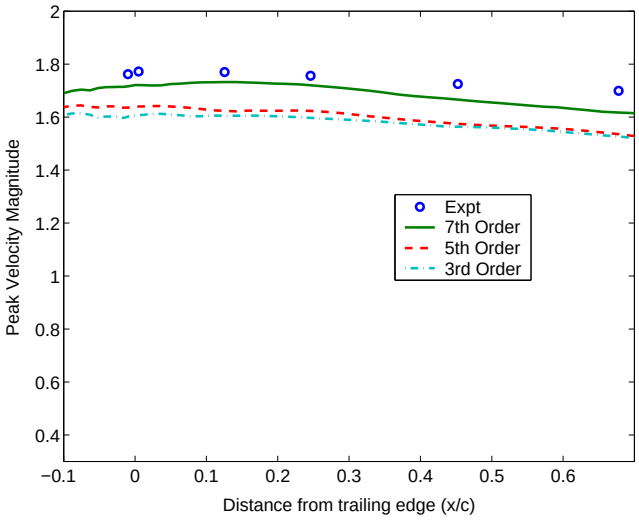

(b) Peak total velocity magnitude

Figure 4.16: Effect of inviscid discretization: Grid 3 (fine grid) used for all computations.

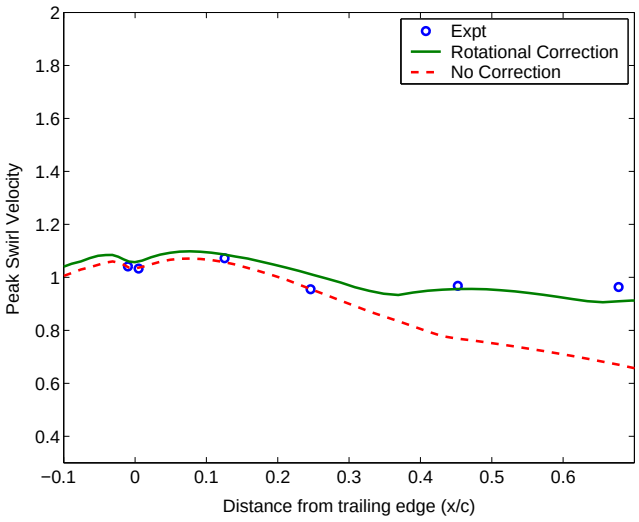

(a) Peak swirl velocity

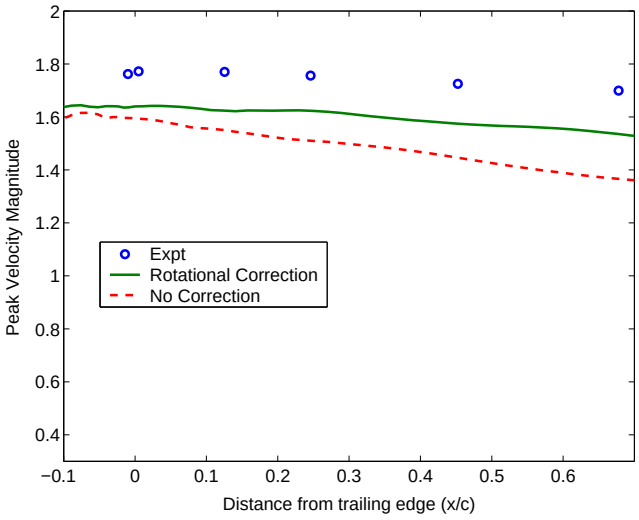

(b) Peak total velocity magnitude

Figure 4.17: Effect of turbulence model correction. WENO5 Inviscid differencing for both cases.

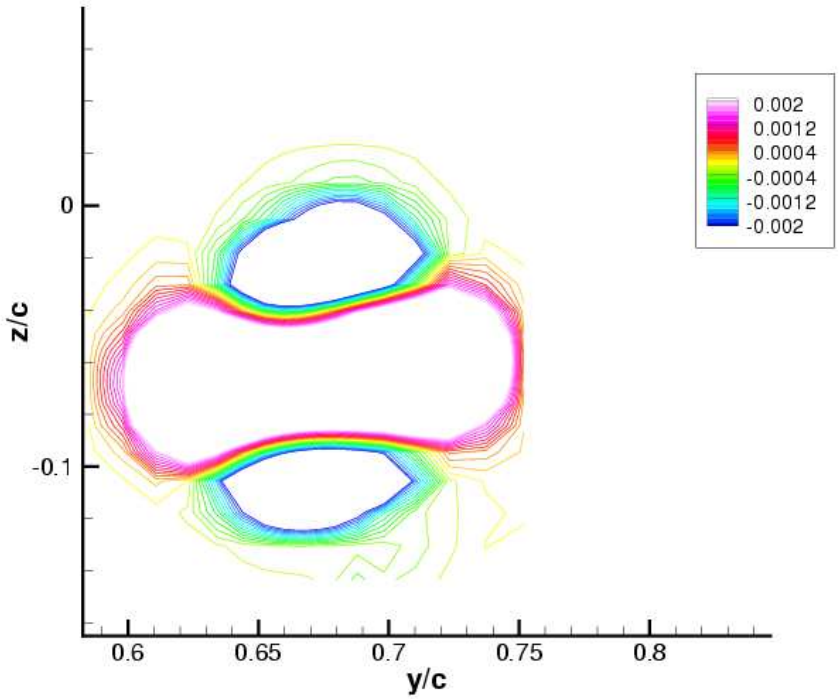

Figure 4.18: Contours of primary Reynolds stress $< v'w' >$ at $x/c = 0.462$ from trailing edge. Turbulence model with no rotational correction.

boundary layer is observed on the pressure (lower) surface, indicating crossflow. This boundary layer acts a *feeding sheet* of vorticity and begins to thicken as it crosses the mean chord line since the driving pressure gradient begins to weaken. As marked in the figure, the boundary layer subsequently separates[1]and the feeding sheet lifts off the surface. This feeding sheet then rolls up under the action of is own induced velocity and the prevailing adverse pressure gradient tapers off as one approaches the inboard section of the wing.

The crossflow velocity at the bottom edge of the vortex core induces a near-wall flow on the top surface (the associated boundary layer is evidenced by the blue patch of negative vorticity) in the outboard direction. Closer to the tip, this region is affected by the velocities induced by the feeding sheet and ultimately thickens in extent, appearing as a secondary vortical region that counter-rotates with the evolving tip vortex.

These primary and secondary structures continue to evolve on the surface until the trailing edge is reached. Off the trailing edge, this counter rotating patch is ingested by the tip vortex as shown in fig. 4.20. The presence of a secondary vortex have been confirmed in the experiment as well as a few others such as Devenport et al. [10], Martin et al. [11]. The interaction of the secondary vortex with the primary vortex severely strains the primary vortex such that the core appears to be elliptical very near to the trailing edge. This explains the apparent "oscillations" in the vertical and swirl velocities in fig. 4.10. A more detailed inspection of the flow very close to the trailing edge reveals the presence of a tertiary vortex which co-rotates with the primary tip vortex. This tertiary vortex is smaller and much weaker compared to the secondary vortex and is

[1]The separation is of a secondary nature since the main flow is in the axial direction.

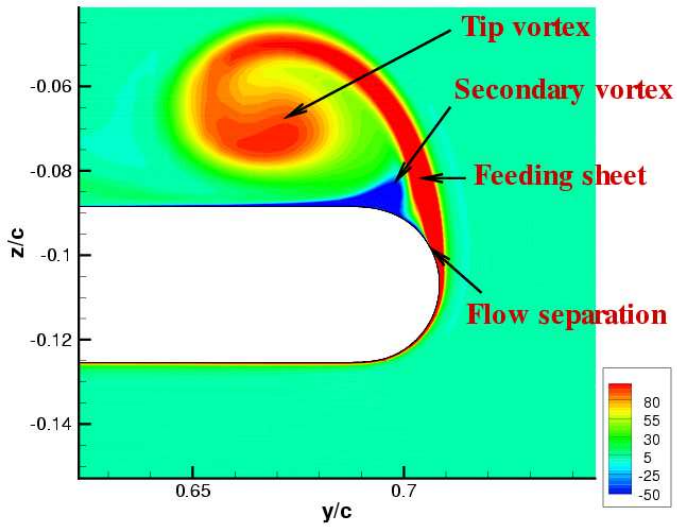

Figure 4.19: Computed axial vorticity magnitudes at a section $x/c = -0.15$ from the trailing edge. (Positive vorticity is in the anti-clockwise sense)

located approximately in between the secondary vortex and the feeding sheet. With these observations in mind, the following section is dedicated solely to the detailed study of vortex formation.

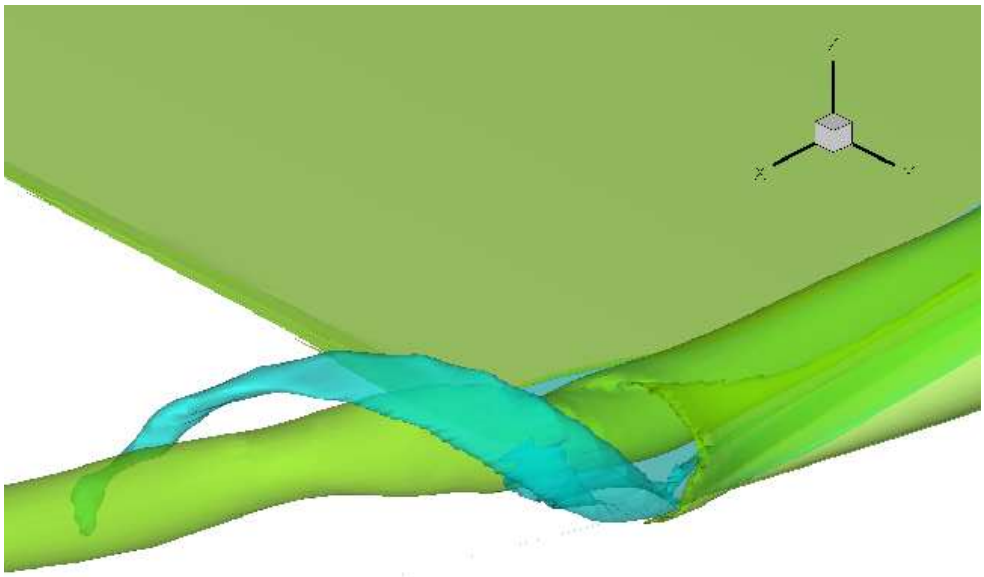

Figure 4.20: Iso-surfaces of axial vorticity (ω_x) near trailing edge. Green surfaces: $\omega_x = +50$, Blue surfaces: $\omega_x = -10$. Vorticity is normalized by free-stream velocity and chord.

Airfoil	Tip	Re	C_L	C_D	$V_{\theta_{max}}$	r_c	$V_{axial_{max}}$
0009	Round	4.6×10^6	0.8186	0.0356	0.806	0.0303	1.475
0012	Round	4.6×10^6	0.8616	0.0298	0.824	0.0307	1.437
0015	Round	4.6×10^6	0.8227	0.0369	0.841	0.0301	1.315
0012	Flat	4.6×10^6	0.8675	0.0301	0.643	0.0500	1.289
0009	Round	4.6×10^5	0.7898	0.0420	0.679	0.0367	1.213
0012	Round	4.6×10^5	0.8013	0.0396	0.654	0.0456	0.923
0015	Round	4.6×10^5	0.8013	0.0390	0.774	0.0309	1.302
0012	Flat	4.6×10^5	0.8018	0.0399	0.552	0.0577	1.035

Table 4.2: Comparison of different cases for wing in free-stream. For all cases, $AR = 4.3$, $\alpha = 10^o$ and $M_\infty = 0.15$. Velocity and core radii information at $x/c = 0.5$ behind trailing edge

4.3 Vortex formation from a fixed wing in free-stream

The validation studies in the previous section involved a low aspect ratio wing (AR=0.69) in a wind tunnel. In this section, vortex formation studies will be conducted on a larger aspect ratio wing (AR=4.3) in free-stream. A range of flow and geometry effects will be explored, while maintaining discretizations similar to that of the previous section. The first 3 columns of table 4.2 summarizes the different test runs. For all the computations, inviscid differencing is done using the 7th order WENO upwind scheme. The rotational correction is added to the baseline SA turbulence model.

4.3.1 Physics of vortex formation

Fig. 4.21 shows the evolution of axial vorticity from the rounded tip 0012 wing at $Re = 4.6 \times 10^6$. It is evident that the cross-stream flow sweeps smoothly over the tip until the quarter-chord location ($x/c = -0.75$) and slightly beyond ($x/c = -0.65$). Further downstream, the crossflow boundary layer is seen to further thicken ($x/c = -0.5$) and ultimately separate and lift off the tip ($x/c = -0.25$). This separation is a consequence of the adverse (spanwise) pressure gradient experienced by the crossflow as it traverses over the mean camber line.

A clearer picture emerges from fig. 4.22, in which the spanwise pressure distribution is plotted along different streamwise sections: For $x/c \leq -0.65$, the adverse pressure gradient seems to be mild enough for the cross flow boundary layer to remain attached on the surface. Further downstream ($x/c \geq -0.5$), the adverse pressure gradient gets stronger and the boundary layer detaches from the surface. The boundary layer separation causes the roll up of the feeding sheet into a tip vortex (fig. 4.21 e) and as a consequence, a region of counter rotating vorticity is developed as explained in sec. 4.2. Figure 4.23 shows the portion of the surface over which crossflow separation is present. Qualitatively and quantitatively, the details of vortex formation were found to be similar to that observed in the low-aspect ratio wind tunnel case. The axial velocity excess was however, found to be $\approx 20\%$ lower in the free-stream case. A possible reason for this could be the absence of the constraining effect of the wind-tunnel walls.

4.3.2 Effect of airfoil thickness

Figure 4.24 (along with fig. 4.21) shows the evolution of the tip vortex on wings with different airfoil sections. Thinner airfoil sections exhibit advanced

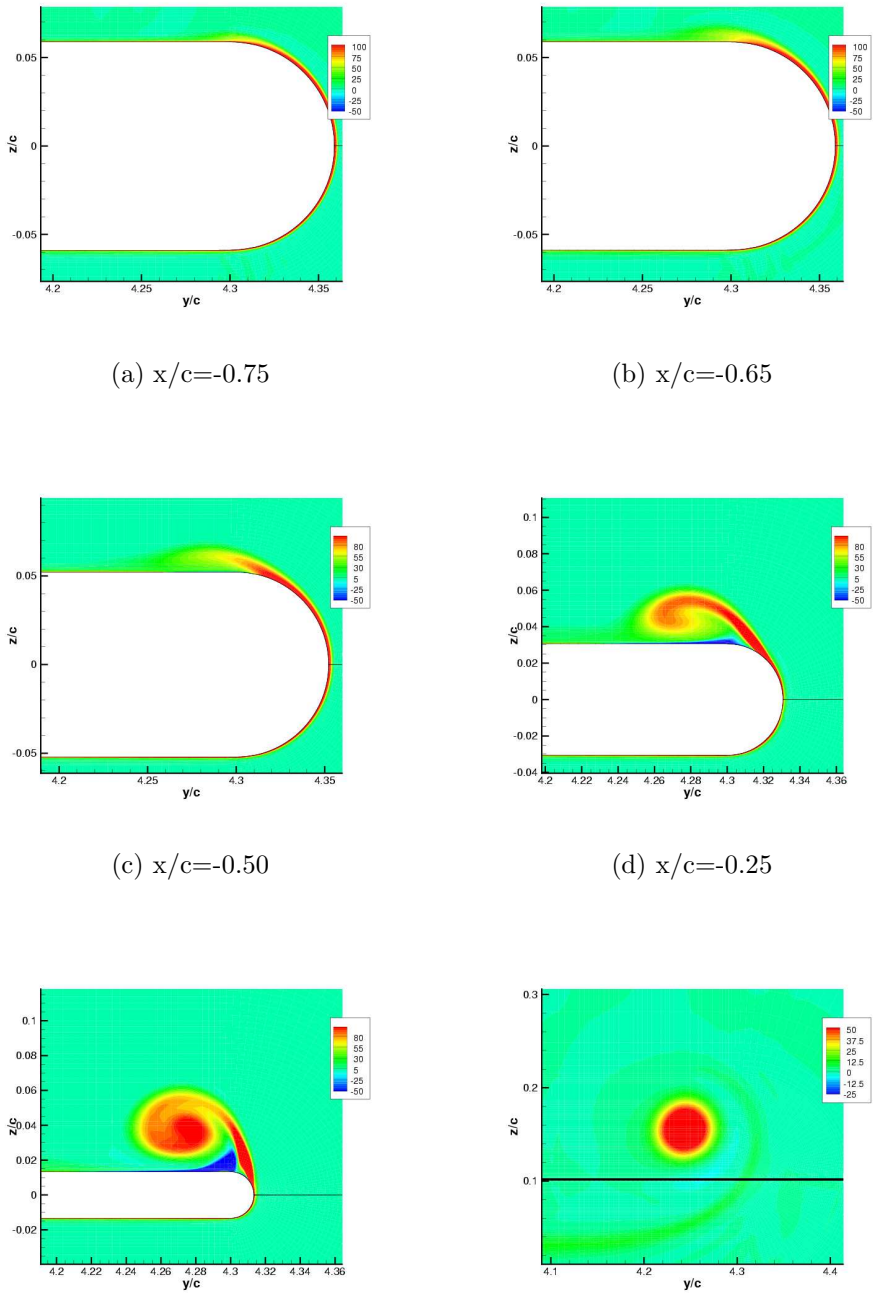

(a) x/c=-0.75

(b) x/c=-0.65

(c) x/c=-0.50

(d) x/c=-0.25

(e) x/c=-0.10

(f) x/c=0.50

Figure 4.21: Formation and rollup of the tip vortex. Axial vorticity contours for NACA 0012 wing with Rounded tip at $Re = 4.6 \times 10^6$. All axial distances referenced to trailing edge.

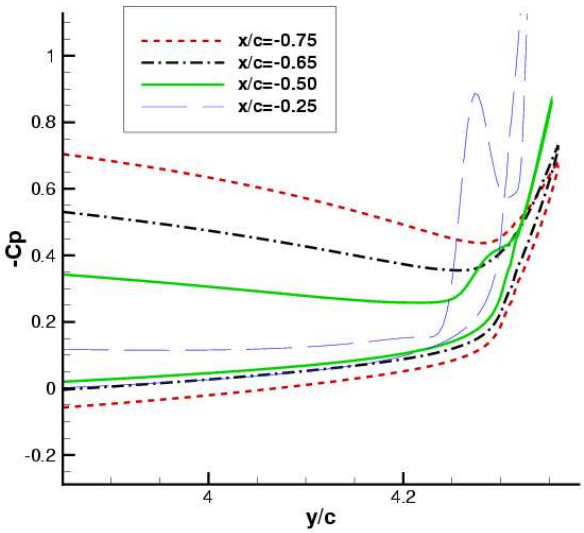

Figure 4.22: Spanwise pressure distribution at different streamwise sections for NACA 0012 wing with Rounded tip at $Re = 4.6 \times 10^6$

Figure 4.23: Region of *crossflow* boundary layer separation: NACA 0012 wing with Rounded tip at $Re = 4.6 \times 10^6$

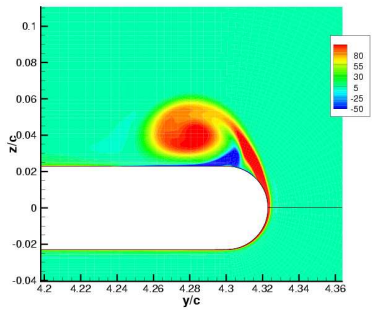

(a) NACA 0009, $x/c = -0.25$

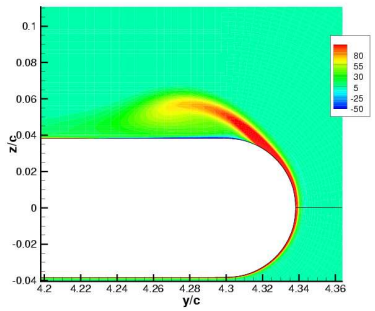

(b) NACA 0015, $x/c = -0.25$

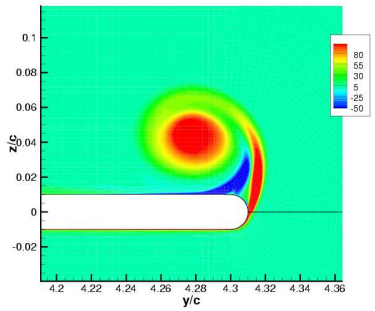

(c) NACA 0009, $x/c = -0.1$

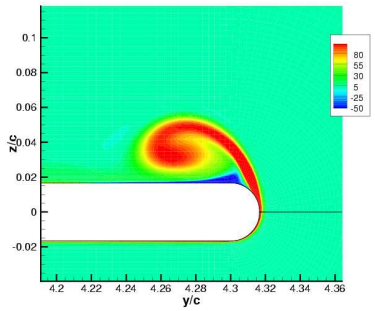

(d) NACA 0015, $x/c = -0.1$

Figure 4.24: Axial vorticity contours for different airfoil sections for wing with Rounded tip at $Re = 4.6 \times 10^6$.

separation since the adverse pressure gradients are larger due to the shorter distance of traverse across the tip. The advanced separation causes the feeding sheet to lift off the surface and results in a more rapidly rolled-up tip vortex compared to the thicker sections. Figure 4.25 shows the corresponding separation regions.

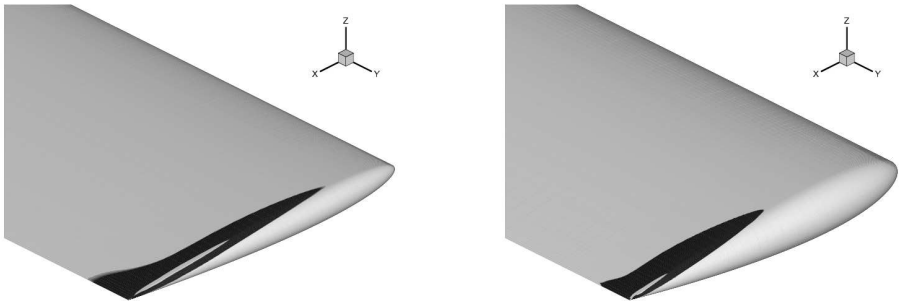

(a) NACA 0009 (b) NACA 0015

Figure 4.25: Effect of airfoil shape on *crossflow* boundary layer separation. $Re = 4.6 \times 10^6$

4.3.3 Effect of Tip Shape

For a rounded tip shape, it is observed that along a streamwise plane, the separation point is related to the magnitude of the adverse pressure gradient along the tip surface. As a consequence, it is seen from figs. 4.23 and 4.25 that crossflow separation always occurs on the suction (upper) surface of the wing tip. However, for a flat tip, separation can be expected to be fixed by the geometry since the flow has to turn more abruptly over the wing-tip.

This situation is evident from figs. 4.26 and 4.27, which correspond to a wing with a NACA0012 airfoil section, but with a flat tip. Even at the quarter chord location, initial traces of the evolving tip vortex are observed (fig. 4.26a). Crossflow separation is observed at two different points along the tip section and hence the resulting tip vortex is much more diffuse. As seen in table 4.2, the peak swirl velocity is smaller compared to the rounded tip and the core-radius is larger. This is qualitatively consistent with the observations of [114], in which the core-radii of square tipped wings were found to be around $30 - 40\%$ higher

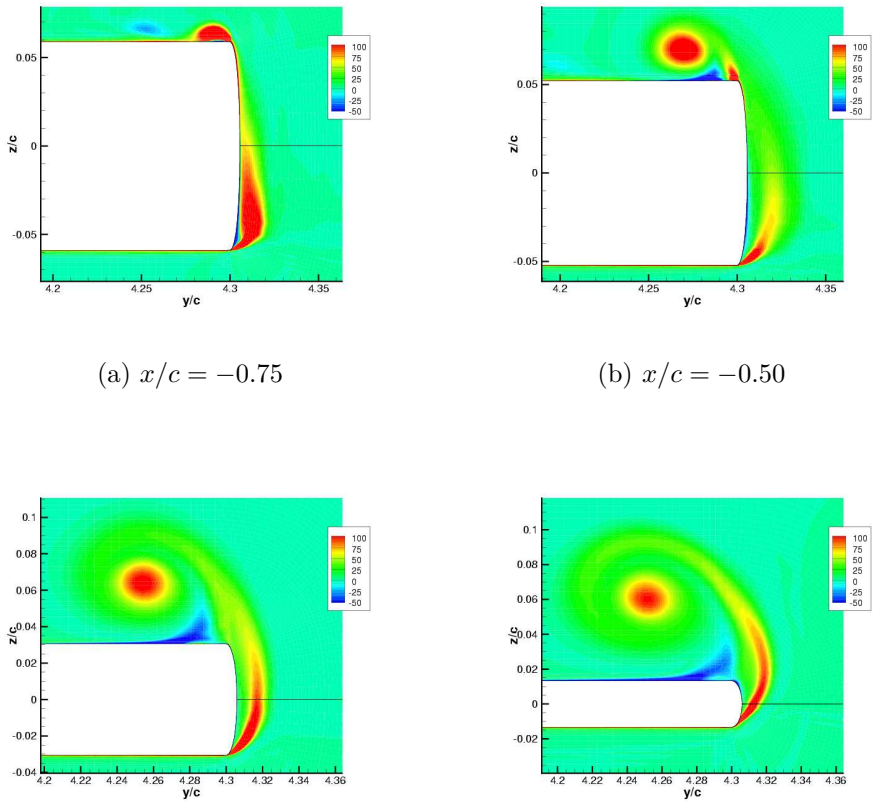

(a) $x/c = -0.75$ (b) $x/c = -0.50$

(c) $x/c = -0.25$ (d) $x/c = -0.1$

Figure 4.26: Axial vorticity contours for NACA 0012 wing with Flat tip at $Re = 4.6 \times 10^6$.

than that of round tips.

4.3.4 Effect of Reynolds number

A smaller Reynolds number would mean that the decelerating viscous forces are larger than the inertial forces that primarily drive the flow. As a result, one would expect increased cross-flow separation and more diffuse tip vortices. Figure 4.28, when compared to figs. 4.21 and 4.23 show the more diffuse nature of the evolving

Figure 4.27: Region of *crossflow* boundary layer separation: NACA 0012 wing with Flat tip at $Re = 4.6 \times 10^6$

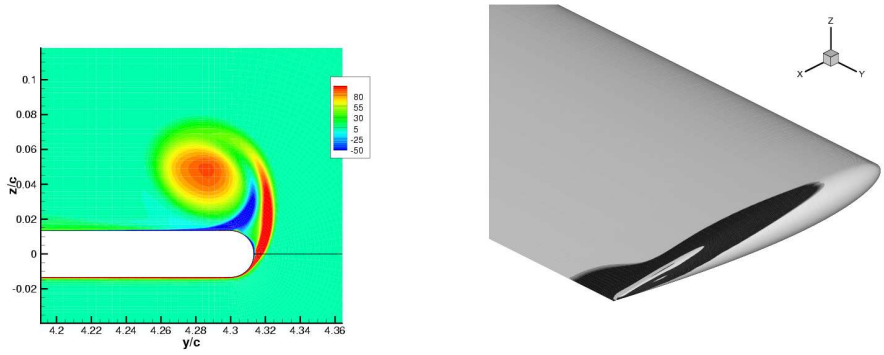

(a) Axial vorticity at $x/c = -0.1$ (b) Cross-flow separation region

Figure 4.28: NACA 0012 wing with rounded tip at $Re = 4.6 \times 10^5$.

tip vortex and the increased separation extent at the lower Reynolds number. Table 4.2 also shows the decreased swirl velocity and increased core radius at the lower Reynolds number.

4.4 Vortex Evolution

The previous sections were focused on the properties of vortex *formation* from a fixed wing in the very near field. In this section, vortex *evolution* properties

Airfoil section	NACA 0012
Tip shape	Rounded (circular)
Chord length (c)	0.15 m
Aspect Ratio	1.0
Mach Number	0.1
Chord Reynolds Number	2.2×10^5
Angle of attack	7.5^o

Table 4.3: Test conditions for Vortex Evolution

(upto 10 chord lengths downstream of the trailing edge) will be studied. The test case chosen for this study corresponds to that of the wind tunnel experiments conducted by Heyes et al. [146]. In the original experiment, the test section dimension was $0.45m \times 0.3m$ and the length was $1m$. The relevant geometry and flow parameters for the half-span wing are given in table 4.3.

Axial and swirl velocity measurements along with vortex core location is available in a data plane that is one chord downstream of the trailing edge. This test case was chosen since a set of steady and oscillatory blowing tests were conducted on the baseline configuration. The steady blowing measurements used for further validation in vortex control simulations are presented in Chapter 6. A key difference between the experiment and the simulation is that the latter assumes the wing to be in free-stream. As will be seen, comparison of the computed vortex velocity profile with the experimental results suggest that the details of the vortex formation are not different.

The computations in the previous sections were focused on the near field. In order to accurately resolve the vortex evolution many chord lengths downstream,

a single structured mesh will be highly inefficient since the clustering of grid points in the cross-stream direction will have to extend to the grid boundaries. In order to avoid this and also to ensure equal spaced grid points (in the cross stream direction), an overset grid is placed approximately in the region of the wake where the tip vortex is expected to be present. Fig. 3.36 shows streamwise planes of the main and overset grids (every other grid point is shown in either direction). The dimensions of the main grid are $227 \times 100 \times 115$ in the streamwise, spanwise and normal directions. The farfield is at a distance of 25 chord lengths from the surface. The overset grid has 199 axial planes of size 133×133. The cross-stream grid spacing is $0.0075c$, assuring atleast 10 points per vortex core-length. This grid spans an axial distance of $0.25 \geq x/c \leq 15.25$ behind the trailing edge.

Figure 4.29 compares the solution along a line in the fringe region of both meshes at $x/c = 0.3$ and confirms the accuracy of the chimera interpolation. Unless mentioned, all the results use the 5th order WENO differencing for inviscid fluxes. As opposed to vortex formation studies, the application of the 7th order WENO scheme for longer spatial evolution problems resulted in small scale oscillations in the vortex evolution properties. Hence it is not used in further calculations.

Figure 4.30 compares the computed vertical and axial velocities on a horizontal line passing through the vortex center at an axial plane that is 1 chord downstream of the trailing edge. The vertical velocity is seen to be accurately represented while the axial velocity defect is slightly underpredicted. The defect in axial velocity is a consequence of the low Reynolds number, implying larger viscous deceleration compared to all previous test cases.

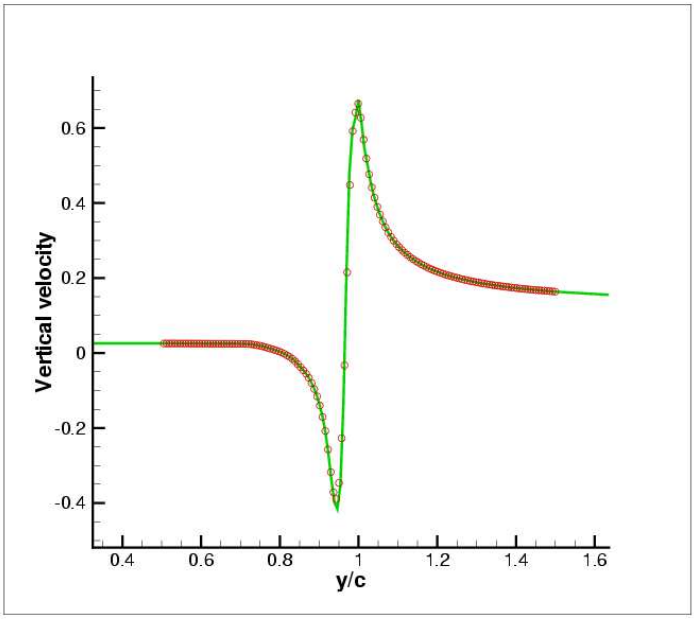

(a) Vertical velocity

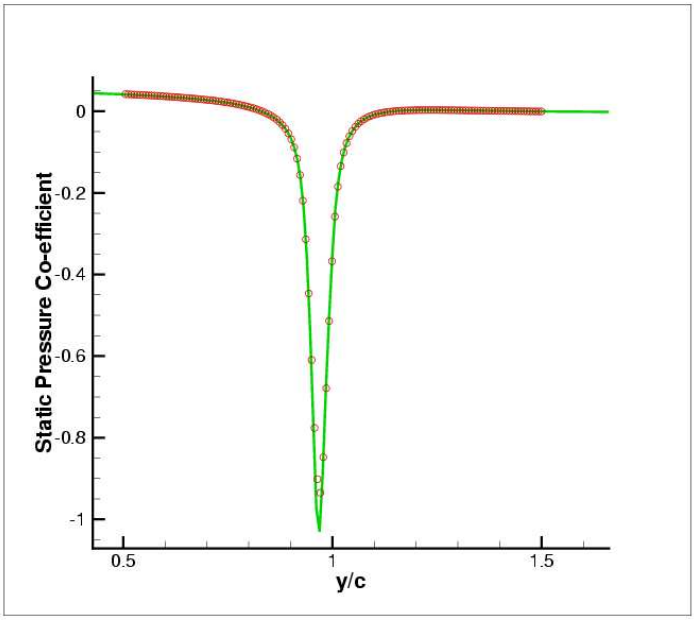

(b) Static pressure co-efficient

Figure 4.29: Comparison of solution on background grid (line) with overset grid (circles) at $x/c = 0.3$

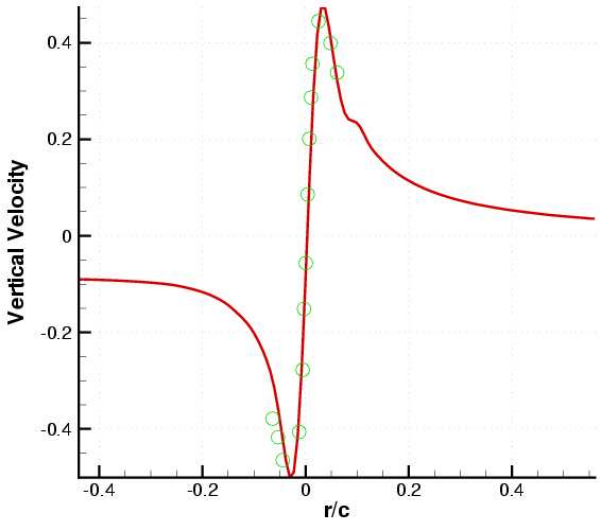

(a) Vertical velocity

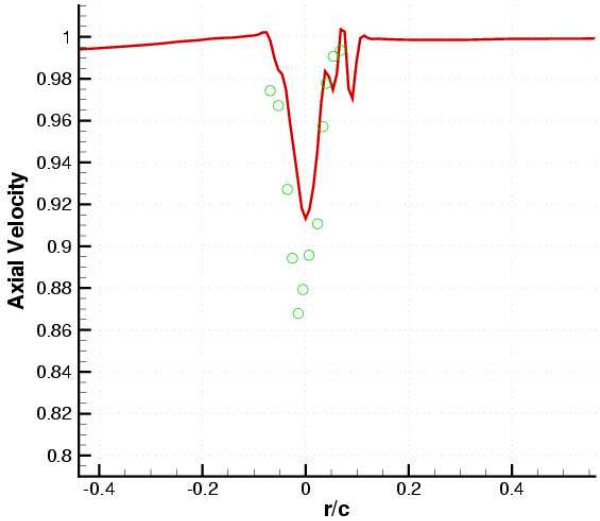

(b) Axial velocity

Figure 4.30: Comparison of computed velocity profile (line) with experiment (circles) at $x/c = 1.0$

As seen in Chapter 2, for an axisymmetric vortex, the core radius (r_c) and peak swirl velocity ($V_{\theta_{max}}$) can be represented by:

$$r_c(t) = \sqrt{(r_c^2)_o + 4\nu\alpha(1+\delta)t} \;\; and \;\; V_{\theta_{max}}(t) = \frac{(V_{\theta_{max}})_o (r_c)_o}{r_c(t)} \qquad (4.1)$$

A laminar vortex would correspond to $\delta = 0$ and other diffusion effects (like turbulence) can be represented by $\delta > 0$. Figure 4.31 shows that the data can be fit by using $\delta = 4$. This lies in the range predicted by [57] and is a useful parameter when comparing different data sets and also to quantify the diffusion rate. Note that the computed data (symbols) shows apparent "oscillations" in the core-size. This was found to be purely an artefact of post-processing: Due to the discreteness of the grid, the location of the core center and periphery were found to switch across nearby points.

Figure 4.32 shows the vertical velocity along the vortex core at different spatial locations. The velocity profiles appear to remain qualitatively similar. The small "bump" that is visible to the right of the vortex center is a result of the shear layer that is rolling-up. Figure 4.33 shows the evolution of the vorticity magnitude and the vortex center in reference to the cross-stream boundaries of the overset grid. From this figure it is apparent that vortex sheet wraps around the tip vortex and decays rapidly. Physically, the stabilizing effects of rotation can be expected to minimize diffusion in the vortical core.

Figure 4.34 shows the computed vortex properties using 1) Same grid, but 3rd order inviscid differencing and 2) Coarser grid (every other point in the cross-stream direction of vortex grid), but with fifth order WENO inviscid differencing. It is seen that both these approaches yield highly diffuse solutions in the initial stages of evolution, but beyond $x/c > 3$, the decay rate is approximately equal to that of the high order solution on the finer grid. This implies that the numerical

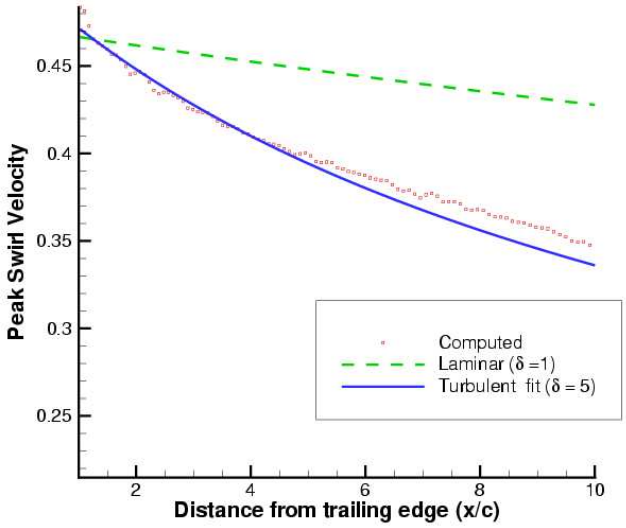

(a) Peak swirl velocity

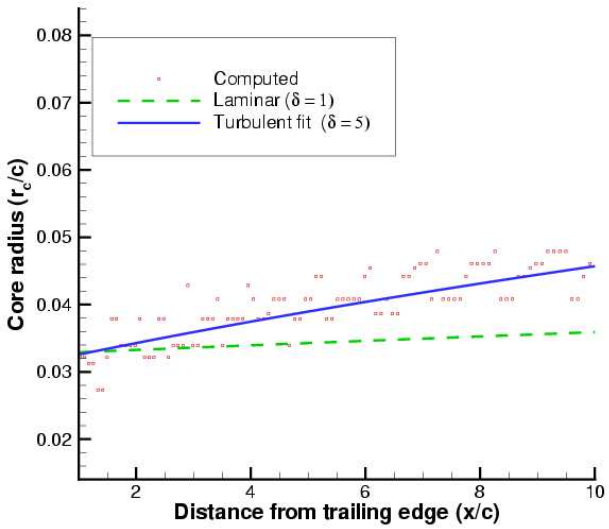

(b) Core radius

Figure 4.31: Tip vortex evolution properties compared to that of an axisymmetric model vortex

methodology is not accurate enough to resolve the vortex in its initial state, but as it diffuses artificially, the core-radius and other features become large enough to be resolved with less numerical error.

4.5 Summary

In this chapter, extensive validation studies were presented on the formation and evolution of a tip vortex in the near-field of a fixed wing. Overall, the computed results showed agreement with the experimental measurements when high order schemes were used along with a simple modification of the turbulence model. These studies are used as guidelines in determining resolution requirements for the rest of this thesis. The physics of vortex formation was studied in detail. The effect of tip shape, airfoil section and Reynolds number on vortex formation were explored.

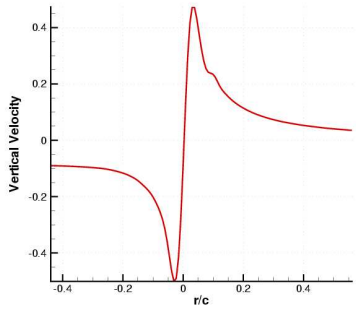

(a) x/c=1

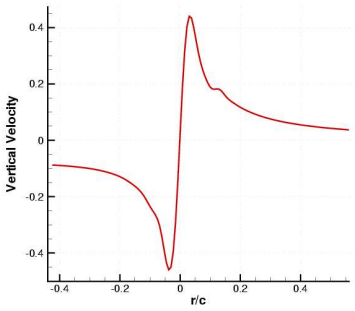

(b) x/c=2

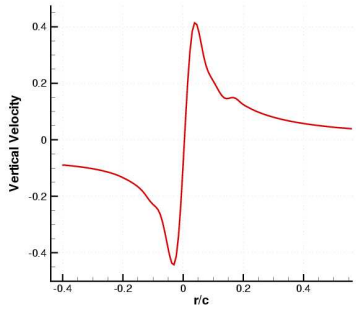

(c) x/c=3

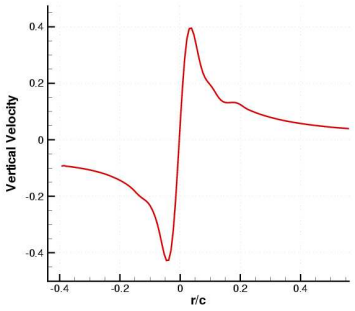

(d) x/c=5

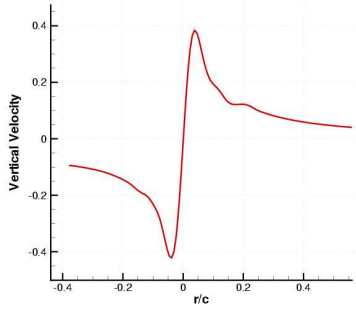

(e) x/c=8

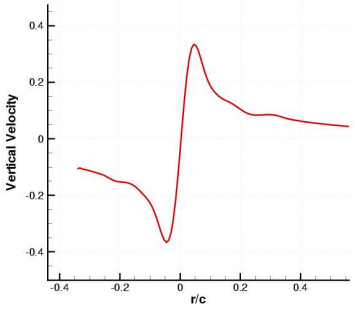

(f) x/c=10

Figure 4.32: Vertical velocity across vortex core at different downstream locations

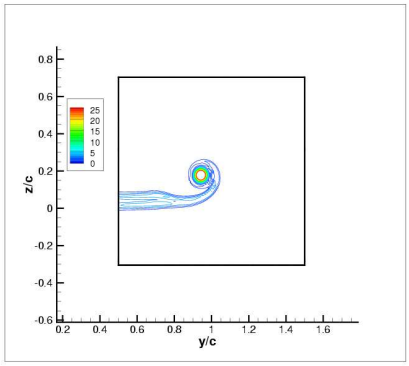

(a) x/c=1

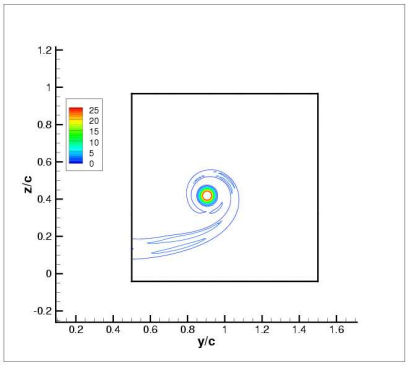

(b) x/c=3

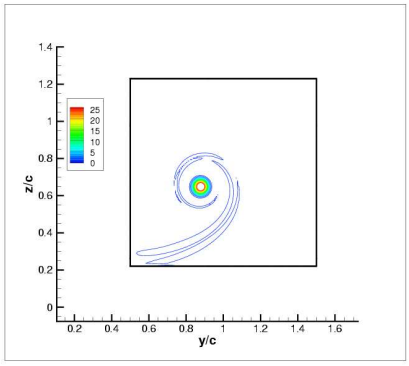

(c) x/c=5

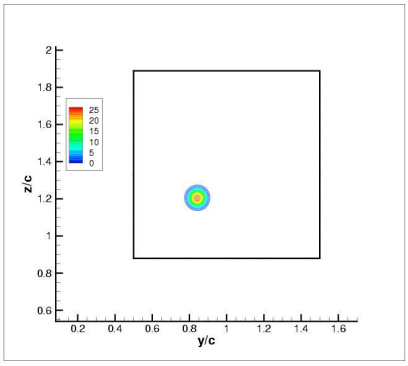

(d) x/c=10

Figure 4.33: Computed vorticity magnitude at different downstream locations

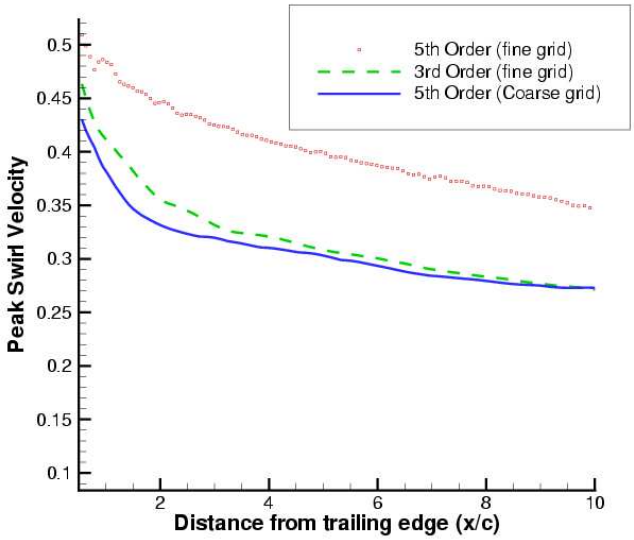

(a) Peak swirl velocity

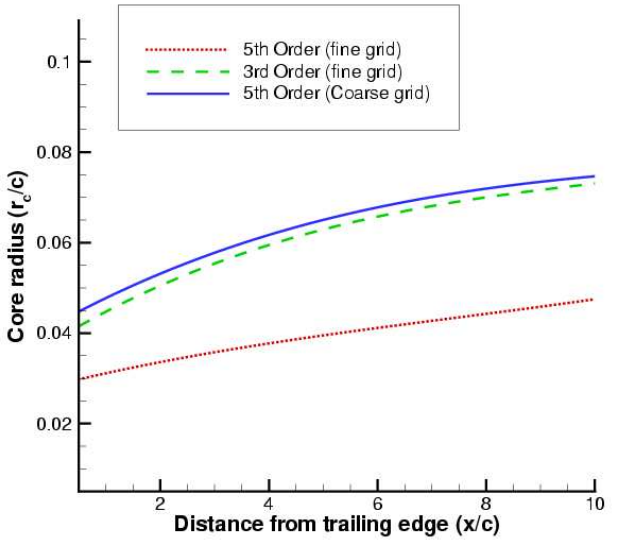

(b) Core radius (Curve-fit)

Figure 4.34: Vortex evolution properties for different validation runs

Chapter 5

Computation of Vortex Formation and Evolution from Rotating Blades

The previous chapter was dedicated to the study of vortex formation and evolution from a fixed wing. In this chapter, the study is extended to single and two bladed rotary systems under hovering conditions. The single bladed study is focused on validating the computed vortex velocity profiles with experimental measurements. The two bladed study is centered around the validation of the blade surface pressure distribution and vortex trajectory measurements. Taken together, these studies represent to a large extent, the spectrum of validations that are of engineering interest in hovering rotor applications.

5.1 Single bladed rotor in hover

The test case chosen for vortex evolution simulation is based on the experiments conducted by Martin et al. [11] at the hover test chamber at the University of Maryland. The relevant parameters for this experimental test run are shown in table 5.1. The single blade is of rectangular planform with a square-tip and

Airfoil	NACA 2415
Blade chord	42.5 mm
Aspect Ratio	9.12
Tip Mach Number	0.26
Chord Reynolds Number at Tip	272000
Collective Pitch	4.5^o
Root cut-out	20%

Table 5.1: Test conditions for Single bladed rotor in hover (Experiments reported in [11])

is untwisted. The experimental set up was such that the wake was allowed to exhaust 18 rotor radii (in the downward direction) before encountering any flow diversions. LDV and PIV based swirl and axial velocity measurements are available at select azimuthal planes, spanning $3^o \leq \psi \leq 371^o$.

As mentioned in Chapter 1, tip vortex measurements suffer from the phenomenon of vortex wandering (usually referred to as *aperiodicity* in rotor wakes). As a result of this apparently random phenomena, the vortex core position at each wake age differs from its mean position at different times. Figure 5.1 shows the measured core locations at specific wake ages at different times and it is found that the wandering amplitude is of the order of core-radii. As a result, the use of uncorrected data will give an apparent "smeared-out" version of the actual flowfield and hence, corrections have to be made. The experimental data was corrected for wandering using the empirical technique of Devenport et al. [10].

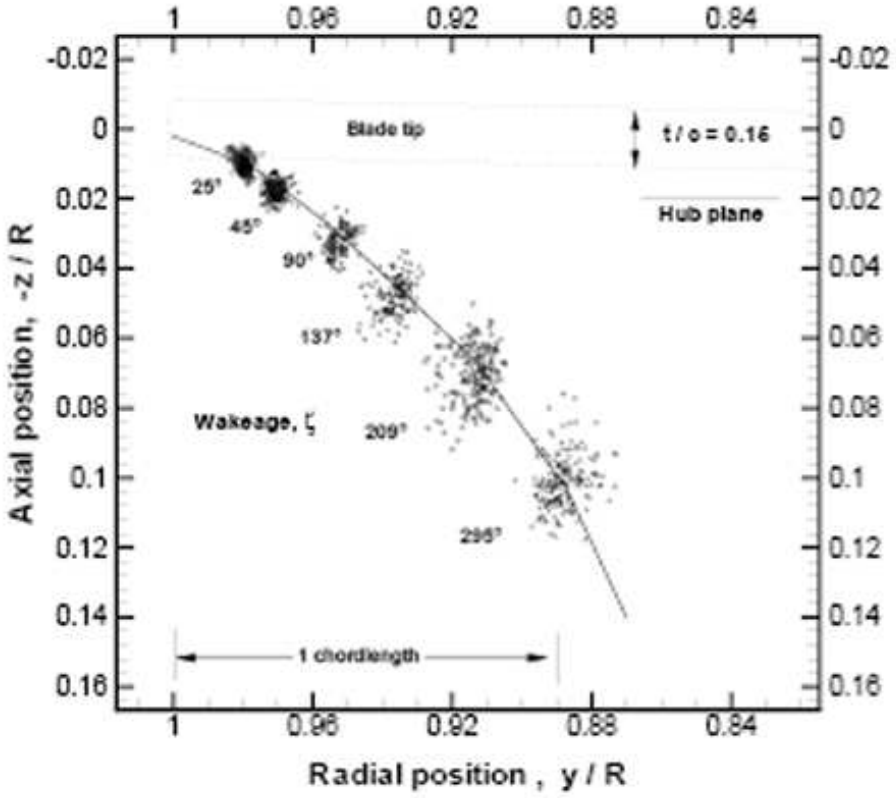

Figure 5.1: Measurements of wandering for single bladed hover case [11]

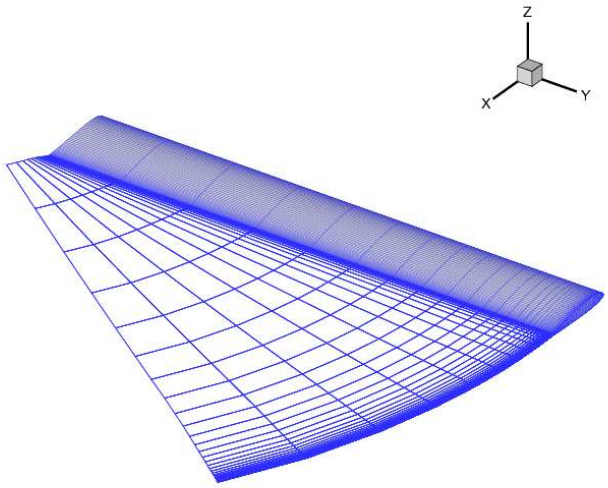

Figure 5.2: Blade mesh for hovering rotor: Rotation of chordwise planes in azimuthal direction.

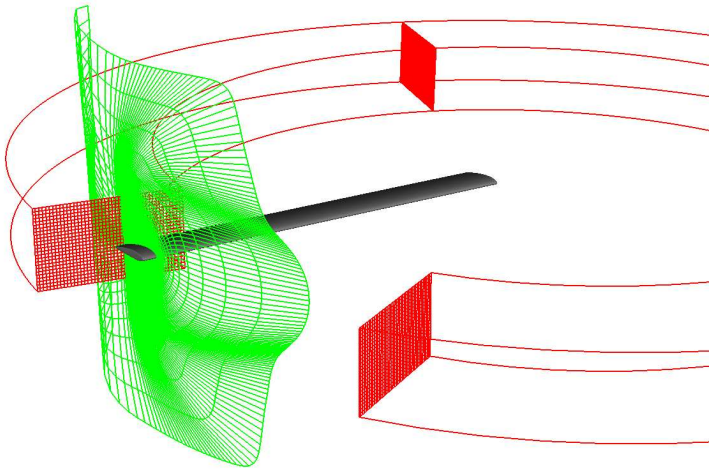

Figure 5.3: Spanwise section of blade grid (green) and streamwise sections of vortex grid (red)

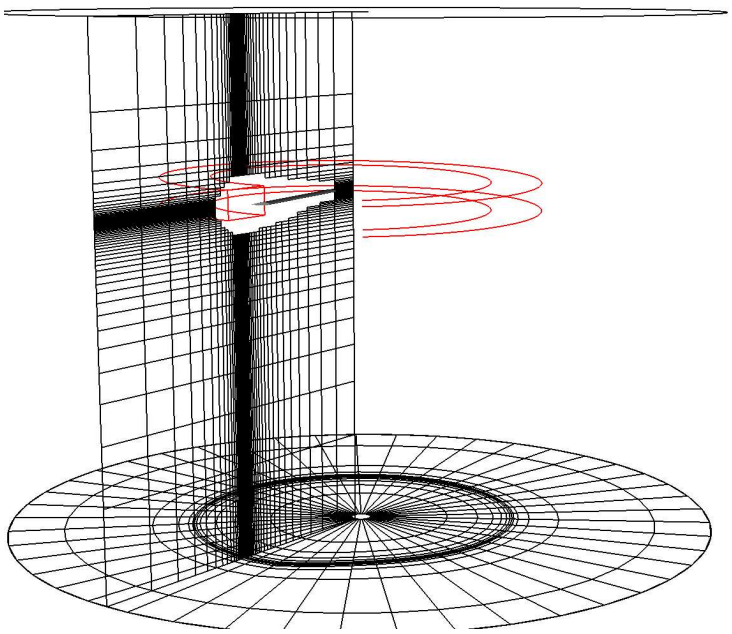

Figure 5.4: Background grid (black) and vortex grid (red)

5.1.1 Grid system

For the computations, a three-grid system is used. A body-conforming C-O type grid of dimension $161 \times 55 \times 48$ (in the streamwise, spanwise and normal directions respectively) is used to discretize the blade region. Since the flow field of a hovering rotor is cylindrical, the spanwise sections of this mesh are roughly aligned with the local flow direction in the wake region (fig. 5.2). Compared to a non-rotated mesh, the computed vortex profiles were found to be much less dissipative as a result of rough alignment with the vortex axis. The grid extends to a normal distance of slightly more than 2 chord lengths and the normal spacing at the wall is $1 \times 10^{-5}c$ (< 1 wall unit). Figure 5.3 shows a spanwise section of the grid near the tip region.

A refined overset grid of dimension $135 \times 176 \times 101$ is used to resolve the tip vortex (figs. 5.3, 5.4). This grid starts at the trailing edge of the rotor and

extends to a wake age of around 330 degrees. Each streamwise section (176×101) of this grid is equi-spaced consisting of square cells of side $0.014c$. The placement and alignment of this grid is based on the predicted wake geometry given by Landgrebe's model [147]. As will be seen from the numerical results, this proves to give a very reasonable estimate of the vortex positions.

In order to account for the far-field boundaries, a cylindrical background mesh of size $181 \times 50 \times 60$ (in the streamwise, spanwise and normal directions respectively) is utilized as shown in fig. 5.4. The radius of the outer boundary of this grid is twice the rotor radius and the top and bottom boundaries are one rotor radius and two rotor radii away from the blade surface respectively. Figure 5.4 also shows that the part of the background grid that overlaps with the blade grid is hole-cut. The number of grid points total 3.37 million.

5.1.2 Far-field boundary conditions

As mentioned in sec. 3.10.2, the downwash velocity in the bottom plane of the rotor can be significant. For this case, momentum theory predicts a downwash of around 6% of the tip speed. In order to account for this and to properly represent the inflow at the other far-field boundaries, the *point-sink* boundary condition approach of Srinivasan et. al. [26] is used. A schematic of this approach is shown in fig. 5.5. It is well known from momentum theory [3] that the asymptotic contraction of the vortex wake of a hovering rotor is approximately $R/\sqrt{2}$ and the downwash velocity at such a section is approximately $2\sqrt{C_T/2}$. As shown in the figure, this is used as the outflow velocity[1]in region marked "Outflow" in the far-field boundary.

In order to satisfy mass conservation, the rest of the far-field boundary is then

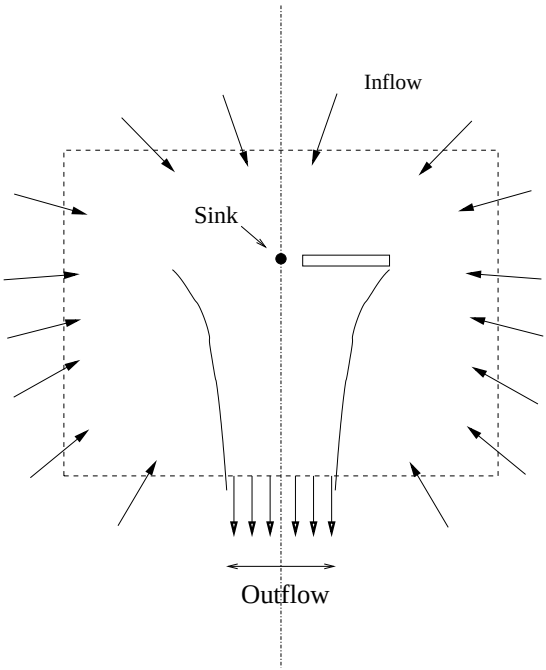

Figure 5.5: Schematic of far-field boundary condition in hover

assumed to be an inflow, the velocities of which are assumed to be induced by a point sink placed on the rotor hub. The magnitude of this spherically symmetric induced velocity is given by:

$$\frac{V_{induced}}{\Omega R} = \frac{1}{4}\sqrt{\frac{C_T}{2}}\left(\frac{R^2}{x^2+y^2+z^2}\right) \tag{5.1}$$

where, $\{x, y, z\}$ is the position vector relative to the placement of the sink. Linearized Riemann invariants are then used to determine the conserved variables at the boundary.

5.1.3 Numerical Results

Figure 5.6 shows the vorticity magnitude along selected azimuthal planes in the overset vortex grid. It is evident that by a wake age of 25^o, the vortex has

[1]This velocity is treated in the characteristic sense.

rolled up completely and the magnitude of vorticity in the tip vortex is very much higher than that in the wake. Also, the vortex structure seems to have approached axisymmetry by the 25^o wake age. Overall, the vorticity in the tip vortex diffuses at a much slower rate than the wake vorticity.

Figure 5.7 compares the computed peak swirl velocity as a function of the wake age. The computations using the 5th order WENO reconstruction for the inviscid fluxes agree well with the wandering-corrected measurements of Martin et. al. [11]. The uncorrected experimental data (simple temporal averaging) is seen to be highly smeared out. It is also obvious that the mesh resolution in the overset vortex grid is inadequate for 3rd order inviscid differencing.

The rapid rate of decay of the vortex in the initial wake ages could be attributed to the turbulence ingested from the separating boundary layer as discussed in the fixed wing vortex formation studies. In addition, the low Reynolds number and the square tip would also contribute to a larger region of counter-rotating vorticity.

Figure 5.8 compares the swirl velocity profiles at specific azimuthal locations. Good agreement is attained with the experimental data except for the $\psi = 209^o$ and 295^o wake ages, probably indicating excessive artificial diffusion either from the numerics or from the turbulence model. However, the experimental (corrected) profile at $\psi = 209^o$ (also seen in fig. 5.7) strangely corresponds to a higher swirl velocity than the previous measured wake age ($\psi = 137^o$).

Figure 5.9 shows the effect of the rotational correction in the turbulence model. As observed in the fixed wing studies in the previous chapter, the baseline SA model with no rotational correction proves to be extremely diffusive since it unphysically predicts maximum turbulence in vortical core. On comparing the

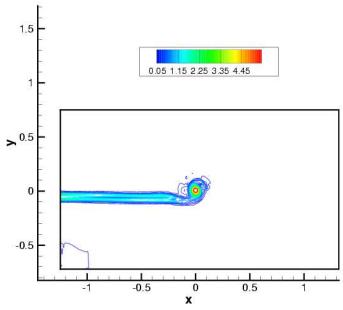

(a) $\psi = 3^o$

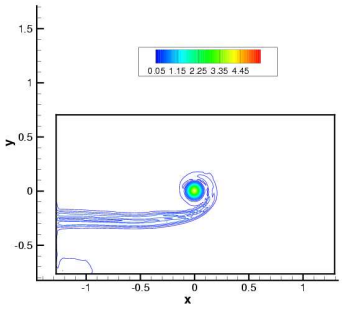

(b) $\psi = 25^o$

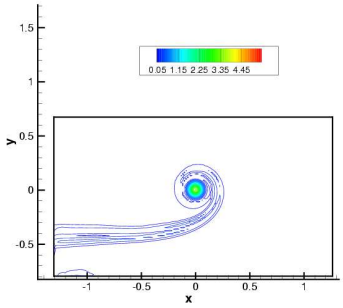

(c) $\psi = 45^o$

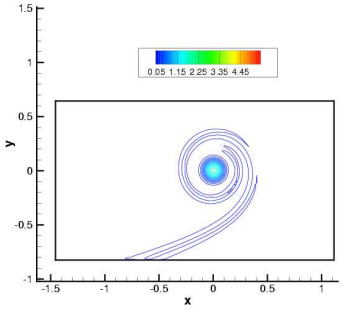

(d) $\psi = 137^o$

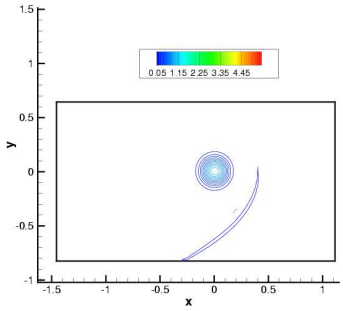

(e) $\psi = 209^o$

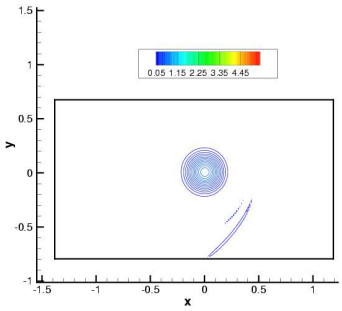

(f) $\psi = 295^o$

Figure 5.6: Contours of vorticity magnitude along selected azimuthal planes in vortex grid

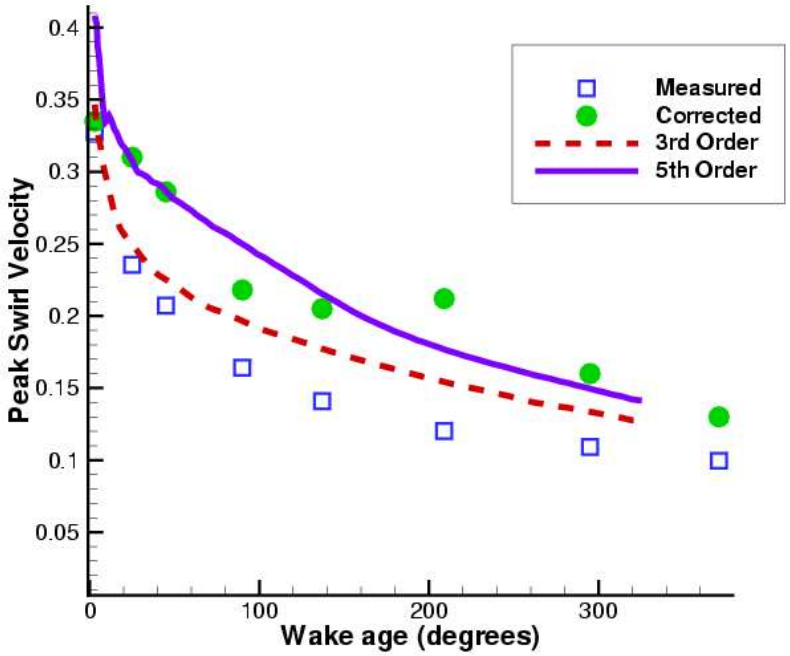

Figure 5.7: Peak swirl velocity (normalized by tip-speed) as a function of wake age

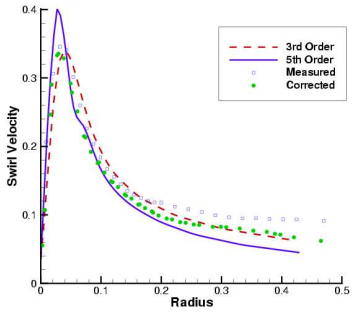

(a) $\psi = 3^o$

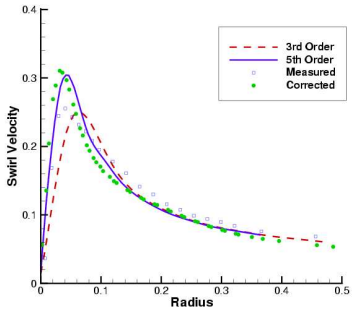

(b) $\psi = 25^o$

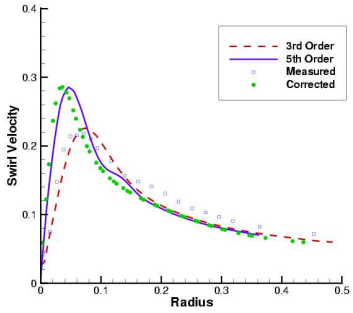

(c) $\psi = 45^o$

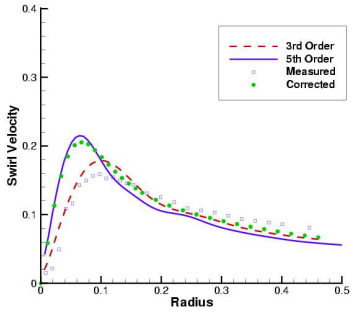

(d) $\psi = 137^o$

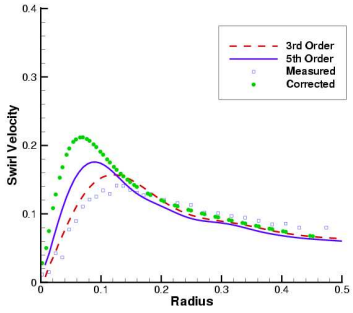

(e) $\psi = 209^o$

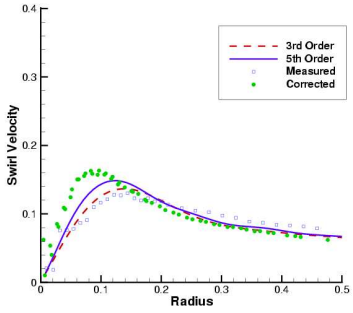

(f) $\psi = 295^o$

Figure 5.8: Comparison of computed swirl velocity profiles with experiments

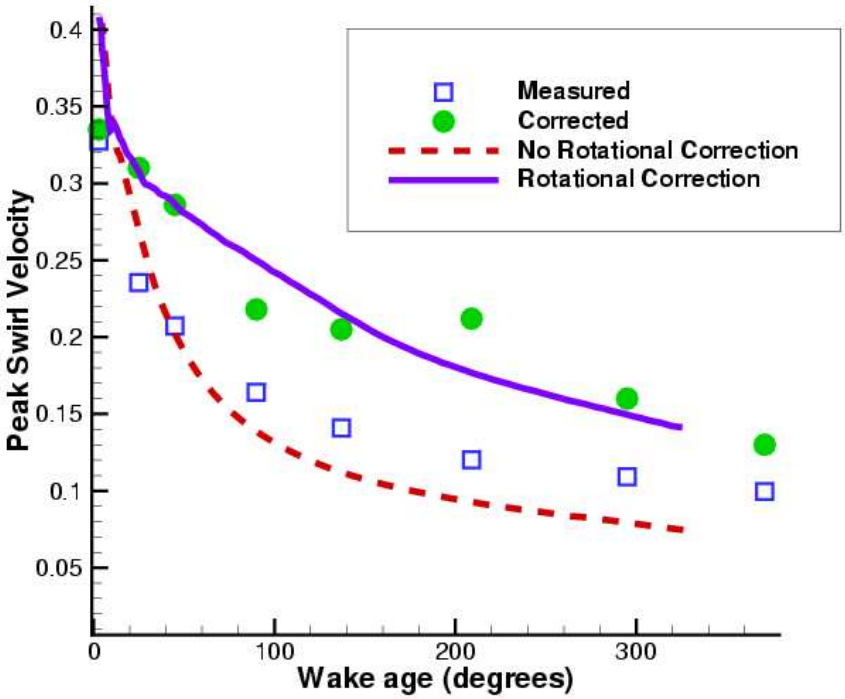

Figure 5.9: Peak Swirl velocity (normalized by tip-speed) predicted by SA turbulence model with and without rotational correction. 5th order Inviscid differencing for both cases.

3rd order solution with rotational correction (fig. 5.7) with the 5th order solution with no correction (fig. 5.9), it is apparent that turbulence modeling errors are much larger than numerical diffusion error for this particular fine computational grid.

Accurate experimental measurement of the axial velocity is difficult because vortex wandering can make the detection of the peak value (which usually occurs at the centroid of the core) highly uncertain. The corrected experimental values are currently unavailable for this experiment and hence comparisons are made

with just the measured values. As seen from the swirl velocity measurements, wandering corrections can be significant and hence the comparisons should be viewed with caution. Figures 5.10 and 5.11 show that the computations predict a much larger peak axial velocity deficit. At the earliest wake age the comparison is reasonable[2], but the measurements predict a much larger decay rate than the computations. The fact that the 3rd and 5th order schemes predict similar amounts of deficit (within 5%) again suggest that numerical diffusion effects are relatively small and cannot completely explain the difference between the measurements and computations. Hence, a possible cause that could explain some of the discrepancy is the isotropic eddy viscosity based turbulence modeling.

5.2 2 bladed rotor in hover

In the previous section, computations were performed on a single bladed hovering rotor, with significant emphasis on the vortex velocity profiles. In this section, simulations will be performed on the 2-bladed experimental setup of Caradonna and Tung [83]. This test case was chosen since it provides detailed blade surface pressure measurements and vortex trajectory data. This test case has also been previously validated using the Euler and RANS equations by several researchers [26, 34, 87].

5.2.1 Experimental configuration

The experimental setup consists of a two bladed rigid rotor in a hover chamber. The blades are of a rectangular planform and are untwisted with a radius of

[2]The measured wandering amplitudes are also lower [11].

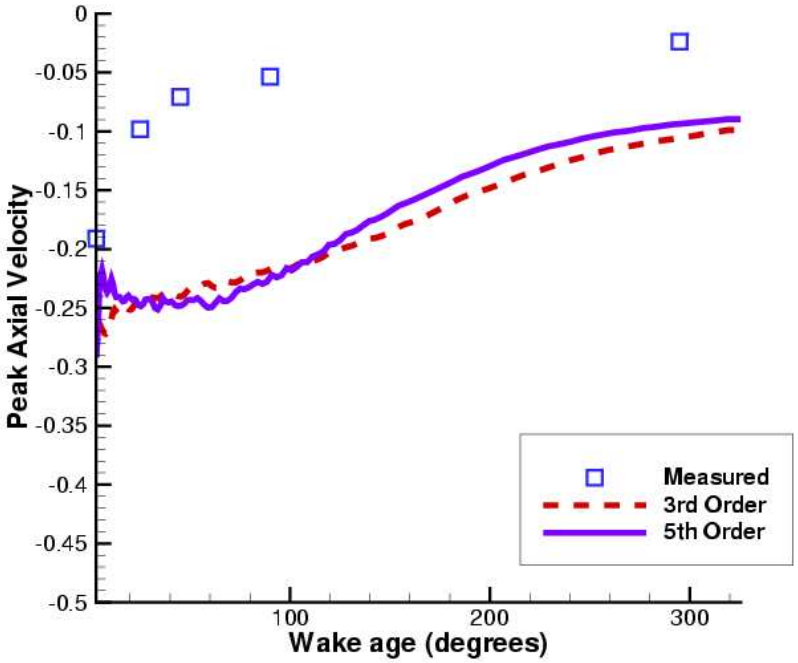

Figure 5.10: Peak axial velocity deficit (normalized by tip-speed) as a function of wake age

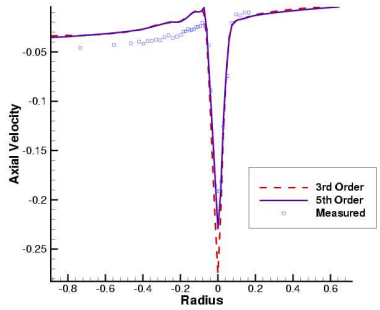

(a) $\psi = 3^o$

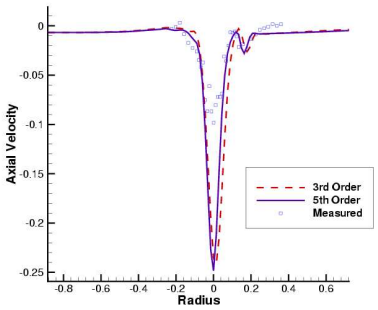

(b) $\psi = 25^o$

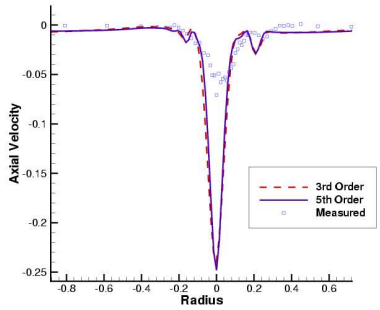

(c) $\psi = 45^o$

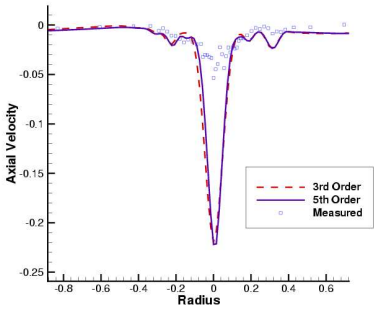

(d) $\psi = 90^o$

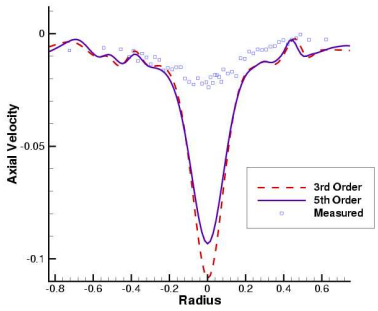

(e) $\psi = 295^o$

Figure 5.11: Comparison of Axial velocity profiles with experimental measurements (Wandering correction not available.)

Tip Reynolds number	Tip Mach number	Collective Pitch	Pre-cone angle
1.92×10^6	0.433	**12°**	0.5^o
1.96×10^6	0.44	**8°**	0.5^o
1.92×10^6	0.433	**5°**	0.5^o

Table 5.2: Test cases for 2 bladed rotor in hover. (Experiments conducted by Caradonna and Tung [83])

1.143m. The aspect ratio of the blade is 6. At a vertical distance of 3m from the plane of the rotor disc, special ducting was provided in order to limit the recirculation of the wake inside the test chamber. The blades use a NACA0012 airfoil section along the entire span length. A pre-cone angle of 0.5^o was set for the blades. Of the different experiments conducted, table 5.2 shows the cases that were chosen for validation in the present study.

5.2.2 Grid and boundary conditions

For the computations, a two grid system was used, the boundaries of which are shown in fig. 5.12. A blade grid of C-O topology is embedded in a cylindrical background mesh. If the two blades are similar, the resulting flow-field can be assumed to be symmetric and hence periodic boundary conditions can be applied at the initial and final azimuthal planes, thus ensuring that only one blade (or *half* of the flow-field) need be modeled. The background grid is clustered in the region where the tip vortex wake is expected to evolve. This is seen in fig. 5.13, where a single azimuthal plane is shown. The dimensions of the background grid are $97 \times 151 \times 199$ in the azimuthal, radial and vertical directions respectively. The top and bottom boundaries are set at 1 and 2 rotor-radii respectively and the

outer boundary in the radial direction is at 2 rotor radii. The finest cross-stream cells in the background mesh correspond to squares of side 0.01c.

Figure 5.14 shows a schematic of the application of the periodic boundary condition. The flow-field variables are solved for in the planes $j = 4$ to $j = jmax - 3$. Since the 5 point WENO upwind scheme is used, 3 overlap planes are used at either boundary. The information for these planes are obtained from the interior of the flow field from the opposite boundary. For instance, $\mathbf{Q}_{j=1} = [\mathbf{T}]Q_{j=jmax-6}$, $\mathbf{Q}_{j=2} = [\mathbf{T}]Q_{j=jmax-5}$ etc, where, $\mathbf{Q}$ is the vector of conserved variables $(\rho, \rho\mathbf{V}, \rho e)$ and transformation matrix the $\mathbf{T}$ preserves scalars (density and energy) and rotates the momentum vector by an angle $\frac{2\pi}{Number\ \ of\ \ blades}$. At all the outer boundaries, the point-sink characteristic boundary condition is used (sec. 5.1.2). Simple extrapolation is used at the axis.

The outer boundaries of the blade grid extend to approximately 1 chord-length from the surface as shown in fig. 5.15. The corresponding hole-cut region of the background mesh is also evident in this figure. For the 12^o and 8^o cases, the returning tip vortex is sufficiently farther away (vertically) from the hole-cut region that it can be accurately resolved in the background grid (the "miss" distances are approximately around 0.5c). For these cases, a blade grid of dimension $199 \times 129 \times 111$ (in the wrap-around, spanwise and normal directions) was used. However, for the 5^o case, the vortex was found to *pass* much closer to the blade surface and the resulting interaction had to be resolved on the blade grid. For this reason, a much finer blade grid of dimensions $239 \times 169 \times 121$ was used. Further discussion on this grid will be provided in sec. 5.2.3. The normal spacing at the wall surface is set to $1 \times 10^{-5}c$, which results in $y^+ < 1$ at all near-blade locations.

5.2.3 Numerical Results

For all the computations, the 5th order WENO upwind scheme was used for discretization of the inviscid fluxes and second order central differencing is used for the viscous fluxes. The Spalart-Allmaras turbulence model with rotational correction is used for the RANS closure.

12^o and 8^o cases

Figure 5.16 shows the surface pressure distribution for the 12^o collective case using the original grid system and a coarse grid system that uses every other point in the cross-stream direction (resulting in one-fourth the number of total points). In these figures, the local streamwise velocity ($U(r)$) is used to normalize the pressure, *i.e.* $C_p = \frac{p-p_\infty}{0.5\rho_\infty U(r)^2}$, where, $U(r) = U_{tip}y/R$. It is seen that the fine grid solution compares well with the experimental measurements at all the radial locations. The coarse grid solution is noticeably poor in the inboard stations, which is possibly a result of the very coarse spacing in the spanwise direction. At the $y/R = 0.99$ station, (experimental measurements not available) the secondary suction peak due to the presence of the tip vortex is evident. The fact that this peak is lower in magnitude in the coarse grid result can be attributed to a more diffuse resolution of the tip vortex.

Figure 5.17 shows the blade pressures for the 8^o collective case (using the fine grid). Again, the results are of good quality except very close to the suction peak in the 80% and 89% span stations, where the agreement is off by slightly higher than 5%.

A good criterion for the identification of flow-field vortices is the so-called q criterion [148]. q is the second-invariant of the velocity gradient tensor and is

defined by $\frac{\partial u_i}{\partial x_j}\frac{\partial u_j}{\partial x_i}$. It can be shown that q is positive in highly vortical regions and is negative in highly strained regions of the flow. This becomes a very useful tool in visualizing vortex dominated flow-fields in that coherent structures can be identified with very little noise. Alternatively, if one relies on the total vorticity magnitude, features like boundary layers and wakes will be difficult to distinguish from tip vortices. Fig. 5.18 shows iso-surfaces of the q variable (non-dimensionalized by tip speed and chord), clearly showing coherent multiple passes of the tip vortex.

Figure 5.19 shows the computed velocity vectors along a sample streamwise plane. The multiple passes of the vortex are clearly visible. The quiescent conditions that exist outside the slipstream (outboard of the tip vortices) are evident. For reference purposes, the magnitude of the tip velocity is shown at the bottom right corner of the picture. This enables a comparison of the relative magnitudes and sense of the inflow velocities on the blade surface and downwash velocities in the planes below the blade surface.

Figure 5.20 shows the position of the vortex center compared to the curve-fitted experimental results. The accelerated downward convection after the first pass under the blade ($\psi = 180^o$) is well represented. This sudden increase in downward convection is the result of the downwash from the blade and the evolving tip vortex on the first passage of the vortex. Overall, the comparison is reasonable, except for the radial contraction of the wake at large wake age. The experimental results are seen to converge at 0.86 R, whereas the computational results were found to converge close to the momentum theory predicted $R/\sqrt{2}$. The asymptotic contraction in the experiment hints at possible recirculation effects. However, the downward convection agrees well with experiments for all

compared wake ages.

5^o case

As mentioned earlier in this section, in this case, the tip vortex was seen to pass close to the blade surface and as a result, had to be resolved within the blade mesh. The mesh points were refined off the surface in the normal direction and in the spanwise direction near the region of the first vortex passage. Figure 5.21 shows a wrap-around plane of the blade grid. The clustering in the spanwise and normal directions are evident. Figure 5.22 compares the computed pressure distribution on the blade surface with the experimental measurements. Again, good agreement is achieved with the experimental data, especially at the 89% spanwise station, which is directly above the first pass of the vortex.

Further evidence of the interaction of the vortex with the blade and its strength can be seen from fig. 5.23, in which the axial vorticity and vertical velocity are shown along a plane passing though the quarter chord position of the blade. The presence of the vortex is clearly seen to disturb the boundary layer vorticity (fig. 5.23a). Figure 5.23b shows that the vortex induces a significant amount of vertical velocity on the blade surface, which in turn would affect the effective angle of attack of the section. The fact that good agreement is seen in fig. 5.22d hints that adequate resolution is achieved.

Figure 5.24 shows the tip vortex trajectory and the effect of the blade on the vortex during the first passage. As the tip vortex is formed and trailed off the blade surface, there is no downward convection in the initial stages. As the vortex nears the blade for its first pass, the downward convection tapers off. When it is directly under the leading edge of the blade, the presence of

the blade downwash is seen to abruptly change the vortex position in such a way that the descent rate is increased very rapidly. Figure 5.25 compares the computed vortex position with curve-fitted experimental measurements. Again, reasonable agreement is achieved until slightly beyond the first pass, after which the experimental measurement reaches asymptotic contraction at 0.88R, whereas the computed wake contracts further.

Figure 5.26 compares the wake positions from the three different cases. Compared to the other cases, the 5^o case shows a much sharper change in downward convection at the first passage. In addition, the downward convection is seen to be accelerated even at the second pass ($\psi = 360^o$). Unlike the other cases, the 5^o case shows a slight tapering off of the vertical convection and radial contraction as the vortex approaches the blade. At the first blade passage, these quantities are seen to be accelerated.

In addition, the 5^o case shows significant waviness in its trajectory. A possible reason for this waviness could be because of the mutual interaction of the different turns of the wake. Figure 5.27 shows that the different turns are closer to each other compared to that of the 8^o and 12^o cases. In addition, the strength of the vortex is smaller and hence the vortical core is more susceptible to re-alignment.

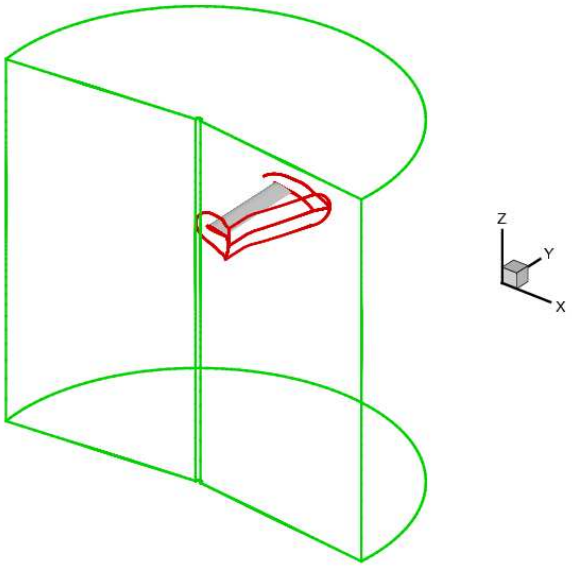

Figure 5.12: Blade and periodic background grid boundaries

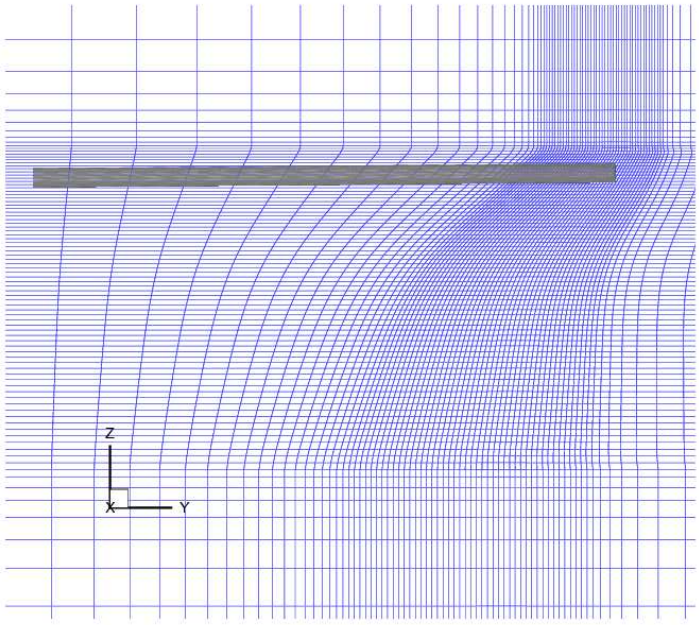

Figure 5.13: Azimuthal section of background grid (every other point in each direction)

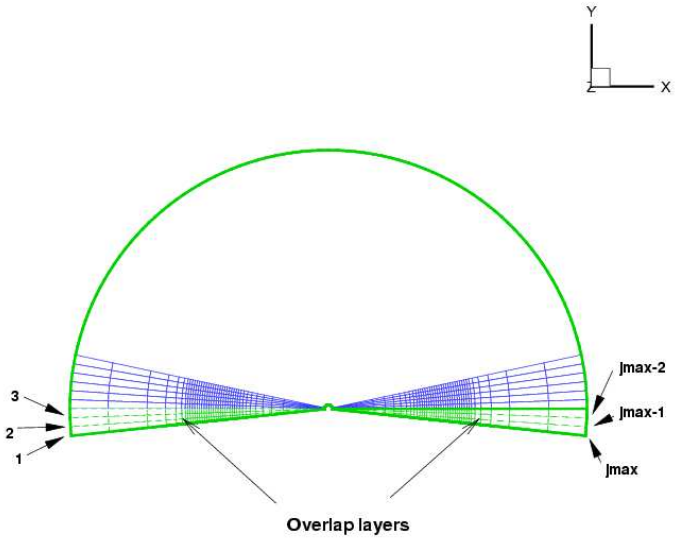

Figure 5.14: Schematic showing *overlap* planes for application of periodic boundary condition.

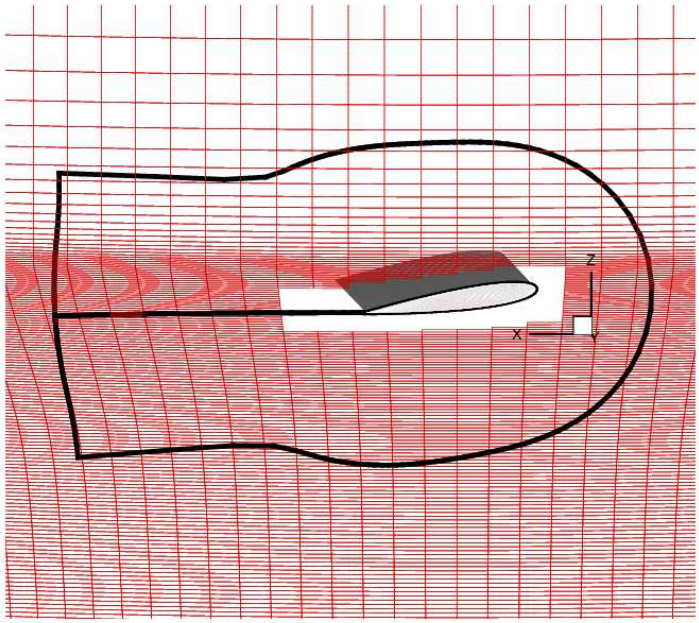

Figure 5.15: Radial section of background grid showing hole cutting

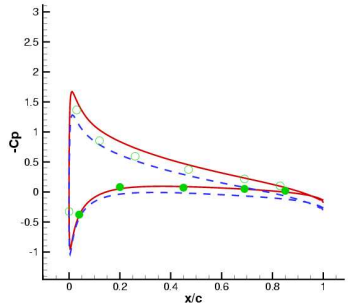

(a) $y/R = 0.5$

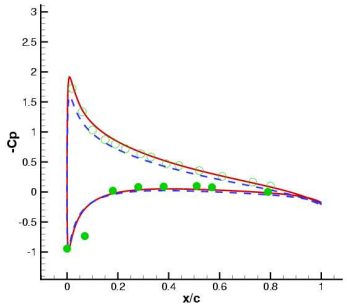

(b) $y/R = 0.65$

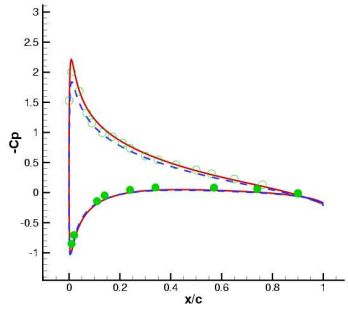

(c) $y/R = 0.80$

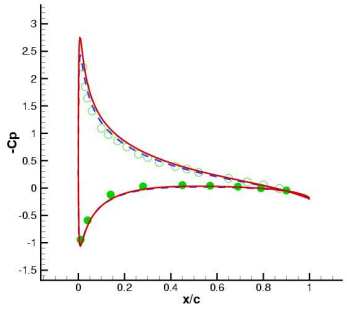

(d) $y/R = 0.89$

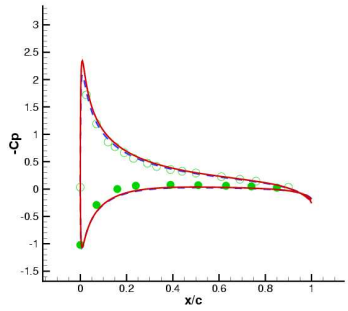

(e) $y/R = 0.96$

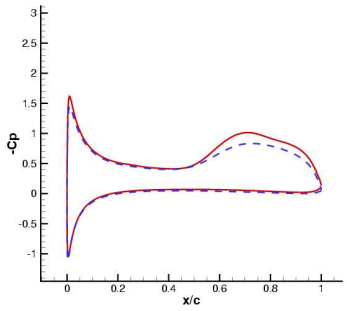

(f) $y/R = 0.99$

Figure 5.16: Comparison of computed blade surface pressure coefficient using Fine (solid lines) and Coarse (dashed lines) grids with experiment (Circles). for the 12^o collective case.

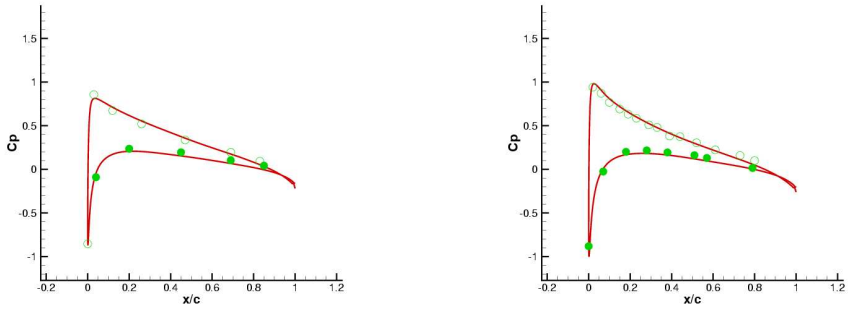

(a) $y/R = 0.5$

(b) $y/R = 0.65$

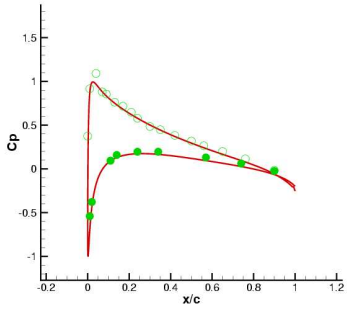

(c) $y/R = 0.80$

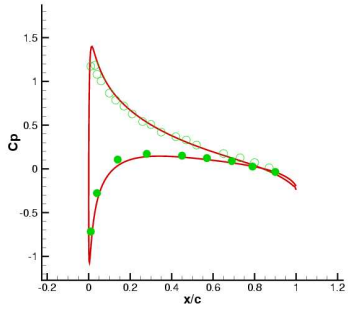

(d) $y/R = 0.89$

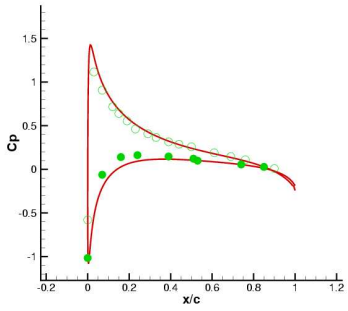

(e) $y/R = 0.96$

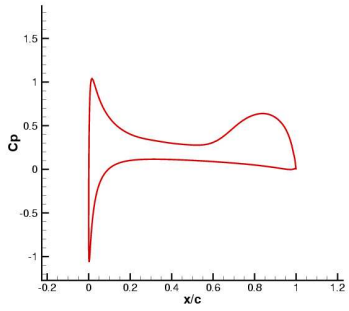

(f) $y/R = 0.99$

Figure 5.17: Comparison of computed blade surface pressure (lines) coefficient with experiment (circles) for the 8^o collective case.

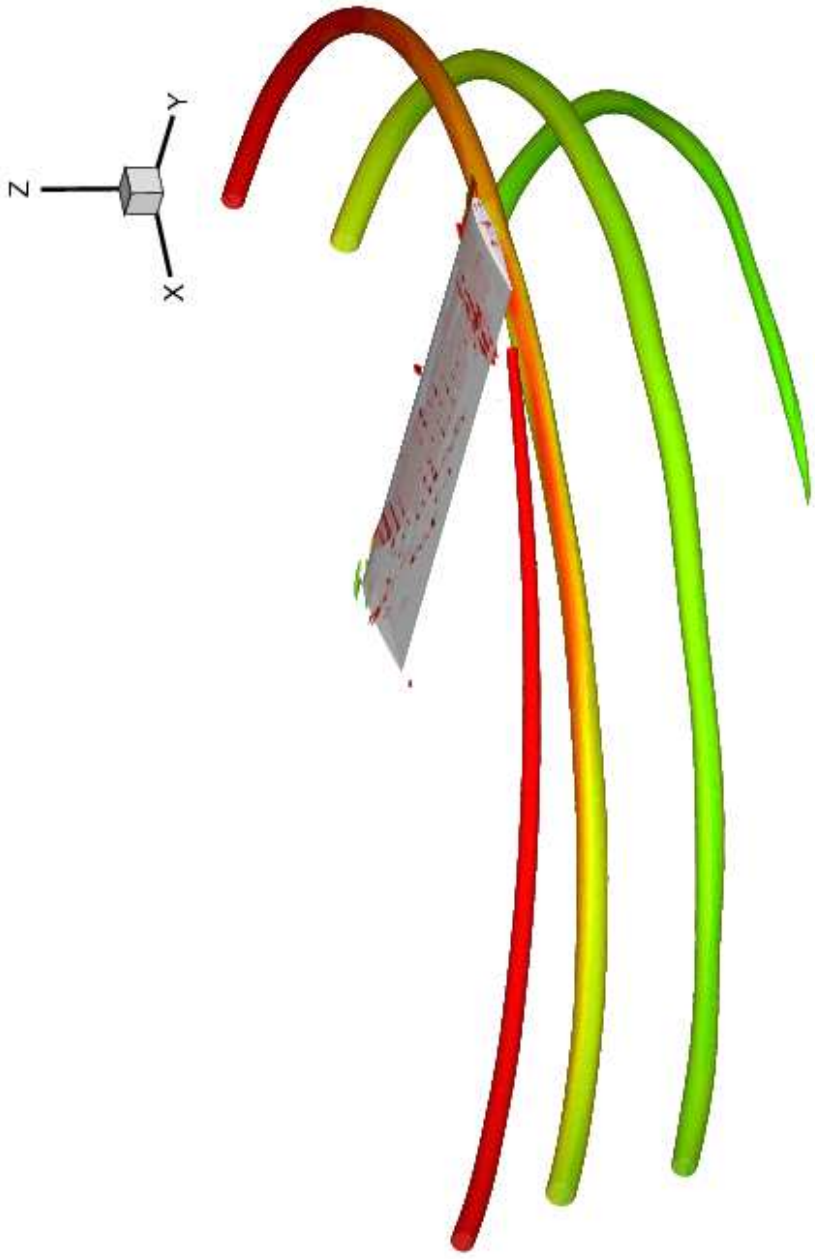

Figure 5.18: Iso-surfaces of $q = 0.5$ superimposed by vorticity contours showing tip vortex evolution for $\theta_0 = 8^o$

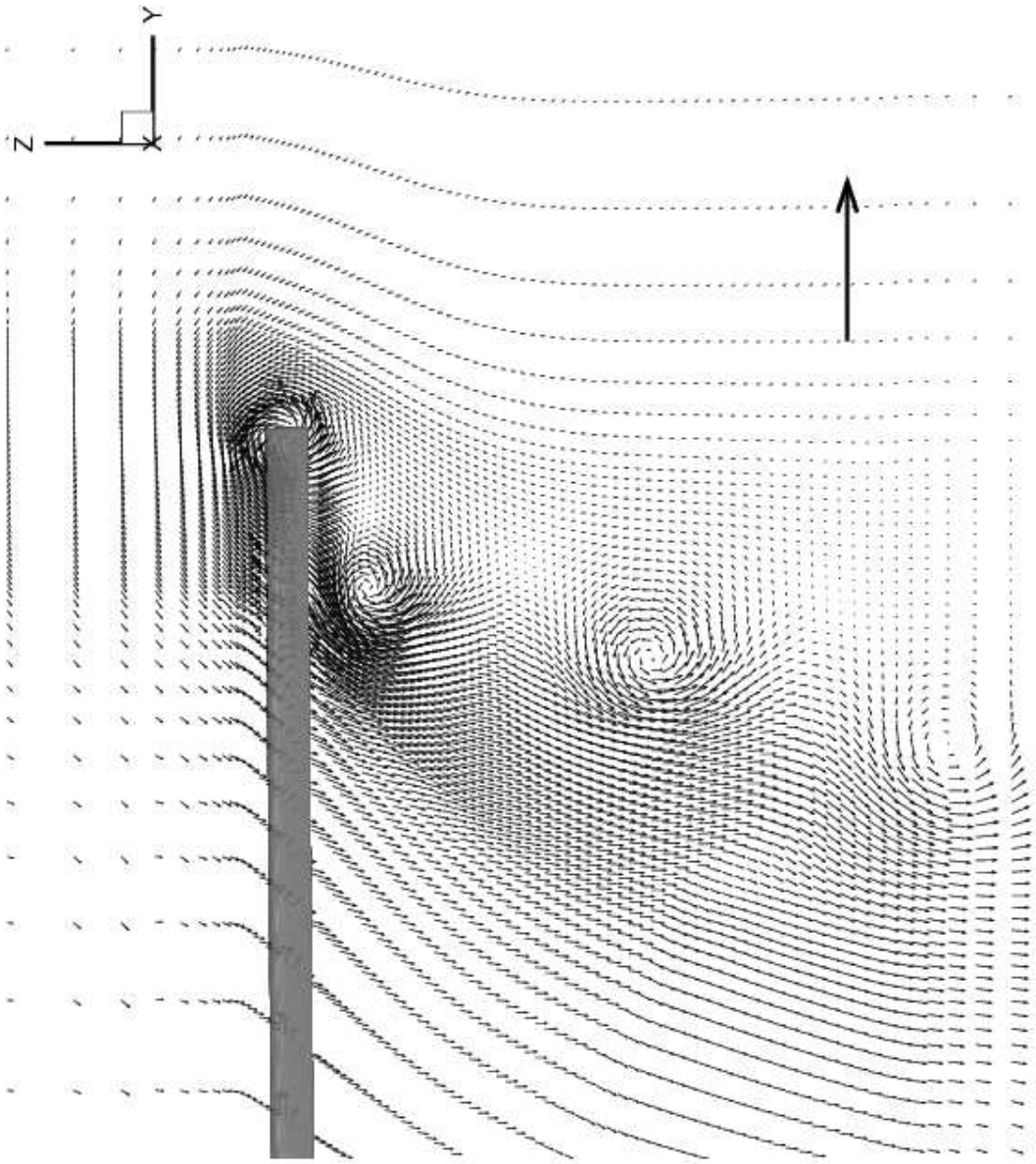

Figure 5.19: Velocity vectors across a streamwise plane passing though the quarter chord point for $\theta_0 = 8^o$

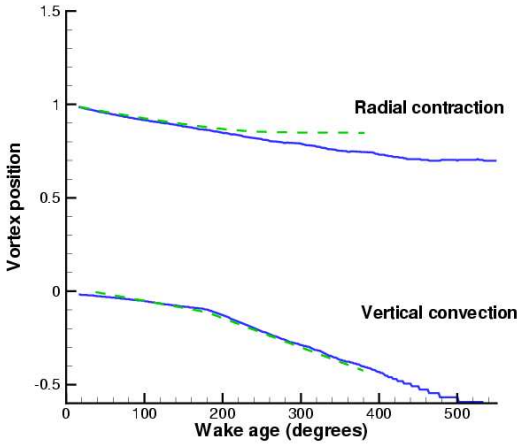

(a) $\theta_0 = 12^o$

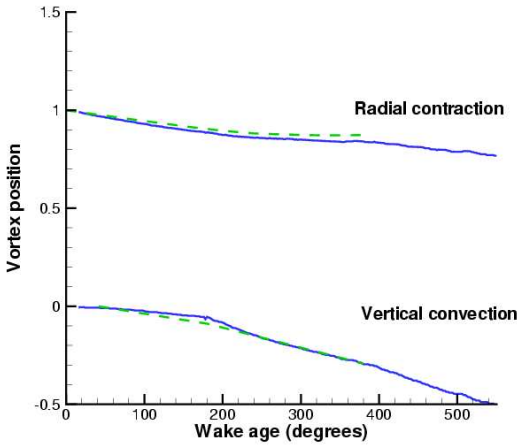

(b) $\theta_0 = 8^o$

Figure 5.20: Comparison of computed vortex center locations (solid lines) with curve-fitted experimental results (dashed lines).

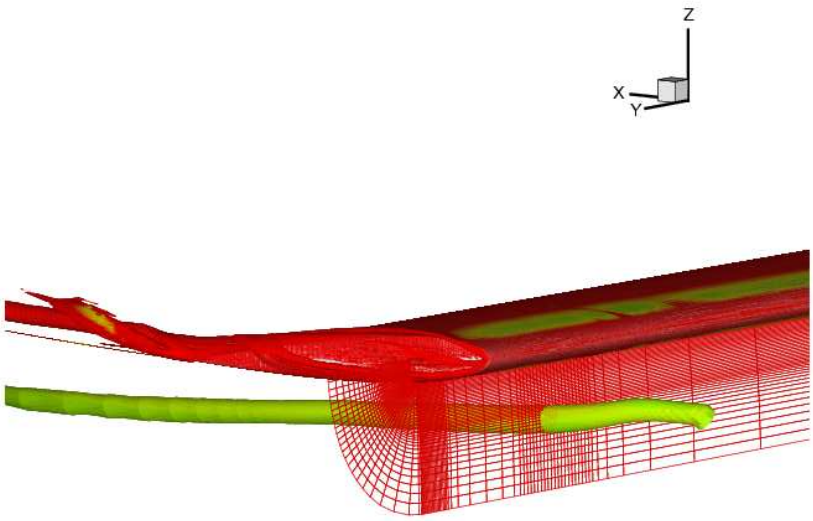

Figure 5.21: Sample wrap-around plane of the blade grid (every other point in each direction) for the $\theta_0 = 5^o$ case

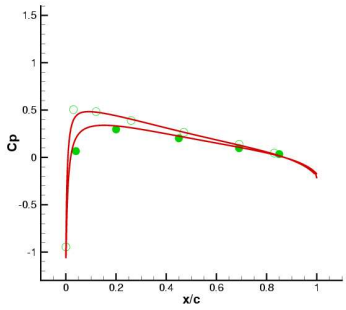

(a) $y/R = 0.5$

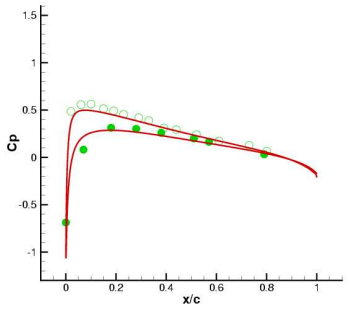

(b) $y/R = 0.65$

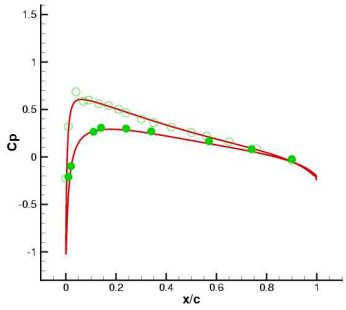

(c) $y/R = 0.80$

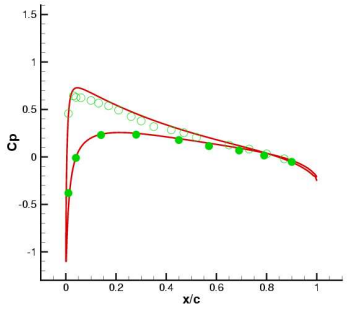

(d) $y/R = 0.89$

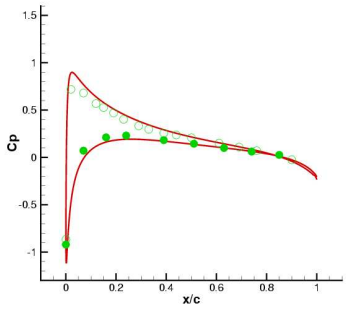

(e) $y/R = 0.96$

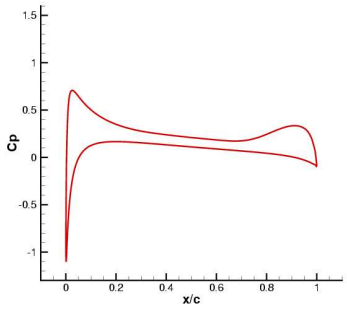

(f) $y/R = 0.99$

Figure 5.22: Comparison of computed blade surface pressure (lines) coefficient with experiment (circles) for the 5^o collective case.

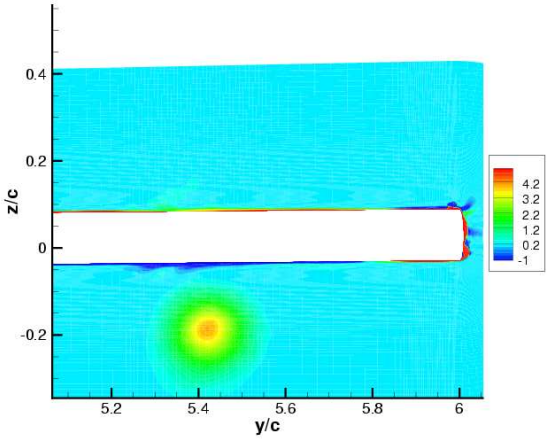

(a) Axial vorticity

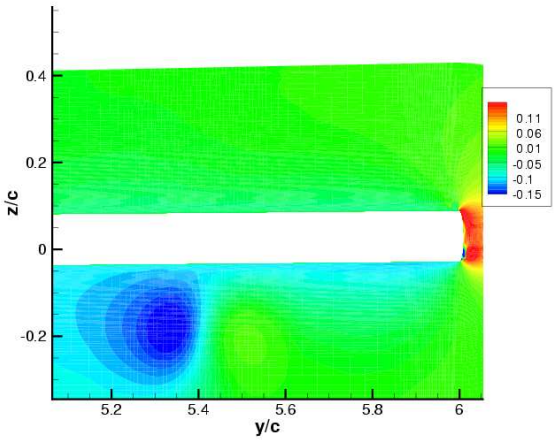

(b) Vertical velocity

Figure 5.23: First pass of vortex at quarter-chord section for $\theta_0 = 5^o$ showing perpendicular blade vortex interaction

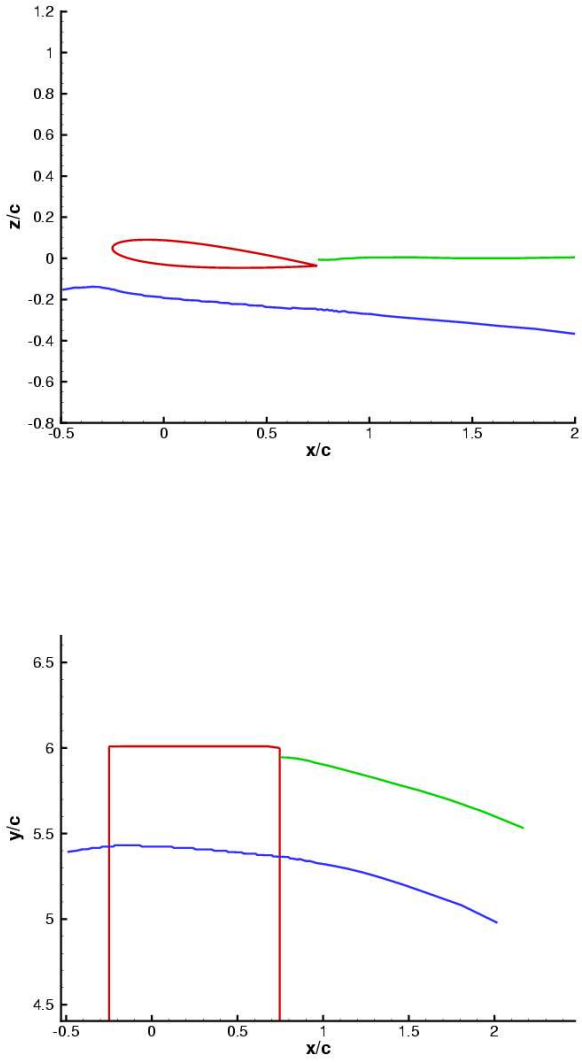

Figure 5.24: Computed near-blade vortex positions for $\theta_0 = 5^o$

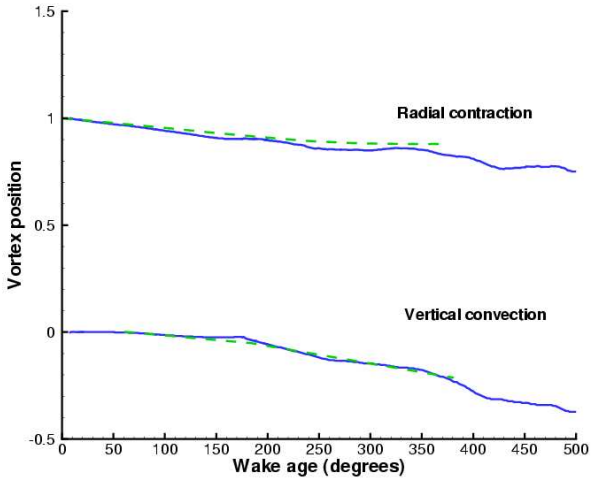

Figure 5.25: Comparison of computed vortex center locations (solid lines) with curve-fitted experimental results (dashed lines) for $\theta_0 = 5^o$

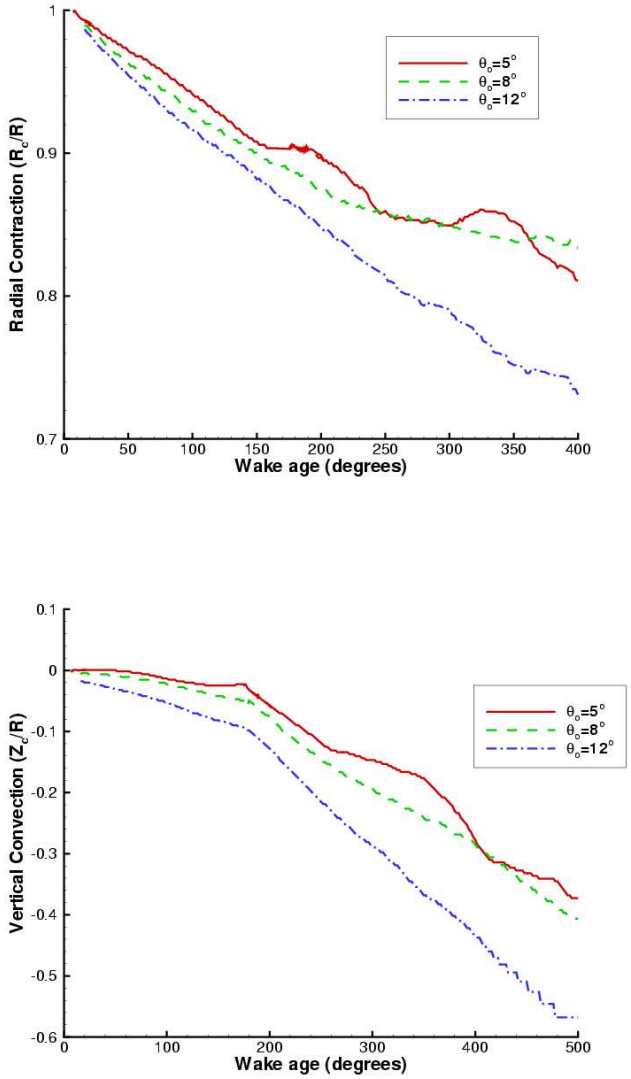

Figure 5.26: Comparison of vortex positions for different cases

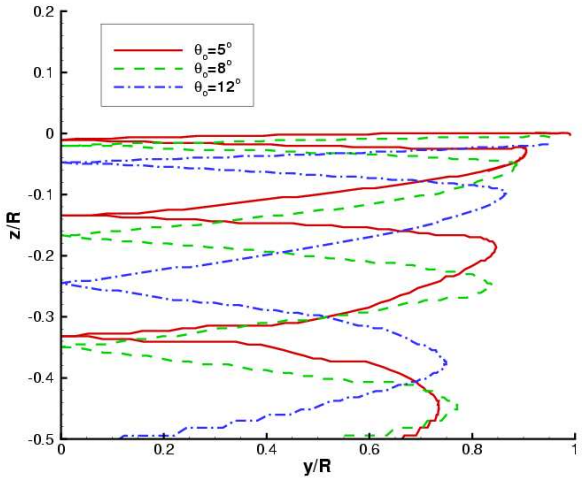

Figure 5.27: Comparison of computed vortex trajectory for different cases

Chapter 6

Tip Vortex Control

In this chapter, the effects of spanwise blowing as a possible tool for tip vortex control will be explored, using the fixed and rotary wing simulations of the previous chapters as baseline conditions. The physics associated with the spanwise blowing is addressed in detail. In addition, for the fixed wing test case, near-field experimental validation is presented for spanwise blowing.

6.1 Fixed wing vortex control

The experimental set up [146] for the spanwise blowing configuration is based on the conditions described in table 4.3. To provide spanwise blowing to the baseline configuration, provisions were made to supply compressed air to the tip via a plenum chamber located near the half-span location of the wing. The air exits along an elongated spanwise slot as shown in fig. 6.1. As shown in fig. 6.1b, the slot geometry is characterized by the length of the slot L, the thickness δ and the jet angle θ_{jet}. The rate of blowing is characterized by the mass blowing

coefficient, which is given by:

$$C_\mu = \frac{\hat{m}}{\rho_\infty U_\infty 2bc} \tag{6.1}$$

where, $\hat{m}$ is the integrated mass rate through the slot and b, c are the half-span and wing chord respectively (in this case, b=c=150mm).

The baseline (sec. 4.4) and blowing computations were carried out on the same grid, which ensured at least 12 points across the slot thickness and 85 points across the length. Modeling in the plenum chamber and the other internal details of the jet flow will prove to be extremely complicated and expensive and hence, the jet exit is modeled as a surface boundary condition. This wall boundary condition was described earlier (see eqn. 3.91 in sec. 3.10.2).

The different spanwise blowing simulations that were performed are detailed in table 6.1. For all cases, AR=1.0, $\alpha = 7.5^o$, $M_\infty = 0.1$ and $Re = 2.2 \times 10^5$.

Of these, C1 corresponds to an experimentally tested case and velocity measurements are available one chord downstream of the trailing edge. Numerical validation of the baseline case with no blowing was presented in Chapter 4.

6.1.1 Numerical results

Figure 6.2 compares the experimental measurements with the computed vertical and axial velocities along a horizontal line passing through the vortex center one chord downstream of the trailing edge. Akin to the baseline case (fig. 4.30), the computed velocities agree well with the experimental measurements.

The vortex structure at two downstream locations in the blowing case is compared with the baseline calculations in fig. 6.3. At $x/c = 1.0$, a reduced swirl velocity and a heightened axial velocity deficit is observed. The disruption

Case	δ/c	L/c	θ_{jet}	U_{jet}/U_∞	C_μ	C_L	C_D	L/D
Baseline	-	-	-	-	-	0.3398	0.03094	10.98
C1	1/150	0.8	0	0.866	0.00108	0.3542	0.0327	10.83
C2	1/150	0.8	0	0.375	0.00047	0.3465	0.0315	11.00
C3	1/150	0.8	0	0.188	0.00024	0.3431	0.0311	11.03
C4	1/150	0.8	15	0.866	0.00110	0.3538	0.0325	10.89
C5	1/150	0.8	-15	0.866	0.00110	0.3539	0.0326	10.83

Table 6.1: Comparison of different spanwise blowing cases. For all cases, the slit ends at $x/c = -0.17$ from the trailing edge

of the cross-flow sweeping across the wing tip caused by the spanwise jet results in weaker swirl velocities. Further, as will be explained, the spanwise blowing introduces turbulence directly in the vortical core and this results in strong decelerating forces, causing a larger axial momentum deficit compared to the baseline case. Equation 2.1.2 offers a physical explanation for the large axial velocity: The decelerating forces can be thought of as contributing to a larger loss of "head" ΔH. As opposed to the baseline case, the large axial velocity deficit in the control case at $x/c = 1.0$ would result in an unstable configuration according to the stability analysis presented in Chapter 2.

Figure 6.4 compares the evolution of the vortex properties for the baseline and blowing cases. The peak swirl velocity is seen to be lower for the blowing case initially and is also seen to decay at a more rapid rate. The heightened axial velocity deficit near the trailing edge is seen to taper off more rapidly compared to the baseline case, but the defect spreads over a much larger area as was observed earlier in fig. 6.3.

The turbulence generated by the jet predominantly arises from the counter-rotating vortex pair that exists at the jet exit as schematized in fig. 6.5.

The physical mechanism of spanwise blowing is illustrated in figs. 6.6 -6.8, in which axial vorticity contours are shown along various streamwise sections. As seen in fig. 6.6a, a counter-rotating vortex pair is formed at the jet exit. In this case, the upper vortex (CWJ) is in the positive sense (anti-clockwise) and co-rotates with the eventual tip vortex and the lower (CCWJ) one is in the "negative" sense. The presence of both these vortices is seen to disrupt the feeding sheet of vorticity. These vortices are formed (as schematized in fig. 6.5 by the roll-up of the vortex sheets at the top and bottom of the jet face. Figure 6.6b shows that the lower vortex is convected much faster to the top surface of the wing since it it not *shielded* from the cross-flow. The slower convection of the upper vortex also makes it roll up faster. As seen from fig. 6.6c, by the quarter-chord location, the upper vortex entrains vorticity from the feeding sheet and slowly develops into the tip vortex. The presence and strength of the tip vortex results in a secondary counter-rotating region of vorticity (SV), similar to that seen in the vortex formation studies (sec. 4.2). As seen from fig. 6.7, as the tip vortex evolves, entraining vorticity from the feeding sheet and the CWJ, its "edges" are seen to interact with the CCWJ and is hence weakened. The interaction with the CWJ and the SV also tends to "lift" the evolving tip vortex off the surface as seen in fig. 6.8a.

Beyond the downstream end of the jet, the large mass-rate of flow from the lower surface is seen to tilt the vorticity vector and severely affect the axial component of vorticity (the result is seen in fig. 6.8b). Remarkably, the rotational effects are strong enough that by 1 chord downstream of the trailing edge, the

tip vortex rolls-up into in a coherent form (fig. 6.8c). However, as compared to the baseline case and blowing case C2 (fig. 6.9), the vortex structure for case C1 is not entirely axisymmetric since there seems to be an interaction with a region of counter-rotating vorticity (blue patch inboard of the tip vortex in fig. 6.8c).

As mentioned earlier, the decelerating effects of the interactions and axial shear cause the large axial momentum deficit.

As seen in table 6.1, the blowing causes higher lift, evidently due to lower downwash velocities. Also, a larger drag force is noticed, which can be attributed to the high viscous losses and streamline disruption occurring during the interaction process.

Effect of jet velocity

Figure 6.10 shows the effect of blowing intensity on the vortex evolution. The reduction in swirl and axial velocities does not appear to be a linear function of the blowing intensity. As seen in table 6.1, the lower blowing rates actually result in a larger L/D efficiency, presumably due to the lower drag penalty.

Effect of jet exit angle

No significant differences in the vortex structure or lift and drag were noticed for the $\theta_{jet} = \pm 15^o$ jet angle cases compared to the $\theta_{jet} = 0$ case.

6.2 Rotary blade vortex control

The baseline configuration for the spanwise blowing was chosen to be the same as that presented in table 5.1. For the blowing cases, four slots on the wing tip,

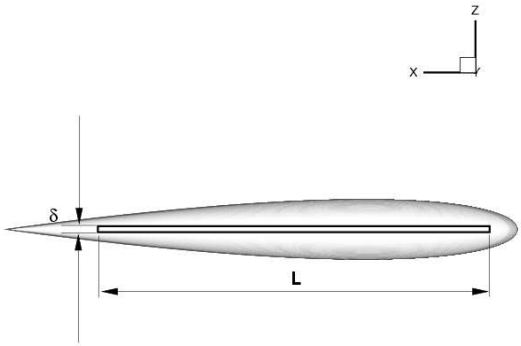

(a) Slot dimensions. (Slot at $\theta_{jet} = 0^o$)

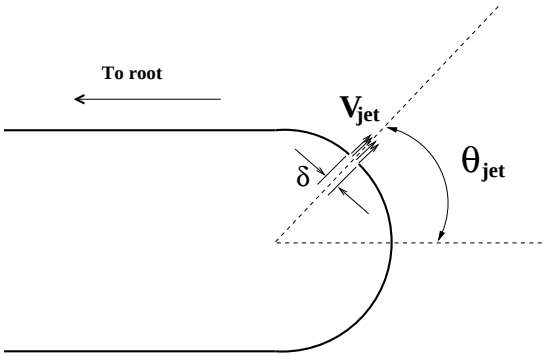

(b) Slot angle

Figure 6.1: Spanwise blowing slot geometry

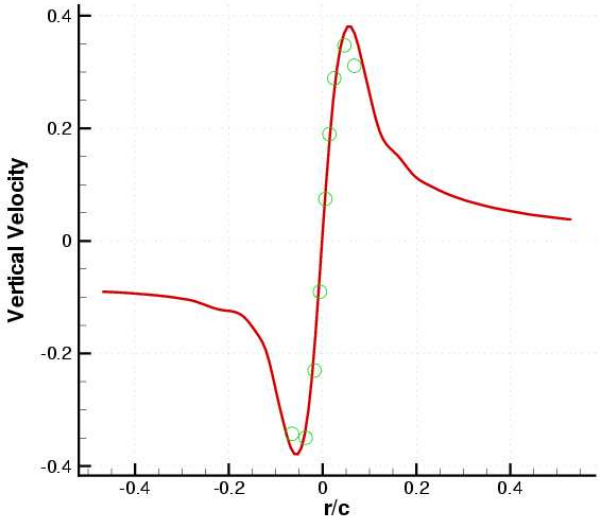

(a) Vertical velocity

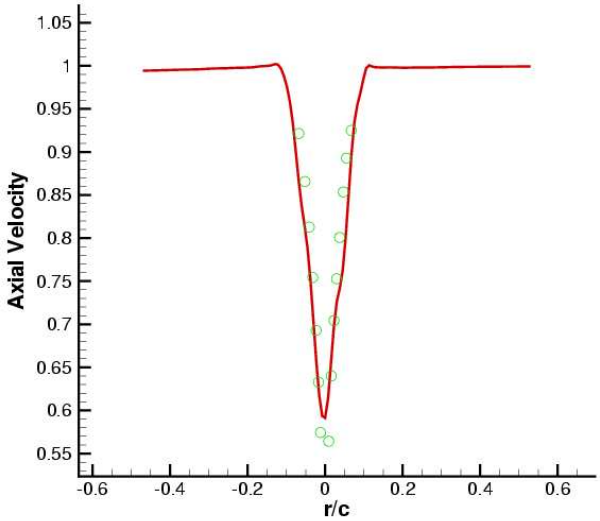

(b) Axial velocity

Figure 6.2: Comparison of computed velocity profile (line) with experiment (circles) at $x/c = 1.0$ for blowing case C1 ($C_\mu = 0.00108$).

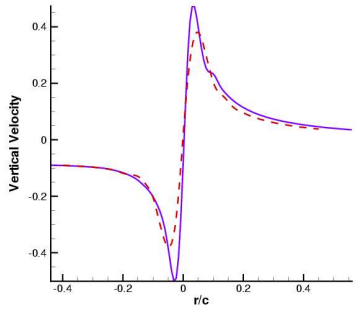

(a) Vertical velocity, $x/c = 1.0$

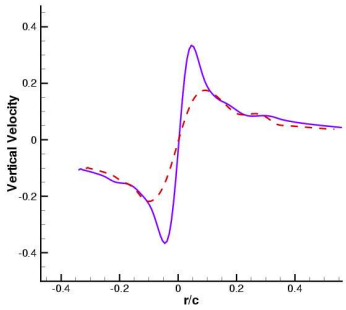

(b) Vertical velocity, $x/c = 10.0$

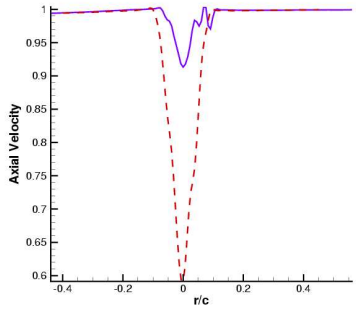

(c) Axial velocity, $x/c = 1.0$

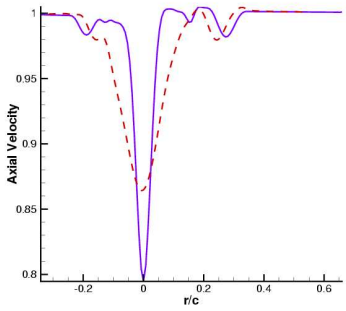

(d) Axial velocity, $x/c = 10.0$

Figure 6.3: Comparison of Baseline velocity profiles (solid lines) with blowing case C1 (dashed lines).

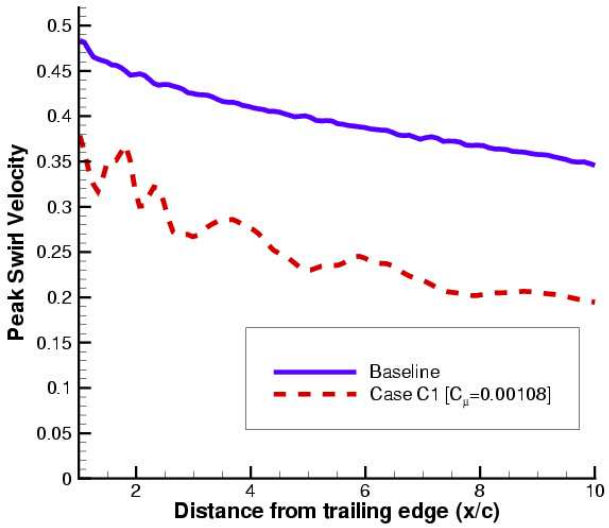

(a) Vertical velocity

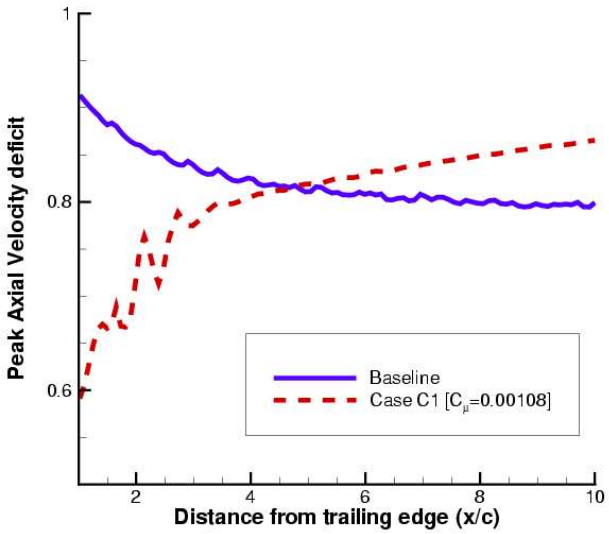

(b) Axial velocity

Figure 6.4: Comparison of Baseline vortex evolution with blowing case C1.

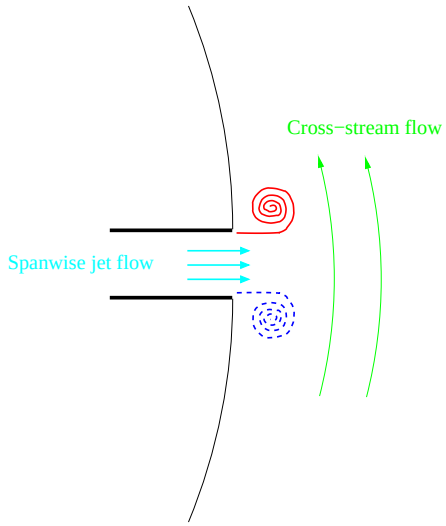

Figure 6.5: Schematic of formation of counter-rotating vortex pair in spanwise blowing.

each approximately of breadth 0.04c and average length 0.07c were used. This configuration was chosen because it resembles the blowing experimental setup of Han et. al. [111]. In their experiment, 4 circular slots of diameter $0.067c$ were used and hence both configurations approximately have the same exit areas. The slot placement was also roughly similar. In the experiment, the inlet of the slots was at the leading edge and hence the internal flow was driven by the dynamic pressure gradient between the slot inlet and exit. In the present computations, the effect of the slot is modeled as a surface boundary condition and the slot exit velocity was prescribed. Hence, the computations do not exactly correspond to the experiment and hence one-to-one comparisons will not be made. It is worth mentioning that the experiment was able to demonstrate upto 50% reduction in swirl velocity within a wake-age of 90^o.

The summary of the blowing simulations is given in table 6.2. Figure 6.11 shows the location of the slots along with velocity vectors in two axial planes.

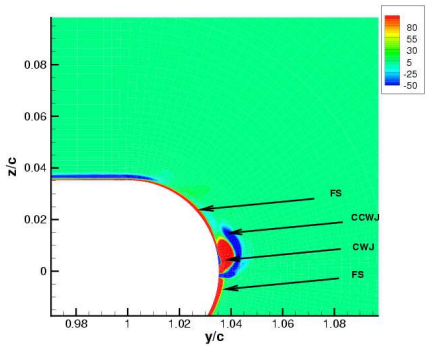

(a) $x/c = -0.95$

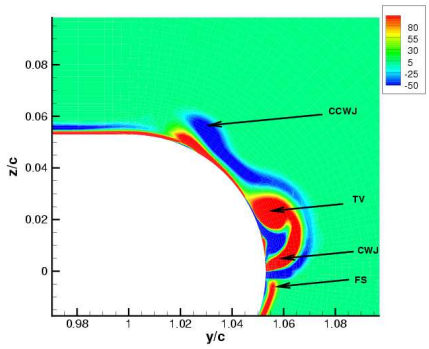

(b) $x/c = -0.85$

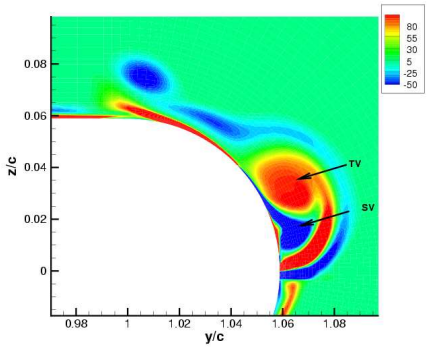

(c) $x/c = -0.75$

Figure 6.6: Axial vorticity evolution for blowing case C1. FS: Feeding sheet, CWJ: Clockwise vorticity from spanwise jet, CCWJ: Counter clockwise vorticity from spanwise jet, TV: Tip vortex, SV: Secondary vortex (Counter-rotating to TV).

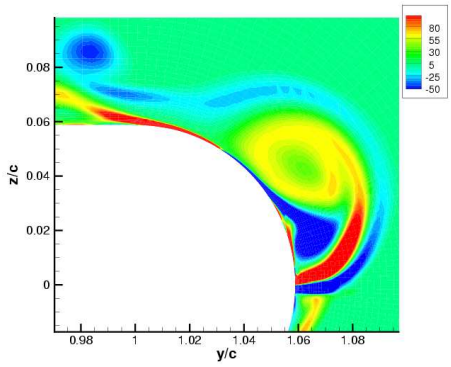

(a) $x/c = -0.65$

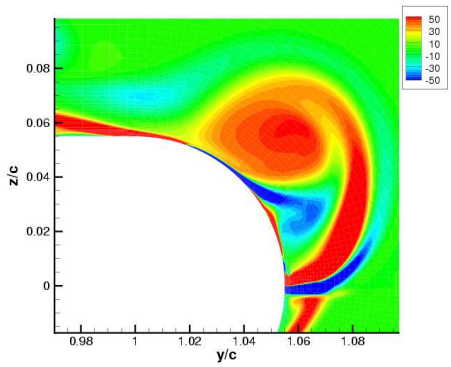

(b) $x/c = -0.55$

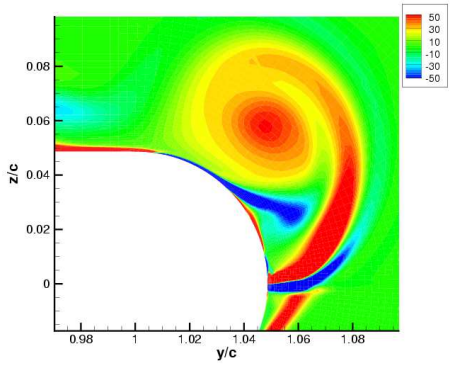

(c) $x/c = -0.45$

Figure 6.7: Axial vorticity evolution for blowing case C1.

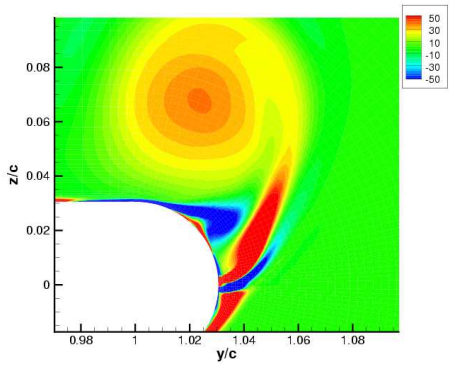

(a) $x/c = -0.25$

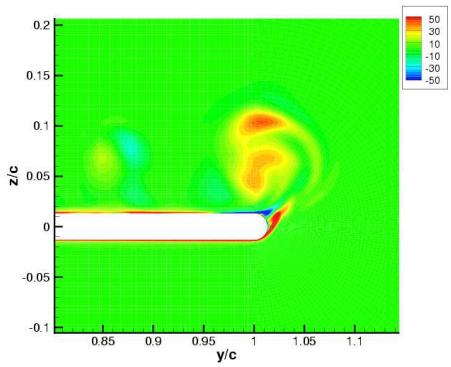

(b) $x/c = -0.10$

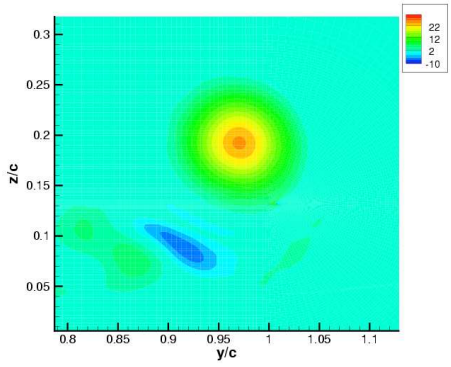

(c) $x/c = 1.0$

Figure 6.8: Axial vorticity evolution for blowing case C1.

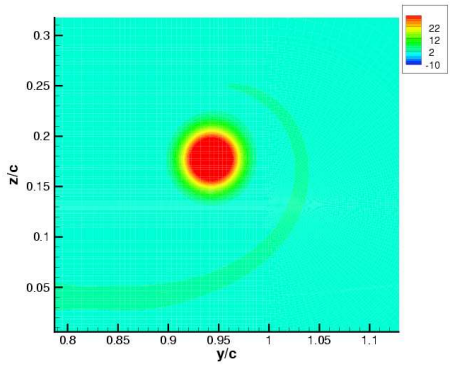

(a) Baseline

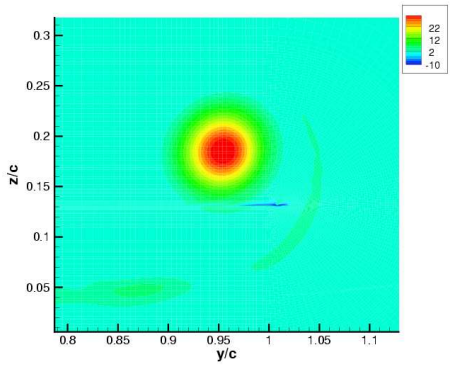

(b) Blowing case C2

Figure 6.9: Axial vorticity contours for baseline case and blowing case C2 at $x/c = 1.0$.

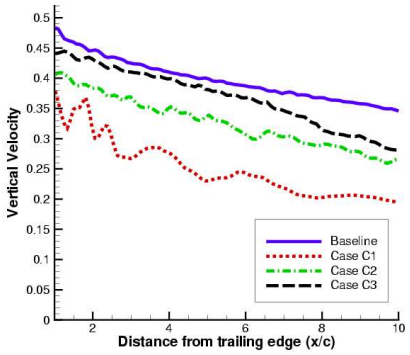

(a) Peak Swirl velocity

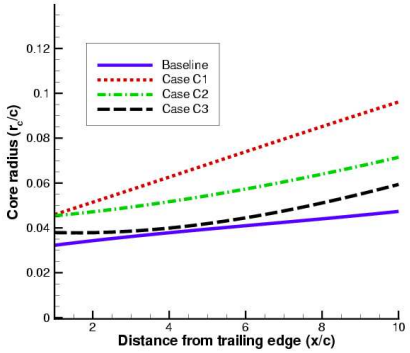

(b) Core radius (Curve-fit)

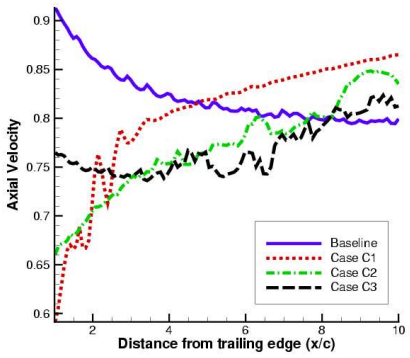

(c) Peak axial velocity deficit

Figure 6.10: Effect of jet velocity on vortex evolution

Case	U_{jet}/U_{tip}	C_μ	C_T	FM
Baseline	-	-	0.00195	0.302
C1	0.025	0.00014	0.00192	0.294
C2	0.05	0.00027	0.00187	0.283
C3	0.1	0.0005	0.00182	0.274
C4	0.2	0.0011	0.00174	0.268

Table 6.2: Comparison of different spanwise blowing cases for the hovering rotor.

The resulting streamlines (not shown) were found to be clearly distorted as a result of the spanwise blowing. The velocity vector plots correspond to blowing case C3. The blowing from the slots appear to serve as effective *riblets* and the flow seems to be accelerated in the region between the slots. When this accelerated flow encounters the mainly streamwise flow on the upper-surface of the wing, large scale mixing occurs and one can expect increased turbulent diffusion. As mentioned earlier in the paper, the separated boundary layer at the tip also contributes to the mixing process. The resulting axial velocity shows a very high deficit, which can be directly attributed to the diffusion process described in sec. 6.1.1.

The large axial velocity deficit also cause a re-orientation of the vorticity in the trailing vortex. This is made clear in the vorticity contour plots shown in fig. 6.12. Consider the baseline case: fig. 6.12a, 6.12c show that the vorticity vector is mainly oriented in the streamwise direction and the magnitude is nominally axisymmetric. In the spanwise blowing case, as seen from fig. 6.12b,d show that the spanwise component is significant and more importantly, asymmetric. The calculated shear strain rates were also high in this case and these two factors

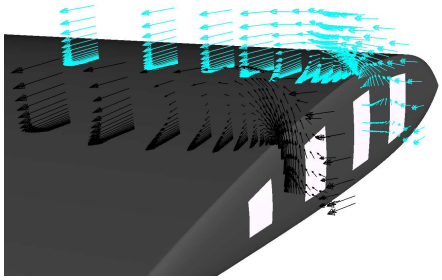

Figure 6.11: Velocity vectors near blade surface for spanwise blowing case (reference frame attached to the blade). Slot locations shown in white.

can result in increased molecular and turbulent diffusion in the core. Figure 6.13 shows the evolution of the vortex properties for different blowing configurations. Similar to the fixed wing cases, no linear relationships were found between the blowing velocity and the reduction in vortex strengths. Figure 6.14 compares sample velocity profiles at a wake-age of 295^o.

As seen in table 6.2, the loss in performance in terms of thrust and figure of merit is not significant compared to the achieved reduction in vortex strength. Hence, spanwise blowing appears to be a promising concept for vortex control.

6.3 Summary

In this chapter, the effect of spanwise tip blowing was studied on the formation and development of tip vortices from a fixed wing and a rotary blade. The physics of vortex formation was found to be complicated. The feeding vortex sheet from the trailing was observed to heavily interact with a pair of counter-rotating vortices that originated at the jet exit, resulting in a diffuse vortex compared to the baseline cases with no blowing. The computations suggest that

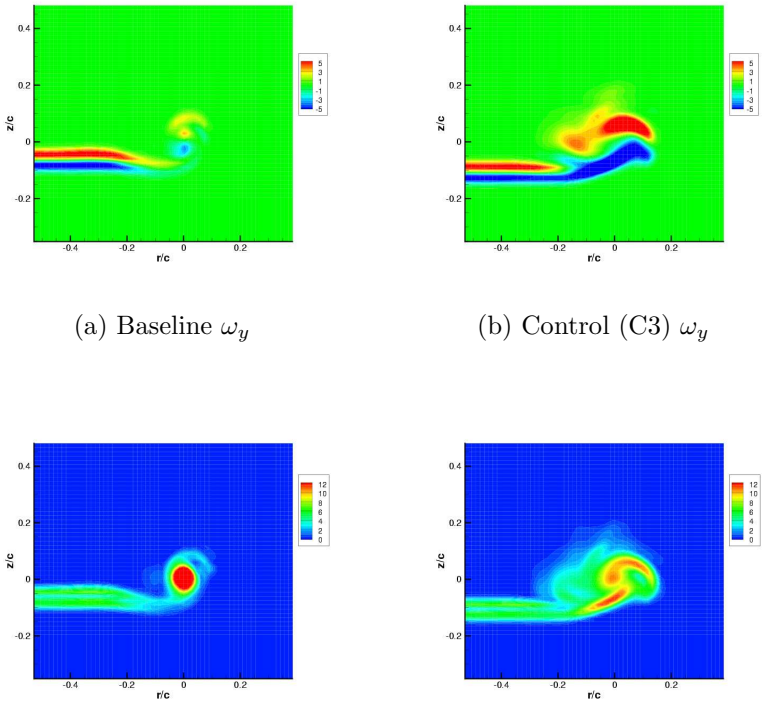

(a) Baseline ω_y

(b) Control (C3) ω_y

(c) Baseline $|\omega|$

(d) Control (C3) $|\omega|$

Figure 6.12: Spanwise and total vorticity contours at $\psi = 3^o$ for baseline and blowing cases

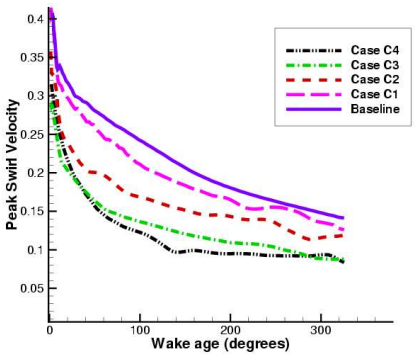

(a) Swirl velocity

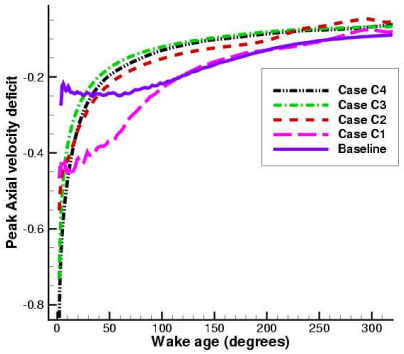

(b) Axial velocity

Figure 6.13: Evolution of vortex properties for different spanwise blowing cases

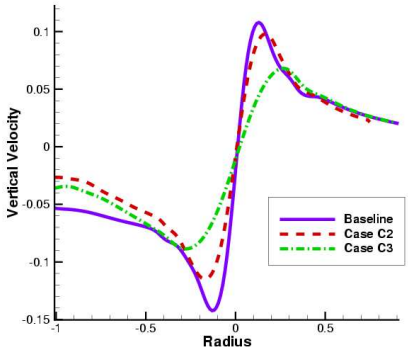

(a) Vertical velocity

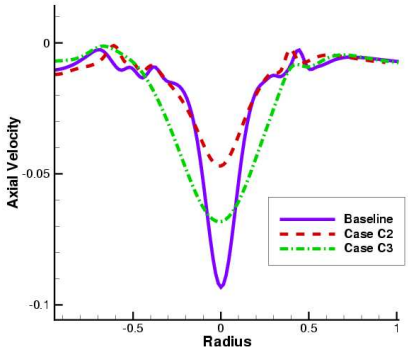

(b) Axial velocity

Figure 6.14: Vortex velocity profiles at $\psi = 295^o$ for different spanwise blowing cases

this concept holds promise in tip vortex alleviation. However, a myriad of issues remain:

- The bleeding mechanism was not addressed and the jet exit was modeled as a surface boundary condition. Though bleeding from the leading edge has been accomplished experimentally [111], the mass flow rate has not been determined and hence, it remains to be seen whether the current requirements are practical.

- As with any RANS calculation, without extensive experimental data, the fidelity of the turbulence model is always an unknown factor. Although the computations compared well with the experimental measurements downstream of the trailing edge, a more detailed validation of the vortex formation process is required to develop full confidence in the methodology. However, the inavailability of experimental data serves to be a hindrance.

- As a result of the problem size, it was not possible to make detailed grid refinement studies for the blowing cases.

Chapter 7

Closure

A detailed understanding of tip vortices and trailed wakes in general is imperative in the design of efficient Aerospace vehicles. The RANS equations represent the highest level of fluid dynamic approximation that is currently feasible in the simulation of high Reynolds number flows. However, practical RANS simulations of tip vortex formation and evolution suffer from:

a) Numerical diffusion, which arises primarily from inaccuracies in the discretization of the convective term in the NS equations, and

b) Inaccurate turbulence modeling, which is a result of the inavailability of a perfect closure model to the RANS equations.

In this thesis, the error due to numerical diffusion is reduced by the use of proper grid resolution (by means of grid clustering and overset meshes) and high order accurate numerical schemes. None of the available turbulence models are accurate or efficient enough to completely describe the complex tip vortex flow-field, but reliable solutions were found to be obtained by adding a simple correction to the production term in the Spalart-Allmaras turbulence model. Using a systematic approach, a wide variety of experimental test cases were sim-

ulated and validated with measured data. The fidelity of the approach allowed for a detailed study of the underlying physics of vortex formation and evolution. In addition, a strategy of vortex control, namely, spanwise blowing was evaluated within the framework of the methodology. The simulation studies are supplemented by simplified theoretical studies of axisymmetric vortices and their stability that are aimed at furthering the understanding of vortex-dominated flow-fields.

7.1 Key observations and conclusions

7.1.1 Theoretical studies of tip vortices

A linear stability analysis was performed on axisymmetric parallel swirling flow with axial velocity.

• For realistic tip vortices, the presence of the swirl was observed to act as a stabilizing influence. The stability characteristics were seen to be largely insensitive to changes in the swirl velocity profile outside the vortical core.

• The presence of axial velocity was confirmed to be a destabilizing influence and the instability modes were found to be highly sensitive to the magnitude and gradient of axial velocity in the core region.

7.1.2 Theoretical numerical studies

A theoretical study was conducted on the accuracy of spatial discretization of the first and second derivatives using Fourier-stability analysis. The novelty of this analysis is that it was extended to the study of discretization errors on geometrically stretched meshes. Based on this analysis, the following conclusions

were drawn:

• On a uniform mesh, the use of fifth or higher order accurate schemes for the first derivative guaranteed an error of less than 0.1% when at least 10 points are used per wavelength of discretization.

• When "stretched" meshes are used, the accuracy was seen to deteriorate and all the schemes formally become first order accurate. However, for moderate stretching ratios (less than 10% stretching), higher order schemes were seen to give reasonable accuracy using $O(10)$ points per wavelength.

• When tested on an idealized inviscid vortex convection problem, fifth and higher order schemes were found to be maintain the vortex structure and peak-to-peak velocity within 0.1% error for long convection times when around 10 points were used per core-length of discretization.

The above-mentioned facts were used as guidelines in mesh resolution in the more complex 3D simulations. For all the calculations presented, the finest grids used $10 - 25$ points per core-length of the tip vortex. Further, in the region of tip vortex formation and evolution, the fine mesh spacing was maintained along with very small (or no) stretching in the cross-stream directions.

7.1.3 Near-field fixed wing vortex formation studies

Initial near-field validation studies were performed on a low aspect ratio round tip NACA 0012 wing in a wind tunnel. For this case,

• Good agreement was achieved with experimental measurement for surface pressure, swirl and axial velocities as well as other overall qualitative flow features.

• Though the magnitude of the primary Reynolds shear stress was predicted

reasonably, the phasing of these terms was different compared to the measurements, a fact that can be attributed to the isotropy of the turbulence model.

• The use of high order schemes (for the inviscid terms) was seen to be critical to reduce numerical dissipation for the grids that were used. A simple modification to the production term of the turbulence model was required to correctly represent the vortex evolution downstream of the trailing edge.

Once a measure of confidence was achieved with the methodology, the physics of vortex formation was explored in detail. This study showed that

• Streamwise-oriented vorticity is developed by a *feeding sheet* comprised of the cross-flow boundary layer. Initial evidence of the tip vortex is seen when this boundary layer separates from the surface. The roll-up of this separated boundary layer forms a system of vortices, which rapidly merge into a single coherent vortex.

• The use of a thinner airfoil section caused advanced cross-flow separation as a result of the heightened spanwise pressure gradients. This causes a lifting-off of the feeding vortex sheet from the wing surface and as a result, the tip vortex was observed to roll up rapidly.

• At lower Reynolds numbers, the larger viscous deceleration resulted in a more diffuse vortex with lower swirl and axial velocities.

• When a flat tip shape was used, the cross-flow separation point was seen to be fixed by the geometry (at either edge) and as a result, the tip vortex was more diffuse.

The studies up to this point concentrated on vortex formation. In order to study vortex evolution in the extended near-field, a highly refined overset mesh was added behind the trailing edge of a fixed wing, with the axis of the mesh

aligned in the free-stream direction.

• With a uniform cross-stream spacing that resulted in 10-15 points per core-length and a fifth order scheme, good agreement with experimental data was achieved 1 chord downstream of the trailing edge and further downstream, the decay was minimal.

7.1.4 Rotary blade studies

Using cylindrical background grids, single and two bladed hovering rotor systems were studied.

• For the computations on the single bladed rotor, fair agreement was achieved with the experimental swirl velocity measurements upto 300^o of wake evolution behind the trailing edge.

• For the 2 bladed rotor, the tip vortex could be tracked upto *4 rotor revolutions* behind the trailing edge. Comparisons with experimental surface pressure measurements and vortex trajectory data established the accuracy and fidelity of the methodology.

• With the use of appropriately refined meshes, the interaction of the blade with the first vortex passage was found to be sufficiently resolved.

7.1.5 Vortex control

Finally, the effect of spanwise tip blowing was studied on a fixed wing and a hovering rotor. The jet exit was modeled as a surface boundary condition.

• For a fixed wing, numerical validation of spanwise blowing with experimental velocity profile measurements showed excellent agreement.

• The effect of spanwise blowing was to reduce the magnitude and development of the axial and tangential momentum. The mechanism behind this effect appears to be the interaction of a pair of counter-rotating vortices generated at the jet exit with the feeding sheet of vorticity. The resulting tip vortex was found to be much more diffuse compared to the baseline case with no blowing.

• Using moderate blowing ratios upto 30% reduction in peak swirl velocity was seen to be achieved in both the fixed and rotary wing cases with a marginal performance penalty. Although the details of the internal jet flow were not addressed, results suggest that concept holds promise as an effective vortex control strategy.

Overall, *the level of agreement of the computed quantities with the experimental measurements suggests that the methodology will prove to be a useful tool in understanding tip vortex flow-fields.* This level of consistent performance has not been demonstrated before over such a variety of test cases. Further, the validations span a wide range of chord ($Re = 2.2\times10^5 - 4.6\times10^6$) and vortex Reynolds numbers ($Re_v \approx 0.8 \times 10^5 - 2 \times 10^6$). As mentioned in the introduction, comparisons of computed vortex structure with experimental measurements beyond a few chord lengths downstream of the trailing edge are lacking in the literature.

In addition to the validation studies, the fidelity of the methodology enabled a detailed study of the underlying flow physics. In a broad sense, the developed methodology and the lessons learnt in the process can be used as guidelines to evaluate future implementations of algorithms and turbulence models that can more accurately and/or efficiently compute the flow-field around general lifting surfaces.

7.2 Recommendations for future work

The computational results presented in this thesis represent some of the best available RANS-based validation studies with experiments. However, there is tremendous scope for improvement in many aspects of the methodology and incentive for potential applications.

7.2.1 Methodology

• The extremely complicated nature of the flow, especially during the vortex formation is a prime example of non-equilibrium[1] flow. In addition, anisotropic effects also seem to be important. Current day RANS models, especially linear eddy viscosity-based models, are not advanced enough to comprehensively address these issues. Therefore, a primary suggestion for the continuation of this work would be to use the same methodology, but with more advanced turbulence models such as the so-called Second Moment Closure models, which, in theory, should be able to represent the turbulent effects better.

• At present, the evaluation of the viscous fluxes is second-order, whereas the inviscid fluxes are computed to much higher order of accuracy. Even though the flow-field is dominated by inertial forces as a consequence of the high Reynolds number, a higher order viscous discretization can be expected to improve the overall accuracy of the flow solver.

• In its present state, run-times for large problems like the hovering rotor exceed many hundreds of CPU hours (refer Appendix C for further information).

[1] Non-equilibrium boundary layers are characterized by multiple length scales and/or a significant imbalance between production and dissipation.

Hence, parallel processing capability would be invaluable in reducing the runtime.

• The interpolation across the overset meshes is not guaranteed to be conservative. This could affect the solution accuracy especially if information is passed across high gradient regions such as the vortex/blade mesh interface. A more rigorous approach could involve matching fluxes across the interface, thus assuring global conservativeness.

7.2.2 Applications

• All the studies in this work have focused on simple wing/blade sections and planforms. A wing in a practical set up, for instance would be more complicated in that a system of flaps/slats or other high-lift devices might be present. In such a case, the bound circulation distribution would be completely different and would significantly affect the vortex formation and wake roll-up, with multiple vortex structures. A possible extension of this work could involve such an application.

• The present rotor calculations involved hovering flight in which the blade mesh was fixed in reference to the background mesh. Under forward flight conditions, the relative motion of the meshes introduces extra complications like dynamic hole-cutting. In addition, efficient time integration schemes have to be designed. The present methodology is general enough to be extended to such applications.

• For the blowing configuration, the bleeding mechanism was not addressed and the jet exit was modeled as a surface boundary condition. Though bleeding from the leading edge has been accomplished experimentally [111], the mass

flow rate has not been determined and hence, it remains to be seen whether the current requirements are practical. A more detailed study could involve using overset meshes to model the internal details of the slot, thus removing the uncertainty of the achievable mass rate of flow.

Appendix A

Resolution Requirements for Various Numerical Simulations

In this section, a *very rough* estimate of the resolution required by various levels of fluid dynamic approximations will be presented. These estimates are purely for demonstrative purposes and are not meant to be used as guidelines for simulations. Computations of the tip vortex of a sample aircraft wing of aspect ratio 10 operating at a Reynolds number of 5×10^6 will be considered.

The spatial extent of the computational domain beyond the trailing edge will be assumed to be 5 span lengths, allowing for complete development of the tip vortex. The domain will be split into two regions:

- The near-wall region that includes the boundary layers and extends to atleast 1 chord length away from the surface, giving a domain volume of dimension $10c \times 1c \times 1c = 10c^3$.

- The wake region that starts from the trailing edge of the wing and extends to a streamwise distance of 5 span lengths, giving a domain volume of dimension $2c \times 2c \times 50c = 200c^3$. (It is further assumed that the wing boundary layer is not important in the wake region and the vortex will be resolved within a cross

stream box of dimension $2c \times 2c$.)

The characteristic length scale of the body (L) is taken to be the wing chord (c).

Direct Numerical Simulations (DNS)

For DNS, the total number of points for a unit cube of side c is $(L/\eta)^3 \approx Re^{9/4}$. Therefore the total number of points required is $\approx 210Re^{9/4}$. The number of time-steps to compute the flow in a unit cube is $\approx Re^{3/4}$. Therefore, to convect 50 chord lengths of travel and assuming atleast 10 periods to obtain the time averaged data, the total number of time steps $\approx 500Re^{3/4}$. Hence the total operation count (No. of grid points times the number of time steps) is $10^5 Re^3 \approx 10^{25}$.

Note: The estimates are based solely on Kolmogorov scales and can be found in any text on turbulent flow such as [19].

Large Eddy Simulation (LES)

For LES, in order to resolve the small dynamic eddies in the near-wall region, the minimum cell sizes are required to be atleast 100 wall units in the streamwise direction, 20 wall units in the spanwise direction and 1 wall unit in the wall normal direction [21]. One wall unit would correspond to $\frac{c}{Re\sqrt{C_f/2}}$ [18], where C_f is the average skin-friction coefficient. For a flat plate, $C_f \approx \frac{0.455}{ln^2(0.06Re)} = 0.0027$ [18]. Therefore, one wall unit $\approx 5 \times 10^{-6}c$. Hence, the total number of wall points is $\frac{10c^3}{100\times20\times1\times(5\times10^{-6}c)^3} \approx 10^{12}$.

In the wake region, in order to resolve the eddies, atleast 20 points are required per vorticity thickness [21]. Assuming the vorticity thickness $\approx 2r_c \approx 0.1c$, one would require $\frac{1}{(0.1/20)^3} \approx 10^7$ points per unit cube. Thus, for the wake region, the total number of points $\approx 10^9$. The time-step size would be governed

by the smallest mesh distance (1 wall unit), and hence the non-dimensional time-step can be expected to be 5×10^{-6}. Again, to convect to 50 chord lengths and to have atleast 10 averaging cycles, the total number of time-steps would be: $500/(5 \times 10^{-6}) \approx 10^8$.

LES with wall-layer models

For LES with wall layer models, savings can be expected in the streamwise and spanwise directions in the near-wall region [24]. At a rather coarse level, spacing requirements would reduce to approximately 600 wall units in the streamwise direction and 300 wall units in the spanwise direction, resulting in 10^{10} points in the near-wall mesh. Also, since the near wall eddies do not have to be resolved, the time-step restriction is assumed to be relaxed by an order of magnitude.

RANS calculations

In the RANS calculations, except for the requirement of the near-wall normal spacing (which is the same as the LES), the other mesh spacings are primarily governed by the required solution accuracy. Hence, using the computations in this thesis and work done by previous researchers (for instance, [40]) as a guideline, an extremely fine near-body mesh can be expected to require the order of 10^7 points. Assuming 10 points per core-length ($2r_c$) in the cross-stream direction of the tip vortex region and an average axial spacing of 0.5 c (far away from the wing surface, the streamwise gradients will be small) the total number of wake points $(50 \times 2 \times 2c^3)/(0.01 \times 0.01 \times 0.5c^3) \approx 10^7$. Also, these are steady state computations and hence a good implicit solver can be expected to converge in less than 10^4 iterations.

Euler equations

For the Euler equations, typically, a factor of 2 or 3 reduction can be achieved in number of points required in the wall-normal direction, along with a more rapid convergence to a steady state.

Inviscid vortex methods

Assume a vortex lattice method with 100 panels (of size $1c \times 0.2c$ in the spanwise and streamwise directions respectively) to model the wing surface and 10 panels shed in wake region every time-step (typical of refined computations shown in [27]). To reach a distance of 50c downstream of the trailing edge, 250 time-steps are required.

Appendix B

Linear Stability Analysis of Axisymmetric Vortices

As mentioned in sec. 2.4, the incompressible NS equations are linearized about a mean axisymmetric flow (U, V, W) in the radial, tangential and axial directions. Imposing disturbances of the form

$$\{u, v, w, p\} = \{iF(r), G(r), H(r), P(r)\}e^{i(\alpha x + m\theta - \omega t)}, \tag{B.1}$$

substituting into the NS equations and linearizing, the following equations are obtained [68]:

The linearized continuity equation is given by:

$$F'' + \frac{F}{r} + \frac{mG}{r} + \alpha H = 0 \tag{B.2}$$

The linearized r, θ and x momentum equations are respectively,

$$-\frac{iF''}{Re_v} + i\left[U - \frac{1}{Re_v r}\right]F' + \left[\omega + i\frac{dU}{dr} - \frac{mV}{r} - \alpha W + \frac{i}{Re_v}\left(\frac{m^2+1}{r^2} + \alpha^2\right)\right]F + \left[\frac{i2m}{Re_v r^2} - \frac{2V}{r}\right]G + P' = 0 \tag{B.3}$$

$$-\frac{G''}{Re_v} + \left[U - \frac{1}{Re_v r}\right]G' + \left[-i\omega + im\frac{V}{r} + i\alpha W + \frac{U}{r} + \frac{1}{Re_v}\left(\frac{m^2+1}{r^2} + \alpha^2\right)\right]G$$

$$+\left[\frac{2m}{Re_v r^2}+\frac{iV}{r}+i\frac{dV}{dr}\right]F+\frac{imP}{r}=0 \tag{B.4}$$

$$-\frac{H''}{Re_v}+\left[U-\frac{1}{Re_v r}\right]H'+\left[-i\omega+im\frac{V}{r}+i\alpha W+\frac{1}{Re_v}\left(\frac{m^2}{r^2}+\alpha^2\right)\right]H$$
$$\left[\frac{2m}{Re_v r^2}+\frac{iV}{r}+i\frac{dV}{dr}\right]F+\frac{idW}{dr}+i\alpha P=0 \tag{B.5}$$

The boundary conditions complete the definition of the eigenvalue problem and are give by:

$$F(\infty) = G(\infty)=H(\infty)=P(\infty)=0 \tag{B.6}$$

$$if \quad m=0, \quad F(0) = G(0)=H'(0)=P'(0)=0 \tag{B.7}$$

$$if \quad |m|>1, \quad F(0) = G(0)=H(0)=P(0)=0 \tag{B.8}$$

$$if \quad m=\pm 1, \quad F(0)\pm G(0) = F'=H'(0)=P'(0)=0 \tag{B.9}$$

The above set of equations are numerically solved by mapping the space $r = [0, r_{max}]$ to a bounded interval $\xi = [-1, 1]$, using the transformation

$$r=a\frac{1+\xi}{b-\xi}, \quad with \quad b=1+2\frac{a}{r_{max}} \tag{B.10}$$

Values of $a = 3$ and $r_{max} = 100$ are recommended in [68] and are found to give good clustering, while maintaining the outer boundary sufficiently far-off. The discretization of the above equations is done using Chebychev polynomials as discussed in [69], [68].

Appendix C

CPU time per iteration for 3D Compressible RANS solver

In this section, in order to obtain an estimate of the computational cost, several of the test cases that were presented in the thesis were evaluated for CPU time. On average, approximately 11 seconds of CPU time was required per iteration per million points on a single Intel Xeon processor with 2GB of RAM and a clock speed of 3.33GHz. Table C.1 shows a break up of the time per iteration for a representative overset mesh computation.

Procedure	Time per iteration
Inviscid RHS	35%
Viscous RHS	26%
LHS and Inversion	20%
Turbulence model	18%
BC and Interpolation	$< 1\%$

Table C.1: Typical break-up of CPU time per iteration

Bibliography

[1] Page, R.D., Clawson, K.L., Garodz. L.J. and Rudis, R.P., "Report on Tower Fly-by testing," *Proceedings of the FAA Wake Vortices Conference*, Washington, D.C., 1991.

[2] Spalart, P.R., "Airplane Trailing Vortices," *Annual Review of Fluid Mechanics*, Vol. 30, 1998.

[3] Leishman, J.G., "Principles of Helicopter Aerodynamics," Cambridge University Press, 1998.

[4] Green, S.I., "Fluid Vortices," Kluwer Academic Publishers, 1995.

[5] Crow, S.C., "Stability Theory for a Pair of Trailing Vortices," *AIAA Journal*, Vol. 8, No. 12, 1970.

[6] Rossow, V.J., "Lift Generated Vortex Wakes of Subsonic Transport Aircraft," *Progress in Aerospace Sciences*, Vol. 35, 1999.

[7] Sim, B.W-C., Schmitz, F.H., and Aoyama, T., "Radiation and Directionality Characteristics of Advancing Side Blade-Vortex Interaction (BVI) Noise," *AIAA/CEAS 6th Aeroacoustics Conference, Hawaii*, 2000.

[8] Moore, D.W. and Saffman, P.G., "Axial Flow in Laminar Trailing Vortices," *Proceedings of the Royal Society, London, A.*, Vol. 333, 1973.

[9] Chow, J.S., Zilliac, G.G., and Bradshaw, P., "Mean and Turbulence Measurements in the Near Field of a Wingtip Vortex," *AIAA Journal*, Vol. 35, No. 10, 1997.

[10] Devenport, W.J., Rife, M.C., Liapis, S.I., and Follin, G.J., "The Structure and Development of a Wing-tip Vortex," *Journal of Fluid Mechanics*, Vol. 312, 1996.

[11] Martin, P.B., Pugilese, G.J., and Leishman, J.G., "High Resolution Trailing Vortex Measurements in the Wake of a Hovering Rotor," *Proceedings of the 53rd Annual Forum of the American Helicopter Society*, 2001.

[12] Ramasamy, M., "Contributions to the Measurement and Analysis of Helicopter Blade Tip Vortices," *Ph.D Thesis, Department of Aerospace Engineering, University of Maryland at College Park*, 2004.

[13] McAlister, K.W., "Rotor Wake Development during the First Revolution," *Proceedings of the 59th Annual Forum of the American Helicopter Society*, 2003.

[14] Jacquin, L., and Pantano, C., "On the Persistence of Trailing Vortices," *Journal of Fluid Mechanics*, Vol. 471, 2002.

[15] Qin, J.H., "Numerical Simulations of a Turbulent Axial Vortex," *Ph.D. Thesis, Department of Aerospace Engineering, Purdue University*, 1998.

[16] Ragab, S. and Sreedhar, M., "Numerical Simulations of Vortices with Axial Velocity Deficits," *Physics of fluids*, Vol. 7, 1995.

[17] Leweke, T., Meunier, P., Laporte, F., and Darracq, D., "Controlled Interaction of Co-rotating Vortices," *Proc. 3rd ONERA-DLR Symposium*, 2001.

[18] White, F.M., "Viscous Fluid Flow," McGraw-Hill, 1991.

[19] Tennekes, H., and Lumley, J.L., "A First Course in Turbulence," MIT Press, 1972.

[20] Moin, P., and Mahesh, K., "Direct Numerical Simulation: A Tool in Turbulence Research," *Annual Review of Fluid Mechanics*, Vol. 30, 1998.

[21] Piomelli, U., Department of Mechanical Engineering, University of Maryland, Personal Communication.

[22] Smagorinsky, J., "General Circulation Experiments with the Primitive Equations," *Monthly Weather Review*, Vol. 93, 1963.

[23] Piomelli, U., "Large Eddy Simulation: Achievements and Challenges," *Progress in Aerospace Sciences*, Vol. 35, 1999.

[24] Piomelli, U., and Balaras, E., "Wall-layer Models for Large-Eddy simulations," *Annual Review of Fluid Mechanics*, Vol. 34, 2002.

[25] Spalart, P.R., Jou, W.H., Strelets, M., and Allmaras, S.R., "Comments on the Feasibility of LES for Wings and on the Hybrid RANS/LES Approach," *Proceedings of the 1st AFOSR International Conference on DNS/LES*, 1997.

[26] Srinivasan, G.R., and Baeder, J.D., "TURNS: A Free-wake Euler/ Navier-Stokes Numerical Method for Helicopter Rotors," *AIAA Journal*, Vol. 31, No. 5, 1993.

[27] Katz J., and Plotkin A., "Low-Speed Aerodynamics: From Wing Theory to Panel Methods," McGraw-Hill, 1991.

[28] Weissinger, J., "The lift Distribution on Swept-Back Wings," *NASA Technical Memorandum*, 1120, 1947.

[29] Rossow, V.J., "On Extended-Betz Methods for roll-up of Vortex sheets," *AIAA Journal of Aircraft*, Vol. 34, No. 5, 1997.

[30] Krasny, R., "Computation of Vortex Sheet Roll-up in the Trefftz Plane," *Journal of Fluid Mechanics*, Vol. 184, 1987.

[31] Bagai, A., "Contributions to the Mathematical Modeling of Rotor-Flow-Fields Using Pseudo-Implicit Free Wake Analysis," *PhD dissertation*, University of Maryland at College Park, MD, 1995.

[32] Bhagwat, M., "Mathematical Modeling of the Transient Dynamics of Helicopter Rotor Wakes using a Time-Accurate Free-Vortex Method," *PhD dissertaion*, University of Maryland at College Park, MD, 2001.

[33] Mansour, N.N., "Numerical Simulation of the Tip Vortex of a Low Aspect Ratio Wing at Transonic Speed," *AIAA Journal*, Vol. 23, No. 8, 1985.

[34] Usta, E.,"Application of a Symmetric Total Variation Diminishing Scheme To Aerodynamics of Rotors," *Ph.D. Dissertation, Department of Aerospace Engineering, Georgia Institute of Technology*, 2002.

[35] Strawn, R.C., and Djomehri, M.J., "Computational Modeling of Hovering Rotor and Wake Aerodynamics," *Journal of Aircraft*, Vol. 39, 2002.

[36] Hirsch, C., "Numerical Computation of Internal and External Flows, Volume 1," Wiley Publishers, 1988.

[37] Hirsch, C., "Numerical Computation of Internal and External Flows, Volume 2," Wiley Publishers, 1990.

[38] Wake, B.E., and Choi, D., "Investigation of high-order Upwinded Differencing for Vortex Convection," *AIAA Journal*, Vol. 34, No. 2, 1996.

[39] Spalart, P.R., "Trends in Turbulence Treatments," *AIAA Paper 2000-2306*, 2000.

[40] Egolf. T.A., "Recent Rotor Wake Simulation and Modeling Studies at United Technologies Corporation," *AIAA Paper 2000-0115*, 2000.

[41] Wilcox, D.C., "Turbulence modeling for CFD", DCW Industries, 1993

[42] Spalart, P.R., and Allmaras, S.R., "A One-equation Turbulence Model for Aerodynamic Flows," AIAA Paper 92-0439, 1992.

[43] Pope, S.B., "A More General Eddy-viscosity Hypothesis," *Journal of Fluid Mechanics*, Vol. 72, 1975.

[44] Jakirlic, S., Hanjalic, K., and Tropea, C., "Modeling Rotating and Swirling Turbulent Flows: A Perpetual Challenge," AIAA Journal, Vol. 40, No. 10, 2002.

[45] Spalart, P.R., and Shur, M., "On the Sensitization of Turbulence Models to Rotation and Curvature," *Aerospace Science and Technology*, Vol. 1, No. 5, 1997.

[46] Pettersson-Reif, B.A., Durbin, P.A., and Ooi, A., "Modeling Rotational Effects in Eddy-viscosity Closures," *International Journal of Heat and Fluid Flow*, Vol. 20, No. 6, 1999.

[47] Dacles-Mariani, J., Zilliac, G. G., Chow, J. S., and Bradshaw, P. "Numerical/ Experimental Study of a Wing tip Vortex in the Near Field," *AIAA Journal*, Vol. 33, No. 9, 1995.

[48] Hall, C.M., and Long, L.N., "High Order Accurate Simulations of Wake and Tip Vortex Flowfields," *Proceedings of the 55th Annual Forum of the American Helicopter Society*, 1999.

[49] Duque, E.P.N., and Srinivasan, G.R., "Numerical Simulation of a Hovering Rotor using Embedded Grids," *Proceedings of the 48th Annual Forum of the American Helicopter Society*, 1992.

[50] Ahmad, J., and Strawn, R.C., "Hovering Rotor and Wake Calculations with an Overset Grid Navier-Stokes Solver," *Proceedings of the 55th Annual Forum of the American Helicopter Society*, 1999.

[51] Potsdam, M., Yeo, H., and Johnson, W., "Rotor Airloads Prediction using Loose Aerodynamic/Structural Coupling," *Proceedings of the 60th Annual Forum of the American Helicopter Society*, 2004.

[52] Dacles-Mariani, J., Kwak, D. and Zilliac, G., "On Numerical Errors and Turbulence Modeling in Tip Vortex Flow Prediction," *International Journal for Numerical Methods in Fluids*, Vol. 30, 1999.

[53] Shur, M., Strelets, M., and Travin, A., " Two Numerical Studies of Trailing Vortices," *AIAA Paper 1998-595*, 1998.

[54] Datta, A., Sitaraman, J., Baeder , J.D., Chopra, I., "Improved Comprehensive Analysis For Prediction of Vibratory Loads in High Speed Forward Flight," *Proceedings of the 60th Annual Forum of the American Helicopter Society*, 2004.

[55] Hoffman, E.R. and Joubert, P.N., "Turbulent Line Vortices," *Journal of Fluid Mechanics*, Vol. 16, 1963.

[56] Batchelor, G.K., "Axial Flow in Trailing Line Vortices," *Journal of Fluid Mechanics*, Vol. 20, 1964.

[57] Iversen, J.D., "Correlation of Turbulent Trailing Vortex Decay Data," *Journal of Aircraft*, Vol. 13, No. 5, 1976.

[58] Phillips, W.R.C., "The Turbulent Trailing Vortex During Roll-up," *Journal of Fluid Mechanics*, Vol. 105, 1981.

[59] Cotel, A.J., and Breidenthal, R.E., "Turbulence Inside a Vortex," *Physics of Fluids*, Vol. 11, No. 10, 1999.

[60] Ramasamy, M., and Leishman, J.G., "A Generalized Model for Transitional Rotor Blade Tip Vortices," *Proceedings of the 60th Annual Forum of the American Helicopter Society*, 2004.

[61] Govindaraju, S.P., and Saffman, P.G., "Flow in a Turbulent Trailing Vortex," *Physics of Fluids* Vol. 14, No. 10, 1971.

[62] Lamb, H., "Hydrodynamics 6th ed," Cambridge University Press, 1932.

[63] Bradshaw, P., "The Analogy between Streamline Curvature and Buoyancy in Turbulent Shear Flow," *Journal of Fluid Mechanics*, Vol. 36, 1969.

[64] Squire, H.B., "The Growth of a Vortex in Turbulent Flow," *Aeronautical Quarterly*, Vol. 16, 1965.

[65] Saffman, P.G., "Vortex Dynamics," Cambridge University Press, 1992.

[66] Uberoi, M. S., "Mechanisms of Decay of Laminar and Turbulent Vortices," *Journal of Fluid Mechanics*, Vol. 90, 1979.

[67] Morton, B.B., "The Strength of Vortex and Swirling Core Flows," *Journal of Fluid Mechanics*, Vol. 38, 1969.

[68] Khorrami, M.R., "On the Viscous Modes of Instability of a Trailing Line Vortex," *Journal of Fluid Mechanics*, Vol. 225, 1991.

[69] Khorrami, M.R., Ash, R.L., and Malik, M.R., "Application of Spectral Collocation Techniques to the Stability of Swirling Flows," *Journal of Computational Physics*, Vol. 81, 1989.

[70] Mayer, E.W., and Powell, K.G., "Viscous and Inviscid Instabilities of a Trailing Vortex," *Journal of Fluid Mechanics*, Vol. 245, 1992.

[71] Rayleigh, L., "On the Dynamics of Revolving Fluids," *Proceedings of the Royal Society of London, A*, Vol. 93, 1916.

[72] Fabre, D., and Jacquin, L., "Viscous Instabilities in Trailing Vortices at Large Swirl Numbers," *Journal of Fluid Mechanics*, Vol. 500, 2004.

[73] Abramovitz, E., and Stegun, I., "Handbook of Mathematical Function," Dover Publications, 1965.

[74] Baker, G.R., Barker, S.J., Bofah, K.K. and Saffman, P.G., "Laser Anemometer Measurements of Trailing Vortices," *Journal of Fluid Mechanics*, Vol. 65, 1974.

[75] Bandyopadhyay, P.R., Stead, D.J., and Ash, R.L., "Organized Nature of a Turbulent Trailing Vortex," *AIAA Journal*, Vol. 29, 1991.

[76] Singh, P.I. and Uberoi, M.S., "Experiments on Vortex Stability," *Physics of Fluids*, Vol. 19, No.12, 1976.

[77] Jacquin, L., Fabre, D., Geffroy, P. and Coustols, E., "The Properties of a Transport Aircraft Wake in the Extended Near-field - An Experimental Study," *AIAA Paper 2001-1038*, 2001.

[78] Phillips, W.R.C. and Graham, J.A.H., "Reynolds-stress Measurements in a Turbulent Trailing Vortex," *Journal of Fluid Mechanics*, Vol. 147, 1984.

[79] Green, S.I. and Acosta, A.J., "Unsteady Flow in Trailing Vortices," *Journal of Fluid Mechanics*, Vol. 227, 1991.

[80] Thompson, D.H., "A Flow Visualization Study of Tip Vortex Formation," *ARL-Aero-Note-421*, 1983.

[81] Heyes, A.L., Jones, R.F., and Smith, D.A.R., "Wandering of Wing-tip Vortices," *Proceedings of the 12th International Symposium on Application of Laser Techniques to Fluid Mechanics, Lisbon*, 2004.

[82] Leishman, J.G., "Measurements of the Aperiodic Wake of a Hovering Rotor," Experiments in Fluids, Vol. 25, 1998.

[83] Caradonna, F.X., and Tung, C., "Experimental and Analytical Studies of a Model Helicopter Rotor in Hover," *NASA Technical Memorandum 81232*, 1981.

[84] Sitaraman, J., "CFD-based Unsteady Aerodynamic Modeling for Rotor Aeroelastic Analysis," *PhD Thesis, Department of Aerospace Engineering, University of Maryland at College Park*, 2003.

[85] Allen, C., "Multi-Bladed Lifting Rotor Simulation in Hover, Forward Flight, and Ground Effect," *AIAA Paper 2004-5288*, 2004.

[86] Steinhoff, J., and Mersch, T., "Computation of vortex formation over ELAC-1 configuration using vorticity confinement," *AIAA Paper 1995-6157*, 1995.

[87] Hariharan, N. and Sankar, L., "High-Order Essentially Nonoscillatory Schemes for Rotary-Wing Wake Computations,", *Journal of Aircraft*, Vol. 41, No. 2, 2004.

[88] Lee, Y-L., and Baeder, J.D., "Vortex Tracking in Overset Method for Quad Tilt Rotor Blade Vortex Interaction," *AIAA Paper 2003-3531*, 2003.

[89] Srinivasan, G.R., McCroskey, W.J., Baeder, J.D., and Edwards, T.A., "Numerical Simulation of Tip Vortices of Wings in Subsonic and Transonic Flows," *AIAA Journal*, Vol. 26, No. 10, 1988.

[90] Lockard, D.P., and Morris, P.J., "Wing-Tip Vortex Calculations Using a High-accuracy Scheme," *Journal of Aircraft*, Vol. 35, No. 5, 1998.

[91] Spall, R.E., "Numerical Study of a Wing-Tip Vortex Using the Euler Equations," *Journal of Aircraft*, Vol. 38, No. 1, 2001.

[92] Wake, B.E., and Baeder, J.D., "Evaluation of a Navier-Stokes Analysis Method for Hover Performance," *Journal of the American Helicopter Society*, Vol. 41, No. 1, 1996.

[93] Russell, J.W., Sankar, L.N., Tung, C. and Patterson, M.T., "Alterations of Tip Vortex Structure from a Hovering Rotor using Passive Tip Devices," *Proceedings of the 53rd Annual Forum of the American Helicopter Society*, 1997.

[94] Russell, J.W., Sankar, L.N. and Tung, C., "High Accuracy Studies of the Tip Vortex Structure from a Hovering Rotor," *AIAA Paper 1997-1845*, 1997.

[95] Yee, H.C., Sandham, N.D., and Djomehri, M. J., "Low-dissipative High-order Shock-capturing Methods Using Characteristic-based Filters," *Journal of Computational Physics,* Vol. 150, No. 1, 1999.

[96] Tang, L., "Improved Euler Simulation of Helicopter Vortical Flows," *PhD Thesis, Department of Aerospace Engineering, University of Maryland at College Park*, 1998.

[97] MacAlister, K.W., Schuker, C.A., Braum, L. and Wu, J.C., "3-D Wake Measurements near a Hovering Rotor for Determining Profile and Induced Drag," *NASA Technical Paper 3577*, 1995.

[98] Corsiglia, V.R., Jacobsen, R.A. and Chigier, N., "An experimental investigation of trailing vortices behind a wing with a vortex dissipator," *Proceedings of Aircraft Wake Turbulence and Detection*, 1971.

[99] Patterson, J.C., Hastings, E.C. and Jordan, F.L., "Ground development and flight correlation of the vortex attenuating spline device," *NASA Symposium on Wake Vortex Minimization, NASA SP-409*, 1976.

[100] Rossow, V.J., "Lift-generated vortex wakes of subsonic transport aircraft," *Progress in Aerospace Sciences, 35*, 1999.

[101] Quackenbush, T.R., Bilanin, A.J., McKillip, R.M., Jr., "Vortex wake control via smart structures technology," *Proceedings of the SPIE - The International Society for Optical Engineering, 2721*, 1996.

[102] Liu, Z., Russell, J.W., Sankar, L.N. and Hassan, A.A., "A study of rotor tip vortex structure alteration techniques," *Journal of Aircraft, 38(3)*, 2001.

[103] Mineck, R.E., "Study of potential aerodynamic benefits from spanwise blowing at wing-tip," *NASA Technical Paper, 3515*, 1995.

[104] Tangler, J.L., "Experimental investigation of the subwing tip and its vortex structure," *NASA CR-3058*, 1978.

[105] Ortega, J.M., "Stability characteristics of counter-rotating vortex pairs in the wakes of triangular-flapped airfoils," *PhD Thesis, Mechanical Engineering, University of California at Berkeley*, 2001.

[106] Orlandi, P., Carnevale, G.F., Lele, S.K. and Sharrif, K., "DNS study of stability of trailing vortices," *Proceedings of Summer Program, Center for Turbulence Research, Stanford University*, 1998.

[107] Smith, D.E., and Sigl, D., "Helicopter Rotor Tip Shapes for Reduced Blade Vortex Interaction," *AIAA Paper 95-0192*, 1995.

[108] Martin, P.B., and Leishman, J.G., "Trailing Vortex Measurements in the Wake of a Hovering Rotor Blade with Various Tip Shapes," *Proc. 58th Annual Forum of the American Helicopter Society*, 2002.

[109] Tangler, J.L., "Experimental Investigation of the Sub-wing Tip and its Vortex Structure", *NASA CR-3058*, 1978.

[110] Gowanlock, D.K., and Mathewson, C.S., "Control of Rotor Tip Vortices," *AIAA Paper 99-0012*, 1999.

[111] Han, Y.O., and Leishman, J.G., "Experimental Investigation of Tip Vortex Alleviation using a Slotted Tip Rotor Blade," *Proc. 59th Annual Forum of the American Helicopter Society*, 2003.

[112] Brooks, T., and Booth, E., "The Effects of Higher Harmonic Control on Blade-Vortex Interaction Noise and Vibration," *Journal of the American Helicopter Society*, Vol. 38, No. 3, 1993.

[113] Jacklin, S.A., Nguyen, K.Q., Blaas, A., and Richter, P., "Full-scale Wind Tunnel Test of a Helicopter Individual Blade Control System," *Proc. 50th Annual Forum of the American Helicopter Society*, 1994.

[114] Anderson, E.A., and Lawton, T.A., "Correlation Between Vortex Strength and Axial Velocity in a Trailing Vortex," *Journal of Aircraft*, Vol. 40, No.4, 2003.

[115] Billant, P., Chomaz, J.M., and Huerre, P., "Experimental Study of Vortex Breakdown in Swirling Jets," *Journal of Fluid Mechanics*, Vol. 376, 1998.

[116] Vinokur, M., "An Analysis of Finite-difference and Finite-volume Formulations of Conservation Laws," *Journal of Computational Physics*, Vol. 81, No. 1, 1989.

[117] Toro, E.F., "Riemann Solvers and Numerical Methods for Fluid Dynamics: A Practical Introduction," Springer-Verlag, 1997.

[118] Titarev, V.A., and Toro, E.F., "Finite-volume WENO Schemes for Three-dimensional Conservation Laws," *Journal of Computational Physics*, Vol. 201, No. 1, 2004.

[119] Van Leer, B., "Towards the Ultimate Conservative Difference Scheme V. A Second Order Sequel to Godunov's Method," *Journal of Computational Physics*, Vol. 32, 1979.

[120] Koren, B., "Upwind Schemes, Multigrid and Defect Correction for the Steady Navier-Stokes Equations," *Proceedings of the 11th International Conference on Numerical Methods in Fluid Dynamics*, 1998.

[121] Roe, P., "Approximate Riemann Solvers, Parameter Vectors and Difference Schemes," *Journal of Computational Physics*, Vol. 43, 1981.

[122] Baldwin, B.S., and Lomax, H., "Thin Layer Approximation and Algebraic Model for Separated Turbulent Flows," *AIAA paper 1978-0257*, 1978.

[123] Hairer, E., and Wanner, G., "Solving Ordinary Differential Equations Vol. 2," Springer-Verlag, 1996.

[124] Yoon, S. and Jameson, A., "Lower-Upper Symmetric-Gauss-Seidel Method for the Euler and Navier-stokes Equations," *AIAA Journal*, Vol. 26, 1988.

[125] Pulliam, T., "Time Accuracy and the use of Implicit Methods," *AIAA Paper 1993-3360*, 1993.

[126] Laney, C.B., "Computational Gasdynamics," Cambridge University Press, 1998.

[127] Cockburn, B., Johnson, C., Shu, C.-W. and Tadmor, E., "Essentially Non-oscillatory and Weighted Essentially Non-oscillatory Schemes for Hyperbolic Conservation Laws in Advanced Numerical Approximation of Nonlinear Hyperbolic Equations," *Lecture Notes in Mathematics*, Vol. 1697, 1998.

[128] Yee, H.-C., Sandham, N. and Djomehri, M., "Low Dissipative High Order Shock-Capturing Methods using Characteristic-Based Filters," *Journal of Computational Physics*, Vol. 150, 1999.

[129] Chung, Y.M., and Tucker, P.G., "Accuracy of Higher Order Finite Difference Schemes on Nonuniform Grids," *AIAA Journal*, Vol. 41, No. 8, 2003.

[130] Hairer, E., Norsett, S.P., and Wanner, G., "Solving Ordinary Differential Equations Vol. 1," Springer-Verlag, 1993.

[131] Hoffman, K.A., and Chiang, S.T., "Computational Fluid Dynamics, Vol. 2," EES Books, 2000.

[132] Hyunh, H.T., "Accurate Monotone Cubic Interpolation," *SIAM Journal of Numerical Analysis*, Vol. 30, 1993.

[133] Baldwin, B.S., and Barth, T.J., "A One Equation Transport Model for High Reynolds Number Wall-Bounded Flows," *NASA TM-102847*, 1990.

[134] Gatski, T.B., and Speziale, C.G., "On Explicit Algebraic Stress Models for Complex Turbulent Flows," *Journal of Fluid Mechanics*, Vol. 254 , 1993.

[135] Srinivasan, G.R., Ekaterinaris J. A., and McCroskey, W. J., "Evaluation of Turbulence Models for Unsteady Flows of an Oscillating Airfoil," *Computers and Fluids*, Vol. 24, No. 7, 1995.

[136] Kalitzin, G., "An Implementation of the $v^2 - f$ Model with Application to Transonic Flows," *Center for Turbulence Research Annual Research Briefs, Stanford University*, 1998.

[137] Walsh, P.C., and Pulliam, T., "The Effect of Turbulence Model Solution on Viscous Flow Problems," *AIAA Paper 2001-1018*, 2001.

[138] Schmitt, V., and Charpin, F., "Pressure Distributions on the ONERA-M6-Wing at Transonic Mach Numbers, Experimental Data Base for Computer Program Assessment," *AGARD Report AR 138,* 1979.

[139] Han, Y.O., and Leishman, J.G., "Hovering Performance of a Rotor with Slotted Blade Tips," *Proc. 60th Annual Forum of the American Helicopter Society*, 2004.

[140] Wesseling, P., "Introduction to Multigrid Methods," *ICASE Report No. 95-11, Institute for Computer Applications in Science and Engineering*, 1995

[141] Gupta, V., "An Investigation of Quad Tilt Rotor Aerodynamics in Helicopter mode," *PhD Thesis, Department of Aerospace Engineering, University of Maryland at College Park*, 2005.

[142] Meakin, R.L., "Object X-Rays for Cutting Holes in Composite Overset Structured Grids," *AIAA Paper 2001-2537*, 2001.

[143] Petersson, N.A., "Hole-Cutting for Three-Dimensional Overlapping Grids," *SIAM Journal on Scientific Computing*, Vol. 21, No. 2, 1999.

[144] Liu, X.-D., Osher, S. and Chan, T., "Weighted Essentially Non-oscillatory Schemes," *Journal of Computational Physics*, Vol. 115 1994.

[145] Zilliac, G., Personal Communication.

[146] Heyes, A.L., and Smith, D.A.R., "Spatial perturbation of a wing-tip vortex using pulsed spanwise jets," *Experiments in Fluids, 37*, 2004.

[147] Landgrebe, A.J., "The Wake Geometry of a Hovering Rotor and its Influence in Rotor Performance," *Journal of the American Helicopter Society*, Vol. 17, No. 4, 1972.

[148] Dubief, Y., and Delcayre, F., "On Coherent-vortex Identification in Turbulence," *Journal of Turbulence*, Vol. 1, 2001.

[149] Young, L.A., "Rotor Vortex Filaments: Living on the Slipstream's Edge," *NASA Technical Memorandum 110431*, 1997.